Integration of the BiSb topological insulator on industrial substrate : from structural to electrical characterisations

Dima Sadek

THÈSE

En vue de l'obtention du
DOCTORAT DE L'UNIVERSITÉ DE TOULOUSE

Délivré par l'Université Toulouse 3 - Paul Sabatier

Présentée et soutenue par

Dima SADEK

Le 25 octobre 2022

Intégration de l'isolant topologique BiSb sur un substrat industriel : des caractérisations structurelles aux caractérisations électriques

Ecole doctorale : **GEETS - Génie Electrique Electronique,Télécommunications et Santé : du système au nanosystème**

Spécialité : **MicroNano Systèmes**

Unité de recherche :
LAAS - Laboratoire d'Analyse et d'Architecture des Systèmes

Thèse dirigée par
Filadelfo CRISTIANO et Sébastien PLISSARD

Jury

M. Ludovic DESPLANQUE, Rapporteur
M. Laurent CERUTTI, Rapporteur
M. Jean François BOBO, Examinateur
M. Filippo GIANNAZZO, Examinateur
M. Thierry CAMPS, Examinateur
Mme Layla MARTIN-SAMOS, Examinatrice
M. Sébastien PLISSARD, Co-directeur de thèse
Mme Véronique BARDINAL, Présidente

الإهداء

فإنّه بسم الله الرحمٰن الرحيم . .

من هنا ،
بمقدار آلاف المسافات التي تمّ إجتيازها ،
وبقدر المسافة بين المشرق والمغرب :
إلى الأكفّ التي كولا ما رفعتها ،لما اجتزت عُباب البحر ،
إلى أمّي ،
قبلة الحبّ ،ومنارة المحبّة ،
إلى صلواتها ودعواتها ،إلى قلقها وخوفها ،
إلى ضحكتها الخفيّة ،
ثمّ إلى أبي الحنون ، إلى وقفته وصموده ،إلى عرق جبينه ،
ألف سلام . . .

إلى الأحبّة :
إلى أخوة الرّحم الواحد والحبّ الواحد :
إلى أختي رانيا الرّوح المكمّلة لروحي ومَلجأي في غربتي
أخي محمّد ، كتفي الثابت حين أميل رأسي وحين يميل العالم بي . .
إلى أجمل ما أهدتني أختي طوال عمري ،
إلى الحبّ الطفوليّ الذي يحرّك طفولة فيني . .
الى فلذتيّ كبدي ، لين و جواد
إلى إخوتي من رحم الحياة ، ابراهيم و ريم
إلى نسمة خفيفة لطيفة وعند الشدّة سند !
سلامٌ وسلام . .
سلامٌ أهدي فيه نجاحاً مكللاً بمحبّتكم ،

من هنا من أقاصي تولوز الفرنسيّة ،إلى مرقد فؤادي لبنان ،وألف تحيّة . .
إلى مدينتين تنبضان في قلبي : بيروت والخيام ،
بيروت بصخبها للحياة ،والخيام بهدوئها الذي يعيد لقلبي الحياة ،
إلى تفاصيل لا أبرح أعيشها في الذاكرة ،
ممن أعماقي إليكم ،
إنما لا يفرح المرء بنجاحاته مهما عظمت إلا بمشاركة الأحبّة ،
فذي هديّتي . .وألف سلام . . .

ديما

Remerciement

Tout d'abord, je tiens à adresser mes sincères remerciements à mon co-directeur de thèse, Sébastien PLISSARD, sans qui ce travail durant ces années de thèse, n'aurait pu aboutir. Son soutien, sa patience, ses conseils judicieux et sa disponibilité pour diriger mes travaux de recherches tout en répondant à toutes mes questions m'ont été d'une aide considérable. Ses connaissances approfondies m'ont permis de mener à bien ce travail. De plus, je tiens à le remercier pour sa bonne humeur et sa positivité qui permettaient de rendre le travail et les réunions agréables. Je ne peux qu'être fier du travail accompli grâce à son immense aide , je lui en suis profondément reconnaissante. Je tiens également à remercier chaleureusement mon directeur de thèse, Fuccio CRISTIANO, pour son aide et pour son écoute en cas de besoin.

Je pourrai ne pas assez remercier Alexandre ARNOULT, avec qui j'ai énormément appris. Je le considère comme étant co-directeur de thèse et je suis très reconnaissante de son aide en salle blanche. Son soutien ainsi que ses recommandations judicieuses ont renforcé ma volonté et ma motivation à accomplir ce travail. J'exprime également mes remerciements à Anne HEMERYCK et Antoine JAY avec qui j'ai exploré le monde du calcul DFT. Je leur suis très reconnaissante d'avoir éveillé ma curiosité scientifique sur cette thématique ainsi que pour leur bonne humeur. Je suis ravie de les avoir rencontré. Je remercie également Corentin DURAND pour m'avoir aidé à explorer le monde du transport électronique, et Quentin GRAVELIER pour son aide précieux concernant la technique d'épitaxie par jet moléculaire. Je souhaite aussi remercier Richard DAUBRIAC, Emmanuelle DARAN, Richard MONFLIER, Benjamin REIG pour toute leur aide lors des différentes caractérisations.

J'exprime ma gratitude à Ludovic DESPLANQUE et Laurent CERUTTI pour avoir accepté d'être rapporteurs de ma thèse et d'avoir consacrer du temps à examiner le manuscrit. Ils m'ont fait l'honneur de bien vouloir étudier avec attention mon travail. Je suis très honorée d'avoir en jury de thèse, Paola ATKINSON et Layla Martin SAMOS et je les remercie d'avoir

accepté l'invitation.

Je remercie également toutes les personnes de l'équipe MPN pour leur accueil chaleureux, leur soutien, leurs encouragements, le partage de leurs connaissances et les échanges amicaux pendant ces trois années. Ils ont toujours été présents pour répondre à mes questions. Je remercie mon collègue du bureau, Peter WIECHA pour sa gentillesse, et je lui souhaite une très bonne continuation dans ses futurs travaux. Je souhaiterais remercier toutes les personnes du laboratoire que j'ai pu fréquenter au cours de ma thèse.

Je voudrais également remercier Liviu NICU, ancien directeur du LAAS et Mohamed KAANICHE, directeur actuel du LAAS de m'y avoir accueilli dans de bonnes conditions de travail. Je les remercie des efforts consentis durant toute la période d'épidémie du coronavirus et de confinement, pour nous tenir informer de l'actualité au quotidien et d'avoir faciliter nos conditions de travail.

Mes remerciements et mes pensées vont également à tous mes amis qui m'ont soutenu lors de mon séjour dans la magnifique ville de Toulouse. Je remercie en particulier Marianne, Alassane, Josué, Barbara, Sébastien, Dany, Asma, Chaymaa et Clara qui m'ont accompagné et encouragé pendant tous ces moments au LAAS et qui m'ont apporté leur support moral tout au long de ces dernières années. Nos souvenirs sont gravés dans ma mémoire et je n'oublierai jamais chaque moment passé avec chacun d'entre eux. Une pensée particulière à Marianne, une soeur de cœur que la vie m'a offert. Je suis très chanceuse et très reconnaissante de l'avoir rencontrée et d'être considérée comme membre de sa propre famille. Merci "Marriano" d'être la personne que tu es, merci de me prêter ton épaule pour que je puisse m'y appuyer et merci pour tous nos beaux moments. "Marriano" on restera des sœurs pour la vie "lal mot ya z8ayar". Je remercie aussi "Alousse", l'homme de toutes les qualités, qui a toujours été à mes côtés et qui m'a toujours fait garder le sourire même dans les moments difficiles. Je ne pourrai jamais remercier Jana à la hauteur de sa gentillesse. Tu es l'une des personnes avec qui je partage des moments agréables. Merci "abbafe" d'être resté à mes côtés. Avec toi, il n'y a vraiment rien que nous ne puissions accomplir. Je présente mes remerciements à tous mes autres amis à Toulouse, ceux du Liban et dans toute la France.

Je ne saurais terminer sans remercier ma famille sans qui ce travail n'aurait pas vu le jour. Un GRAND MERCI à tous les membres de ma famille au Liban qui m'ont soutenu et qui malgré la distance, ont toujours été présents pour moi depuis mon arrivée en France. Avant tout, je remercie DIEU, le tout puissant de m'avoir accordé la vie, la santé, la force et le courage de surpasser et surmonter les difficultés de la vie. Je LE remercie de m'avoir bénie d'être dans une famille telle que la mienne. Les mots ne

pourront pas décrire les sentiments que j'éprouve d'être bien entourée. Je remercie ma mère et mon père pour leurs tendresses, pour leurs prières et pour leur amour inconditionnel. La confiance qu'ils m'ont accordée m'a permis de ne jamais douté de mes capacités. Ils m'ont toujours épaulée dans mes études et mes décisions. Je ne pourrais jamais assez les en remercier! Je suis très reconnaissante envers ma soeur Rania, qui m'a aidée à avoir confiance en moi et dont son soutien rend les difficultés banales et surmontables. Être sans ma soeur, c'est comme être sans coeur et sans âme. Je remercie profondément mon frère Mohammad "Habibi" mon pilier, mon repère, pour ses encouragements et qui est pour moi un pilier du fondamental de la personne que je suis. Je ne pourrai pas imaginer une vie sans toi "big brother". Je remercie également Ibrahim et Rim, mon beau-frère et ma belle-soeur d'avoir été l'épaule sur lequel je m'appuie. Merci de faire partie de ma famille et d'avoir partager avec moi de beaux moments. Je ne pourrai pas terminer sans exprimer mon amour envers mes neveux, Leen et Jawad. Je vous adore tous les deux et merci d'être dans ma vie!!! Enfin, je remercie Liban, mon beau pays, qui survit malgré les difficultés. Ce pays, a contribué à faire de moi la femme que je suis et à garder certaines valeurs : la patience, la persévérance et l'esprit de combativité pour arriver à mes buts. A travers son histoire, j'ai appris surmonter et à me relever à chaque difficulté de la vie. Je remercie également la France, mon deuxième pays de m'avoir accueillie et de m'avoir appris qu'il n'y a rien d'impossible.

DU FOND DU COEUR, MERCI A TOUS !!

Contents

Notation

This section provides the notations used all along the thesis.

- C_H: Hall concentration.
- E_F: Fermi energy.
- F: element flux
- h: Film thickness.
- R_H: Hall coefficient.
- N_H: Hall sheet concentration.
- p: Specularity parameter.
- Z: atomic number.
- Z_2: Topological Invariant.
- μ_H: Hall mobility.

Acronyms

This section provides the acronyms used all along the thesis.

- AFM: Atomic Force Microscopy.
- ARPES: Angle Resolved Photo Emission Spectroscopy.
- BiSb: Bismuth-antimony alloy.
- BZ: Brillouin zone.
- CB: Conduction band.
- ES: Ehrlish-Schowbel.
- FCC: Face Centered Cubic.
- FS: Fuchs and Sondheimer model.
- FWHM: Full width at half maximum.
- GaAs: Gallium arsenic.
- IC: Integrated Circuit.
- LDOS: Local Density of States.
- MBE: Molecular Beam Epitaxy.
- MF: Majorana Fermion.
- MRAM: Magnetoresistive Random Access Memories.
- MS: Mayadas and Shatzkes model.
- MZM: Majorana Zero mode.

- NASA: National Aeronautics and Space Administration.
- QSH: Quantum Spin Hall.
- QW: Quantum Well.
- RHEED: Reflection High Energy Electron Diffraction
- SEM: Scanning Electron Microscopy.
- SOI: Spin-Orbit Interaction.
- SOT: Spin-Orbit Torque
- SRAM: Static Random-access memory.
- STM: Scanning Tuneling Microscopy.
- STT: Spin Transfer Torque.
- TEM: Transmission Electron Microscopy.
- TI: Topological Insulator.
- VB: Valence band.
- UHV: Ultra high vacuum.
- WSM: Weyl Semimetals.
- XRD: X-Ray Diffraction.

Introduction

In the 16th century, a "computer" was describing a person who made computations and enter results into tables. During the Industrial Revolution, the British mathematician Charles Babbage decides to find another way to carry out these calculations with less manpower. In 1822, he succeeded in inventing a device capable of making complex calculations faster with fewer errors. This device is considered as the first computer and called "Analytical Engine". Since then the inventors have adapted the Babbage design and tend to upgrade its functionalities in order to meet the commercial needs. At the beginning, computers were big and required high power due to their design based on thousands of vacuum tubes. In 1947, a "second generation" of computers arises thanks to the invention of the first transistor [1]. The latter was intended for use in place of vacuum tubes to reduce computer size and power consumption. Thanks to their small size, many transistors can be integrated on a small semiconductor material forming an Integrated Circuit (IC), which is suitable for computer design. This leds to the success of modern computers. Subsequently, motivated by Moore's law, the number of transistors implemented in IC doubled every year in order to further improve the computer power. From the fundamental point view, each transistor is a binary switch that allows current to flow through it or not. Generally, the Static random-access memory (SRAM) of a computer uses six transistors to store information in a one "bit". To make it easy for humans to understand, the inventors describe a "bit" by using the boolean convention: "0" and "1": "0" indicates that the current flow is interrupted in the transistor whereas "1" indicates that the current flow is allowed. Therefore, increasing the number of transistors in IC gives more possibilities to store and manipulate information in the computer memory.

Despite their optimisation, modern computers do not respond all consumer needs as they cannot handle some complex scientific or mathematical problems. In 1981, Richard Feynman proposed a quantum version of the classical binary "bit", called quantum bit (Qubit). Similarly to "bits", Qubits also have two states "0" and "1" but what distinguishes them from "bits" is

the use of two important quantum mechanics phenomena: superposition and entanglement. The consequence is that for two quantum levels, $|0\rangle$ and $|1\rangle$, the whole Bloch sphere is available and thus an infinite number of states exist. This fundamental proposal has attracted a lot of attention in computer science and was first used by Peter Shor in 1994 to develop a quantum algorithm. Despite early success in fabricating the first quantum computer by Chuang, Gershenfeld and Kubinec in 1998, a lot of difficulties limit their development such as high level of noise in Qubits and the loss of quantum coherence due to material and fabrication imperfections. In October 2019, Google, in cooperation with the U.S. National Aeronautics and Space Administration (NASA), claimed the Quantum supremacy on a limited problem, which is still far from the universal Quantum computer.

Qubits can be constructed by any two-level quantum system, allowing them to be implemented in multiple ways such as photons, electrons, nucleus, optical lattices, Josephson junctions, Quantum dots, etc. and based on diverse physical principles such as the polarisation of light, the spin or the charge of electrons or atoms, etc. Josephson junctions, one of the most advanced method, are devices builded by sandwiching an insulator between two superconductors. Another interesting possibility to build a Qubit without the need for extremely cold temperatures is to take advantage of the defects in crystals. These defects can act as electron traps allowing researchers to control their spin and construct Qubits having long coherence time. In 2011, a group of researchers proposed a new method to create topologically protected Qubits based on the implementation of Majorana fermions (MFs) in hybrid interfaces. These fermions are "real" solution of the Dirac equation and thus are particles that are their own antiparticles. The implementation of quasiparticles that have the same properties than MF is possible in condensed matter. One of the possibilities is to couple a superconductor (Al, NbN) and a high electron mobility III-V nanowire such as InAs and InSb. The strong spin-orbit interactions in these nanowires allows to create Majorana zero modes (MZM) at their interface with a superconductor. Nevertheless, disorder in the hybrid interface is considered a serious bottleneck since it can mimic Majorana signature. Meanwhile, the discovery of a new phase of matter called the topological insulator (TI) has attracted much attention and is considered promising for quantum information processing. In such condensed matter systems, the electronic surface states are topologically protected from the environment, making them an ideal platform for future quantum devices. They show promises for hosting and protecting Majorana zero modes (MZM) from the environment, thus leading to improve the MZM quality and increase the Qubit coherence time. In their pioneer paper, Kane and Mele [2] predicted the existence of topological insulators, which are insulators in the

bulk and exhibit metallic surface states. These states are topologically protected by time-reversal symmetry and spin-orbit interactions. Shortly after this theoretical proposal, TIs were first realised in 2D systems containing HgTe quantum wells, and in Bismuth-Antimony alloys ($Bi_{1-x}Sb_x$) for 3D TIs. Despite numerous TIs being reported thereafter, including most of the chalcogenides, BiSb remains the most promising for spintronic applications thanks to its large conductivity ($\sim 10^5\ \Omega^{-1}m^{-1}$), its colossal spin Hall angle ($\sim 52°$) and the possibility to build low current spin-orbit-torque (SOT) magnetoresistive random access memories (MRAM). Moreover, it is possible to control the alloy composition, and thus to tune precisely its electronic properties. Indeed, $Bi_{1-x}Sb_x$ is predicted to behave as a topological semimetal for 0.04<x<0.07, as a topological insulator for 0.07<x<0.22 or as a Weyl semimetal for x=0.5 or x=0.83.

This thesis deals with the development of new nanoscale $Bi_{1-x}Sb_x$ Topological Insulators grown by Molecular Beam Epitaxy (MBE) and integrated on industrial substrates. It is organised as follows:

- In **Chapter 1**, we present an overview about the Topological Insulator materials and briefly report some key historical dates on the most well-known TIs. We also provide an overview of the reasons for our interest in working on the exciting $Bi_{1-x}Sb_x$ alloys.

- In **Chapter 2**, we address the crucial role of the "epitaxy" method in the nanomaterials manufacturing. We briefly describe the different types of epitaxy by presenting all the parameters involved in the epitaxial process. Next, the two main processes, thermodynamics and kinetics, that control the growth mechanism are discussed. Finally, we address the crucial role of the substrate which is considered as the "basic building block" to achieve high quality epitaxy.

- In **Chapter 3**, we present the fabrication and characterisations techniques used during my thesis. This chapter starts by describing the standard Molecular Beam Epitaxy (MBE) system followed by a brief description of in-situ characterisation tools such as the Bayard-Alpert gauge, reflection high energy electron diffraction (RHEED) and Wafer Curvature Optical Control. Next, an introduction to Electron Microscopy is presented, followed by a brief description of Scanning Electron Microscopy (SEM), Transmission Electron Microscopy (TEM) and Scanning Tunnelling Microscopy (STM). Similarly, Atomic Force Microscopy (AFM), X-Ray Diffraction measurements and Hall measurements are presented.

- In **Chapter 4**, we investigate the direct integration of high quality BiSb layers on industrially available GaAs(001) substrates using a MBE 412 system. We study the effect of the growth conditions such as temperature, stoichiometry, film thickness and growth rate on the structural quality of the grown layer. Finally, advanced characterisations such as TEM and STM are performed to highlight the clear epitaxial relationship between the quasi-hexagonal $Bi_{1-x}Sb_x$ material on the standard GaAs(001) cubic substrate and the high quality of the epitaxial layers.

- In **Chapter 5**, we report the epitaxial growth of quasi-hexagonal BiSb materials on semi-insulating hexagonal GaAs(111)A substrates using MBE. All parameters involved such as substrate surface, temperature, Sb composition, BiSb film thickness and growth rate are studied one by one in order to optimise the growth conditions. We prove that optimised growth conditions result in very smooth and organised surface morphology of epitaxial BiSb films. Finally, a TEM characterisation of the $Bi_{1-x}Sb_x$ films is performed.

- In **Chapter 6**, we address the effect of substrate and growth conditions on the electrical properties of $Bi_{1-x}Sb_x$ films. Transport measurements performed on GaAs(001) and GaAs(111)A by the four-terminal method are reported using a Van der Pauw configuration. On both substrates, we study the effect of the Sb composition and the sample thickness on the electrical properties. Finally, we prove that optimised growth conditions lead to the appearance of the topological phase in BiSb films.

Team Contribution

This thesis benefited from the support of the LAAS-CNRS micro and nanotechnologies platform, which is a member of the French RENATECH network.
I grew all samples in the MBE reactor, characterised them by XRD, AFM and SEM. I built Hall effect devices for GaAs(001) substrates with my colleague Richard Daubriac and their electrical measurements were performed by colleagues from the MPN team. The device fabrication and electrical measurements on the GaAs(111)A wafers was handled by colleagues from the MPN team and STM measurement was performed by Roland Coratger and Corentin Durand from the CEMES-CNRS lab. Moreover, TEM characterisations were operated by Remi demoulin, Fuccio Cristiano and Pier Francesco Fazzini and EBSD ones by Arnaud Proietti. I managed the DFT calculation by collaborating with Anne Hemeryck and Antoine Jay.

1

$Bi_{1-x}Sb_x$ Topological Insulator

1.1 Overview

Topological insulators (TIs) are a new family of materials that were developed over the last decade and are promising for quantum computers and spintronics applications [3, 4]. This new phase of matter is characterised by an inverted bulk bandgap driven by strong spin-orbit interactions. As a direct consequence, the TI surface exhibits metallic states topologically protected [5] by the combination of time-reversal symmetry and spin-orbit interactions [6,7]. Contrary to hybrid semiconductor-superconductor devices that are noisy due to junction imperfection [8,9], a TI coupled to a superconductor [10] should allow to harbour and protect Majorana bounds [11] states from environment. It is thus possible to build extremely robust quantum memory bits with these interfaces [12]. Moreover, the presence of spin-orbit torques (SOT) [13, 14] at the TI surface provides an energy efficient writing method for magnetoresistive random access memories (MRAM), due to the TI large spin Hall angle, and its high electrical conductivity [14]. Both applications require the integration of TIs on industrial substrates.

This chapter starts with a brief description of the TIs in Section 1.2, where we show how the presence of an unusual metallic states at the edge of a material motivated a large number of theoretical and experimental studies. We show how TIs completely changed the vision of condensed matter and sparked a revolution in quantum computing and spintronics. In Section 1.3, I describe the first topological insulator realised in a 2D system containing HgTe quantum wells. In Section 1.4, $Bi_{1-x}Sb_x$ alloys, the first experimentally confirmed 3D topological insulator are presented, as well as their crystalline structure and electronic properties. Other Bi-based TIs compounds are presented in Section 1.5 starting with BiTe, BiSe, BiSbTe, BiTeSe and BiSbTeSe. At the end of the chapter, Section 1.6 provides our motivations to grow BiSb materials.

1.2 Topological Insulator

The birth of the TIs materials began in 1985 when two researchers Volkov and Pankratov noticed an exotic phenomenon in the PbTe/SnTe heterostructure resulting in a 2D Dirac cone at their interface [15]. They propose the existence of non-degenerate 2D metallic states at the interface between two semiconductors provided that one of them has an inverted band structure. This discovery encouraged them to expand their collaboration with Pakhomov. In 1987, they suggested that a HgTe layer sandwiched between two CdTe layers has the same features as the PbTe/SnTe heterostructure [16], which was confirmed experimentally at the beginning of the 21st century [17, 18]. Despite numerous theoretical studies, this new class of materials was considered strange and fuzzy by scientists until the publication of Kane and Mele's pioneering article [2] in 2005. They distinguish these materials from ordinary insulators by introducing a new topological invariant "Z_2". Physically, this new topological index highlights the importance of time reversal symmetry in the protection of metallic states, which makes them robust against disorder and interactions. Besides the time reversal symmetry, they explained the crucial role of strong spin-orbit interactions on the material band structure: the electron spin cannot be neglected anymore. Therefore, the combination of these two quantum characteristics leads to the creation of a topological phase called the quantum spin Hall one. Shortly after this theoretical proposal, A.Bernevig et al. [17] suggest a reasonable realisation of a 2D TIs system containing HgTe quantum wells. They proposed the existence of a critical HgTe thickness, where a transition from a normal insulator to quantum spin Hall phase occurs. One year later, this theoretical proposal was verified experimentally by another research group [18].

Subsequently, Fu and Kane [19] introduced "3D topological insulators" and differentiate them from the two-dimensional quantum spin-Hall phase by the number of Z_2 invariants. They defined a single Z_2 for 2D-TIs, while four Z_2 are needed for 3D TIs. They also distinguish two types of TIs: trivial (weak TIs) or nontrivial (strong TIs) ones. Strong TIs are distinguished from weak ones by an odd number of crossings between the Fermi level and the surface states. This prevents the metallic states from being gapped even in the presence of non-magnetic perturbations [20] and regardless of the position of the chemical potential [21]. In the case of 3D TIs, the four Z_2 indexes are denoted "ν_0, ν_1, ν_2 and ν_3" and for a $\nu_0 = 0$ the TI behaviour is considered as "weak" whereas for $\nu_0 = 1$, it is considered as "strong". This study allowed to identify "strong" TIs including Bi compounds such as $BiSb$, Bi_2Se_3, Bi_2Te_3, $BiTeSe$ and $BiSbTeSe$.

In the following, we will briefly discuss in a chronological order the most

important topological insulators.

1.3 HgTe quantum wells

At the start of the 21st century, researchers were interested in obtaining a new state of matter, the quantum spin Hall phase (QSH). In 2006, a group of researchers proposed a reasonable strategy based on the HgTe system to establish a topological phase transition. Based on this proposal, the group of L. Molenkamp [18], succeeded in experimentally confirming the QSH phase in HgTe QW, thus becoming the first 2D topological insulator to be observed experimentally.

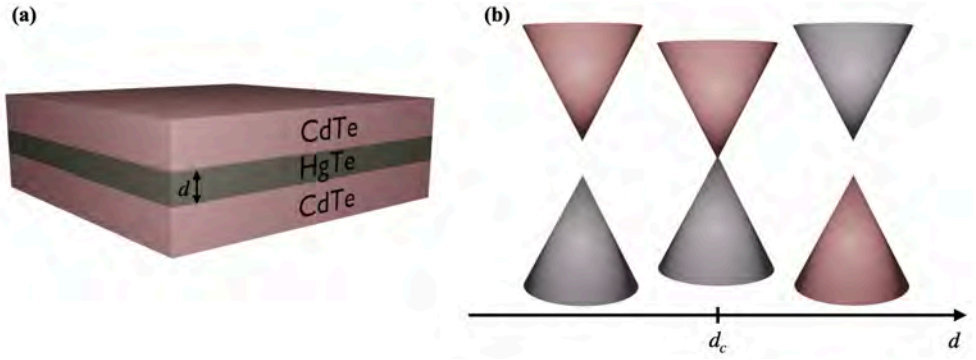

Figure 1.1: *A typical HgTe quantum well. (a) Schematic illustration of a HgTe quantum well sandwiched between two CdTe layers. (b) Sketch of the transition from a normal band structure to an inversion band structure when the HgTe thickness becomes greater than* d_c.

In order to obtain a HgTe QW, they sandwiched a thin layer of HgTe between two CdTe films as illustrated in Figure 1.1a. CdTe is an insulator with a bandgap of 1.5 eV, while HgTe is a non-trivial topological insulator due to the inversion of the conduction and the valence bands at $\mathbf{k} = 0$ in the Brillouin zone (i.e. negative band gap). The inverted bandgap is caused by a strong spin-orbit coupling. Then, they tested the QW electronic properties to find the TIs signature. They realise that for a critical thickness ($d_c \approx 6.3$ nm) of the HgTe layers, a transition from a trivial topological insulator to a non-trivial topological insulator occurs. In other words, the device transport properties are dominated by the CdTe electronic structure (normal band structure) for thicknesses lower than d_c whereas it is dominated by the band inversion of HgTe for thicknesses greater than d_c as shown in Figures 1.1b and 1.2a [22]. As a result, for $d > d_c$, the device exhibits conductance

plateaux with values proportional to an integer multiple of (e^2/h) without the presence of an external magnetic field (see Figure 1.2b). This is regarded as signature of the QSH phase. Importantly, their measurements reveal the $(2e^2/h)$ plateau appearance independently of sample width indicating that conductivity is occuring through edge channels.

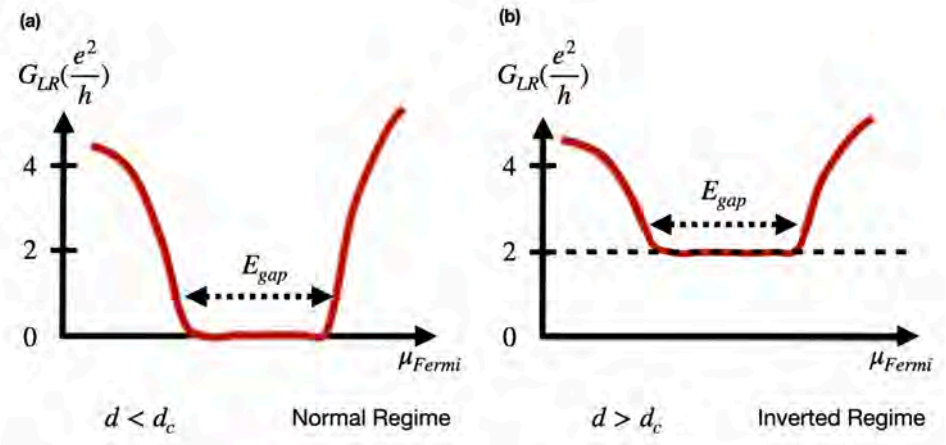

Figure 1.2: *Transport measurements on a Hall bar of a HgTe layer sandwiched between two CdTe layers [17]. The plot of Hall conductance versus Fermi energy level in (a) normal regime and (b) inverted regime.*

1.4 The $Bi_{1-x}Sb_x$ alloys

$Bi_{1-x}Sb_x$ alloys are the first 3D TI experimentally confirmed [23] after being theoretically predicted by Fu and Kane [19]. They are considered to be one of the most interesting materials due to their inverted band structure caused by strong spin-orbit interactions. As a direct consequence, an odd number of Dirac cones appears at the $Bi_{1-x}Sb_x$ surface leading to topologically protected metallic surface states. These states open the possibility for applications in the fields of quantum computing and spintronics [24].

Bismuth (Bi) and antimony (Sb), constituents of $Bi_{1-x}Sb_x$ alloys, are considered heavy elements and belong to the V_A column of the periodic table. Their crystalline structure is rhombohedral as the $Bi_{1-x}Sb_x$ alloys and their space group is $R\bar{3}m$ [4] with two atom in each unit cell (see Figure 1.3). It is easier to see their lattice structure as two inter-penetrating face centred cubic (FCC) sub-lattice elongated along the trigonal direction of the FCC diagonal (see Figure 1.3a). Due to the C_3 symmetry of the trigonal axis, it is easier to use the hexagonal notation instead of the Cartesian coordinates to present

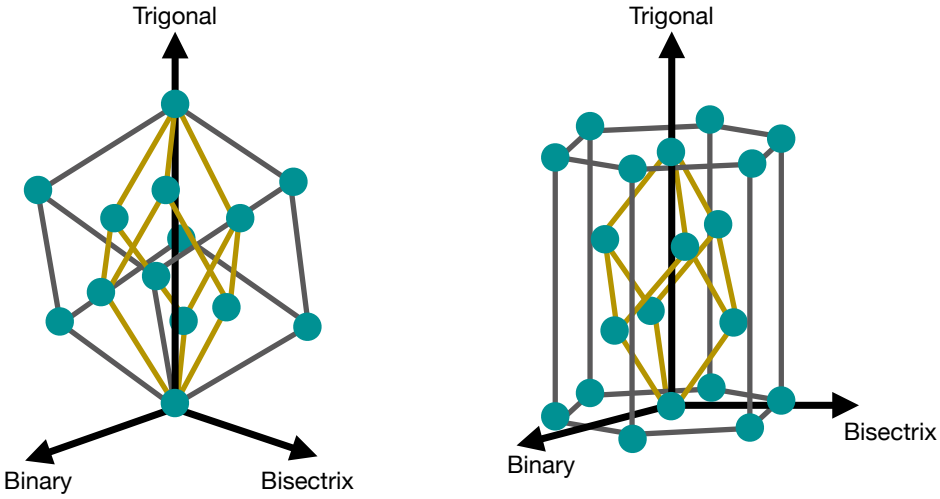

Figure 1.3: *Crystalline structure of the $Bi_{1-x}Sb_x$ alloys under a distorted cubic system (left) and an hexagonal coordinate (right).*

the different crystalline directions, as shown in Figure 1.3. In this case, the trigonal axis, the binary axis and the bisectrix axis are denoted, respectively, by [0001], $[1\bar{2}10]$ and $[10\bar{1}0]$. It must be noted that the Bi and Sb elements are interchangeable in the $Bi_{1-x}Sb_x$ matrix because they both belong to the group V elements. In addition, the $Bi_{1-x}Sb_x$ lattice parameter is Sb composition (x) dependent, as shown in Table 1.1. The lattice parameter **a** change linearly with x, obeying the Vegard's law, contrary to the lattice parameter **c**.

Sb (%)	a (Å)	c (Å)
100	4.3085	11.2732
95	4.3198	11.3195
90	4.3313	11.3588
85	4.3427	11.3945
80	4.3542	11.4282
75	4.366	11.4605
70	4.3772	11.4906
65	4.3887	11.52
60	4.4	11.548
55	4.412	11.576
50	4.4242	11.6037

Sb (%)	a (Å)	c (Å)
50	4.4242	11.6037
45	4.436	11.631
40	4.4483	11.6585
35	4.4605	11.6846
30	4.473	11.7105
25	4.4855	11.736
20	4.4978	11.7615
15	4.51	11.7867
10	4.5225	11.812
5	4.5347	11.8365
0	4.5465	11.8616

Table 1.1: *$Bi_{1-x}Sb_x$ lattice parameter as a function of Sb composition at 300 K [25].*

Since Bi and Sb have similar chemical properties, they have almost the same electronic band structures. Both are semimetals with an indirect negative bandgap [26]: the Bi electronic band structure shows that the conduction band (CB) minima at the L points of the Brillouin zone is below the valence band (VB) maxima at the T point leading to an indirect negative bandgap of 40 meV (see Figure 1.4). Similarly, the CB minima of Sb at L points lie below the VB maxima at the H points giving an indirect bandgap of 180 meV. Note that the CB minima of Bi has L_s symmetry while that of Sb has L_a antisymmetry. Nevertheless, they do not exhibit the same band orders and thus have different Z_2 topological invariant due to different spin-orbit interaction strength. Bi is topologically trivial ($Z_2 = 0$) with strong spin-orbit interactions (SOI) since the CB at L point and VB at T point have reverted band ordering (parity of both L and T points are -1). On the contrary, Sb is a topologically nontrivial material ($Z_2 = 1$) [27] and exhibits a SOI strength weaker than that of Bi by a factor of 3. Thus, substituting Bi atoms by Sb ones, the SOI strength is reduced, allowing to tune the material properties [28]. In other words, by reducing the SOI strength, the parity of L point becomes $+1$, while T remains -1 and therefore a nontrivial TI is obtained [28].

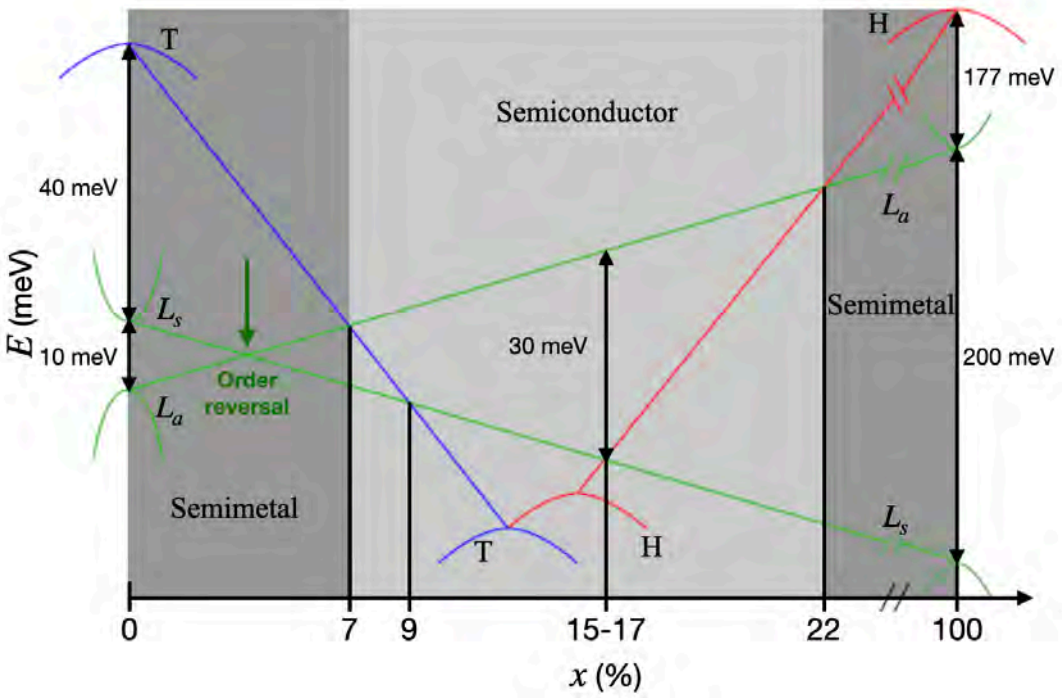

Figure 1.4: *$Bi_{1-x}Sb_x$ band structure as a function of Sb composition (x) [29].*

The band structure of the alloy depends on the Sb composition. For a Sb composition lower than 7%, the $Bi_{1-x}Sb_x$ band structure is the same as that of pure Bi. In other words, $Bi_{1-x}Sb_x$ behaves as a semimetal since there exists an overlap between the VB at T and the CB at L. Importantly, at $x = 4\%$, the gap between the CB and the VB at the three equivalent L-points closes leading to the appearance of a massless, three-dimensional (3D) Dirac cone (see Figure 1.4). It should be noted that the $Bi_{1-x}Sb_x$ alloys inherit from pure Sb its nontrivial topological class [19]. By further increasing x, the CB minima and VB maxima switch places and are located respectively at L_a and L_s points. The gap between them (Δ) reopens with inverted symmetry ordering, leading to a negative band gap Δ at each of the three equivalents L-points in the Brillouin zone. As x is further increased ($x \geq 7\%$), the VB maxima at T becomes lower than the CB minima at L_a leading to an indirect bandgap SC. For a concentration greater than 9%, the $Bi_{1-x}Sb_x$ material behaves as a direct bandgap SC since the VB at L falls below the CB at L. Once the Sb concentration exceeds 15-17%, the direct bandgap reaches its maximum value of order of 30 meV and then the VB at point L falls below the VB at point H. The system becomes therefore an indirect bandgap SC. Finally, increasing x above 22%, leads to a semimetal behaviour.

In the pioneering article of Fu and Kane [19], the narrow gap SC $Bi_{1-x}Sb_x$ is predicted to be a strong TI for $0.07 < x < 0.22$, which was then verified experimentally by Hsieh et al [23] using Angle Resolved Photo Emission Spectroscopy (ARPES) measurements on a $Bi_{0.9}Sb_{0.1}(111)$ surface (see Figure 1.5). These measurements showed that there is an odd number of Dirac cones that cross the Fermi energy level along a path connecting $\bar{\Gamma}$ and $\bar{M}$, which confirms that $Bi_{0.9}Sb_{0.1}$ is a non-trivial TI with a negative Z_2 ($= -1$) topological invariant. Roushan et al [21] choose another way to determine the TI behaviour of $Bi_{1-x}Sb_x(111)$. Since the topological surface states are characterised by their chiral spin texture and an associated Berry's phase [5] making them robust against backscattering, they examined the chiral nature of these states by verifying the suppression of backscattering between states of opposite momentum and opposite spin on the BiSb(111) surface. Their results underlines one of the most important characteristic of a TI.

However, changing the $Bi_{1-x}Sb_x$ surface orientation affects the band topology and thus the number of Dirac cones. Zhu et al. [30] have shown that $Bi_{1-x}Sb_x(110)$ exhibits similar topological metallic surface states as that of $Bi_{1-x}Sb_x(111)$ but with three Dirac cones instead of one. Similarly, other studies have shown that making a 2D $Bi_{1-x}Sb_x$ films allows the control of their band structures by changing the film thickness and growth orientations [31, 32]. For example, by decreasing the film thickness, the signature of

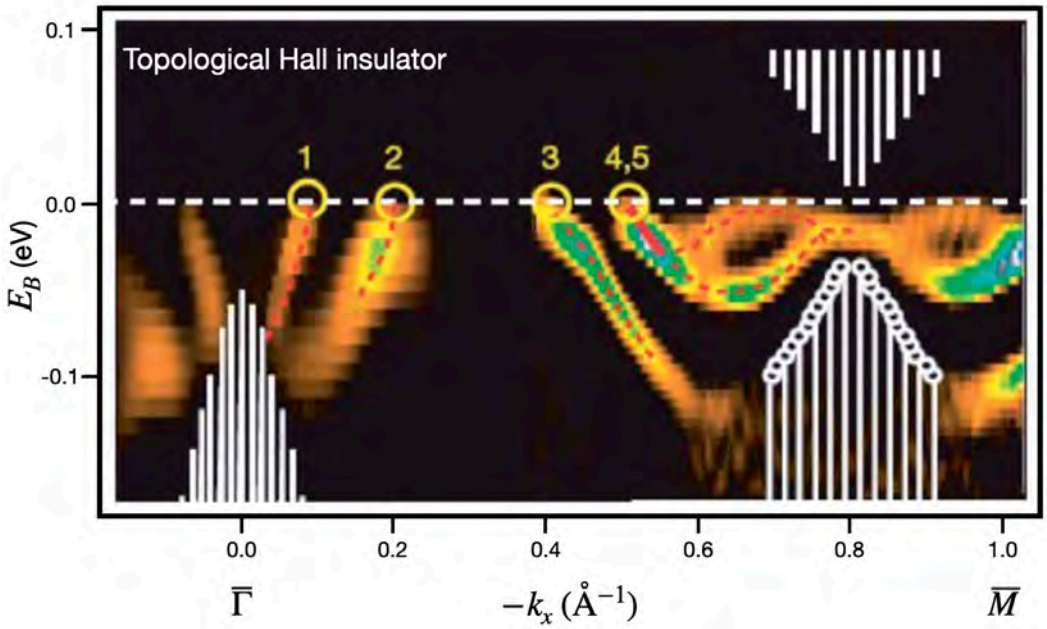

Figure 1.5: *ARPES measurements performed on $Bi_{0.9}Sb_{0.1}$ confirm the presence of an odd number of Dirac cones in $Bi_{0.9}Sb_{0.1}$. This was the first experimental confirming the 3D topological insulator behaviour of $Bi_{0.9}Sb_{0.1}$ [23].*

metallic surface states can be detected over a wide temperature range due to the reduced bulk contribution [33]. Finally, it is possible to build single-, bi-, and tri-Dirac cone surfaces with BiSb by changing its growth orientation [31].

In 2017, a group of researchers noticed the violation of Ohm's law in $Bi_{0.96}Sb_{0.04}$ only when exposed to a magnetic field (B) parallel to an electric field (E). This result has been considered as a hallmark of the emergence of Weyl semimetals (WSMs) phase in $Bi_{0.96}Sb_{0.04}$ [34]. Recently, the group of Yu-Hsin Su [27] theoretically proposed that $Bi_{1-x}Sb_x$ materials exhibit a WSMs phase also for $x = 50\%$ and $x = 87\%$. Similarly to TIs, WSMs exhibit linearly-dispersing surface states, which are topologically protected against disorders. In the case of WSMs, the linear dispersion of CB and VB touch via the Weyl points. These points are doubly degenerate and act as monopoles of the Berry curvature with opposite chirality leading to a non-zero topological charge [27] .

1.5 Bi-based Topological Insulator

Despite $Bi_{1-x}Sb_x$ being the first 3D topological insulator confirmed experimentally, many researchers prefer to work on other TIs. Indeed, $Bi_{1-x}Sb_x$ atom arrangement shows a random substitutional disorder, its surface states are extremely complex (presence of many Dirac cone) and cannot be described by a simple theoretical models. In addition, the $Bi_{1-x}Sb_x$ alloys show tendency to host impurities bands within their bulk bandgap, which could mimic the surface state signatures [35]. That motivate many researchers to search for new TIs materials that reveal well-defined electronic structures with the presence of a single Dirac cone. Owing to the Bismuth features, the Bi-based compounds have been the most important candidates. Bismuth has a unique electronic properties; it can acts as an electron donor and acceptor, which allows it to interact with other elements of the periodic table [36]. So far, many theoretical and experimental efforts have focused on the V_2VI_3 type Bismuth-chalcogenides materials in order to synthesise a new type of TI bulk materials. In the following, we will describe the V_2VI_3 series systems Bi_2Se_3, Bi_2Te_3 , $(Bi_{1-x}Sb_x)_2Te_3$ and $(Bi_{1-x}Sb_x)_2Te_3Se$.

1.5.1 The Bi_2Te_3 material

Based on numerous theoretical studies [35,37], the Bi_2Te_3 material is considered as a non-trivial 3D TI with extremely simple topological surface states and a large bulk bandgap. Its surface states present only one Dirac cone at the Γ point ($\mathbf{k} = 0$) in the Brillouin zone. As a result, this material is considered promising in high-temperature spintronics applications [38]. However, theoretical and experimental studies [38, 39] have shown that the Dirac cone is buried inside the bulk valence band (see Figure 1.6a and b), which makes it difficult to detect the topological surface states signature. This is due to the dominant contribution of electron donors on the bulk Bi_2Te_3 electronic properties, leading to the Dirac cone moving away from the Fermi energy level E_F. Nevertheless, doping the material with holes enables to tune E_F into the bulk gap, thus suppressing the bulk conduction [38]. In [40], authors show that the bulk conduction disappears by doping the system with 0.27% Sn ($(Bi_{0.73}Sn_{0.27})_2Te_3$) and 1% Cd, respectively.

The crystalline structure of Bi_2Te_3 is rhombohedral ($R\bar{3}m$) with five atoms in each unit cell [35]. The trigonal axis has a three-fold rotation symmetry C_3, the binary axis has two-fold symmetry C_2 and the bisectrix axis is perpendicular to the first two axes. The Bi_2Te_3 layer structures can be seen as a repeated Te/Bi/Te/Bi/Te stacking quintuple-layer groups [41] along the trigonal axis (see Figure 1.6c). Inside a quintuple layer, the bond

between two atomic layers is strong, while there is a Van der Waals coupling (weak bond) between two quintuple layers.

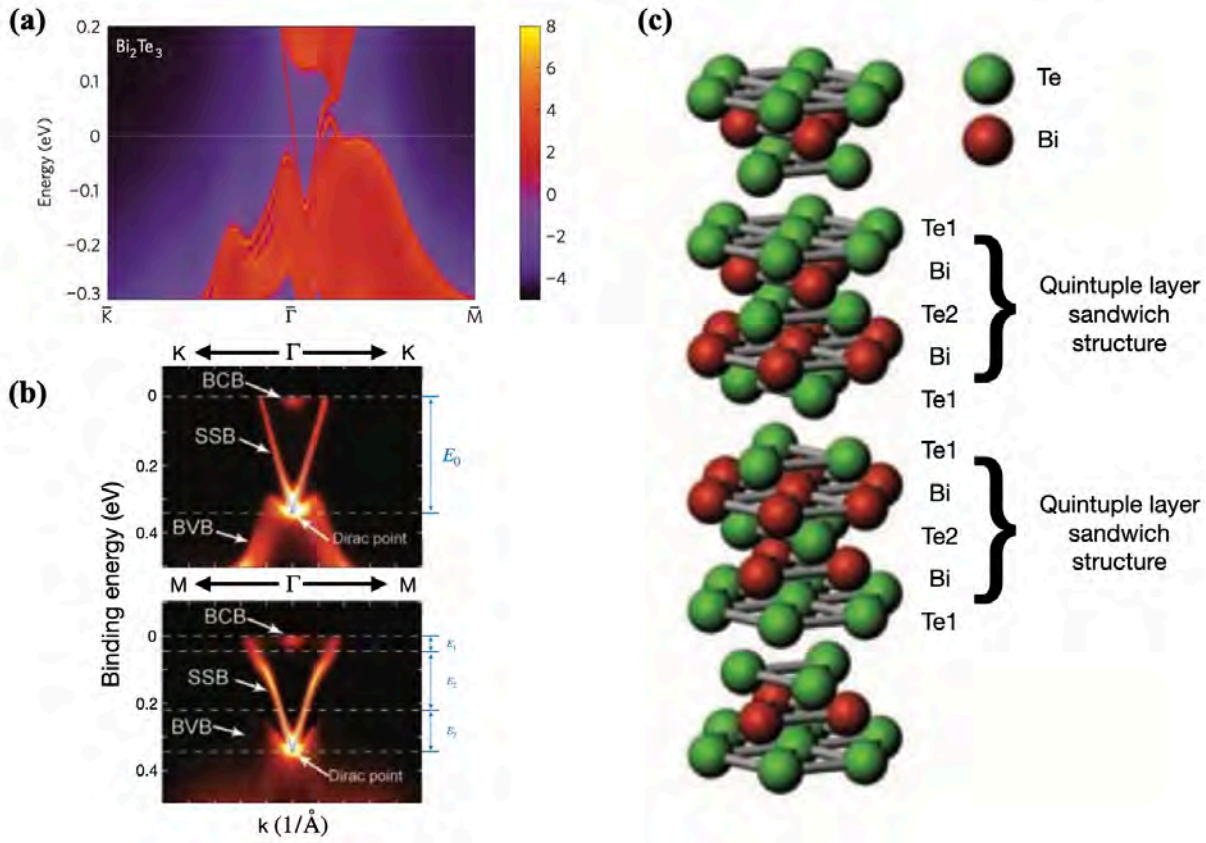

Figure 1.6: *Electronic band structure of Bi_2Te_3 (a) theoretically predicted [35] and (b) experimentally measured by ARPES [38]. (c) The rhombohedral crystalline structure of Bi_2Te_3 contains layers of Bi and Te stacked on top of each other [38].*

1.5.2 The Bi_2Se_3 material

Bismuth Selenide Bi_2Se_3 is one of the most studied chalcogenides TIs. This material shares almost the same electronic and structural properties as Bi_2Te_3 (rhombohedral crystalline structure and well-defined electronic band structure with a single Dirac cone), making it one of researchers's favourite TIs. Bi_2Se_3 alloys are stoichiometric crystals, easy to synthesise with a simple electronic band structure. Bi_2Se_3 has a semiconducting bulk belonging to the Bi_2X_3 thermoelectric materials class. Depending on the sample growth

conditions, the Bi_2Se_3 bulk electronic properties may have different transport properties [42,43] but generally reveal n-type conductivity due to excess Se or to atomic vacancies [44]. The excess electron pins the E_F within the bulk band conduction. Based on theoretical prediction, Bi_2Se_3 has a large bandgap of 0.24-0.3 eV [45, 46] in agreement with experimental measurements (0.35 eV) [47, 48]. The Brillouin zone at Bi_2Se_3 (111) surface shows an hexagonal shape with two time-reversal invariant momenta $\overline{\Gamma}$ and $\overline{M}$. Unlike Bi_2Te_3, the electronic spectral weight distribution along the $\overline{\Gamma}-\overline{M}$ (see Figure 1.7a) and $\overline{\Gamma}-\overline{K}$ directions (see Figure 1.7b) shows that the single Dirac point is inside the bulk bandgap at 0.09 $Å^{-1}$ along $\overline{\Gamma}-\overline{M}$ and at 0.10 $Å^{-1}$ along $\overline{\Gamma}-\overline{K}$ [43]. The upper Dirac cone crosses the E_F within the bulk conduction band. In both directions, the Fermi velocity is estimated to be $5 \times 10^5\ ms^{-1}$, similar to that of Bi_2Te_3. These experimental results are in

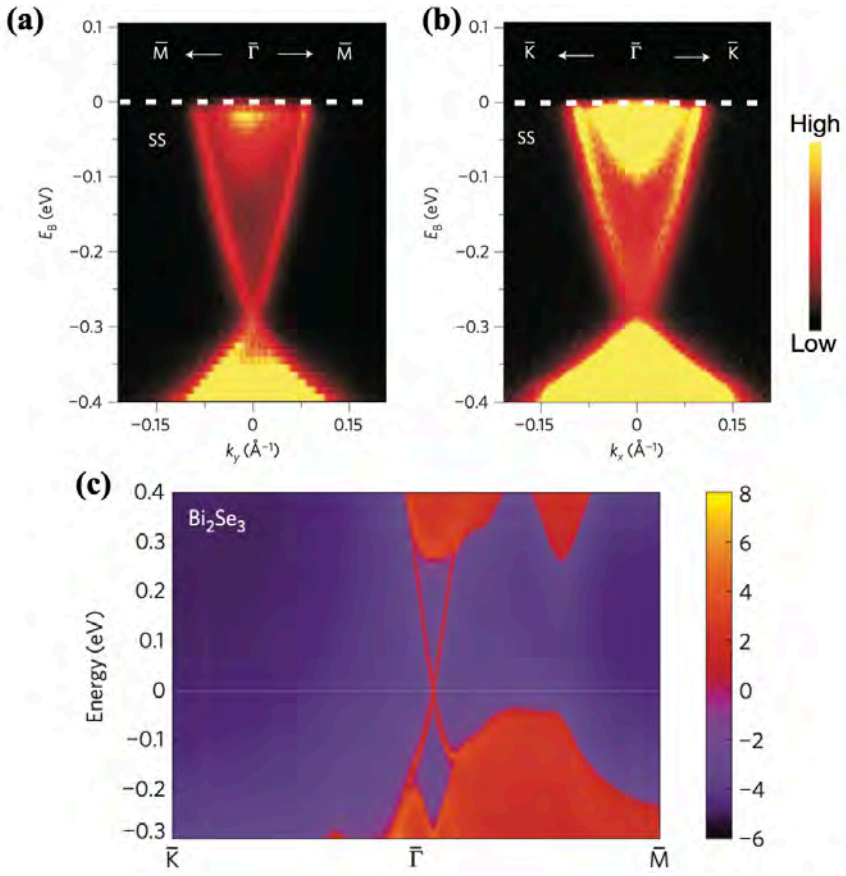

Figure 1.7: *Electronic band structure of Bi_2Te_3 measured experimentally by ARPES [43] along (a) $\overline{\Gamma}-\overline{M}$ and (b) $\overline{\Gamma}-\overline{K}$ momentum-space cuts and (c) predicted theoretically [35].*

good agreement with those theoretically predicted: Figure 1.7c [35] shows the surface local density of states (LDOS) on the Bi_2Se_3 (111) surface obtained by *ab initio calculation*. The single Dirac cone is detected in the Bi_2Se_3 bulk bandgap around the $\overline{\Gamma}$ point.

As mentioned earlier, Bi_2Se_3 has the same atomic plane arrangement as Bi_2Te_3, i.e a rhombohedral crystalline structure with a quintuple layers arrangement. Each unit cell features five atoms distributed as three Se and two Bi ones [6]. The Bi_2Se_3 layer structure consists of five layers distributed along the trigonal axis, defined as quintuple layers. The five layers are ordered in each quintuple layer as Se(1)/Bi/Se(2)/Bi/Se(1) where the labels Se(1) and Se(2) are used to distinguish the different types of Se.

1.5.3 The $(Bi_{2-x}Sb_x)_2Te_3$ alloys

As mentioned earlier, the main problem preventing the dominance of the surface states transport in Bi_2Te_3 is the large bulk conduction. In fact various defects in the bulk reduce the charge carriers mobility [35]. Many research attempted to suppress the bulk conduction either by chemical doping with different elements [38] or by electrical gating [49,50] but unfortunately the investigation of the metallic states existence still remains difficult. On another hand, the ternary compounds $(Bi_{1-x}Sb_x)_2Te_3$ has a lower bulk conductivity, which allows to measure surface states. Across the whole Sb composition, this material presents a single Dirac cone which makes it a nontrivial TI [50]. Fortunately, this new TI material has been successfully grown with chemical vapour deposition [51] and molecular beam epitaxy (MBE) [52]. A recent article [50] provides that the lowest bulk conductivity is reached for a Sb composition of 50%. In this case the sheet carrier density is $n_s \approx 3 \times 10^{12}$ cm^{-2}. Interestingly, the Sb composition controls the $(Bi_{1-x}Sb_x)_2Te_3$ electronic properties: by changing the Fermi energy position, Zhang et al [52] found that for $x = 88\%$, the Dirac point (DP) and E_F are in the bulk bandgap, making this material an ideal TI. It is worth to note that changing the Sb composition from 94% to 96% shifts the E_F from above the DP to below it and therefore change the surface transport from n to p type. Owing to a back-gate, it is also possible to control the charge carrier type over the entire thickness [50].

1.5.4 The Bi_2Te_2Se material

As indicated in Subsections 1.5.1 and 1.5.2, the Bi_2Te_3 and Bi_2Se_3 materials have a p-type and n-type semiconducting bulk, respectively. Due to the difficulty of examining the surface states transport in these materials

as they are hindered by bulk conductivity, some researchers have proposed to combine these two materials [53–55]. By combining them, each Se atom is trapped between two Bi atoms (strong Bi−Se bond), which leads to the suppression of the Se vacancies formation. Since Bi−Se bonds are strong contrary to Se−Te bonds, it is estimated that the formation of the antisite defects between Te and Bi is also suppressed [53]. As a result, the E_F lies in the bulk bandgap and a large bulk resistivity of 6 Ωcm is measured [54].

Bi_2Te_2Se is isostructural to Bi_2Te_3 and Bi_2Se_3 materials. It has a rhombohedral crystalline structure with the space group $R\bar{3}m$ with five atoms in one unit cell. The structure reveals a basic building block presented by five stacking layers in an order Te/Bi/Se/Bi/Te [56]. It is worth to note that due to the well-defined atom arrangement (no random Se/Te sites), the additional disorder is minimised [53].

1.5.5 The $Bi_{2-x}Sb_xTe_{3-y}Se_y$ alloys

The previous Subsection 1.5.4 has shown that it is appropriate to dope the Bi_2Te_3 alloys with Se to adjust the Dirac point within the large bulk bandgap and widen the bulk bandgap. Despite numerous efforts to improve the Bi_2Te_2Se bulk insulating behaviour, the measurements reveal a residual bulk carrier of the order of 10^{17} cm^{-3} [53]. Nevertheless, by adding the Sb element to the tetradymite Bi_2Te_2Se alloys, the bulk insulating behaviour can be optimised and thus allowing for measurement of surface states [57]. This results from the compensation between acceptors and donors in the $Bi_{2-x}Sb_xTe_{3-y}Se_y$ alloys [56], giving bulk resistivity exceeding 1 Ωcm for x and y combination of 0.5 and 1.3. Moreover, the $Bi_{2-x}Sb_xTe_{3-y}Se_y$ bandgap is estimated to 0.45 eV [56], which is 1.5 larger than that of Bi_2Se_3.

Obviously, the $Bi_{2-x}Sb_xTe_{3-y}Se_y$ crystalline structure is rhombohedral as that of Bi_2Se_3, Bi_2Te_3 and Bi_2Te_2Se with an ordered Se(1)/Bi/Se/Sb/Te quintuple layers [57]. The center of inversion symmetry at the Se atom site makes the connection between the Bi(Se(1)) atoms and Sb(Te) atoms. Note that changing the x and y combinations does not modify the $Bi_{2-x}Sb_xTe_{3-y}Se_y$ crystallinity except for a range of x and y combinations close to 2 and 3 (Sb_2Se_3).

1.6 Motivation for choosing the BiSb alloys

As already reported in Section 1.4, $Bi_{1-x}Sb_x$ alloys are prime candidates for future applications in quantum computing and spintronics due to the possibility to control their electronic band structure by changing the stoichiom-

etry, the thickness and the temperature. Moreover, the high conductivity ($\sim 10^5\ \Omega^{-1}m^{-1}$) [58] and the colossal Hall angle ($\sim 52°$) [14] make BiSb the most interesting spintronic materials. Besides being the first experimentally confirmed 3D topological insulator, $Bi_{1-x}Sb_x$ thin films are expected to exhibit a different number of Dirac cones depending on their crystal orientation. It is predicted that $Bi_{1-x}Sb_x(10\bar{1}0)$ has a single Dirac cone, while $Bi_{1-x}Sb_x(1\bar{2}10)$ presents a double Dirac cone, and $Bi_{1-x}Sb_x(0001)$ has three. From the experimental point of view, the existence of three Dirac cones on the $Bi_{1-x}Sb_x(11\bar{2}0)$ surface and a single Dirac cone on the $(11\bar{2}1)Bi_{1-x}Sb_x$ surface has already been reported in [23, 30].

In contrast to Bi_2Te_3 and Bi_2Se_3, E_F lies within the $Bi_{1-x}Sb_x$ bulk bandgap, which facilitates the detection of metallic surface states at low temperatures. This therefore makes $Bi_{1-x}Sb_x$ materials the most attractive TI materials, even after obtaining a large bandgap in $(Bi_{2-x}Sb_x)_2Te_3$ materials and even after the successes of moving E_F inside the bulk bandgap of Bi_2Te_3 and Bi_2Se_3 materials. This displacement of E_F in these two materials is ensured by adding a dopant (adding Se to Bi_2Te_3 materials and adding Te to Bi_2Se_3 ones). However, the more compounds there are, the more defects are induced. As a result, carrier transport in these ternary and quaternary compounds is generally affected by dopants via impurity scattering and therefore the electronic properties are impacted.

Generally, the fabrication of any type of TIs on a large scale, hinders the transport contribution of metallic surface states due to the dominance of the bulk one. This is the main driver for reducing the material dimensions to the order of nanometer. Moreover, the synthesise of nanoscale materials creates quantum confinement effects and therefore allows to probe new physical properties. In the case of TIs, the surface electronic transport is enhanced and the bulk contribution is suppressed leading to the appearance of a topological phase. Nevertheless, the fabrication of 3D TI nanostructures such as nanowires, nanoflakes and nanoribbons greatly increases the *Surface/Volume* ratio, which is considered a serious problem to control and characterise their surface properties. In addition, these nanostructures can be easily oxidised, which hampers the metallic surface states signatures. However, recent studies [14,31] have shown that by optimising the growth conditions, it is possible to explore the metallic surface states of 2D $Bi_{1-x}Sb_x$ and even to control their physical properties [31]. Here, our interest consists in synthesising 2D $Bi_{1-x}Sb_x$ thin films. We grow $Bi_{1-x}Sb_x$ films on two different substrates, GaAs(001) and GaAs(111)A. At first, our interest is to show the possibility of integrating a BiSb film on a standard industrial substrate. In a second step, our objective is to further improve the quality of the grown BiSb films.

2
Epitaxial processes

2.1 Overview

Progress in the synthesises of materials has always been a qualitative leap for developing new electronic devices. Over the past decades, the semiconductor industry has been the driver of the computer revolution and led to the information age. One of the reasons for the successful development of new materials, is the development of a new synthesis processes such as "epitaxy". "Epitaxy" is a Greek words composed of two words "epi" and "taxi". The first one means "above" and the second means "in an ordered manner". This synthesis process is based on the use of a monocrystalline material, called substrate, on which the atoms will be "epitaxially" deposited with therefore the same crystalline order as that of the substrate. Besides the choice of the substrate, the deposited material and the environment are also key ingredients for a successful epitaxial process.

The objective of this chapter is to present a global description of the epitaxial processes. In Section 2.2, two kind of epitaxy methods are presented and the key parameters are introduced. Next, the classical procedure towards successful growth is described and three growth mechanisms are presented. In Section 2.3, the global theory about thermodynamic and kinetic processes is developed. At this stage, we will present how the competition between these two processes controls the growth mechanism. Section 2.4 focuses on the substrate surface atomic structure. It underlines the critical role of the substrate surface in controlling and obtaining high quality epitaxial layers. It also describes the structural defects which can occur on the substrate surface and highlights their influence on the absorption-diffusion-incorporation of deposited atoms. Finally, Subsection 2.4.1 introduces the substrates used during my thesis. It confirms the need for prior knowledge of the surface atomic structure to achieve high quality films.

2.2 Epitaxy

“Epitaxy” refers to the crystal growth of a material on a monocrystalline substrate on which an "epitaxial layer" is formed with a well-defined orientation mimicking the substrate one. The choice of a suitable substrate plays a key role in the epitaxial growth. If the substrate and the deposited material are identical, the process is called “homoepitaxy” and it is “heteroepitaxy” otherwise. In both cases, the atoms behaviour (such as their diffusion length, adsorption residence time and chemical potential, as shown in Figure 2.1) strongly depends on the growth conditions such as the substrate surface reconstruction, the growth temperature, the stoichiometry, the film thickness and the growth rate.

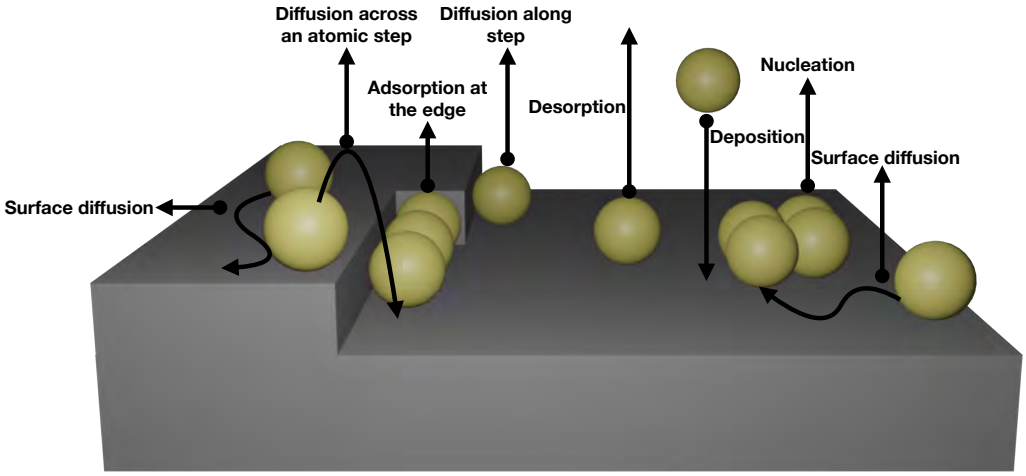

Figure 2.1: *Schematic illustration of the surface processes during growth.*

2.2.1 The Homoepitaxy

The growth temperature has the biggest influence since it influences other parameters. The different growth modes in the case of "homoepitaxy" are:

- **Multi-layers growth:** In that case, the adatoms cannot move sufficiently on the substrate surface due to a short diffusion length, which prevents them from finding their minimal energy position. As a result, they tend to find a local minimum by forming islands with their neighbourhood. As the potentiel barrier at the step edge of the lower terrace of an island is high, the adatoms arriving on the upper facet of this terrace remain there and contribute to the formation of a rough cluster.

This leads to the "mound formation" growth mode (see Figure 2.2a). An increase of the deposition flux (F) leads to a transition from the "mound formation" to the "self-affine" growth mode (see Figure 2.2b) due to a decrease of the adatoms diffusion length at the surface. As a result, they are forced to bind randomly with neighbouring adatoms, leading to a self-affine, rough surface.

- **Layer-by-layer growth:** adatoms are more free to move on the substrate surface because their diffusion length is longer. As a result, full monolayers are developed, leading to layer-by-layer growth, as shown in Figure 2.2c.
- **Step-flow growth:** it is illustrated in Figure 2.2d. The probability of adatoms finding the step edge increases due to their sufficiently long diffusion length or to the small terrace width between the steps edge. As a result, the adatoms get incorporate in the step edge, leading to the "step-flow" growth. Note that the adatoms diffusion lengths are larger than those in the case of "layer-by-layer" growth due to the low F or high surface mobility [59].

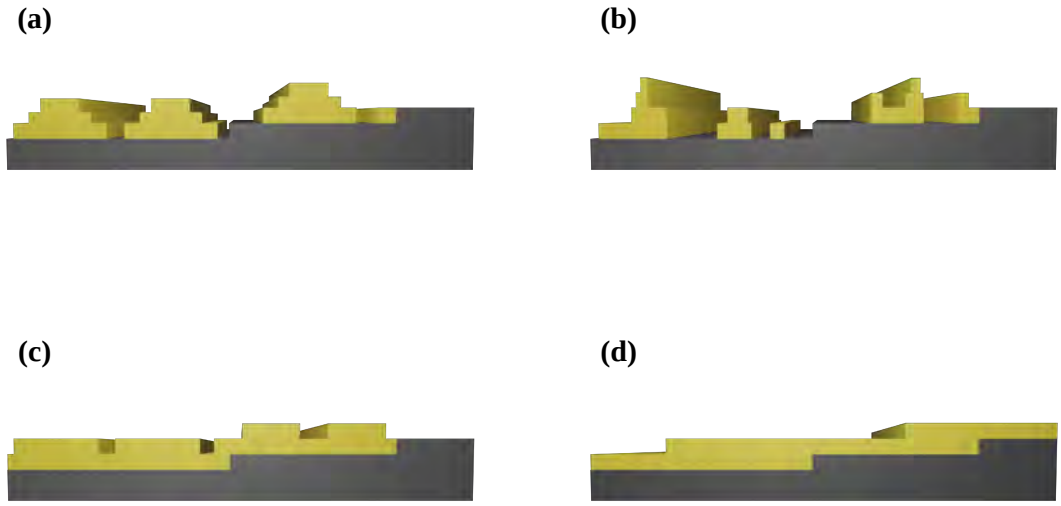

Figure 2.2: *Illustration of the different growth modes in the case of "homoepitaxy": (a) mound formation, (b) self-affine (c) layer-by-layer and (d) step-flow growth.*

2.2.2 The Heteroepitaxy

In the case of heteroepitaxy, the substrate must be chosen in order to reduce the strain, crack and dislocation density in the epitaxial material. For this reason, the substrate and the deposited material must share the same crystallographic symmetry and a close in-plane lattice constant. The lattice mismatch is measured by the misfit (f) as follow:

$$f = \frac{a_m - a_s}{a_s} \tag{2.1}$$

Where a_m is the lattice constant of the grown material and a_s is the lattice constant of the substrate.

Most substrates have a native oxide on the surface, which affects the growth quality. That's why, it is necessary to clean the substrate surface before any growth. The native oxide elimination is done differently depending on the substrate. For example, the Silicon (Si) surface is cleaned using an ex-situ chemical wet etching (hydrofluoric acid 1%); while, the GaAs one is removed in-situ by heating it up the substrate to a high temperature (625°C) under an As flux in the MBE growth chamber. Once it is eliminated, the epitaxy can start and is controlled by three important parameters: the growth temperature, the evaporated element flux and the ratio between the deposited elements. First of all, the growth temperature must be adjusted because of its influence on all the other parameters and thus on the crystal growth. It affects one of the most important parameters in crystal growth, the surface diffusion length. The crucial role of the latter on growth will be discussed in Section 2.3. The other parameters are optimised in order to control the grown material morphology, the composition and the thickness. The deposited atoms arrive at the substrate surface where they migrate until they incorporate or re-evaporate depending on these parameters (see Figure 2.1).

Therefore, 2D (layer-by-layer) or 3D (islands, quantum dots, nanowire and etc ...) growth can be achieved. In fact, the parameters listed above play a determining role in the growth mechanism by controlling two physical aspects of a growth which are thermodynamics and kinetics. The thermodynamic approach supposes that the kinetic is low enough for the system to reach its equilibrium (lowest energy) [60]. In contrast, the kinetic approach supposes that the equilibrium state cannot be reached and that all of the deposited material characteristics are controlled by kinetics equations [60]. In a "real" epitaxy, both kinetics and thermodynamics are necessary to model crystal growth.

2.2.3 The 2D growths

2D growth takes place when the Frank Van Der-Merwe growth mechanism is applied (see Figure 2.3a). This growth mode is known as layer-by-layer growth. It is obtained when f is very small ($\leq 2\%$) [61] and the following inequality is satisfied:

$$\gamma_l + \gamma_{l/s} < \gamma_s \tag{2.2}$$

Where γ_l is the layer surface free energy, $\gamma_{l/s}$ is the interface free energy between the deposited atoms and the substrate surface and γ_s is the substrate surface free energy.

This inequality shows that it costs less energy to cover the entire substrate surface rather than creating a second layer before filling the first one: the elements have therefore more tendency to grow layer-by-layer. Generally, within the first monolayer, the epitaxial growth orientation is defined.

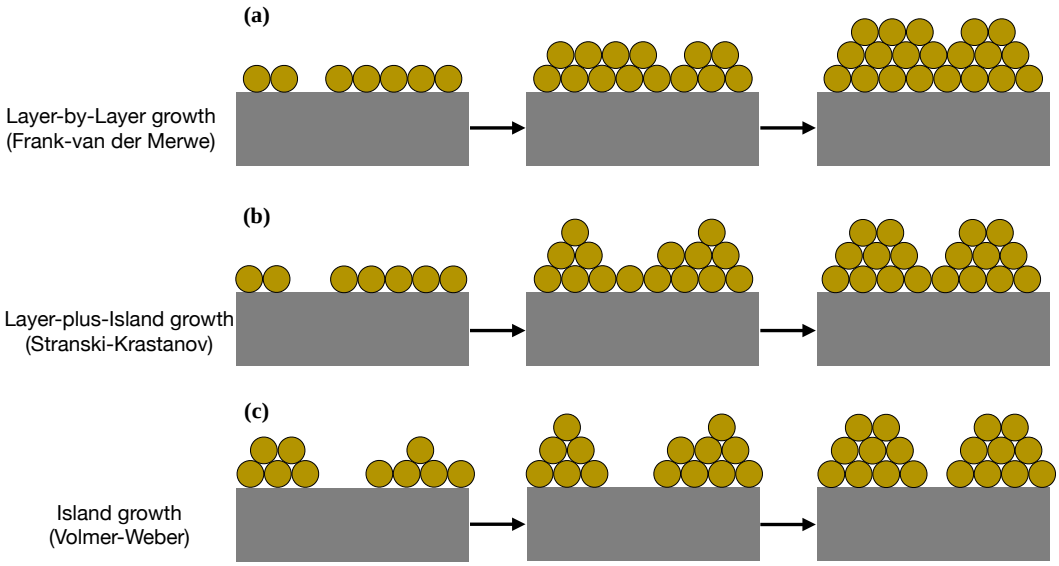

Figure 2.3: *Schema of the primary growth modes.*

The more the misfit (f) increases, the more the strain is important at the interface between the substrate and the deposited layer. The latter can thus be deformed elastically in order to adapt to the substrate and keep its in-plane lattice constant identical to the substrate one. That involves either the appearance of a compressive strain if $a_m > a_s$ or a tensile one if $a_m < a_s$ as shown in the top image of Figure 2.4. The epilayer thickness (h) influences strain relaxation and thus leads to two types of growth: a pseudomorphic and a dislocation one. The first occurs when h is small. In this case, the strain

is uniformly distributed over the lattice and thus the epilayer is laterally strained. This strain is known as the "misfit strain" [62] and illustrated in Figure 2.4a. Once h exceeds a critical thickness (h_c), a misfit dislocation occurs causing a slip in the epilayer atomic arrangement. These dislocations are induced at the interface between the epilayer and the substrate in order to relax the strain. This is known as "dislocation misfit" and shown in Figure 2.4b. Note that the smaller f is, the more h_c increases.

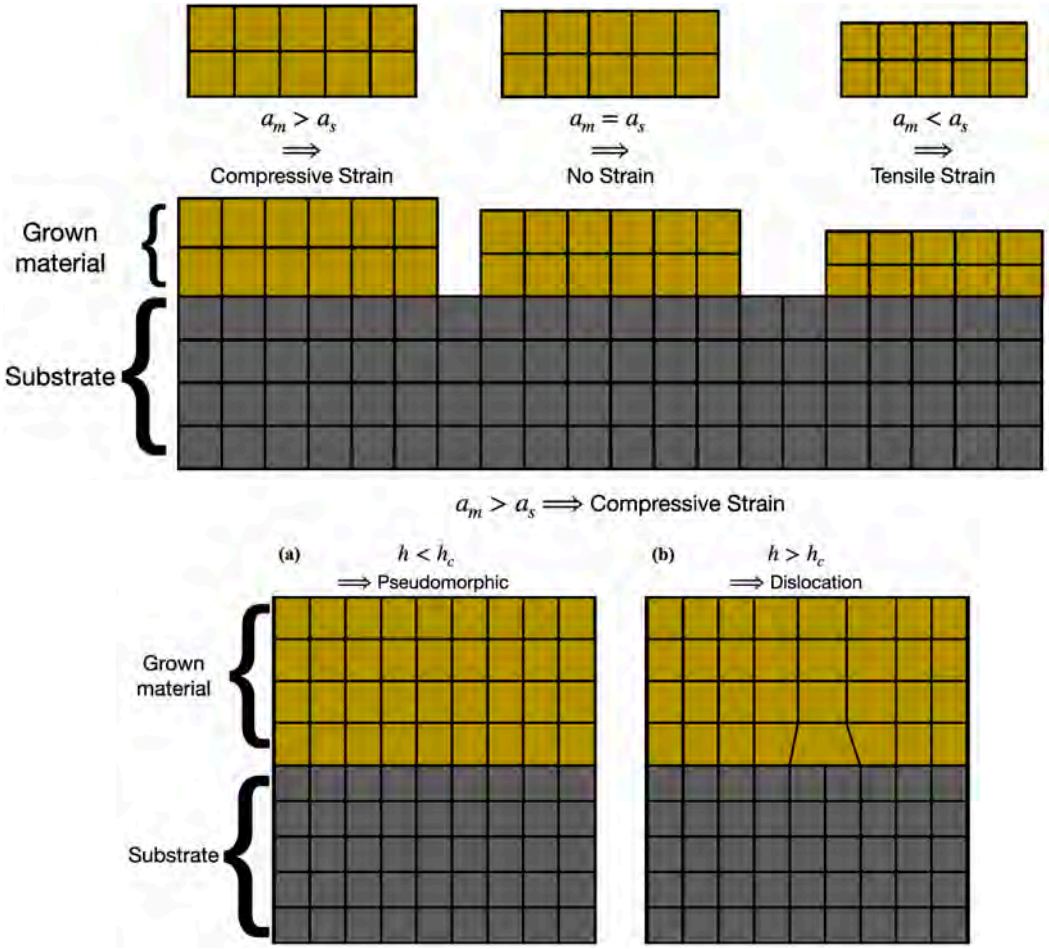

Figure 2.4: *Schematic illustration of different strain types depending on the lattice parameters of the substrate and the grown material (top figure). The bottom figure shows the schematic illustration of layers (a) pseudomorphically strained and (b) relaxed by dislocations.*

2.2.4 The 3D growths

Several growth mechanisms lead to 3D growth. One of them is the Stranski-Krasntanov growth mechanism, also known as 'layer-plus-islands growth'. This mode occurs when the misfit is greater than 2% [63] and is described by the following equation:

$$\gamma_l + \gamma_{l/s} \approx \gamma_s \tag{2.3}$$

Here, the growth starts with the formation of a layer called "wetting layer", and is followed by the formation of 3D-islands as shown in Figure 2.3b. When atoms stick to the substrate surface, they have more tendency to cover the entire substrate surface before creating a second layer since the interface free energy is smaller than the surface energy. The growth of the initial layer follows therefore a Frank Van-Der-Merwe mechanism. Then, when the layers thickness reaches a critical thickness (generally the higher f , the smaller the critical thickness (h_c)), the 3D-islands growth occurs: the elastic strain accumulated in the deposited layers increases and relaxes once a 3D surface is formed. At this stage, a transition from 2D to 3D growth occurs since island formation is energetically favourable.

In Volmer-Weber growth mode, 3D islands are grown directly on the substrate surface (Figure 2.3c). Their formation is promoted when the substrate surface free energy is lower than the sum of the layer surface free energy and the interface free energy:

$$\gamma_l + \gamma_{l/s} > \gamma_s \tag{2.4}$$

Importantly, most polycrystalline films are grown through this growth mode [64]. Once islands are nucleated on the substrate surface, they start to grow. At a critical thickness, the islands become large enough and stick together. As a result, they coalesce leading to the formation of a continuous layer after being widely reorganised. Epitaxial orientations can be defined later in the growth process.

2.3 Thermodynamic and kinetic processes

Crystal growth is a dynamic phenomenon governed by thermodynamic and kinetic processes. In a MBE, when incident atoms arrive at the surface of a suitable substrate, many possible processes can occur. Processes such as adsorption (physisorption, chemisorption), desorption, diffusion and incorporation, are controlled by the interplay of thermodynamics and kinetics. The adsorption process can be either a physisorption (physical adsorption) or a

chemisorption (chemical adsorption). Both are classified as an exothermic process because they lead to a decrease in the energy of the system. Physisorption mainly depends on the substrate surface and takes place when the force between the substrate and the atoms is weak such as Van Der Waals bonds (see Figure 2.5). Its enthalpy is weak, around 40 kJ/mol [65]. On the contrary, chemisorption is obtained when chemical bonds are formed between the substrate and the arriving atoms as shown in Figure 2.5. It depends on the substrate nature and has a high enthalpy of 400 kJ/mol [65]. Note that if the temperature increases, the physisorption could be changed into chemisorption.

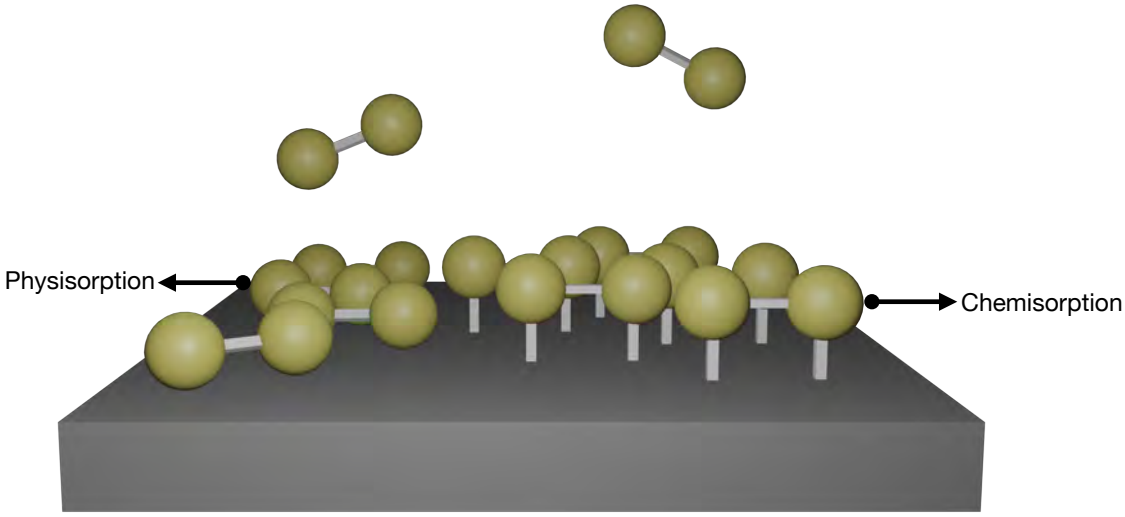

Figure 2.5: *Illustration of the difference between physisorption and chemisorption.*

2.3.1 Thermodynamic considerations

Once atoms reach the substrate surface, thermodynamics controls the system behaviour at equilibrium while kinetics drives it during transitions. In thermodynamics, the chemical potential (μ_i) is a change in energy related to a change of quantity (N_i) of a given particle "i". It is expressed by:

$$\mu_i = (\frac{\partial G}{\partial N_i})_{P,T,N_{j\neq i}} \tag{2.5}$$

Which can be written in another way:

$$dG = \sum_{i=1}^{n} \mu_i dN_i \tag{2.6}$$

G is the Gibbs free energy, also known as free enthalpy. It is used to calculate the maximum of reversible work performed by a thermodynamic system at a constant temperature and pressure and it is defined as:

$$G = H - TS \tag{2.7}$$

Where H is the enthalpy, T is the temperature and S is the entropy.

The enthalpy of a system is presented by:

$$H = U + pV \tag{2.8}$$

Where U is the internal energy of the system, p is the pressure of the system and V is the volume of the system.

So, by substituting the expression of H in equation 2.7, G becomes:

$$G = U + pV - TS \tag{2.9}$$

Deriving the equation 2.9, it gives:

$$dG = dU + pdV + Vdp - TdS - SdT \tag{2.10}$$

For a closed system, the derivative of the internal energy is expressed by:

$$dU = TdS - pdV \tag{2.11}$$

Therefore, the Gibbs free energy derivative for a closed system is:

$$dG = Vdp - SdT \tag{2.12}$$

Considering that the temperature is fixed during the growth, dG becomes

$$dG = Vdp \tag{2.13}$$

To study the variation of the Gibbs free energy between two states, the equation 2.13 must be integrated. It gives:

$$\int_{G}^{G_\infty} dG = \int_{p}^{p_\infty} Vdp \tag{2.14}$$

$$G(p_\infty) - G_(p) = \int_{p}^{p_\infty} Vdp \tag{2.15}$$

In the case of an ideal gas, $pV = Nk_BT$ where N is the number of gas molecules (N=1 for simplicity) and k_B is the Boltzmann constant. Thus, the equation 2.15 becomes:

$$G(p_\infty) - G(p) = k_BT \int_{p}^{p_\infty} \frac{1}{p} dp \tag{2.16}$$

$$G(p_\infty) - G(p) = k_B T ln(\frac{p_\infty}{p}) \tag{2.17}$$

In the case of crystal growth, the change of free enthalpy (ΔG) after transferring one atom from the gas phase to the solid phase can be written as:

$$\Delta G = \mu_s^i - \mu_v^i \tag{2.18}$$

Where μ_s^i and μ_v^i are respectively solid and vapour chemical potential of the ith element.

In the equilibrium state between these two phases, the system should be in chemical equilibrium and $\Delta G = 0$. The chemical equilibrium for two different phases is presented in term of chemical potential:

$$\mu_s^i = \mu_v^i \tag{2.19}$$

Considering a flat surface (infinite radius), the chemical potentiel is expressed:

$$\mu_{s_\infty}^i = \mu_{v_\infty}^i \tag{2.20}$$

Subtracting equation 2.20 from equation 2.19, we obtain:

$$\mu_{s_\infty}^i - \mu_s^i = \mu_{v_\infty}^i - \mu_v^i \tag{2.21}$$

By considering the case of an ideal gas ($\mu_{v\infty} = 0$), we obtain:

$$-\mu_v^i = \mu_{s_\infty}^i - \mu_s^i \tag{2.22}$$

From equation 2.22 and 2.17

$$\Delta G = -\mu_v^i = k_B T ln(\frac{p_\infty}{p}) \tag{2.23}$$
$$\implies \mu_v^i = k_B T ln(\frac{p}{p_\infty})$$

Where $\frac{p}{p_\infty}$ presents the vapour-phase supersaturation.

When the two phases are not in equilibrium, the thermodynamic driving force to reach equilibrium is [66]:

$$\Delta\mu = k_B T ln(\frac{p}{p_\infty}) \tag{2.24}$$

When the system is supersaturated ($\frac{p}{p_\infty} > 1 \implies ln(\frac{p}{p_\infty}) > 0$), $\Delta\mu$ is greater than 0 which means that growth is possible. While growth cannot occur in the case of an undersaturated system ($\frac{p}{p_\infty} < 1 \implies ln(\frac{p}{p_\infty}) < 0 \implies \Delta\mu < 0$).

2.3.2 Kinetics considerations

In order to discuss the role of kinetic process, we need to introduce the Fick's law. It is defined as:

$$J = -D\frac{d\phi}{dx} \tag{2.25}$$

Where J is the diffusion flux, ϕ is the atomic concentration, x is the position and D is the diffusion constant.

This equation shows that the adatoms diffusion at the surface is proportional to the gradient of their concentration. It shows that the adatoms move from a high concentration region to a low concentration one. It is important to note that this law is only valid in the case of diffusion of non-interacting particles, which is not the case of Bi atoms since they agglomerate to form islands (this will be demonstrated in Chapter 4, Section 4.8).

In the case of a crystal matrix, thermal agitation is required to allow the atoms to cross a diffusion energy barrier and diffuse from one site of the crystal lattice to another. Each transition path from an initial position "x" to a final position "y" has its own transition rate Γ_{xy}. It is defined as follows [67]:

$$\Gamma_{xy} = \nu_{xy}(T)e^{-\frac{E_{xy}}{k_B T}} \tag{2.26}$$

Where k_B is the Boltzmann constant, T is the temperature and ν_{xy} is the atomic diffusion vibration frequency also called attack frequency and is about $10^{13}\ s^{-1}$ in the case of crystalline material [68].

By combining all possible path transition rates from one configuration to another that ensure a Poisson distribution, we can calculate the diffusion coefficient D using the following equation:

$$D = f(\{a_{xy}\}_n, \{\Gamma_{xy}\}_n) \tag{2.27}$$

Where a_{xy} is the diffusion step between x and y sites and the function f is a set of n possible basic diffusion mechanisms.

From equation 2.26, the life time τ_x can be extracted using the equation 2.28 [69]:

$$\tau_x = -\frac{ln(\mu)}{\sum_{i=1}^{n} \Gamma_n} \tag{2.28}$$

Where μ is a random number between 0 and 1.

2.4 The crystalline substrate: the basic building block

As mentioned earlier, there are two types of epitaxy: homoepitaxy and heteroepitaxy. Homoepitaxy only allows the formation of "homojunction" devices, that are based on a unique material with different doping types in the junction (such as bipolar and MOS transistors). On the contrary, heteroepitaxy is a broader field that allows to tune the electronic and optoelectronic properties of materials [70]. Here, more parameters influence the crystal growth such as the lattice mismatch between the substrate and the deposited material, crystalline matrices, the surface free energy and the dislocations formation energy. In this case, several growth modes can appear such as Volmer-Weber, Franck van Der Merwe and Stranski-Krastanov (see Figure 2.3, Section 2.2).

The first parameter to consider is the substrate surface preparation. It contributes to define the morphology, the growth orientation and the quality of the grown layer. In fact, when atoms arrive at the surface of a solid material, they interact with the surface. The atom-surface collision defines the atoms behaviour: adsorption, desorption, surface atom diffusion, incorporation and evaporation (see Figure 2.1). Adsorption-desorption phenomena can be described by the difference between the adatom chemical potential (μ) and the adsorption energy (E_a). When the atom chemical potential is greater than the adsorption energy, the atom sticks to the substrate surface otherwise it re-evaporates ($\mu < E_a$).

In reality, there is no perfectly flat surface since it may present roughness or some structural or chemical defects. They are usually classified in two categories [71]:

- **Zero-dimensional or point defects:** it comprises vacancies, impurities, kinks, dislocations, etc.
- **One-dimensional or line defects:** it includes step edges and domain boundaries.

In order to describe these defects, a Terrace Ledge Kink (TLK) model is introduced [72]. Figure 2.6 shows the TLK model by taking a simple cubic crystal. Each atom is represented by a cube. This model focus on the thermodynamic stability of adatoms on the surface. It shows that the atom position on the surface is influenced by the number of bonds with neighbouring atoms. For example, the adatom that collides with a step edge has a higher binding energy than the adatom that sticks on the terrace because it

has a large number of nearest neighbours compared to that on the terrace. According to this model, defects can be divided into two types:

(a) Thermodynamically stable defects such as impurities, vacancies, step kinks and step vacancies are present at equilibrium for a temperature greater than 0 K. Their formation depends on two parameters: the temperature and their formation energy. Note that this energy changes from one site to another depending on the number of nearest atoms.

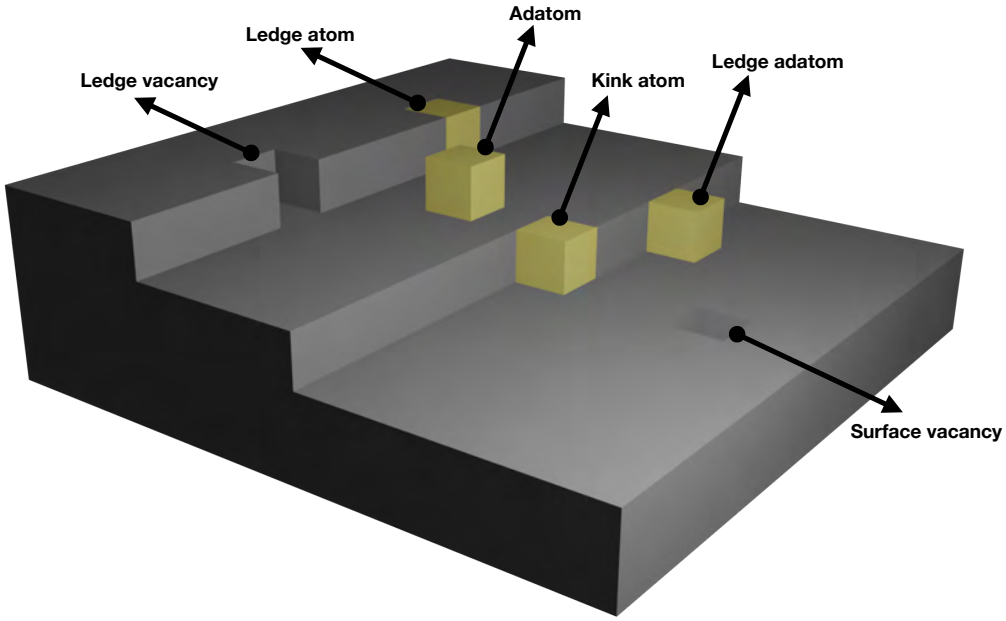

Figure 2.6: *Schematic illustration of typical atomic sites and surface defects.*

(b) Kinetically stable defects are dislocation emergence points at the surface (edge dislocation and screw dislocation) [71]. An edge dislocation (see Figure 2.7a) can be seen as an extra atoms half-plane introduced halfway though the substrate. Thus, it disrupts the atoms arrangement on the substrate surface. It is characterised by a Burgers vector which is perpendicular to the dislocation line. The Burgers vector determines the direction and the magnitude of the defect. Contrary to edge dislocation, a screw dislocation has its Burgers vector parallel to its dislocation line as shown in Figure 2.7b. A screw dislocation is defined as a topological defect of a crystal lattice [71]. When the screw dislocation is produced, the atoms are organised in a helical pattern around the defect.

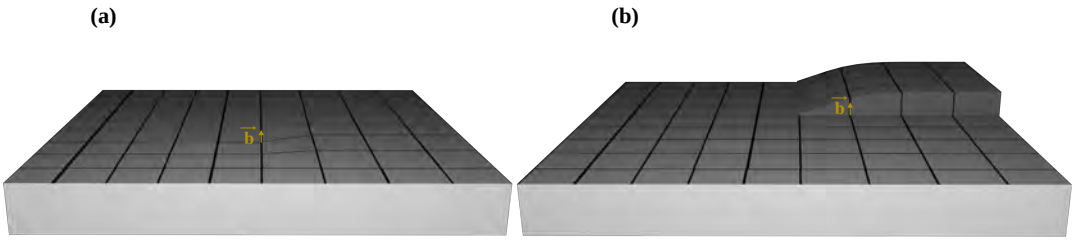

Figure 2.7: *Difference between (a) an edge dislocation and (b) a screw dislocation.*

Ehrlish-Schowbel (ES) attempted to better understand the adatoms behaviours when they collide with the substrate surface, particularly around an atomic step. They proposed their famous ES barrier which results from the effect of an atomic step as shown in Figure 2.8. Adatom 1 colliding with the upper side of the surface cannot easily diffuse to the lower surface and sticks to the atomic step. This is due to the presence of a potential barrier, the ES barrier. This barrier is due to the fact that the number of nearest neighbours on the upper side is greater than that of the lower surface. Therefore, Adatom 1 requires an energy greater than the ES barrier to pass through the atomic step and descend to the lower surface. On the opposite, Adatom 2

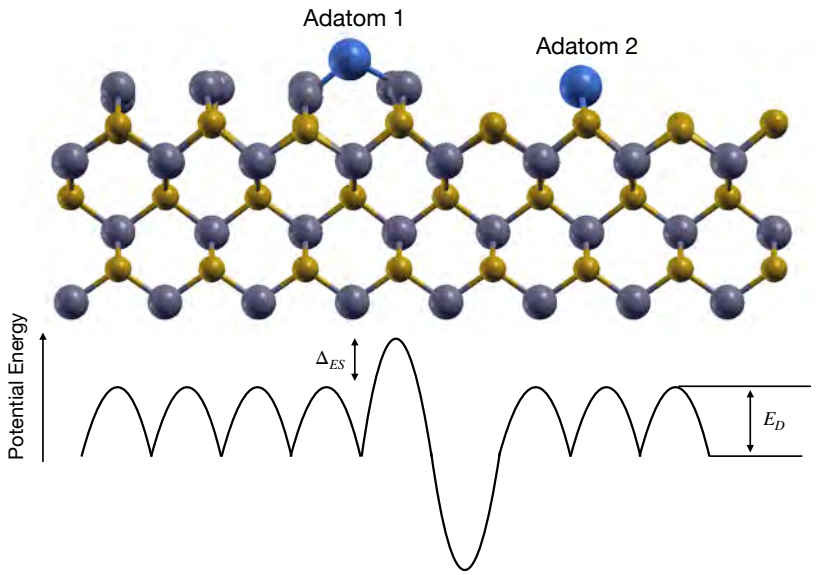

Figure 2.8: *Illustration of the diffusion of adatoms in the presence of an Ehrlich-Schwoebel barrier potential (Δ_{ES}) and the schematic plot of the potential energy of diffusion of adatom at the surface. E_D is the diffusion barrier.*

tends to cling to the atomic step more than to stay on the terrace. Therefore, the probability of incorporation depends on the site where the adatom arrives. It is clear that the probability of incorporation by crossing a step is very low. In fact, this type of incorporation causes a thickness variation on the surface and can lead to an accumulation of steps called macro-steps (constituted by many monolayers) [73].

The substrate plays a crucial role in determining the growth processes and improving the quality of the epitaxial layers. As mentioned in Section 2.2, the increase in the lattice mismatch (f) generates strain in thin layers ($h < h_c$) or misfit dislocations in thick layers ($h > h_c$). To reduce the strain density in the layer, the substrate and the deposited material must share the same atomic arrangement and a close in-plane lattice constant. This is the case of $Al_xGa_{1-x}As/GaAs$ low-strain heterosystems, where the misfit (f) is 0.1%. This material has been the basis of many device structures and has been used for 30 years [70, 74]. In fact, Indium phosphide (InP), gallium arsenide (GaAs), Silicon (Si) and Germanium (Ge) are the most widely used semiconductor materials for optoelectronics and nanoelectronics devices [75]. In the nanoelectronics sector such as integrated circuit (IC), transistor and diode manufacturing, the standard substrate was initially Ge semiconductor [75]. Due to the high resistivity of Si oxide compared to that of Ge oxide, Si became the most commonly used in industry. However, the indirect band gap of Si limits its use in the optoelectronic field. GaAs is a direct bandgap semiconductor which make it an ideal candidate for optoelectronic applications. It can absorb and emit light with high efficiency. Similarly, the InP semiconductor is also widely used as a substrate, especially for solar cells and photonics applications [76].

In this thesis, our first objective is to integrate $Bi_{1-x}Sb_x$ films on an industrial substrate for applications in nanoelectronics and optoelectronics. From the industrial point of view, the (001) oriented substrates are the most widely used for both applications. Adding to this that the lattice mismatch between GaAs(001) and BiSb(0001) ($f_{BiSb/GaAs}$) is 19.5%, which is smaller than $f_{BiSb/InP}$ (22.5%) and $f_{BiSb/Ge}$ (19.7%), we will thus use GaAs(001) substrates. Although $f_{BiSb/Si}$ (16.3%) is smaller than $f_{BiSb/GaAs}$, we prefer to work on GaAs since its surface preparation is easier in our system. Note that we tried to deposit BiSb on Si but only 3D growth was achieved. Our second objective is to grown $Bi_{1-x}Sb_x$ films on a substrate that share a close crystalline matrix close to that of BiSb. $Bi_{1-x}Sb_x$ being a quasi-hexagonal material, our choice fell on the hexagonal GaAs(111)A substrate.

In the following, the main characteristics of the GaAs(001) and GaAs(111)A substrates used during my thesis are presented.

2.4.1 The GaAs material

GaAs is a Zinc-blende semiconductor belonging to the $F\bar{4}3m$ space group with a lattice constant of 5.65 Å. It can be seen as two interpenetrating face-centered cubic (FCC) sublattices (see Figure 2.9), where Ga atoms (group III elements) occupy each corner and center of each facet of the cubic lattice whereas As atoms (group V elements) occupy only half of the tetrahedral voids (i.e 4 of the tetrahedral interstitial sites).

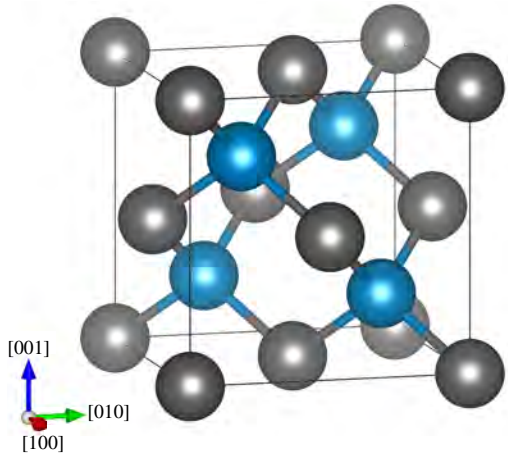

Figure 2.9: *Structure of bulk GaAs materials. As and Ga atoms are represented by blue and gray atoms, respectively.*

The GaAs(001) substrate

The GaAs(001) surface has a cubic pattern, consisting of alternating layers of Ga and As atoms, as shown in Figure 2.10.

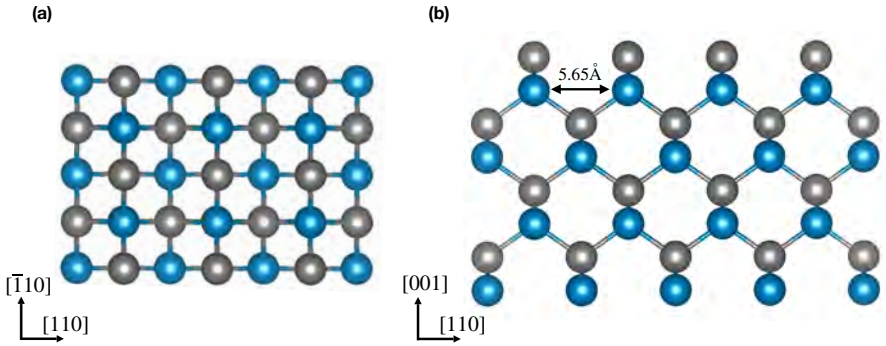

Figure 2.10: *(a) Top view and (b) side view of the GaAs(001) structure model. As and Ga atoms are represented by blue and gray atoms, respectively.*

It is polar and can be terminated by an As or a Ga layer. GaAs(001) is considered one of the most important substrates in the nanoelectronics and optoelectronics industry [77,78]. The GaAs(001) presents a variety of surface reconstructions depending on the preparation conditions such as temperature and the V/III ratio. In the case of an As-rich environment, the $c(4\times4)$ and (2×4) reconstructions are reported, and the latter one presents four different structural models: γ, β, β_2 and α. They have the same (2×4) symmetry but different atomic sequences. Generally, they are distinguished by observing differences in the RHEED pattern spot intensities. Otherwise, under Ga-rich conditions, (4×2) and (6×6) surface reconstructions are mostly reported [79].

In this thesis, the surface of our GaAs(001) substrates was prepared under As-rich conditions. This is why in the following, we are only interested in the As-rich $c(4\times4)$ and (2×4) surface reconstructions of the GaAs(001). Generally, the $\alpha(2\times4)$ phase is obtained at a temperature above 595°C, the $\beta(2\times4)$ phase at $\sim$ 550°C, the $\beta_2(2\times4)$ structure is stable at a temperature between 550°C and 510°C [80], the $\gamma(2\times4)$ reconstruction at a temperature between 510°C and 505°C and finally the GaAs(001)-$c(4\times4)$ surface at a temperature lower than 505°C [81,82]. Their atomic structures are shown in Figure 2.11.

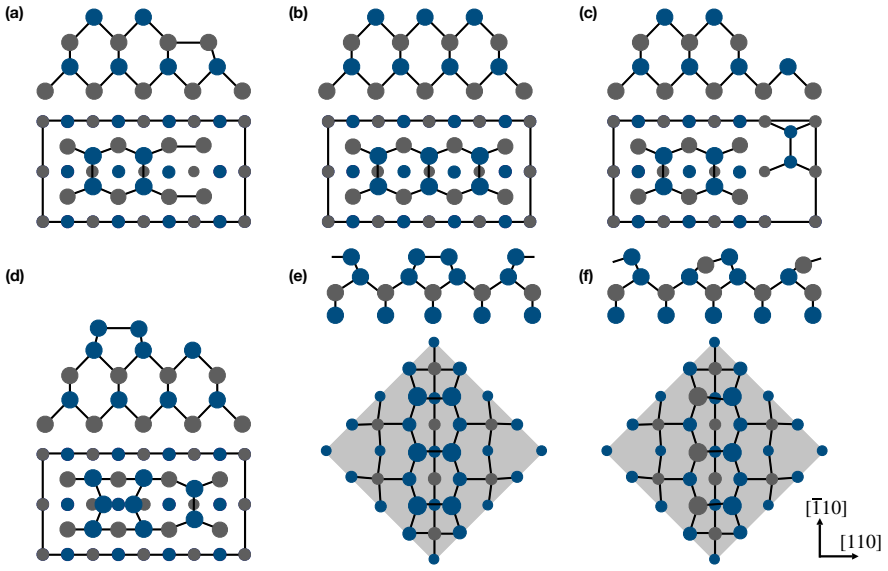

Figure 2.11: *Top view and side view of the surface reconstruction models of GaAs(001). (a) α, (b) β, (c) β_2, (d) γ structural models of the GaAs-(2×4) surface reconstruction. (e) $c(4\times4)$ and (f) $c(4\times4)-hd$ surface reconstructions of GaAs(001). As and Ga atoms are represented by blue and gray atoms respectively and their sizes reflect the distance from the surface.*

The surface preparation of the GaAs(001) substrate used during my thesis is based on many successive steps. These steps will be described in detail in Chapter 4, Section 4.2. With each step change, a change in growth temperature occurs. Thanks to RHEED, a transition from $\beta_2(2\times4)$ to $c(4\times4)$ surface reconstruction is observed as soon as the temperature is lower than 505°C (see Figure 2.12), which is in good agreement with the literature [81, 82]. Thus, our BiSb films are synthesised on the GaAs(001)-$c(4 \times 4)$ surface. This surface reconstruction is one of the most used for the epitaxial growth of III-V semiconductor heterostructures [83]. This surface has three As dimers on top of the As layer, followed by a missing dimer in the [110] direction (see Figure 2.11e). Interestingly, the As dimers form an hexagonal shape close to that of our quasi-hexagonal BiSb material. A group of researchers [84] proposed another structural model of the $c(4 \times 4)$ with three Ga-As hetero-dimers in the outermost layer instead of the three As dimers, as shown in Figure 2.11f. They called this ordered phase $c(4 \times 4) - hd$. Another group also proposed that the $c(4\times4)$ surface reconstruction consists of a combination of symmetric and asymmetric As dimer [85]. Given our As-rich growth conditions, we will assume that the reconstruction of GaAs(001) is the $c(4 \times 4)$ structural model.

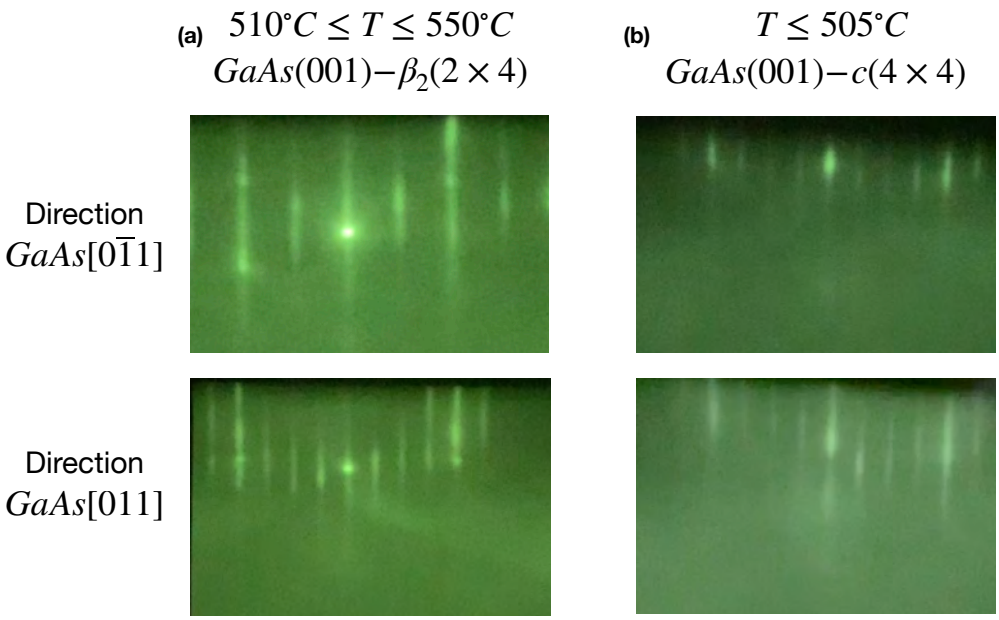

Figure 2.12: *RHEED patterns during the surface preparation of the GaAs(001) substrate. They show a transition from (a) $\beta_2(2\times4)$ to (b) $c(4\times4)$ surface reconstruction while decreasing the temperature below 505° C.*

The GaAs(111)A substrate

GaAs(111)A is a cubic material with an hexagonal surface arrangement that appears as alternating planes of III and V elements along the [111] direction (see Figure 2.13). It can be seen as a ABCABC bilayer stacking sequence. Its surface is of great interest to many researchers especially in the optoelectronics field, because the critical strain relaxation thickness is 30% greater than that obtained in GaAs(001) [73]. It is thus possible to obtain strained layers without crystalline deformation, which makes it possible to emit light at longer wavelength [73]. Here, our interest is based on the atomic arrangement on the GaAs(111)A surface. The atoms have an hexagonal arrangement close to that of BiSb(0001) contrary to the GaAs(001) cubic substrate. Moreover, the misfit between BiSb(0001) and GaAs(111)A is 13.65% whereas it is 19.5% between BiSb(0001) and GaAs(001).

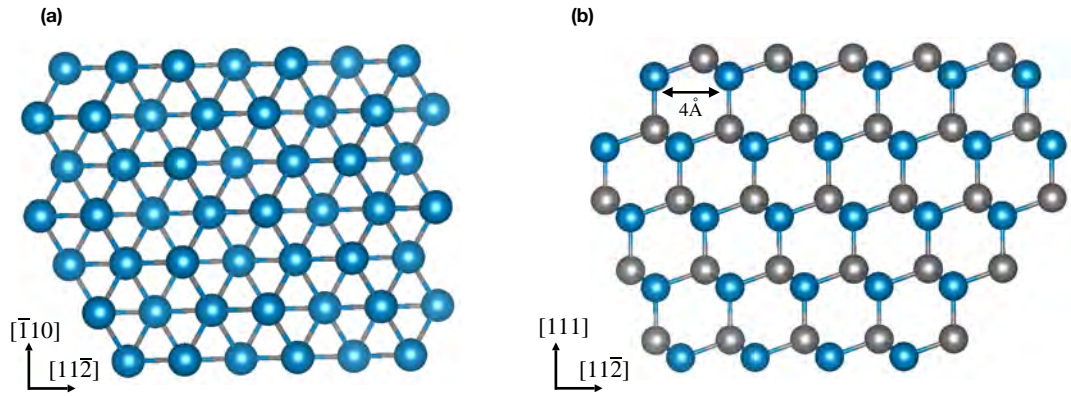

Figure 2.13: *(a) Top view and (b) side view of the structure model of GaAs(111)A substrate. As and Ga atoms are represented in blue and gray, respectively.*

The GaAs(111) surface is polar [86–88] and thus have not the same atomic termination in the [111] and [$\bar{1}\bar{1}\bar{1}$] directions: in the [111] direction, the surface terminates with Ga atoms while it ends with As in the [$\bar{1}\bar{1}\bar{1}$] one. In short, the GaAs surface in the [111] and [$\bar{1}\bar{1}\bar{1}$] directions is known as (111)A and (111)B, respectively. Importantly, a V atom arriving on the (111)A surface can only be bonded to a single atom of the underlying layer while it is to three atoms in the case of (111)B [73]. As the GaAs(111)A surface is polar, it holds surface charges, which makes it unstable. Consequently, surface reconstructions are required to minimise the surface energy. Contrary to GaAs(001), GaAs(111)A manifests only one surface reconstruction: the GaAs(111)A-(2 × 2) one [86] (or rather the only one discovered to date). Nevertheless, there are two possible configurations for this reconstruction

surface [88]. The first is obtained in an As-rich environment ($\sim$ V/III ratio $\geq$ 8) at a temperature lower than 400°C. In this case, the outermost layer is composed of an As trimer forming a triangle shape, as shown in Figure 2.14a. The three As atoms are bonded to three Ga atoms of the second layer [89]. The transition from As-rich condition to Ga-rich condition gives rise to a configuration change; a configuration with Ga vacancy is obtained, as shown in Figure 2.14b. As consequence, the surface has equal numbers of As and Ga atoms leading to a nonpolar surface [88, 90]. This configuration is considered energetically favourable [90].

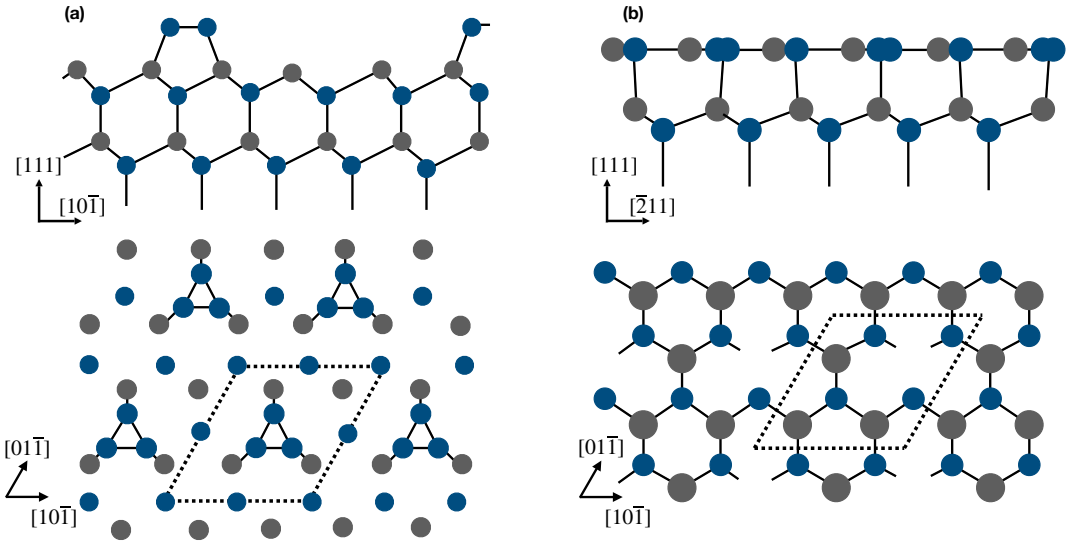

Figure 2.14: *Top view and side view of the (a) As-dimer and (b) Ga vacancy configurations of the* (2×2) *surface reconstruction of GaAs(111)A. As and Ga atoms are represented by blue and gray atoms, respectively.*

During my thesis, the process that was used to prepare the surface of GaAs(111)A substrate requires a temperature change at each step change. This process will be discussed in more detail in Chapter 5, Section 5.2. Regardless of the substrate temperature, the RHEED pattern only showed the GaAs(111)A-(2×2) surface reconstruction (see Figure 2.15), which is in good agreement with the literature [86]. Considering our As-rich growth conditions and the low growth temperature of BiSb (around 200°C), we will assume that the surface of our GaAs(111)A substrates exhibits the As dimer configuration.

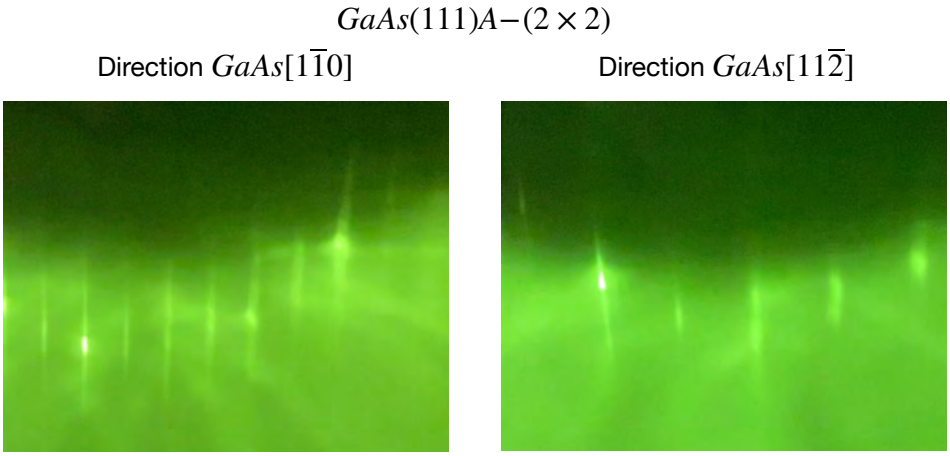

Figure 2.15: *RHEED patterns of the GaAs(111)A-*(2×2) *surface reconstruction along the* $[1\bar{1}0]$ *and* $[11\bar{2}]$ *direction of GaAs.*

3
Tools

3.1 Overview

In this chapter, our objective is to introduce the fabrication and characterisation techniques used during the thesis. As known, the physical properties of topological insulators (TIs) are strongly affected by impurities and point defects [91]. Many TIs exhibit a degenerate doped bulk semiconductor behaviour due to defects [92, 93]. As a result, the industrial integration of TIs is hampered. Molecular beam epitaxy (MBE), one of the best advanced synthesis techniques, holds promise for achieving high quality TIs since growth is precisely controlled at the submonolayer level and performed in an ultra-high vacuum (UHV) environment [94]. Advantages of this method are layer-by-layer growth, atomic abruptness, high purity and few defects and will be discussed in detail in Section 3.2. Next, the different chamber features will be presented in Subsections 3.2.1, 3.2.2, 3.2.3 and 3.2.4. At the end of Subsection 3.2.4, all the in situ characterisation tools will be presented including the Bayard-Alpert gauge, the Reflection High Energy Electron Diffraction (RHEED) and the wafer curvature optical control setup.

This chapter also introduces the ex-situ characterisation tools used after each growth, which consist in studying the topographic, morphological, crystallographic, compositional and electrical features. In Section 3.3, a brief introduction on electron microscopy will be presented and then the Scanning Electron Microscopy (SEM), Transmission Electron Microscopy (TEM) and Scanning Tunnelling Microscopy (STM) will be described in Subsections 3.3.1, 3.3.2 and 3.3.3, respectively. The SEM gives information about the sample surface morphology with a resolution better than 5 nm. The crystallography properties are probed by TEM and STM since they are able to image with a very high resolution ($\sim$ 1 Å). Section 3.4 presents Atomic Force Microscopy (AFM) that was used to study the sample surface topography. X-Ray Diffraction (XRD) measurements used to determine crystalline orientation and macroscopic composition of samples are shown in Section 3.5. Finally, Section 3.6 starts with a quick reminder of the Hall effect theory, followed by the electrical measurement procedures that were used for this

work.

3.2 Molecular beam epitaxy

In the late 1960s, after an increasing interest in manufacturing high quality III-V compound semiconductors, J. R. Arthur and Alfred Y. Cho from the Bell Telephone Laboratories invented the MBE [95]. It quickly became one of the most popular deposition technique not only for high quality crystal growth, but also for in situ characterisations. This deposition technique was developed for the growth of thin films on single crystalline substrate. In general, the epitaxial film develops with one or more well-defined orientation with respect to the substrate surface.

Using this growth method, atoms or molecules are evaporated from the source cells (effusion cells, cracker cells and plasma RF cells) to the heated crystalline substrate in an UHV environment. Each source cell contains a pure element either in solid, or liquid phase and sometimes in gas phase. Once the element flux is evaporated, a collision-free environment is assured between atoms or molecules from the cell to the substrate through the UHV, which leads to precise control of real time growth conditions and high purity of the synthesised samples. Importantly, the substrate temperature must be high enough to allow the atomic arrangement of the deposited material. When atoms or molecules arrive on the substrate surface, they react and several processes can occur such as adsorption, desorption, dissociation, migration, evaporation and incorporation (see Figure 2.1 in Chapter 2, Section 2.2). Interestingly, an atomic abruptness from layer to layer is possible: the deposition of the epitaxial film can be started or stopped abruptly thanks to the quick opening or closing ($\sim$ 1 sec) of the shutters, which thus provide immediate changes of impinging fluxes. A MBE system can thus synthesise ultra-thin films with precise control of the layer thickness as the growth rate can be as low as 0.01 monolayer/sec (ML/s).

Moreover, a MBE system is equipped with advanced in situ characterisation tools, which allow real-time observation of the growth surface. Two of them are the RHEED and the optical monitoring of the wafer curvature. RHEED is used to monitor surface roughness and reconstruction while optical monitoring of the wafer curvature probes the stress accumulation in the deposited layer. Interestingly, prior to any growth the substrate surface can be processed in the preparation chamber, making the MBE system an ideal platform for studying growth mechanisms.

During my thesis, in the LAAS-CNRS laboratory, all growths were performed in a MBE-412 system from Riber (see Figure 3.1). This system is

composed of the following parts: the loading, the preparation and the growth chambers; all of them connected through the cluster one. They are separated by electro-valves, and each has an independent pumping system insuring an UHV environment. Importantly, it is possible to perform an automatic transfer between the different chambers and prepare batches in this semi industrial MBE-412 system. Note that this system supports the loading of wafers up to 4 inches. Each individual chamber will be briefly described in the following section.

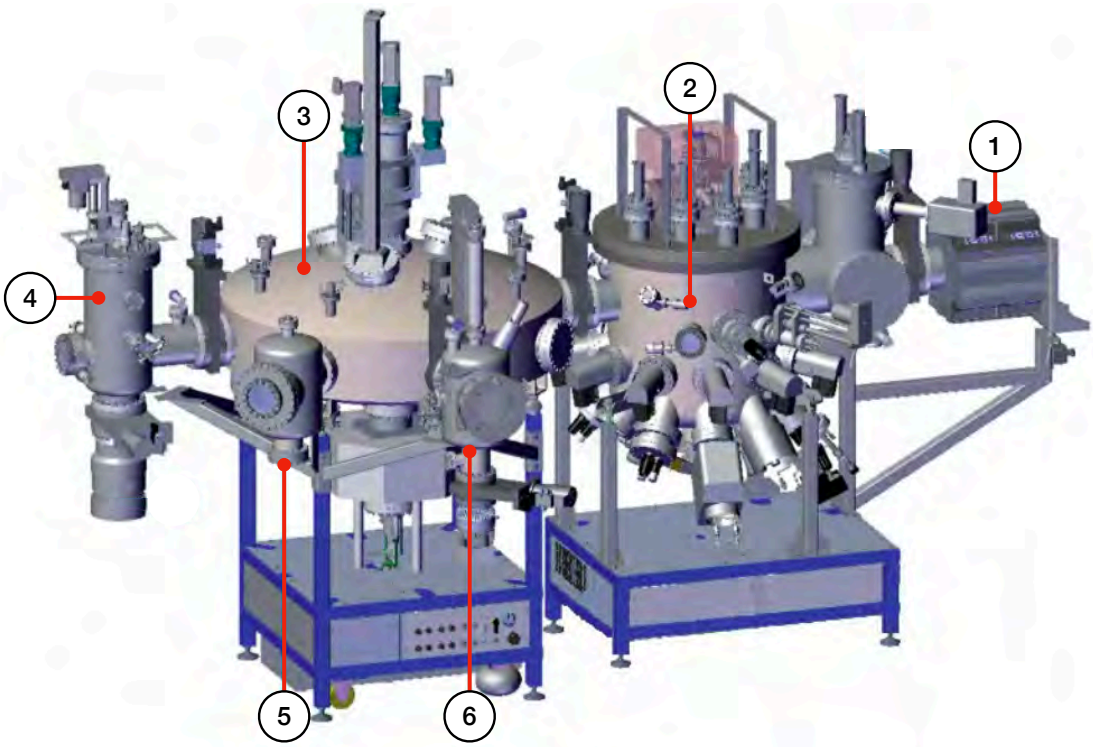

Figure 3.1: *Riber MBE-412. (1) The pumping system, (2) the growth chamber, (3) the cluster, (4) the preparation chamber, (5) the parking and (6) the loading chamber. (http://www.riber.com)*

3.2.1 The Cluster

The cluster is the heart of the MBE-412 system (see Figure 3.2). It allows the transfer of wafers between the different chambers, thanks to a robotic arm. Since it is connected to all the other chambers, the cleanliness of this part is crucial (pressure in the 10^{-11} Torr range) and is guaranteed by an ion getter pump.

This central chamber contains a parking zone that can store up to 5 wafer-holders at the same time. This parking zone is typically used to store wafers after growth, in a UHV environment and thus to avoid contaminations. Overall, the MBE-412 can accommodate up to 15 wafers at the same time: 10 in the loading chamber and 5 in the parking.

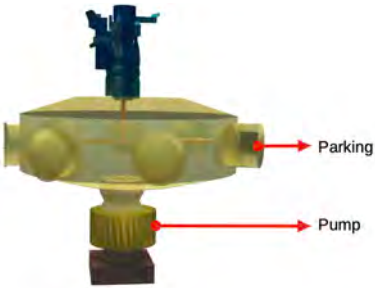

Figure 3.2: *3D schema of the cluster.*

3.2.2 The Loading Chamber

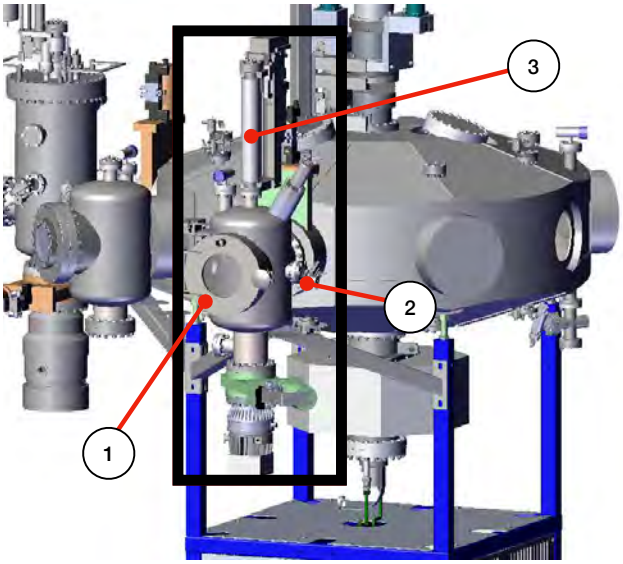

Figure 3.3: *3D schema of the loading chamber. (1) The Loading door, (2) the laser barrier and (3) the manipulator. (http://www.riber.com/assets/files/documentation/mbe412-imp2.pdf)*

The loading chamber is the link with the outside. The wafers carried by moly-blocks are loaded inside this chamber (see Figure 3.3), after having being exposed to an ex situ chemical preparation (if necessary). This chamber contains a cassette, which can load up to 10 wafers at the same time, and is carried by a lift equipped with a laser barrier. Using this laser, it is possible to detect the position of each sample-holder. Once the cassette is loaded into the system, a turbo-molecular pump (Varian Turbo-V 551 Navigator) quickly ensures that the UHV conditions ($< 10^{-8}$ Torr) are reached within 10 min.

3.2.3 The Preparation Chamber

The preparation chamber also called the degassing one, allows to degas the loaded wafer at high temperature before introduction into the growth chamber. The wafer is placed under an oven, consisting of a series of coil resistances, in which a temperature of 750°C can be reached (see Figure 3.4). Contaminations and gases can thus been eliminated by high temperature annealing. In addition, this chamber is water cooled and equipped with a turbo molecular pump (similar to that of the loading chamber) that guarantee the UHV conditions.

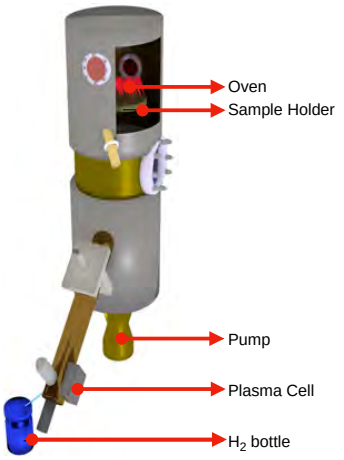

Figure 3.4: *3D schema of the preparation chamber.*

3.2.4 The Growth Chamber

The growth chamber is the most important part of the MBE system where materials are deposited (see Figure 3.5). Standard effusion cells and cracker ones (see Figure 3.6) are placed at the bottom hemisphere of the chamber facing upwards. Generally, different cell types are used for III and V elements due to their different chemical and physical properties. Standard effusion cells are designed for evaporation of low partial vapour pressure materials such as III elements and Bi, whose fluxes are controlled by temperature. In our system, an ABN150DF effusion cell is used for Bi, while Ga is placed in an ABN300DF cell. On the contrary, other V elements are evaporated by cracker cells due to their high saturation vapour pressure. The As cracker cell in our system is VAC500 and that of Sb is VCOR110. During growth, the sample holder is placed in the middle of the reactor under an oven (circular heating coils). It is controlled by an automated manipulator rotating at a controlled speed which avoids inhomogeneities during the growth process. The degassed substrates are positioned downwards on the sample holder, facing the cells. The angle between each cell and the sample holder is 45°. The distance between the 2inch wafer and the oven is approximately 1 cm and its temperature is controlled by a thermocouple. Elements used in our MBE system are characterised by their high purity (6-7 N) leading to a negligible residual doping level of 10^{14} $atoms/cm^3$.

Inside each effusion cell, a boron nitride crucible is present, containing the high purity materials. Two thermocouples measure the base and tip temperatures, that are regulated differently in order to avoid droplets formation at the cell tips. It is possible to control and stabilise the temperature in

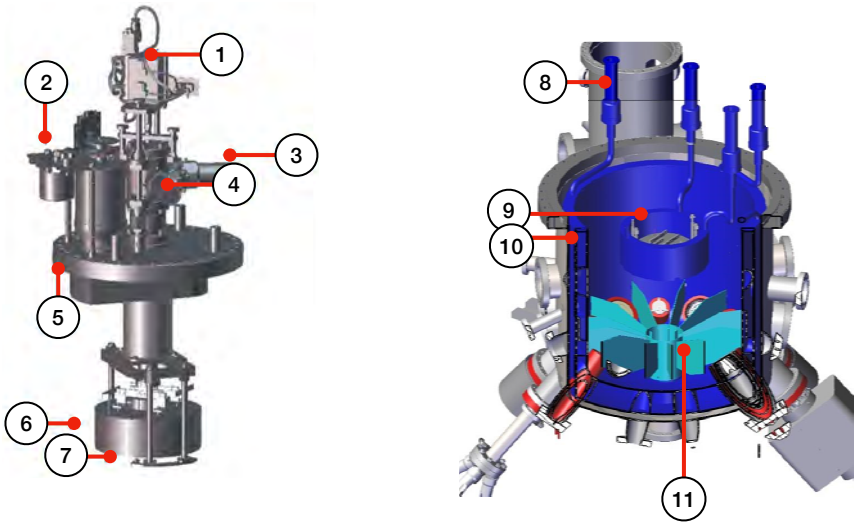

Figure 3.5: *3D schematic of the growth chamber: The substrate manipulator on the left, and the cryopanel on the right. The substrate manipulator is positioned at the center of the growth chamber, surrounded by the cryopanel. Other numbers represent: (1) the oven movement, (2) the substrate rotation, (3) the thermocouple feedthrough, (4) the electrical feedthrough, (5) the CF 250 assembly flange, (6) the heater, (7) the platen positioning forks, (8) the VBC TAL A-5 inlet and outlet connections, (9) the platen manipulator cryopanel LN_2 cooled, (10) the growth chamber cryopanel LN_2 cooled and (11) MBE Source Dividers. (http://www.riber.com/assets/files/documentation/mbe412-imp2.pdf)*

each zone using Proportional-Integral-Derivative (PID) controllers. On the other hand, cracker cells are composed of a digital electro-valve allowing fast control of the group V fluxes (up to 0.1%). With the valve's rapid shut-off capability, it is possible to reproducibly control the flux, and thus build complex heterostructures (Vecsel, Braggs). A valve cracker cell is built of two thermally isolated parts: the titanium tank where group V elements are loaded and the cracker stage.

The pumping system is composed of a Cryo-Torr 8 Cryopump and an ion getter pump, which ensure the UHV environment. Moreover, a cryopanel filled with liquid Nitrogen maintains the vacuum level and thus reduces the contamination level of deposited materials. Water cooling panels surround each effusion cell to dissipate heat and thermally insulate them. Furthermore, in situ flux calibration and structural characterisation are performed using a Flux Gauge, a RHEED system and a homemade optical monitoring of the wafer curvature. The flux Gauge placed below the sample holder is

used to calibrate the fluxes. The RHEED system consists of an electron gun and a detector that face each other. The goal of the RHEED is to probe the structural modifications of the growing surface. Finally, the optical monitoring of the wafer curvature requires the use of a white light and a camera in order to study the strain accumulated in the deposited materials.

Figure 3.6: *Effusion cell (left) and cracker cell (right).* (*http://www.riber.com*)

The Flux Gauge

Figure 3.7: *Flux Gauge*

The Flux Gauge used in our MBE system is an ionisation one called the Bayard-Alpert Gauge. It is a sensor that measures the beam equivalent pressure (BEP) of atomic or molecular fluxes. It allows a precise calibration of cells and thus of the material composition before starting any growth. Note that the Flux Gauge cannot be used during growth as it interrupts the

beam, and thus affects the growth process. To measure fluxes, the gauge must be translated into the beam. Once molecules arrive to the head, electrons accelerated by the gauge's hot filament (see Figure 3.7), go through the inner volume of the grid, ionise the gas molecules and generate an ion current. The element flux (F) is determined by the following equation:

$$F = \frac{Ck}{\eta} P \left(\frac{M}{T}\right)^{\frac{1}{2}} \tag{3.1}$$

Where C is the Gauge constant ($\approx 8 \times 10^{20}$), k is the geometric factor (~ 1 if the Gauge is close to the substrate), P (Torr) is the measured BEP, M (g/cm^3) is the molar mass and T (K) the cell temperature.

Unfortunately, the measured pressure (P) is not the real one since each element has a different ionisation efficiency depending on its atomic number (Z). The ionisation sensitivity of an element $'j'$ is given by η_j in the following equation 3.2 and increases linearly with Z [96].

$$\eta_j = \frac{0.6 Z_j}{14} + 0.4 \tag{3.2}$$

Figure 3.8 shows the ionisation sensitivity for each element III and V present in our MBE system.

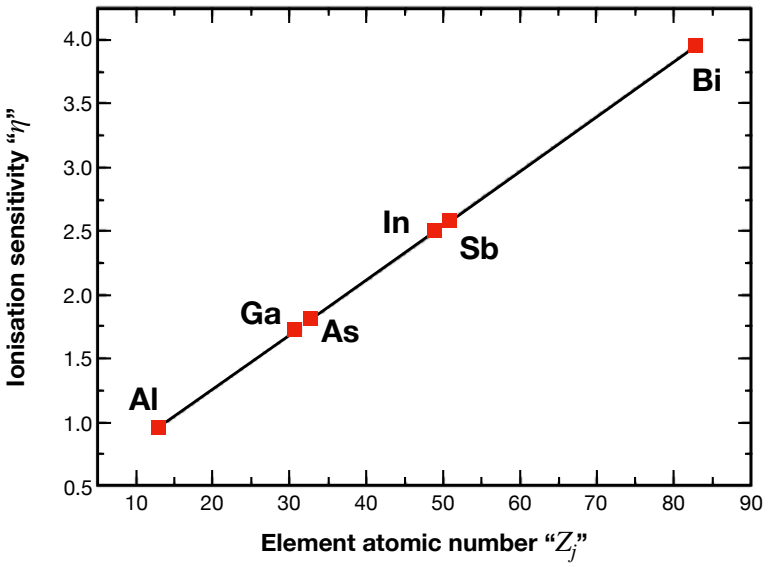

Figure 3.8: *Ionisation sensitivity of element III and V contained in our MBE system according to their atomic number.*

The RHEED

Reflection High-Energy Electron Diffraction (RHEED) is a technique that allows in-situ structural characterisation of the sample. It consists of an electron gun, a photoluminescent detector screen and a CCD camera (see Figure 3.9). The electron gun generates a grazing beam of collimated mono-energetic electrons with an energy of 20 kV. Electrons arrive on the sample surface with an incidence angle lower than 4° and are diffracted by the crystalline surface arrangement (see Figure 3.9). Note that due to the low incident angle, electrons can only penetrate a few atomic layers ($\sim$ 2-3 monolayers) of the surface. The diffracted electrons give a pattern which can be captured by the CCD camera located on the opposite side of the electron gun. In addition to structural characterisation, RHEED oscillations can be useful to determine the growth rate and give thus an overview of flux calibrations.

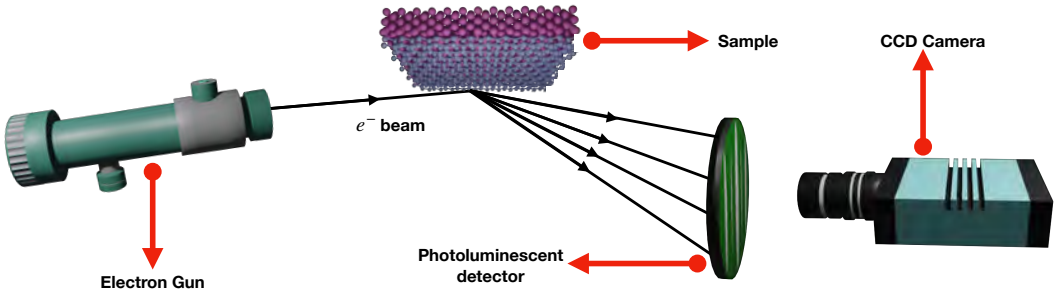

Figure 3.9: *Systematic setup of the RHEED system.*

The standard method used for a RHEED measurement is performed on a non-rotating substrate. However, as mentioned earlier, in a MBE system, the substrate should be in continuous rotation for homogeneity reasons and therefore this method is only suitable for small test samples. During the project, we used a method that gives access to the information carried by the RHEED diffraction patterns during the substrate rotation using a PC-based analysis system in addition to the tools mentioned above [97]. A cyclic recording of the RHEED diffraction pattern is obtained at several azimuthal angles during each complete revolution. It can be seen as a collection of images taken with multiple RHEED guns placed at different angles. Figure 3.10a shows the RHEED basic diffraction geometry [97]. Considering that the diffracted electrons are detected by the photoluminescence detector with an incidence angle θ, the Ewald sphere is constructed provided that the wave vectors k_0 and k' terminate on a reciprocal lattice rod. Only the upper half of the reciprocal space is scanned by the Ewald sphere, as shown by the shaded yellow zone in Figure 3.10b. Note that the smaller θ, the larger

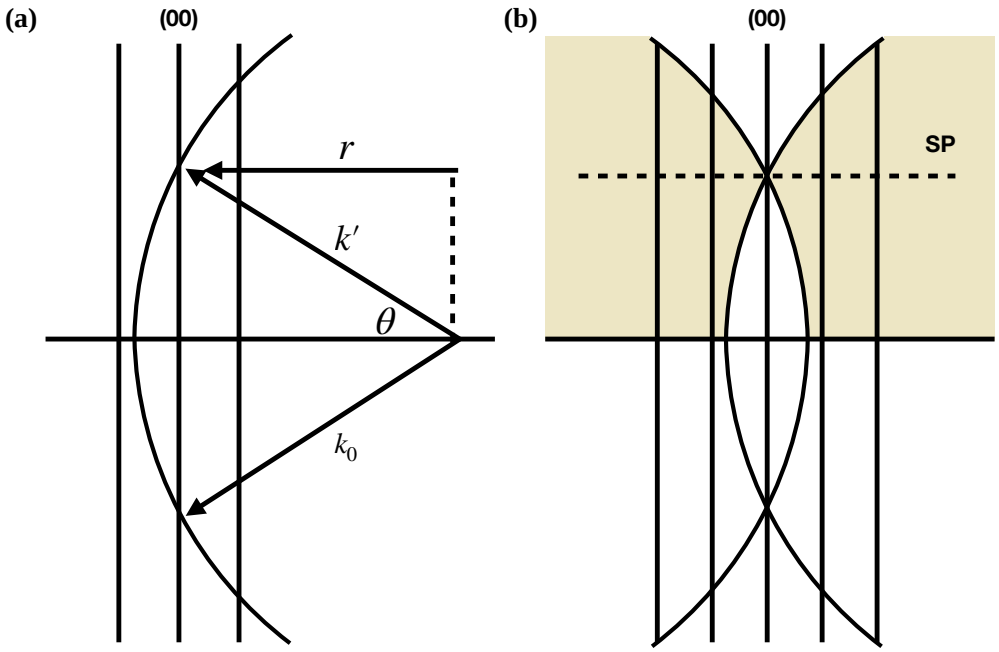

Figure 3.10: *The basic reciprocal space diffraction geometry for (a) RHEED static and (b) during substrate rotation. The shaded yellow zone in panel (b) shows the upper half of the reciprocal space scanned by the Edward sphere. The dashed line represents the specular plane (SP) that passes through the specular spot in the (00) rod [97].*

the scanned volume. However, due to the limited capacity of the PC-based analysis system, it is difficult to access all the informations contained in the upper half of the reciprocal space. This is why the software developed by Dr.Alexandre Arnoult focuses only on the plane that passes through the specular spot since it is the only surface-parallel plane that has no void in its center (see Figure 3.10b and Figures 3.11a,b). This plane is known as the specular plane (SP) and will be recorded as a function of the azimuthal angle as long the substrate is in rotation. For each azimuthal angle, the software will reconstruct each curved line of radius r that crosses the SP by a point including the specular spot. Finally, once a continuous rotation is accomplished, the azimuthal scan is completed as shown in Figure 3.11c. It is worth to note that the azimuthal RHEED can be used as a static RHEED by recording RHEED patterns at specific azimuthal angle. For example, in Figures 3.11a,b, for each 90° rotation spacing, the RHEED patterns are recorded and correspond to those obtained in static RHEED.

During this thesis, we only used RHEED to determine the surface reconstruction of the GaAs substrate and to get an idea about the atomic arrangement of BiSb surface. During growth, we had the opportunity to record the RHEED pattern throughout the substrate rotation. The $\alpha(2 \times 4)$ and $c(4 \times 4)$ surface reconstructions of GaAs(001) have been detected (see Figure 2.12, in Chapter 2, Subsection 2.4.1) and the transition from island growth to layer growth of BiSb is observed.

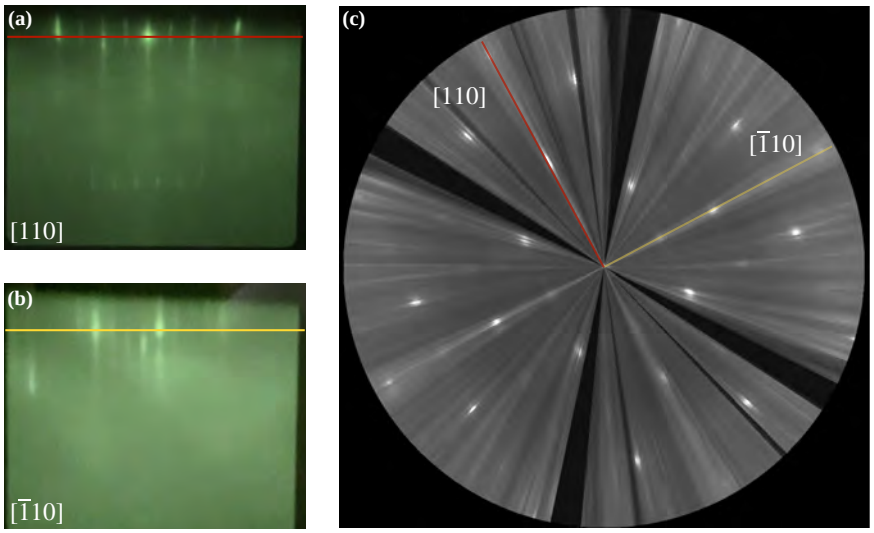

Figure 3.11: *Azimuthal RHEED. The intensity distributed along the red line in (a) and the yellow line in (b) are plotted against the azimuthal angle during the substrate rotation, giving thus the full azimuthal scan in (c).*

The Optical Monitoring of the Wafer Curvature

One of the most powerful tools for controlling and understanding the growth process is the Wafer Curvature Optical Control. Over the past two decades, techniques based on laser deflectometry have been used to measure changes in curvature of an optically reflective surface. These techniques consist in detecting the deflection of the laser beam induced by the deposited layer, and thus measuring the surface deformation. This instrument was later updated by Chason and Floro [98, 99] by adding a sensor matrix (generally a CCD), which makes it possible to measure the relative spacing of reflected laser spots.

Nevertheless, this tools does not meet industrial needs. In fact, industrial growth conditions requires the continuous rotation of the wafer (to ensure homogeneity), which makes it difficult to detect continuously the curvature

deformation by laser deflectometry. Additionally, industrial standard substrates have large thicknesses (of the order of 300 to 600 μm for 2 inches) which is not compatible with this technique. Fortunately, Dr.Alexandre Arnoult and Dr.Jonathan Colin succeeded in developing a new technique called Magnification Inferred Curvature (MIC) [100]. This new method uses a white light source instead of a monochromatic source (used in the case of the deflectometry-based systems) in order to be less sensitive to the surface reflectivity.

In this curvature measurement tool, known as EZ-CURVE, a beam of white light passes through an array of holes drilled in an opaque disk, which generates a matrix of light spots. The latter is then reflected specularly by the studied sample surface and its virtual image is captured by a camera placed on the opposite side of the substrate (see Figure 3.12). Finally, the wafer curvature radius ($\overline{R}$) is deduced after analysing the captured image using the developed software.

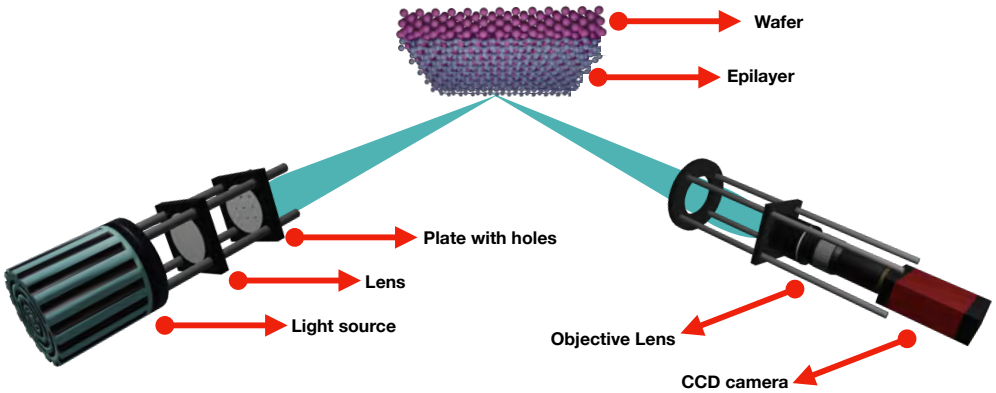

Figure 3.12: *Schematic setup of curvature measurements.*

From a theoretical point view, depositing a layer on top of an unclamped wafer induces stress accumulation which can be deduced by the change of the wafer curvature radius. From Stoney's equation (equation 3.3), the mean stress in the deposit film (σ_f) is linked to $\overline{R}$ and can be expressed as:

$$\sigma_f \cong \frac{M_s h_s^2}{6\overline{R} h_f} = \overline{\kappa}\frac{M_s h_s^2}{6 h_f} \tag{3.3}$$

Where $\overline{\kappa}$ is the curvature, h_f is the thickness of the deposited film, h_s is the substrate thickness and $M_s$is the biaxial modulus.

The analysing software used in this system displays the magnitude ($\sigma_f h_f$)

using the following equation:

$$\sigma_f h_f = \overline{\kappa} \frac{M_s h_s^2}{6} \tag{3.4}$$

At the end, it gives the plot of $\sigma_f h_f$ as a function of the growth duration.

3.3 The Electron Microscopy

The nanotechnology revolution has contributed to the development of several types of microscopy tools. They belong to different families but share the same purpose: probe the structure of small objects by creating high magnification images. Two of the main microscope families are optical microscopes and electronic ones. The optical microscopes use visible light as an illumination source, to obtain magnified images. On the opposite, electron microscopes are based on electrons waves interacting with the material.

Despite numerous improvements, optical microscopes do not meet all research needs due to the limited image resolution, which strongly depends on the light wavelength. As the visible light wavelength is between 400 and 700 nm, the microscopes cannot detect nanostructures smaller than 300 nm. On the other hand, the electron wavelength is inversely proportional to the square root of the acceleration energy ($\lambda = \frac{h}{\sqrt{2mE}}$ with h the Plank's constant, m the electron mass and E the acceleration energy). This means that the electron wavelength in electron microscopes can be tuned by changing E: increasing E makes λ smaller, and thus makes electrons an ideal source for nanoscale microscopy. Indeed, the wavelength of an electron can be up to 100,000 times shorter than that of visible light. As a consequence, the wavelength of the incident "light" is no longer a limit for image resolution in electron microscopes. As compound microscopes, electron microscopes use multiple electromagnetic lenses to focus the electron beam directly on the sample. Despite the name of electromagnetic lenses, they do not have the same structure as lenses. They consist in several electromagnets, generating a magnetic field that allows to focus the incident beam on the sample.

Globally, electron microscopy can provide more informations than optical microscopy since electrons have a mass and a charge: electrons can interact with the studied sample in different ways, resulting in different sources of signal (transmitted electrons, backscattered electrons, secondary electrons, elastically and inelastically scattered electrons, etc ...). Each one carries different informations about the sample that can be obtained after filtering and can be processed by different tools and techniques. These informations

may be related to the crystal structure, the topography, the strain or the composition of materials at nanoscale.

During my thesis, all the measurements have been performed on three different types of electron microscopes: the scanning electron microscope (SEM), the transmission electron microscope (TEM) and the scanning tunnelling microscope (STM). The aim of the SEM is to probe the surface topology. Quantitative informations about the sample are provided by electrons scattered around the sample surface: the magnified image of the surface morphology is generated from secondary electrons while informations about the elemental composition are carried by backscattered electrons. On the other hand, the TEM provides informations about the crystalline structure, the composition, the growth direction, the interface abruptness and the crystal quality. In contrast to SEM, all this information are obtained by electrons crossing the sample. Finally, the operating mode of a STM is different from the first two; it is based on a quantum mechanical phenomenon: the tunnelling effect. The STM allows to determine the morphology of a sample surface with atomic resolution and to perform tunnelling spectroscopy.

3.3.1 The Scanning Electron Microscopy

The purpose of SEM is to project a scanning electron beam on a sample surface in order to obtain a SEM image. This electron beam is generated by an electron gun and is focused on the sample surface using electromagnetic lenses. When electrons arrive at the sample surface, they interact with the near-surface atoms. A fraction of the electrons are reemitted, the secondary electrons (SE), and are detected by the Everhart-Thornley detector (SE detector). The intensity of each electrical signal depends on the impact between the electron and the sample atoms, and thus depends on the nature of the sample. Furthermore, the SEM is equipped with a detector that collects the backscattered electrons (BSE). Scanned elements emit different quantities of BSE, which increase with their atomic number. Therefore, heavy elements appear brighter in the image than light ones, allowing to qualitatively probe the sample chemical composition. Note that SE are low-energy electrons and are generated by an inelastic interaction between the electron beam and the sample atoms, while BSE are high-energy electrons and are reflected back after an elastic interaction between the beam and the sample. Consequently, SE come from the sample surface, while BSE come from deeper areas. Importantly, a low acceleration voltage is suitable for observing sample surface morphology, while high energies are preferred for studying chemical composition.

As mentioned earlier, the electron beam is generated by an electron gun

in a SEM which schematic can be seen in Figure 3.13. It is then accelerated by a negative potential of 1-40 kV before reaching the annular anode. Next, the beam is focused using electro-magnetic lenses placed in the center of the columns. The alignment of the electron beam is done in two steps. In the first step, the beam is focused into a narrow diameter of a few nanometers using condenser lenses. In the second step, a lens system called objective lenses is responsible for focus and aberration corrections. In between, a couple of coils are used to accelerate the beam across the specimen in order to scan it pixel by pixel. Finally, the SE and BSE detectors collect the electrical signals coming respectively from the secondary and the backscatter electrons. These electrical signals are then probed by an analysis system which reconstructs an image using the signals amplitudes. Note that all these equipments are placed in a high vacuum environment in order to avoid any interactions of incident electrons before reaching the sample. The high vacuum is obtained by the turbo-molecular pump.

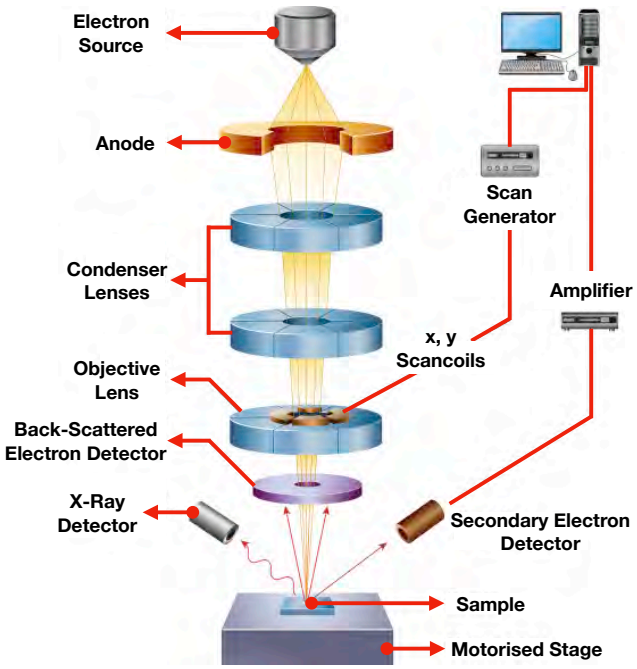

Figure 3.13: *3D scheme of the SEM [101].*

Unfortunately, the resolution of a SEM is limited to 1-20 nm due to the incident beam properties (the beam diameter and etc ...) and to electron-matter interactions. The beam diameter mainly depends on spherical, chromatic and astigmatism aberrations. A spherical aberration is the blurriness at the edge of an image. In fact, electrons passing near the lens edge bent

more towards the axis than those passing through the centre. As a result, the electron beam is not focused at the same point, causing the image of a point object to appear as a finite disk. A chromatic aberration takes place when the electrons in the beam are not perfectly mono-energetic and can be minimised by using modern electron sources. An astigmatism aberration occurs when the magnetic field of the lens is not homogeneous in plane. The use of stigmators can prevent this.

3.3.2 The Transmission Electron Microscopy

TEM is a microscopy that gives valuable informations about the sample internal structure such as: the crystal structure, the composition, the growth direction, the interface abruptness and the crystal quality. Contrary to the SEM, a TEM extracts the information carried by electrons that pass through the sample.

In a TEM, an electron gun composed of a filament (usually tungsten) is either heated to high temperature (thermionic emission gun) or exposed to an intense electric field (field emission gun) in order to generate a high energy electron beam (typically in the range of 100-300 kV). The more coherent the electron beam (electron in phase), the better the resolution of the image. This beam is then directed towards the examined sample using a system of condenser lenses (see Figure 3.14). Note that the sample is deposited on a

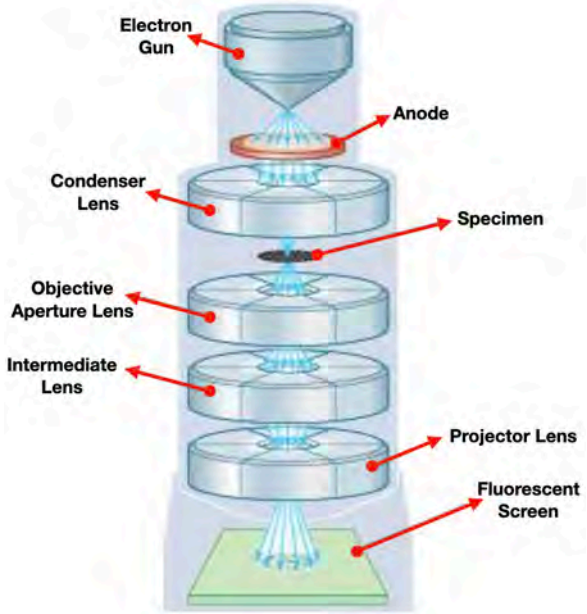

Figure 3.14: *3D schema of the TEM [102].*

sample holder which can be oriented in different directions with respect to the electron flow. Once the electron beam passes through the tested sample, a magnetic lens, called an objective lens, collects the electron beam and thus provides a magnified image of the object (usually magnified 10 to 100 times). The obtained image is captured by an intermediate lens, then it is magnified by a projector lens and imaged on the fluorescent screen. Finally, the electron beam is collected by a detector and then processed by computer to produce an image. All of these procedures should be performed under high vacuum (up to 10^{-10} Torr) provided by a vacuum pump system. The sample thickness must be less than 500 nm to allow the electron beam to pass through it.

There are two different operating mode: the diffraction mode and the image mode. The first one focuses on the wave behaviour of electrons. From a fundamental point view, an electron beam can be treated as a light wave because electrons present the wave-particle duality. Therefore, the interaction between the electron beam and a crystalline sample can be described by the Bragg's law. This law states that diffraction can only occur if

$$2dsin(\theta) = n.\lambda \tag{3.5}$$

Where λ is the electrons wavelength, d is the distance between atomic layers in the crystal, θ is the scattering angle and n is a positive integer.

In other words, electron diffraction can only occur at specific θ angles which are characteristic of the sample crystalline structure. Hence, a diffraction pattern is collected and used to observe characteristics of the studied sample such as crystal structure and crystal phase.

The second mode consists in placing the detector in the image plane in order to observe a transparency image of the irradiated area. The contrast of the final image results from the different interactions between the electrons beam and the sample. These interactions lead to the scattering of electrons by the sample. For transmitted electrons, the scattering depends on two factors: the sample thickness and the atomic number Z of the atoms constituting the sample's atomic lattice . For the first factor, the thinner the irradiated area, the greater the number of electrons that pass through it. As a result, the image obtained of this area is brighter. For the second factor, the higher the Z of the sample's atoms (i.e there are more electrons around the atom nucleus), the greater the number of interactions between these electrons and the electrons beam. As a consequence, scattering increases and fewer electrons are transmitted.

3.3.3 The Scanning Tunnelling Microscopy

The STM working principle is based on the tunnelling effect, as shown in Figure 3.15. A metallic tip attached to a piezodrive is placed very close to the sample surface. The distance between the tip and the surface (typically 1 nm) is controlled by a piezoelectric. Upon applying a voltage between the probe tip and the sample, the electrons can cross the vacuum barrier between the tip and the sample by tunnelling effect. This established tunnelling current exponentially decays with the tip-surface distance increasing.

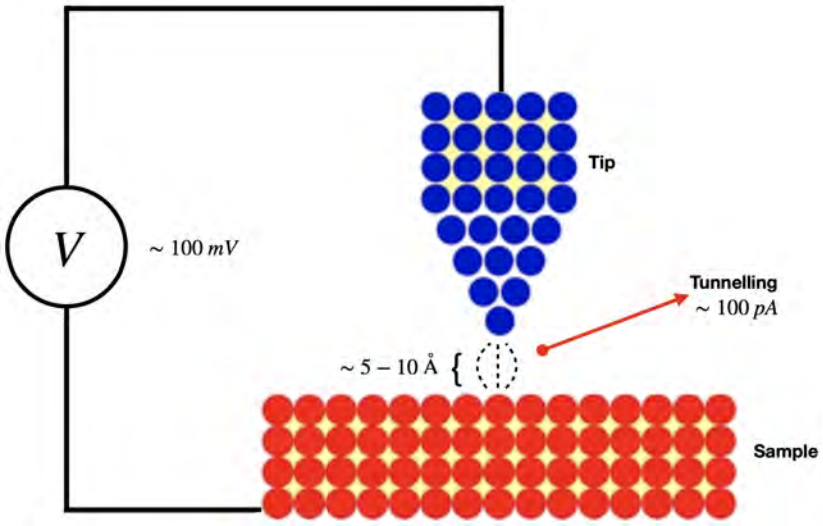

Figure 3.15: *Systematic setup of the STM [103].*

By scanning the tip over the sample and measuring this tunnelling current, there are two ways to obtain a STM image, either by a constant height mode or constant current mode. With the first mode, the image is obtained directly by mapping the measured tunnelling current variation as function of the tip position, while in the constant current mode, the tunnelling current is kept constant during scanning by using a feedback loop adjusting the tip-sample distance. For this reason, the topographic image is obtained by recording the voltage required by the piezoelectric to adjust the distance between the tip and the surface while scanning. With a probe tip preparation, this latter has an apex ended by a single atom, enabling to resolve surface topography with atomic resolution.

3.4 The Atomic Force Microscopy (AFM)

An AFM belongs to the same family than STM: both are a scanning probe microscope giving a very high resolution image of the scanned sample surface. Both use a probe tip to scan the entire sample surface, but, they have a different basic operational principle: the AFM measures the small force between the sample surface and the tip while the STM (described above) measures the tunnelling current between the surface and the tip. Additionally, the AFM can be used to scan the surface of conductors and insulators due to its ability to measure several forces such as Van Der Waals force, Pauli repulsive force, electrostatic force and etc. . . , while the STM can only measure the surface of a conductive sample since a tunnelling current cannot be generated between the tip and an insulator.

Figure 3.16 presents the schematic setup of the AFM. It consists of a tip placed at the end of a cantilever and an optical system composed by a laser and a photodiode. The nanometric-sized tip placed at the end of a cantilever is brought into proximity with the sample surface. The interaction forces between the tip and the surface cause changes in the cantilever movement,

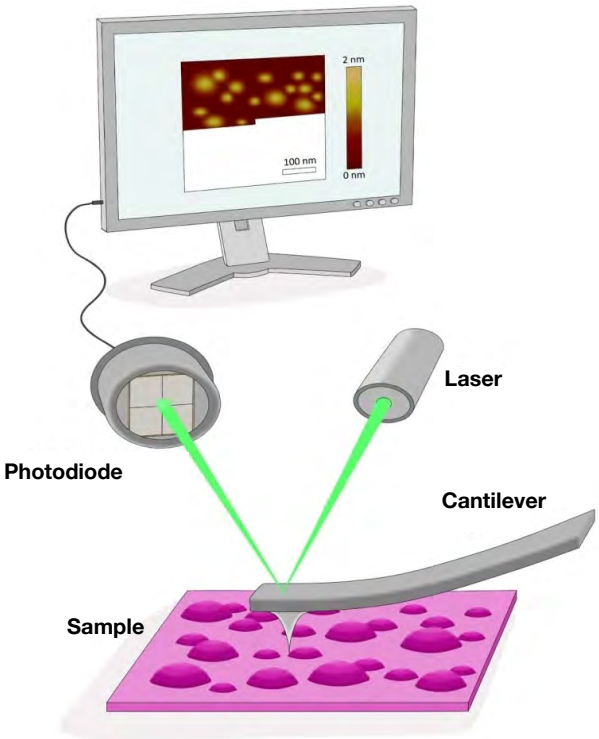

Figure 3.16: *Schematic setup of the AFM [104].*

which is detected by a laser beam reflected from the rear side of the cantilever. To perform topographic imaging, the tip is moved over the surface, keeping the force constant, thanks to a feedback loop.

There are three imaging modes knows as: the contact mode, the tapping mode and the non-contact mode. During my thesis, I used the tapping mode because it gives a topographic image of the sample without damaging the sample surface and the tip used, contrary to the contact mode. Its working principle is to oscillate the cantilever up and down. The tip establishes a repulsive contact with the sample surface at the lowest point of oscillation. The oscillations characteristics (frequency, amplitude and phase) are changed by the tip-sample interaction. When keeping the change in amplitude constant (ΔA), a high resolution image can be obtained. This mode, called "amplitude modulation" AFM measurement was the one used during my thesis.

3.5 The X-Ray Diffraction

X-Rays are high energy light with a wavelength similar to the interatomic distances in a crystal. When an X-Ray encounters the sample atoms, it interacts with their electrons: since the X-Ray energy is not enough to release them. Electrons oscillate and emit a new X-Ray having the same energy as the incident X-Ray: this is called elastic scattering. In a crystal, atoms form a periodic arrangement (see Figure 3.17) and thus form distinct planes (the separating distance is d). When an X-Rays beam hits atomic planes, constructive interferences occur if the Bragg's law is satisfied (see equation 3.5 and Figure 3.17). This is called X-Ray diffraction. The Bragg's law can be expressed as:

$$sin(\theta) = \frac{\lambda}{2d_{hkl}} \tag{3.6}$$

Where θ is the angle between the incident X-Ray wave vector and the diffraction plan, $\lambda = 1.54059$ Å is the wavelength corresponding to the K_{α_1} emission of Copper and d_{hkl} is the interplanar distance (h, k and l are Miller indices).

The X-Ray diffractometer gives information on the layer thickness, composition and structural quality based on different non-destructive methods such as high resolution XRD (HR-XRD) and grazing incidence XRD (GI-XRD). Strain and relaxation of thin layers can also be calculated from these measurements.

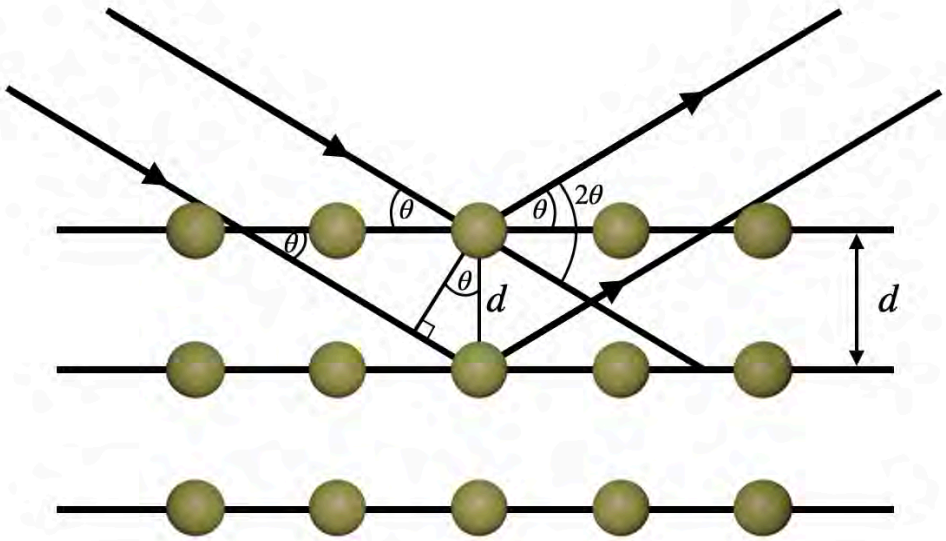

Figure 3.17: *Illustration of X-ray diffraction by the crystalline lattice of the sample obeying Bragg's law.*

HR-XRD is used to characterise almost perfect crystalline material. The high resolution is obtained using very high quality mirror and monochromator combinations. To obtain all the possible diffraction directions, the sample is scanned through a range of 2θ angle (the angle between the incident and the scattered X-Ray). A detector on the other side of the X-Ray source records the intensity of the observed X-Ray beam at each 2θ angle. The treatment of the diffraction peaks reveals d_{hkl} and thus makes it possible to identify the sample composition. Generally, this is achieved by comparing the measured pattern with a reference one.

On the other hand, the GI-XRD is used to analyse a randomly oriented crystalline material and also to analyse the surface of thin films. The sample is exposed to an X-Ray beam with a small incident angle ($\alpha < 5°$) close to the critical angle of total X-Ray reflection. The advantage of using a small angle is to reduce the signals coming from the substrate and to improve the signals coming from the surface. During the analysis, the incident angle (α) is fixed and 2θ is varied by moving the detector.

Moreover, the XRD-diffractometer can be used to obtain pole figures that display the 2D projection of the 3D distribution of crystallographic lattice planes using polar coordinates. Once the 2θ is taken at the Bragg diffraction angle corresponding to the (hkl) studied plane, the sample is rotated around the ϕ axis and tilted at different χ in order to record the intensity variation of the specific (hkl) plane (see Figure 3.18). During my thesis, we used the

LinXeye 0D mode during the realisation of pole figures in order to obtain the best sensitivity. Each time we tilt the χ angle, we rotate the sample around the ϕ axis to obtain the orientation variation distribution of the (hkl) plane.

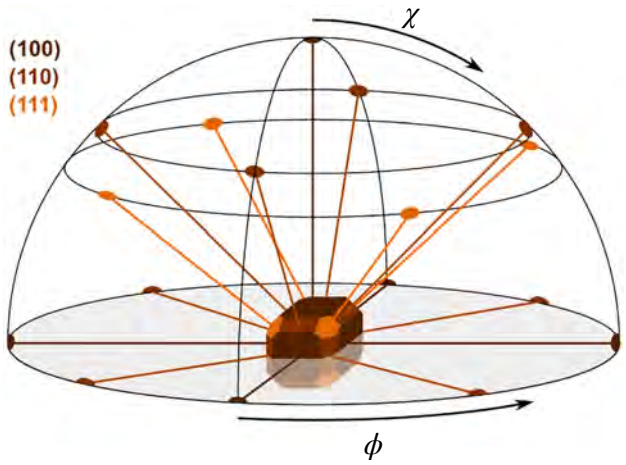

Figure 3.18: *Pole figure measurement: detection of the (100), (110) and (111) poles of a cubic crystal on a hemisphere by rotating the sample around ϕ and χ axes [105].*

During this thesis, we worked on the Bruker's X-ray Diffraction D8-Discover instrument. X-Rays are engendered in a cathode ray tube by heating a filament to produce electrons. The electrons are accelerated by applying a voltage and directed towards the target element. If their energy is high enough, they dislodge inner shell electron of the target material (Cu, Fe, Mo, Cr) and thus produce spectra with different wavelengths classified as K_{α_1}, K_{α_2} or K_{β_1}. A Göbel mirror is placed just after the X-ray source to collimate the X-ray beam into a narrow, intense beam. This beam is directed towards a monochromator where only one of its constituents is selected according to the chosen wavelength (in our case, the K_{α_1} wavelength is selected). Finally, the X-Ray beam reaches the sample, diffracts and is then captured by the secondary optics. The latter reduces the divergence height and the diffusely scattered rays and allows only one wavelength to reach the detector.

3.6 The Hall Effect Measurement

The Hall effect measurement is used to assess the transport properties of a sample such as its resistivity, its carrier concentration and its mobility. In order to perform this measurement, samples are prepared in a Van der Pauw configuration as reported in the top image of Figure 3.19.

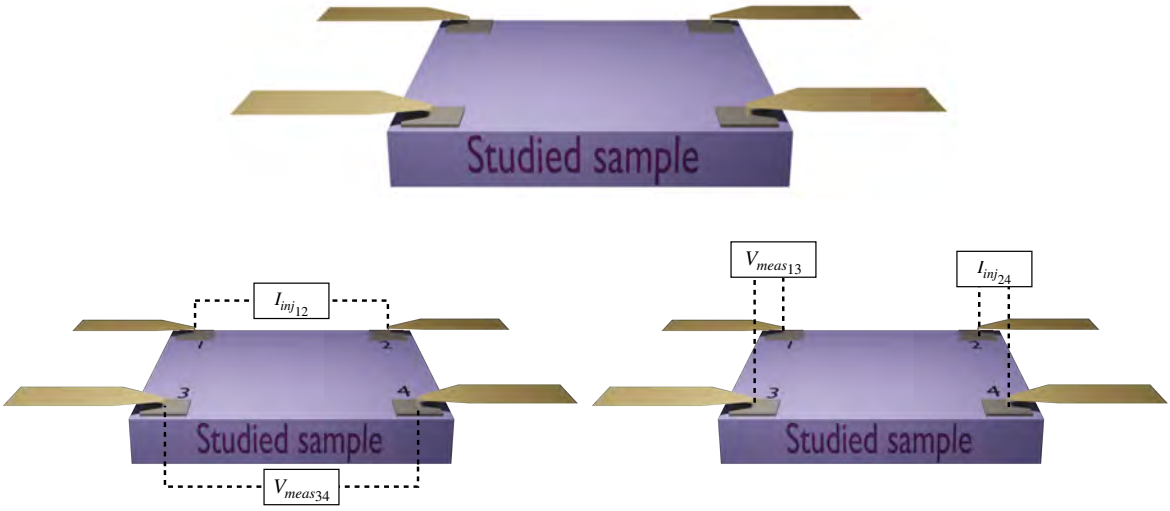

Figure 3.19: *Schema of the Van der Pauw devices (top figure) and illustration of the configurations required to obtain the sheet resistance (bottom figure).*

In this thesis, we used a Nanometrics Hall Measurement (HL5500) for the electrical characterisations. In order to carry out a measurement, the system performs an automatic operation series, which will be presented in this section. In general, the sheet resistance (R_S) is the first parameter to be measured since there is no need for a magnetic field, and then the Hall coefficient (R_H) is extracted once the magnetic field is applied. To measure the sheet resistance, two currents must be injected separately: the first between contacts 1 and 2 and the second between 2 and 4 as shown in the bottom image of Figure 3.19. In both cases, a voltage is measured between the opposing contacts. Hence, the sheet resistance is determined using the following equation:

$$\begin{aligned} R_s &= \frac{\pi}{2ln(2)} \times \frac{V_{meas_{34}} + V_{meas_{13}}}{I} F(Q) \\ &\approx 2.2662 \times \frac{V_{meas_{34}} + V_{meas_{13}}}{I} F(Q) \\ &with \quad I = I_{inj_{12}} = I_{inj_{24}} \end{aligned} \tag{3.7}$$

Where $F(Q)$ is the geometrical correction factor and is function of the symmetry coefficient Q, given by:

$$F(Q) = 1 - 0.35\left(\frac{Q-1}{Q+1}\right)^2 - 0.09\left(\frac{Q-1}{Q+1}\right)^4 \tag{3.8}$$

$$with \quad Q = \frac{V_{meas_{34}}}{V_{meas_{13}}}$$

Obviously, $F(Q) = 1$ when the two measured voltage ($V_{meas_{34}}$ and $V_{meas_{13}}$) are equal while the system will automatically take the inverse of Q before calculating $F(Q)$ if $Q < 1$. The system sheet resistance is finally obtained by calculating the average of the sheet resistances measured from all the adjacent contacts combinations. From the sheet resistance, the resistivity (ρ) can be derived using the following equation 3.9, provided the sample thickness (t) is known:

$$\rho = R_S \times t \tag{3.9}$$

In 1861-1862, James C. Maxwell suggested that a charge current moving longitudinally across a material temporarily interacts with an applied transverse magnetic field leading to a transient phenomenon. Once a steady state is reached, the internal electric field counters the external magnetic field. While this pioneer work predicted the existence of a transient phenomenon, it did not study it in detail. Later, Edwin Hall and his thesis supervisor Henry Rowland assumed that, when a magnetic field is applied perpendicularly to a conductive slab (see Figure 3.20) which charge carriers move longitudinally, they will deflect toward one side of the slab due to a Lorentz force $q(\vec{v} \times \vec{B})$ (where q is the charge carrier, $\vec{v}$ is the charge carrier velocity and $\vec{B}$ is the magnetic field). Thus, a charge accumulations on the conductive slab edges is obtained, which induces a transverse electric field E_y (later known as Hall field E_H). This electric field compensates the Lorentz force and thus eliminates the magnetic field force.

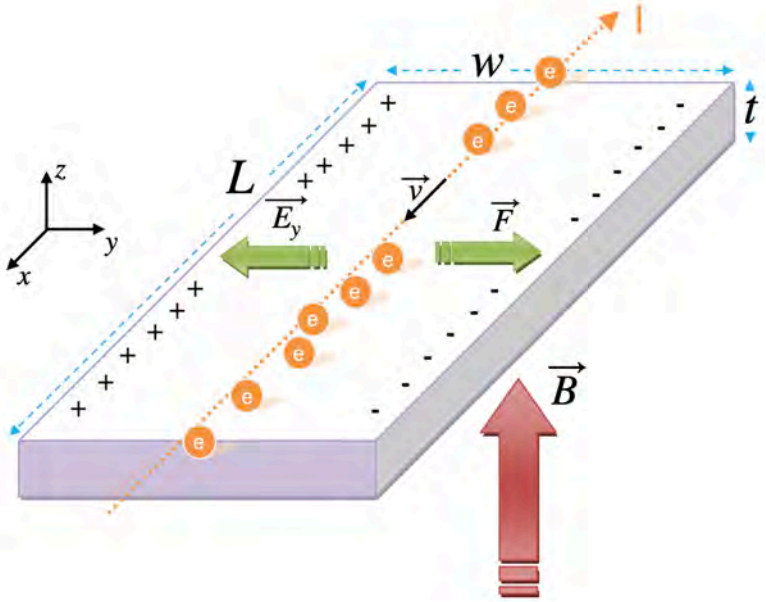

Figure 3.20: *Schematic illustrating the Hall effect in a conductive slab [106].*

Mathematically, the Lorentz force (F) is expressed by:

$$\vec{F} = q(\vec{E} + \vec{v} \times \vec{B}) \tag{3.10}$$

Or

$$\vec{F} = q(E_x\vec{u_x} + (E_y - v_xB_z)\vec{u_y} + E_z\vec{u_z}) \tag{3.11}$$

Where $\vec{E} = (E_x, E_y, E_z)$ is the electric field, $\vec{v} = (v_x, v_y, v_z)$ is the charge carrier velocity, $\vec{B} = B_z\vec{u_z}$ is the magnetic field and $\vec{u_x}$, $\vec{u_y}$ and $\vec{u_z}$ are the unit vectors.

At equilibrium, the current (I) is along the x axis, while no charge current is revealed along the y axis, due to the balance between the electrical and magnetic forces in that direction and therefore:

$$q(E_y - v_x.B_z) = 0 \implies E_y = v_x.B_z \tag{3.12}$$

Where E_y is know as the Hall field E_H ($E_y \equiv E_H$) and is directly connected to Hall voltage (V_H) by:

$$V_H = -\int_0^w E_H dy = -E_H w = -v_x B_z w \tag{3.13}$$

Where w is the studied sample width.

Considering that $I_x > 0$, v_x is positive if the charge carriers are holes ($q = +1.6 \times 10^{-19}$C) otherwise negative if the carriers are electrons ($q = -1.6 \times 10^{-19}$C). This means that V_H is negative in the case of holes while it is positive in the case of electrons.
The current I_x is expressed as follows:

$$I_x = J_x \times S = J_x wt \tag{3.14}$$

Where S and t are the section and the thickness of the conductive bar and J_x is the current density presented by:

$$J_x = nqv_x \tag{3.15}$$

Where n is the Hall charge carrier concentration. Note that J_x is positive regardless of the charge carrier type.

So from equations 3.14 and 3.15, the charge carrier velocity is expressed by:

$$I_x = nqv_x wt \tag{3.16}$$

$$\Longrightarrow \quad v_x = \frac{I_x}{nqwt} \tag{3.17}$$

Therefore, from equation 3.17, the Hall voltage is represented by:

$$V_H = -v_x B_z w = -\frac{I_x}{nqwt} B_z w = -\frac{1}{nq}\frac{I_x B_z}{t} = -R_H \frac{I_x B_z}{t} = -R_{H_S} I_x B_z \tag{3.18}$$

With

$$R_H = \frac{1}{nq} \tag{3.19}$$

Where R_H is the Hall coefficient and $R_{H_S} = R_H/t$ is the sheet Hall coefficient.

In our setup, the Hall coefficient R_H is measured in the presence of a perpendicular magnetic field of 0.3 T. Unlike the sheet resistance measurement, a current is injected between two opposite contacts and a voltage is measured between the other two as illustrated in Figure 3.21. Each voltage is measured four times due to the direction permutation of the current and the magnetic field i.e $V_{H_{23}}$ is obtained by measuring $V_{H_{23}}^{+B+i}$, $V_{H_{23}}^{+B-i}$, $V_{H_{23}}^{-B+i}$

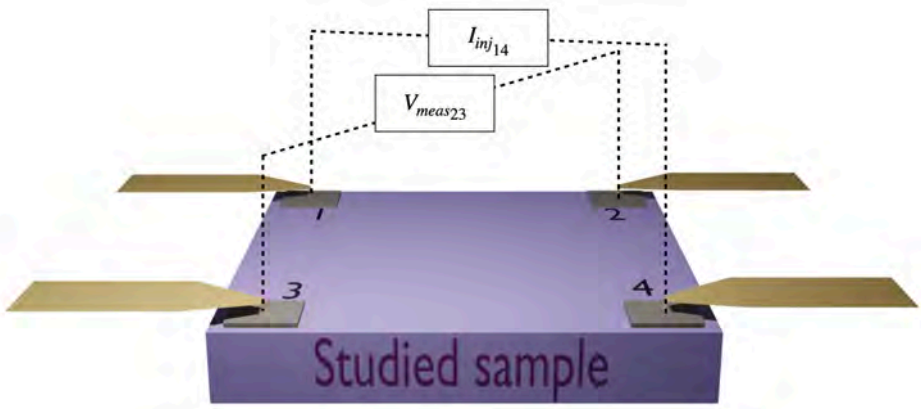

Figure 3.21: *Illustration of the configuration required to obtain the Hall coefficient.*

and $V_{H_{23}}^{-B-i}$ and can be written as:

$$V_{H_{23}} \approx \frac{(V_{H_{23}}^{+B+i} - V_{H_{23}}^{+B-i}) - (V_{H_{23}}^{-B+i} - V_{H_{23}}^{-B-i})}{4} \tag{3.20}$$

Finally, after having calculated $V_{H_{14}}$ using the same method as $V_{H_{23}}$, the Hall voltage V_H is calculated by:

$$V_H = \frac{V_{H_{23}} + V_{H_{14}}}{2} \tag{3.21}$$

Once the V_H is obtained, three parameters can be calculated: the Hall coefficient R_H, the Hall concentration n and the Hall mobility μ. From equations 3.18 and 3.21, the Hall coefficient becomes:

$$R_H = -\frac{V_H t}{I_x B_z} \tag{3.22}$$

After calculating R_H, n can be deduced from equation 3.19 and thus:

$$n = \frac{1}{R_H q} \tag{3.23}$$

In the electron transport case, R_H and q are both < 0, while > 0 in the hole case. The conductivity σ is defined as $1/\rho = \mu n q$. By using equation 3.9 and equation 3.19, we can thus calculated the mobility:

$$\frac{1}{\rho} = \mu n q \implies \mu = \left|\frac{1}{\rho} \times \frac{1}{nq}\right| = \left|\frac{R_H}{\rho}\right| = \left|\frac{R_{H_s} t}{R_S t}\right| = \left|\frac{R_{H_s}}{R_S}\right| = \left|\frac{V_H}{R_S I_x B_z}\right| \tag{3.24}$$

The Hall measurements are therefore an effective way to determine the carriers concentration and their types, in addition to the possibility of measuring mobility even if the sample thickness is unknown.

4

Integration of the Rhombohedral BiSb(0001) Topological Insulator on a industrial GaAs(001) Cubic Substrate

4.1 Overview

Since our goal is to use TI physical properties in future devices, it is important to study their integration on industrial standard substrates. In this chapter, we report the 2D integration of BiSb(0001) thin layers on GaAs(001) substrates. This is a challenge because of the different crystalline matrices and to the large lattice mismatches. As a consequence, only a few research groups attempted to grow BiSb on GaAs(001) and only textured BiSb thin film were obtained [107].

First, we establish the epitaxial 2D growth of $Bi_{1-x}Sb_x$ thin films on industrially compatible GaAs substrates by Molecular Beam epitaxy (MBE). The antimony composition ranges from 5 to 20%, covering almost the whole TI window. We evaluate the influence of each of the growth parameters in order to achieve the growth of high-quality BiSb thin films on GaAs(001).

This chapter is structure as follows. In Section 4.2, we describe the surface preparation that was used during this work and allowed the epitaxial growth of a fully relaxed polycrystalline BiSb thin film. In Section 4.3, the initial growths are discussed. In essence, we looked at the influence of temperature on $Bi_{1-x}Sb_x$ growth and found its optimum range to grow high quality $Bi_{1-x}Sb_x$ films on a GaAs(001) substrate. In Section 4.4, the influence of the Sb composition on the crystalline orientation of BiSb grains is investigated. This section also discusses the link between the Sb composition, the growth temperature and the crystalline quality of BiSb layers. Next, the BiSb growth mode and mechanism on GaAs(001) are discussed

respectively in Section 4.5 and Section 4.6. In Section 4.7 full structural characterisations are performed to study the BiSb crystalline structure and the BiSb/GaAs interface. In Section 4.8, our target is to theoretically confirm some experimental results using the Density Functional Theory (DFT) calculations. Finally the chapter ends with conclusions in Section 4.9.

4.2 Method

$Bi_{1-x}Sb_x$ thin films are grown on 2 inches undoped GaAs(001) wafers from AXT in our MBE system. Once the wafers are loaded into the MBE cluster and that the ultra-high vacuum (UHV) is reached, they are transferred into the preparation chamber for degassing at 300°C during 1 hour. Next, they are loaded in the growth chamber, which is equipped with a 20kV STAIB reflection high energy electron diffraction (RHEED) set up. Prior to growth, atomic fluxes (atomic beam equivalent pressures) are calibrated using a Bayard-Alpert Gauge. For all the samples, the Ga and As fluxes are chosen in order to obtain a V/III ratio of 2 and the Sb and Bi fluxes are adapted for each samples. The substrate temperature is gradually increased from 100 to 635°C under an As flux of 1.2×10^{-5} Torr for temperatures above 400°C. The wafer is deoxidized at 635°C for 10 min and then the temperature is cooled down to 580°C to grow a $1\mu m$-thick GaAs buffer layer with a V/III ratio of 2 in 1 hour. Next, the temperature is cooled down to the BiSb growth temperature by keeping the same arsenic flux on (1.2×10^{-5} Torr) for temperature above 400°C. According to RHEED records, the change in temperature leads to the GaAs(001) surface reconstruction transitioning from $\beta_2(2 \times 4)$ to $c(4 \times 4)$ when the temperature is below 505°C [82]. The latter exhibits three As-dimers parallel to the [110] direction, that are forming an hexagonal shape [82]. Finally, after temperature stabilisation the BiSb growth is initiated (terminated) by opening (closing) simultaneously the Bi and Sb shutters. The BiSb thickness and composition are determined by X-Ray diffraction (XRD) in a Bruker D8-Discover diffractometer and the surface morphology characterised by Scanning Electron Microscopy (SEM, FEI Aztec-600i) and Atomic Force Microscopy (AFM). Further Electron Back Scattering Diffraction (EBSD) measurements are carried out in a FEG-SEM JEOL JSM 7100F equipped with a Nordlys Nano EBSD camera (Oxford Instruments) in order to obtain an EBSD map and EBSD-pole figures of the samples. XRD-pole figures are obtained using the Bruker D8-Discover diffractometer. Finally, Hall measurements are performed in order to investigate the electronic properties of BiSb films.

4.3 The Influence of temperature

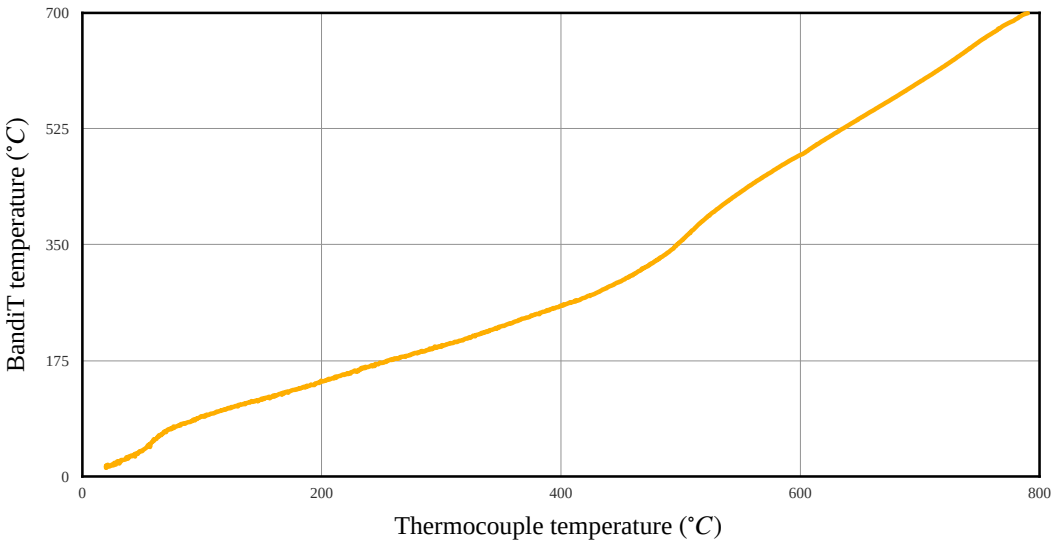

Figure 4.1: *Evolution of the band edge measured temperature (BandiT in °C) as a function of the thermocouple one (°C).*

The initial growths are performed in order to find the optimum temperature window to grow $Bi_{1-x}Sb_x$ films on GaAs(001) substrates with x being in the TI range. Five 250 nm thick layers are thus grown with an antimony composition of 10% and thermocouple growth temperatures (T_g) of 180, 200, 220, 240 and 260°C. An estimation of the "real" substrate temperature (T_r) can be obtained using Figure 4.1. The Bi and Sb fluxes are 4.5×10^{-7} Torr and 5×10^{-8} Torr, respectively.

Scanning Electron Microscopy (SEM) images of these samples are presented in Figure 4.2. It shows that the growth is polycrystalline and that the surface morphology is directly dependent on the temperature. For Tg = 180°C (see Figure 4.2a), the surface is rough and present a large number of misoriented grains. Increasing the temperature (see Figures 4.2b,c) decreases the surface roughness, increases the grain size and optimises their orientations: more grains present a flat top facet for Tg = 220°C. However, increasing the temperature ($T_G \geq 240°C$) further (see Figures 4.2d,e) worsens the situation: the density of misoriented grains increases and holes appear in the BiSb film. This can be explained by an evaporation of bismuth adatoms from the substrate surface due to its low saturation vapour pressure. Figure 4.2f clearly shows the effect of high temperature ($Tg = 260$°C): the red arrow highlights a BiSb droplet that was evaporated after being absorbed at the substrate surface. The melting point of the BiSb system under UHV seems

to be around $T_g = 260°C$ (corresponding to a real temperature about 177°C), lower than that calculated at the atmospheric pressure ($\sim 271°C$, [24]). According to this series, a growth window around 220°C is favoured in order to achieve a high crystallinity of $Bi_{0.9}Sb_{0.1}$ films.

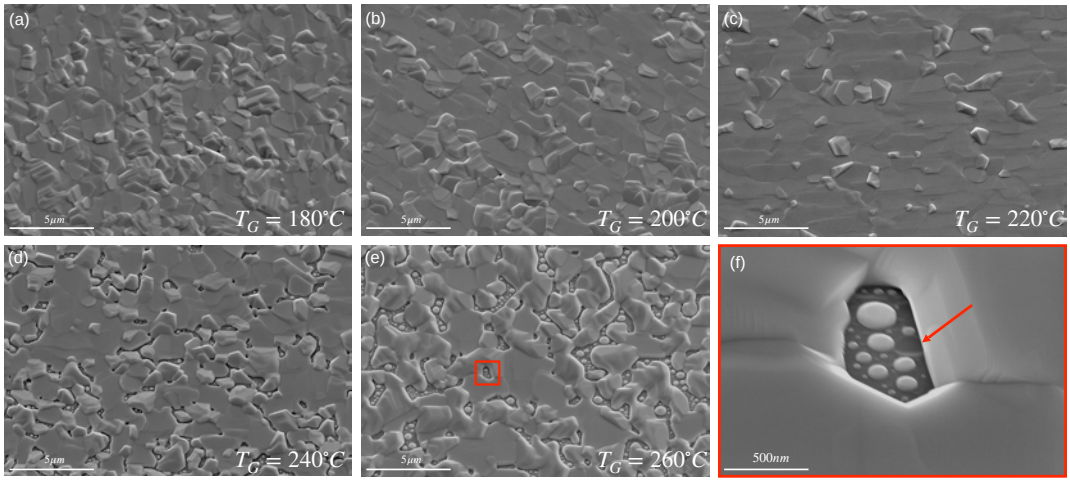

Figure 4.2: *Secondary electron (SE) SEM images showing the surface morphology of the as-grown $Bi_{0.9}Sb_{0.1}$ layer at a growth temperature of (a) 180° C, (b) 200° C, (c) 220° C, (d) 240° C and (e) 260° C. The SEM image in panel (f) is a zoomed image of the area indicated by the red square in panel (e) where adatoms are re-evaporated.*

In order to investigate the in-plane epitaxial relationship between the BiSb layer and the GaAs(001) substrate and to probe the temperature dependence of the BiSb texture, XRD pole figure measurements were carried out (see Figure 4.3). For reference, the pole figure of the GaAs(001) substrate taken at the Bragg diffraction angles of the BiSb(0006) is presented in Figure 4.3a . It can be noticed that no peak is present at $\Psi = 0°$, and that {011}, {112}, {113}, {311} diffraction peaks are observed with a typical square geometry. Figures 4.3b-f present the stereographic projection of BiSb films. All these figures are obtained at $\theta \sim 23°$ corresponding to the (0006) planes of the BiSb layers. The x axis corresponds to the [110] direction and y axis to the $[\bar{1}10]$ one. First in Figures 4.3b-f, the central peak, corresponding to $\Psi = 0°$, has a strong intensity, which demonstrates a preferential growth direction of the BiSb layer. Moreover, all diffraction spots detected in the reference pole figure are also observed at the same position in Figures 4.3b-f giving evidence that the BiSb(0001) does not present any rotation with respect to the GaAs(001) substrate: $[11\bar{2}0]_{BiSb} = [110]_{GaAs}$.

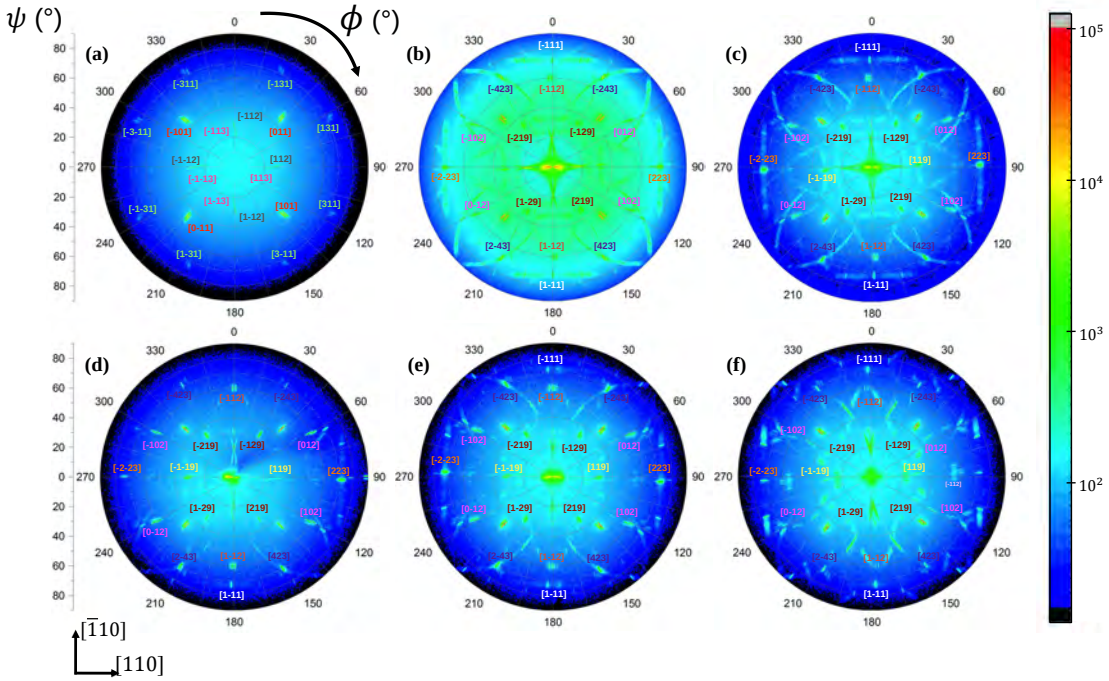

Figure 4.3: *XRD pole figures of different samples using a theta - two theta configuration around the diffraction Bragg angles of the BiSb* {0006} *planes. A reference measure on a GaAs(001) substrate is provided in (a). The XRD pole figures of the BiSb thin films are reported in (b) for a growth temperature of* 180°*C, in (c) for* 200°*C, in (d) for* 220°*C, in (e) for* 240°*C and in (f) for* 260°*C. The colour scale on the right corresponds to the X-Ray diffracted intensity of the samples in a logarithmic scale. Labels near each spot corresponds to the (hkl) planes. All pole figures are performed by rotating the sample around its normal axis (*ϕ*), at an angular orientation (*Ψ*) of the sample, ranging from 0 to 90°.*

This is in good agreement with the theoretical model reported in Figure 4.4. Interestingly, the central peak is elongated along the [110] direction for all $Bi_{0.9}Sb_{0.1}$ samples (see Figures 4.3b-e) except the one grown at $Tg = 260$°C (see Figure 4.3f). This indicates a [110] anisotropic tilt direction for temperatures below 240°C. For $Bi_{0.9}Sb_{0.1}$ films grown at $Tg = 180$°C , the intensity is distributed over the entire pole figure (see Figure 4.3b) indicating that the grain orientations are randomly distributed. On the contrary, increasing the temperature to 200°C leads to a focus of peak intensities at specific Ψ angles and the appearance of axiotaxial rings [108]. This indicates that the surface is starting to organise but still presents an axiotaxial texture and misoriented grains. No more rings are visible and spots are more intense at $T_G = 220$°C,

which highlights a good crystalline arrangement and surface organisation. Finally, axiotaxial rings appear again for temperatures above 240°C indicating an increase of the misoriented grain density in different direction. For $Tg = 260$°C, the partial disappearance of the central peak shows the loss of the (0001) preferential growth orientation.

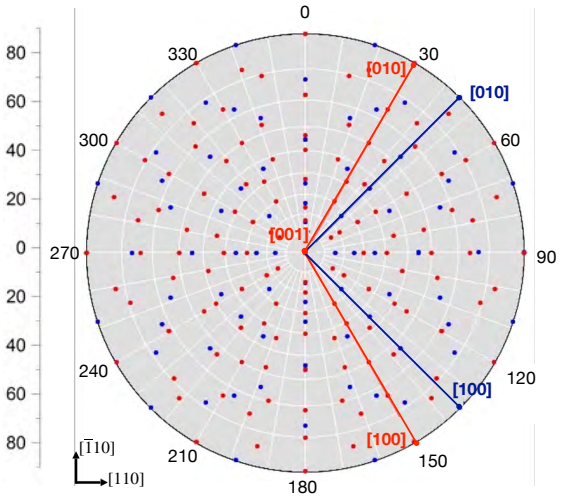

Figure 4.4: *Modelling of the pole figure of a* {0001} *BiSb film deposited ontop of a GaAs(001) substrate. The red and blue spots correspond to the BiSb and GaAs planes, respectively.*

4.4 The influence of the composition

After a fine tuning of the growth temperature to 215°C in order to reduce the surface roughness, we worked on the antimony composition of the BiSb layer. Four 250 nm thick samples were grown by keeping a Bi flux of 4.5×10^{-7} Torr and adapting the Sb one for compositions of 5, 10, 15 and 20%. Interestingly, the final composition of the BiSb layer, measured by XRD, corresponds roughly to the beam equivalent pressure (BEP) ratio of each element. Consequently, Sb fluxes (BEP) of 2.26×10^{-8}, 5×10^{-8}, 7.94×10^{-8} and 11.25×10^{-8} Torr are used for composition of 5%, 10%, 15% and 20% respectively.

The surface morphology of the $Bi_{0.95}Sb_{0.05}$, $Bi_{0.9}Sb_{0.1}$, $Bi_{0.85}Sb_{0.15}$ and $Bi_{0.8}Sb_{0.2}$ samples is shown in Figures 4.5b,c,e and f, respectively. It can be noticed that in the case of a low Sb composition (5%), the surface is rough, disorganised and has a large number of holes compared to other samples. On the opposite, when the Sb composition is 10%, the surface morphology

becomes organised due to the nucleation of a great number of grains having a flat top facet. It can be noticed additionally that some grains have a triangular shape pointing upward (see the red triangles) or downward (see the black triangles) in the $[\bar{1}10]$ direction. This indicates a good epitaxial relationship between BiSb films and GaAs(001) substrate. Finally, increasing further the Sb composition (15 and 20%) leads to an increase in the misoriented grain density and to the appearance of holes which affect the BiSb films quality. This trend proves the necessity to adapt the growth temperature to the Sb composition. Feutelais et al. [24] have shown that the phase diagram of Bismuth-Antimony alloys exhibits a continuous solid solution phase, which is strongly affected by the Sb composition. More antimony yields to an increase of the melting point and therefore change the optimal growth temperature.

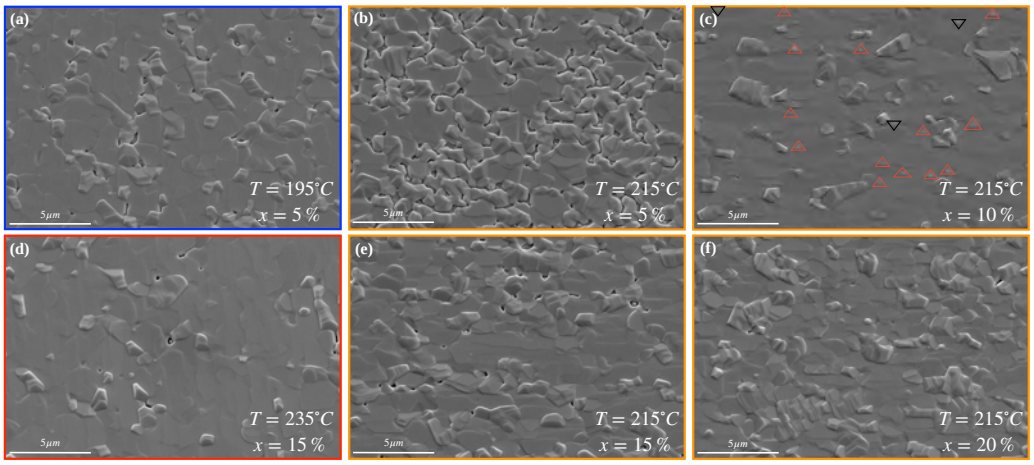

Figure 4.5: *Evolution of the BiSb surface morphology as a function of the temperature (T_G) and the Sb composition (x). SEM images of the BiSb layer grown on a GaAs(001) substrate with different compositions (a) and (b) 5%; (d) and (e) 15%; (c) 10%; (f) 20%. The blue, orange and red frames indicate growth temperatures of* $195°C$, $215°C$ *and* $235°C$, *respectively.*

To assess the relationship between the composition (x) and the growth temperature (T_g), $Bi_{0.95}Sb_{0.05}$ and $Bi_{0.85}Sb_{0.15}$ samples were grown at 195°C and 235°C respectively (see Figures 4.5a,d). Interestingly the surface morphology of these samples is totally different from those grown at 215°C for the same Sb compositions: they are smoother and better organised. The BiSb alloy quality therefore strongly depends on the x and T_g combination: $Bi_{0.95}Sb_{0.05}$ is optimised around 190°C, $Bi_{0.9}Sb_{0.1}$ at 215°C and $Bi_{0.85}Sb_{0.15}$ has a better surface morphology at 235°C. Consequently, increasing the composition must be accompanied by an increase of the growth temperature in order to achieve high crystallinity.

In order to investigate the crystalline orientation and the size distribution of the $Bi_{1-x}Sb_x$ grains, electron backscattering diffraction (EBSD) measurements were carried out on the four samples grown at $Tg = 215°C$ and confirmed the high crystallinity of the $Bi_{0.9}Sb_{0.1}$ film since it has more than 80% of grains having a negligible tilt (lower than 5°) with respect to the substrate (see Figure 4.6). Moreover, a Sb composition dependence of the grain orientation was directly detected; increasing antimony promotes a grain tilting around 10°, while it is between 20 and 35° for low antimony compositions (see Figure 4.6e). Interestingly, there is a link between the grains size and their orientation: the more negligible their tilt, the larger they are (see Figure 4.6f). Indeed, grains having a flat top facet overgrow laterally until they develop enough and coalesce. On the other hand, some misoriented grains keep developing while others disappear and merge with flat top-faced grains. The BiSb nucleation mechanism will be further discussed in the following section.

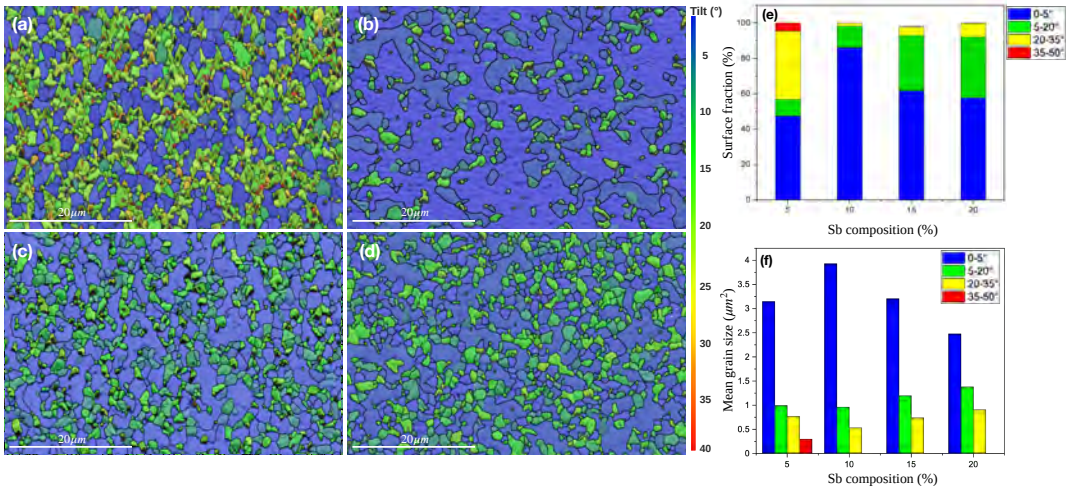

Figure 4.6: *Determination of the grain orientation. EBSD map showing the angular deviation between the (0001) (a) $Bi_{0.95}Sb_{0.05}$, (b) $Bi_{0.9}Sb_{0.1}$, (c) $Bi_{0.85}Sb_{0.15}$, (d) $Bi_{0.8}Sb_{0.2}$ grains and the GaAs(001) substrate. The colour scale corresponds to the tilt ranging from 0 to 40° with respect to the substrate direction. (e) and (f) Statistics about the grain tilting angle and the grain size as a function of the antimony composition.*

In order to probe the influence of the Sb composition on the grain tilting direction, pole figures obtained from EBSD measurements were analysed on these samples. Figures 4.7 shows the {0001} EBSD pole figures where the x axis corresponds to the [110] direction and the y axis to the $[\bar{1}10]$ one. It can be noted that the grain tilting directions depend on the Sb composition. For

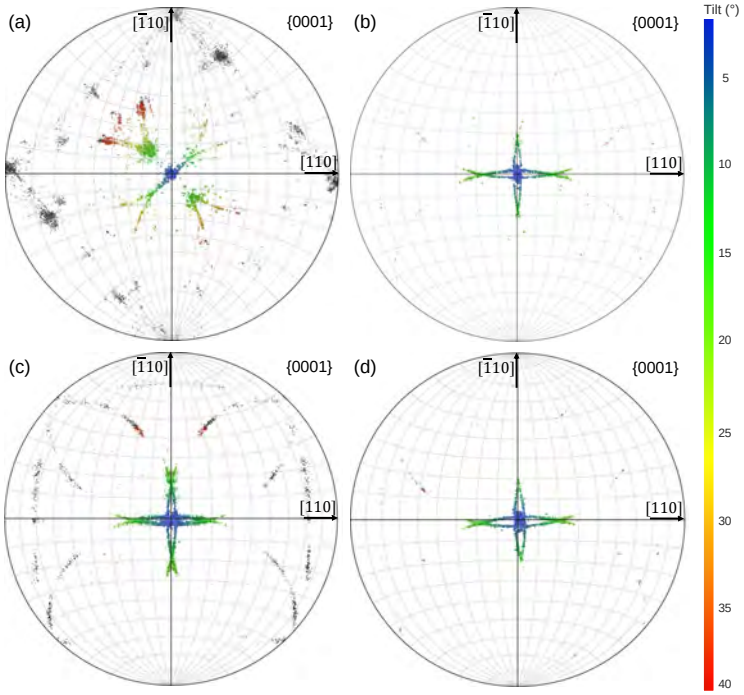

Figure 4.7: *EBSD pole figures of the* {0001} *planes for different BiSb compositions: (a)* $Bi_{0.95}Sb_{0.05}$*, (b)* $Bi_{0.9}Sb_{0.1}$*, (c)* $Bi_{0.85}Sb_{0.15}$ *and (d)* $Bi_{0.8}Sb_{0.2}$*. The x-axis corresponds to the GaAs* [110] *direction, whereas it is* [$\bar{1}$10] *for the y-axis. The color scale on the right presents tilt angle ranging from 0 to 40°.*

a Sb composition of 5% (see Figure 4.7a), the grains having a tilt lower than 40° present two preferential tilt direction, the [100] or [010] ones. Moreover, grey spots of unknown orientation are observed and form a 45° tilt square. On the contrary, for a Sb composition greater than 5%, the grains tilt direction is distributed uniformly in either the [110] or the [$\bar{1}$10] directions (see Figures 4.7b-d). These results reveal that more antimony ($\geq$ 10%) improves the grain nucleation mechanism, which promotes uniformity in grain tilt distribution. They also make it possible to deduce that reducing the Sb composition to 5% with $Tg = 215$°C leads to a rotation of the BiSb layer of 45° with respect to the GaAs(001) substrate. Finally, to define grain orientation indexed in grey, {10$\bar{1}$0}, {11$\bar{2}$0}, {1$\bar{1}$02} and {1$\bar{1}$0$\bar{1}$} pole figures were taken for the four samples (see Figure 4.8). Regardless of the composition, no specific grain orientation is observed.

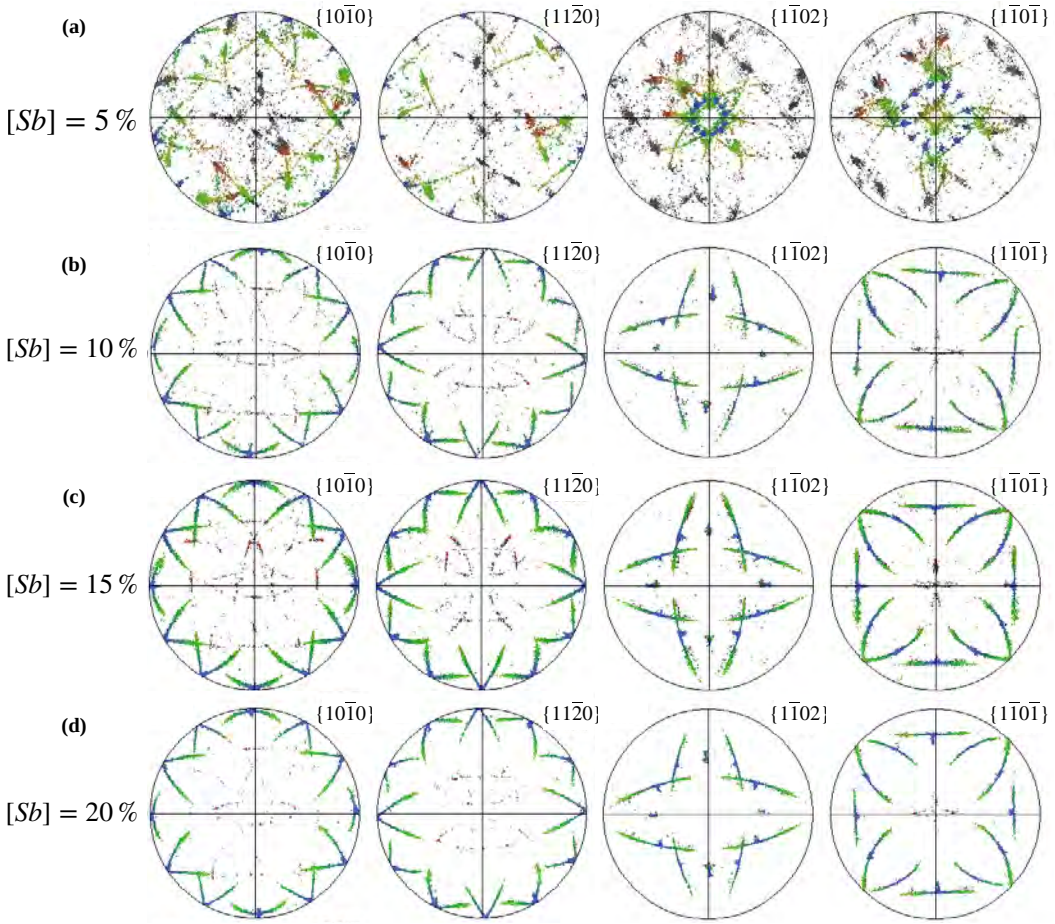

Figure 4.8: *EBSD pole figures of the* {10$\bar{1}$0}, {11$\bar{2}$0}, {1$\bar{1}$02} *and* {1$\bar{1}$0$\bar{1}$} *planes of the (a)* $Bi_{0.95}Sb_{0.05}$*, (b)* $Bi_{0.9}Sb_{0.1}$*, (c)* $Bi_{0.85}Sb_{0.15}$ *and (d)* $Bi_{0.8}Sb_{0.2}$ *samples.*

4.5 The influence of the thickness

To further investigate the growth mode, a thickness series was synthesised. Six samples of different thicknesses ranging from 2 to 450 nm are grown under the same conditions. The $Bi_{0.9}Sb_{0.1}$ growth is initiated by opening both Bi and Sb shutters at the same time with a flow of 4.5×10^{-7} and 5×10^{-8}Torr, respectively. The growth temperature is fixed at $Tg = 215$°C and the growth is terminated once the sample thickness is established. After growth, AFM and SEM are carried out on these samples.

Figures 4.9a-f show AFM images of different $Bi_{0.9}Sb_{0.1}$ thin films having a thickness of 2, 20, 30, 60, 90 and 450 nm, respectively. At the early stage of growth (2 nm), different islands can be observed at the substrate surface (see

Figure 4.9a), which indicates a Volmer Weber growth mode. These islands will expand over time and merge with neighbour ones to form bigger grains as observed for the 20 nm thick layer (see Figure 4.9b). Once a critical density is achieved, for sample thicknesses above 30 nm, the grains develop, become larger and coalesce leading to the formation of a continuous layer (see Figures 4.9c-f).

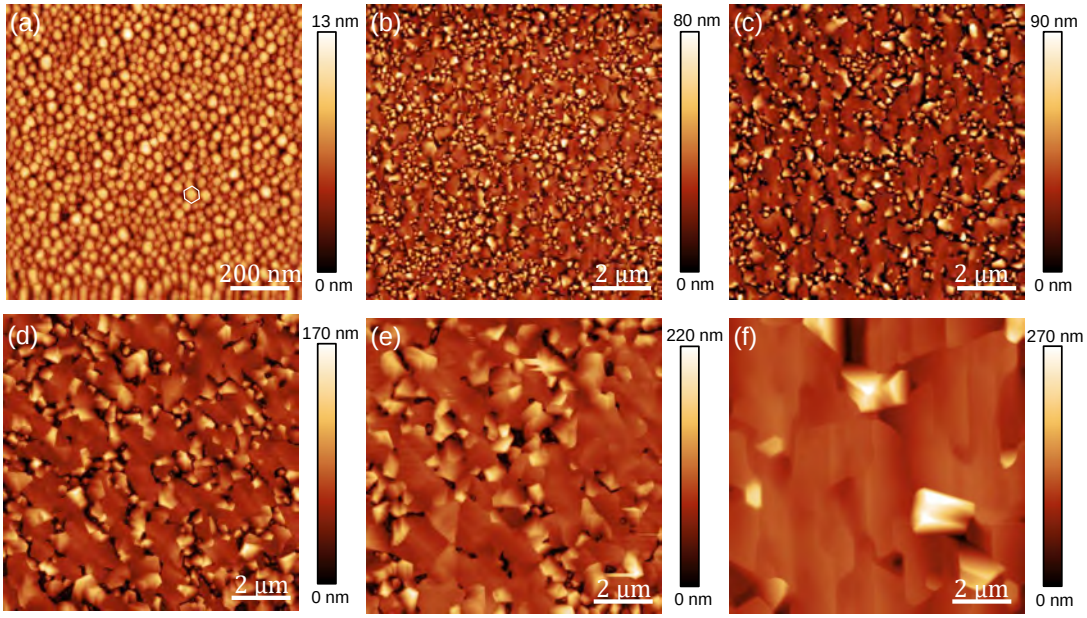

Figure 4.9: *Evolution of the surface morphology as a function of the BiSb layer thickness. The AFM images are taken for thicknesses of (a) 2 nm, (b) 20 nm, (c) 30 nm, (d) 60 nm, (e) 90 nm and (f) 450 nm. Note that all other growth parameters are kept fixed ($T_G = 215°C$ and $x = 10\%$).*

In order to define a critical thickness, corresponding to the grain coalescence, an in-situ optical monitoring of the wafer curvature was carried out on the 90 nm thick sample [100]. This measurement records the accumulated stress during the BiSb growth (see Figure 4.10). At the beginning of the BiSb growth, a compressive stress appears on the wafer corresponding to the grain nucleation. After a 12 nm growth, the compressive strain change into a tensile one, which corresponds to the coalescence of small islands as confirmed in Figures 4.11a,b. Finally, after 30 nm, the accumulated stress reaches a plateau when the interconnected grains start forming a continuous network, slowly transforming into a continuous layer (see Figures 4.9c-f). Importantly, the larger the thickness, the larger the grains with a flat upper facet become.

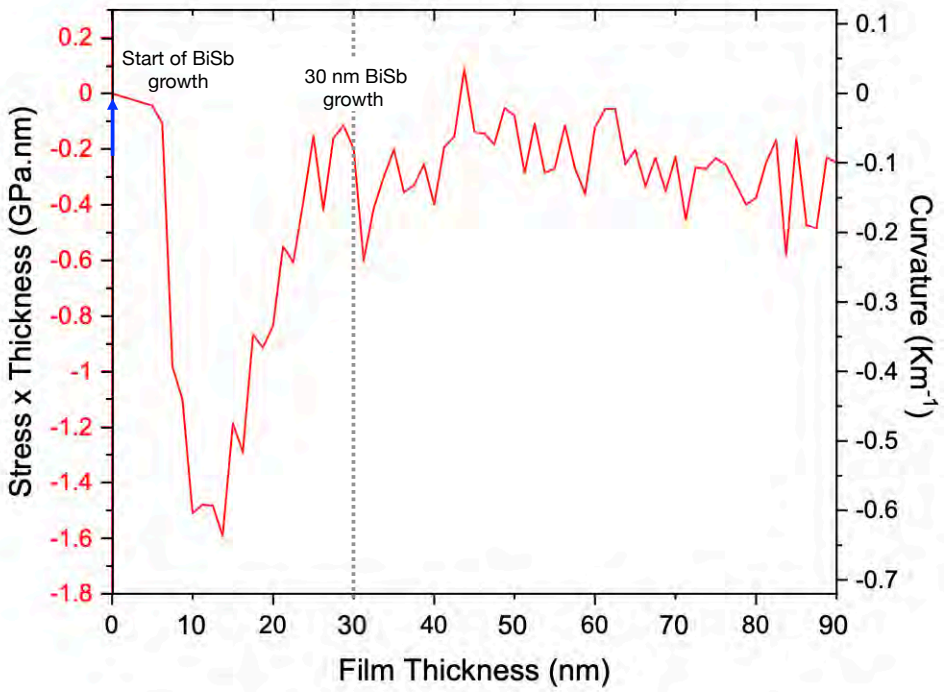

Figure 4.10: *In situ optical monitoring of the wafer curvature measurements performed on a 90 nm-thick BiSb film. Stress × Thickness and the associated curvature as a function of the BiSb film thickness. Note that BiSb growth starts with the simultaneous opening of the Bi and Sb shutters, indicated by the blue arrow. The curvature measurement shows that a compressive stress of* ~ -1.6 *GPa.nm occurs once BiSb growth begins and reaches a plateau after* $\sim$ 30 *nm growth, as indicated by the gray dotted line.*

Initially for a thickness of 2 nm, the grains seem to have almost the same size and have an homogenous arrangement on the substrate (see Figures 4.9a and 4.11a). However, this distribution becomes a little less homogenous by increasing the sample thickness to 10-20 nm (see Figures 4.9b and 4.11c,d), where some grains develop and other disappear. These results indicate that the larger the grains, the more stable they are since they minimise their surface energy. As a result, the adatoms on the substrate surface and even the small grains tend to migrate and merge with the larger grains, causing them to grow and some existing small ones to disappear.

Starting from 30 nm, corresponding to Figure 4.9c and 4.11d, adatoms accumulate around the flat-topped grains, which lead to their lateral overgrowth and finally to their coalescence with neighbours leading to the creation of a continuous layer. These results confirm that our $Bi_{1-x}Sb_x$ growths are controlled by thermodynamics rather than kinetics: it is favorable for

adatoms to stick to an existing island compared to nucleate a new one. Small islands are desorbed and absorbed by bigger ones. In order to favour this mechanism and grow large and flat grains, the kinetics of the system should be slowed down to promote thermodynamics (see following Section 4.6). Moreover, it is worth mentioning that hexagonal shape grains are observed in Figure 4.9a confirming a (0001) growth direction from nucleation.

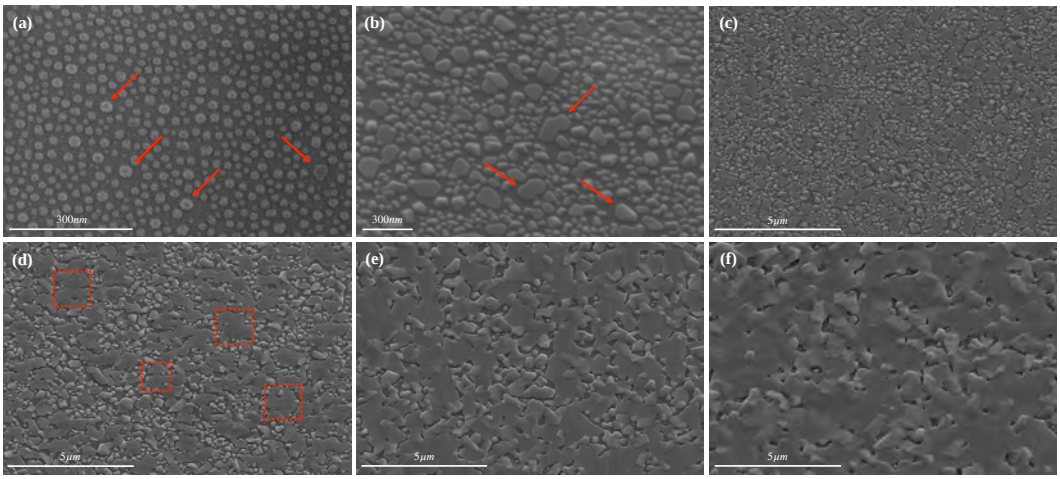

Figure 4.11: *SEM images of the (a) 2, (b) 10, (c) 20, (d) 30, (e) 60 and (f) 200 nm-thick BiSb layer. The grains which have absorbed their neighbouring grains are indicated by red arrows in panel (a) and (b) and the red dotted square in panel (d) highlights the grains coalescence. All samples were grown at* $215°C$ *with a Sb composition of 10%.*

4.6 The influence of the kinetic on the growth

In order to probe further the growth mechanisms of the BiSb layer, four samples with a Sb composition of 10% were synthesised with different growth rates and a total layer thickness of 200 nm. Once the sample temperature is stabilised at 215°C, the Bi and Sb shutters are opened simultaneously for different growth rates of 0.064 $\mu m/h$, 0.129 $\mu m/h$, 0.26 $\mu m/h$ and 0.385 $\mu m/h$ and closed simultaneously after 200 min, 100 min, 50 min and 30 min, respectively. At this growth temperature, the BiSb system is in stable phase according to the BiSb phase digram [24], which means that the evaporation rate is almost zero.

A SEM imaging of these samples is reported in Figure 4.12. It can be noticed that a high growth rate favours islands growth (see Figure 4.12a) whereas a low growth rate favours 2D layers growth (see Figure 4.12d). As a result, the surface morphology for a high growth rate is less organised and presents more misoriented grains (see Figure 4.12a) compared to a low growth rate (see Figure 4.12d). This can be explained by thermodynamics

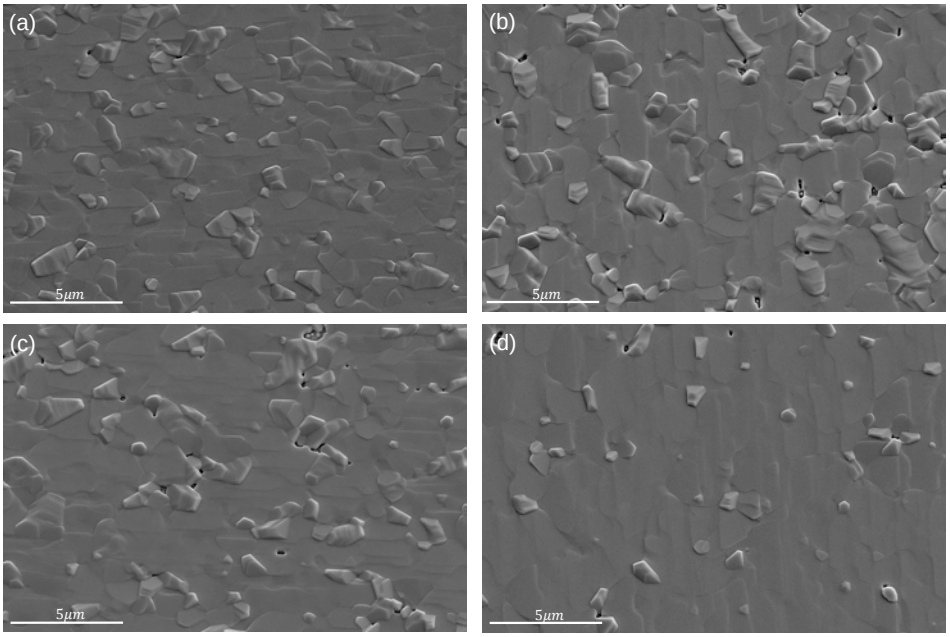

Figure 4.12: *Evolution of the BiSb surface morphology as a function of the growth rate. All layers have the same composition and thickness, and the respective growth rates are: (a) 0.385, (b) 0.26, (c) 0.129 and (d) 0.064 $\mu m/h$.*

and kinetics considerations. Indeed, the adatoms density (n) at a time t and the mean time interval (Δt) between the atoms arrival at the substrate surface will change with the growth rate. When the growth rate increases, n increases while Δt decreases and reciprocally. A large Δt (low growth rate) indicates a high probability that an adatom will reach its thermodynamics equilibrium and stick to an existing island. As consequence, low energy islands, i.e. flat-topped grains in our system, are favoured while decreasing the growth kinetics. They will therefore attract a larger number of adatoms if the growth rate decreases, so that their lateral size increases. In the extreme case of a very low growth rate (see Figure 4.12d), a continuous layer of flat-topped grains is achieved leading to an optimised surface morphology of the BiSb layer and improved electrical properties.

4.7 The Interface between BiSb and GaAs

In order to explore the BiSb/GaAs interface and to assess the crystalline quality of the optimised 200 nm-thick $Bi_{0.9}Sb_{0.1}$ sample reported in Section 4.4 (see Figure 4.5c and Figure 4.6b), the stress of the system was probed during the growth using in situ wafer curvature measurements (see Figure 4.13a). Moreover, the same sample was taken out from the MBE system after growth and examined by X-Ray diffraction (XRD) measurements, transmission electron microscopy (TEM) and scanning tunnelling microscopy (STM) (see Figures 4.13b, 4.14, 4.15 and 4.16).

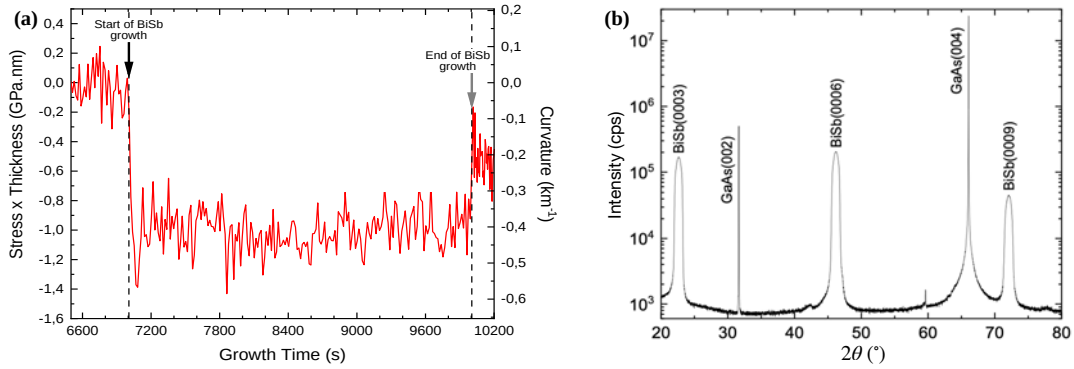

Figure 4.13: *Stress × thickness and related curvature as a function of growth time. The black and grey arrows indicate the start and end of BiSb growth, respectively. Note that Bi and Sb shutters are opened and closed simultaneously and that the growth time is 50 min corresponding to 200 nm thick.*

Figure 4.13a indicates that once the Bi and Sb shutters are open, the stress accumulates for 70 s before reaching a step. Importantly, the presence of stress during nucleation excludes a Van der Waals growth process and highlights the creation of covalent bonds between the GaAs(001) and the BiSb(0001) layer. To investigate the crystalline orientation of the grains, X-ray diffraction measurements are performed in a symmetric $2\theta - \omega$ configuration in a Bruker D8 Discover diffractometer. Figure 4.13b shows the diffraction pattern of the sample presented in Figure 4.5d. The GaAs(002) and GaAs(004) peaks correspond to the GaAs(001) substrate and the 1µm thick buffer layer. The BiSb(0003), BiSb(0006) and BiSb(0009) peaks reveal grains having the same c axis than the GaAs(001) substrate. Importantly, no other grain orientation can be found in this pattern. According to Figure 4.13b, the vertical (0001) orientation of the $Bi_{0.9}Sb_{0.1}$ grains is again confirmed indicating that the quasi-hexagonal BiSb matrix grows on top of the cubic GaAs one.

In order to plunge further in the structural investigation of the BiSb layer, a thin lamella of the sample, obtained by focused ion beam (FIB), was examined by transmission electron microscopy (TEM) (see Figure 4.14).

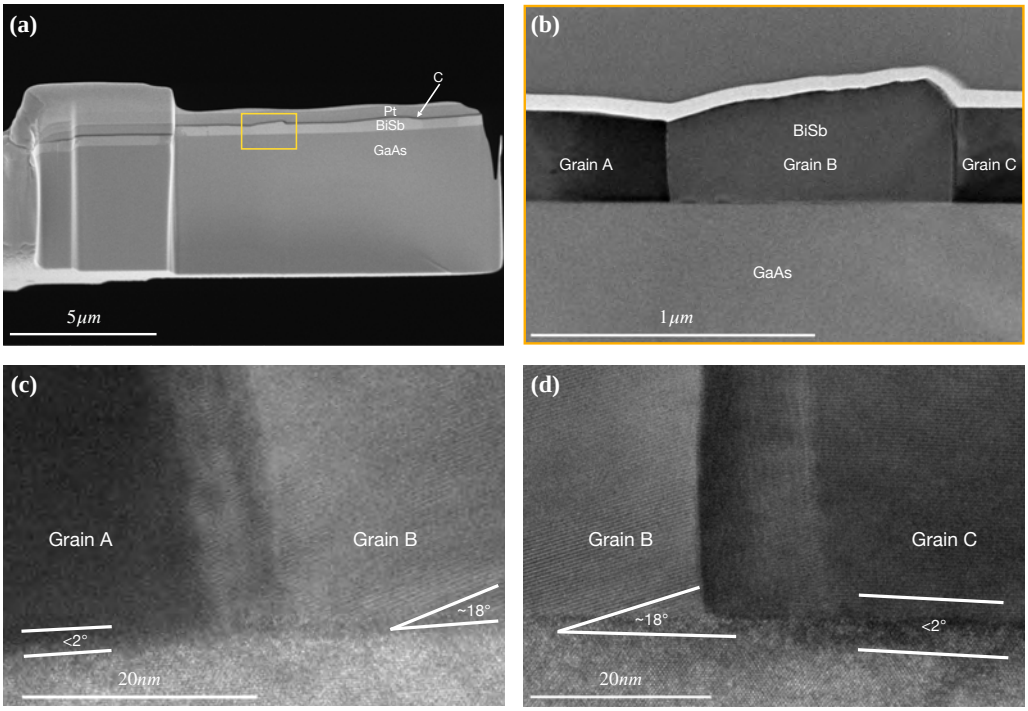

Figure 4.14: *Cross-sectional measurement of the sample. (a) SEM image of the FIB cut once carbon and palladium have been deposited. (b) Zoomed TEM images of the BiSb/GaAs interface indicated by a yellow square in panel (a) and showing the existence of different grains (A, B and C). (c) Boundary between the grain A and B. (d) Boundary between the grain B and C.*

In order to protect the sample, a layer of carbon and another of platinum are deposited on top of the BiSb layer prior to the FIB cut as illustrated in the SEM image of the lamella reported in Figures 4.14a. To further study the BiSb/GaAs interface, a zoomed TEM image is obtained in Figure 4.14b, where three grains A, B and C can be observed. In addition, High resolution images of the interface between the three grains and the GaAs substrate are reported in Figures 4.14c,d. Noticeably, grains A and C have a rather flat surface (cf. Figure 4.14a), while their (001) planes rows are almost parallel to the GaAs ones ($< 2°$ in Figures 4.14c,d). On the contrary, the B grain surface is rough and its (0001) planes are inclined with respect to the GaAs ones ($\sim 18°$ in Figures 4.14c,d). Moreover, the grain boundaries are mostly

vertical as shown in Figures 4.14c,d and low strain can be observed at their junction. No further structural defects can be observed in any of the grains, proving their high structural quality.

In order to gain knowledge about their crystalline structure and the BiSb/GaAs interface, high-resolution transmission electron microscopy (HR-TEM) measurements were performed on grains A (see Figure 4.15a) and grain B (see Figure 4.15b).

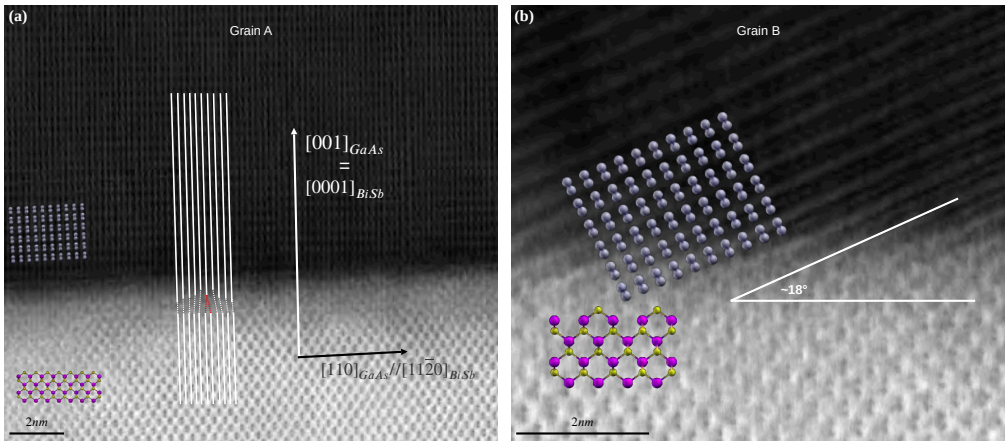

Figure 4.15: *Interface between the BiSb layer and the GaAs substrate. The HR-TEM images are taken in the* $[1\bar{1}0]$ *zone axis of the GaAs and show the interface between GaAs and grain A in (a) and grain B in (b). The grain growth direction is* [0001] *with a tilt less than* 2° *for the grain A and of* 18° *for the grain B.* 90° *dislocation are detected at the grain A / GaAs interface indicated by red dash lines in panel (a). The inset images in (a) and (b) show the side view of the crystal structure of grain A, grain B and GaAs(001). Bi, As and Ga atoms are represented by grey, yellow and pink atoms respectively.*

In the case of grain A, the [0001] growth direction is confirmed by Figure 4.15a. A low tilt can be observed ($< 2°$) between the GaAs substrate and the BiSb layer, which corresponds to the blue family in Figure 4.6b. The [110] direction of the GaAs corresponds to the $[11-20]$ of the BiSb and the c axis is identical for both crystals. 90° dislocations are present at the interface (see red dash line) and the BiSb grain is fully relaxed. On the contrary, for grain B a 18° tilt can be observed between the GaAs [001] and the BiSb [0001] directions (see Figure 4.15b). These measurements are in good agreement with both the XRD measurements in Figure 4.13b and the EBSD one in Figure 4.6a,b. The BiSb layer is fully relaxed, covalent bonds are formed during the BiSb nucleation and each grain has a high structural quality.

Finally, in order to investigate the surface topography, Scanning Tunnelling Microscopy (STM) experiments have been performed at liquid nitrogen temperature (T = 77.8 K) on a commercial STM (LT Omicron) working with a base pressure of 3×10^{-11} mbar. The BiSb/GaAs(001) sample was introduced in the preparation chamber and outgassed during 10h at a temperature of $250°C$ and a vacuum below 10^{-10} mbar. Thereafter, the sample was introduced in the STM chamber to be cooled down at liquid nitrogen temperature. STM tips made of PtIr wires 0.2 mm in diameter were prepared by mechanical cutting and cleaned in UHV using tip pulses on a clean Ag(111) substrate. The tip quality is estimated from atomic resolution images on a Ag(111) surface and from dI/dV curves showing the typical electronic surface state 70 meV below the Ag Fermi level. The bias voltage indicated in the text was always applied to the sample.

Figure 4.16a shows a 20×20 nm^2 STM image of a BiSb terrace (on the left) and a stepped area (on the right). The step edges present characteristic kink that demonstrates the perfect film crystallinity. The larger terraces observed can be several thousand of nanometers large on top of the crystallites. These large domains are surrounded by stepped areas as presented in Figure 4.16a corresponding to the sides of these crystallites. The corrugated areas can be used to measure the monoatomic step height. A profile across a step band is presented in Figure 4.16b. The cross-section performed on another large-scale image shows the presence of small terraces about 2 nm wide separated by monoatomic steps whose average height is 3.56 ± 0.4 Å, which corresponds to one third of the c $Bi_{0.9}Sb_{0.1}$ lattice parameter at 77 K (1/3 of 11.76 Å at 77 K) . The surface of a terrace with atomic resolution is presented in Figure 4.16c. The used bias voltage is 600 mV and the tunnelling current is 5 pA. As expected, the Bravais lattice is hexagonal (see the white hexagon superimposed on the atomic network in Figure 4.16c). The lattice parameters can be measured from this kind of image or from Fast Fourier Transform (FFT) performed on larger scale topographies with atomic resolution. A typical example is presented in Figure 4.16d. and shows the characteristic diffraction pattern. From these measurements, a lattice parameter of 4.4 ± 0.4Å is obtained, close to the theoretical 4.51 Å for a fully relaxed layer at 77 K. Another point concerns the bias voltage that can be used in the STM experiments. During the STM investigations, it appears that very reproducible surface topographies can be obtained for bias voltages as low as 40 mV (for tunnelling currents in the picoampere range). This suggests a large conductivity of the layer at liquid nitrogen temperature which is consistent with a metallic surface.

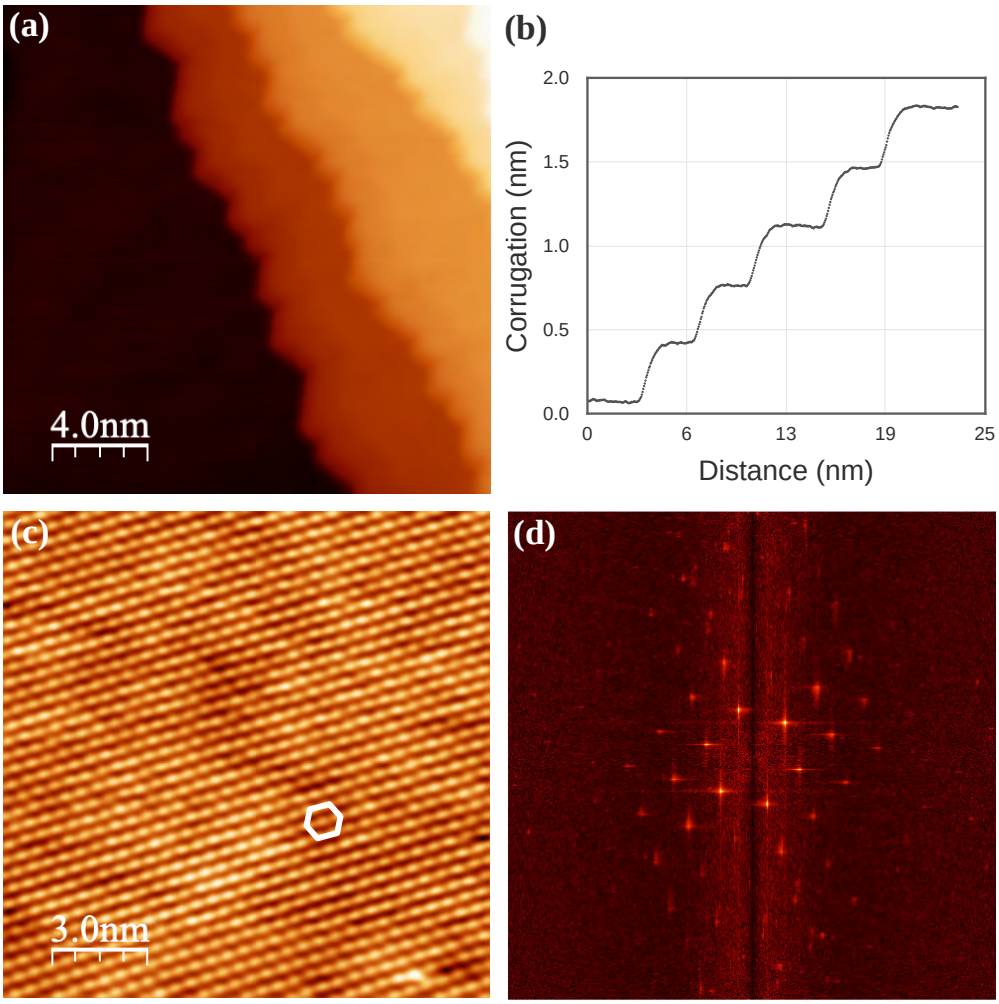

Figure 4.16: *STM measurements of the surface. (a) Large scale STM topography (20×20 nm^2) of the BiSb surface (V=1V, I= 10 pA, T=77 K). The step on the right are monoatomic and present characteristic kinks. (b) Typical cross section performed across monoatomic steps separating small terraces. (c) Atomic resolution on a BiSb terrace (15×15 nm^2) showing the hexagonal network (V=1V, I= 10 pA, T=77 K). (d) A characteristic FFT pattern of a large-scale STM image (20×20 nm^2) with atomic resolution conducted on the BiSb surface. From the central hexagonal pattern, a lattice parameter of 4.4 ± 0.4 Å can be obtained.*

4.8 The DFT analysis

The objective of this section is to understand the experimental results by constructing a theoretical study using DFT calculations for probing the processes of adsorption, diffusion and the growth mode of BiSb atoms on a GaAs(001) substrate. In this theoretical study, we investigate the deposition process of Bi atoms by adding one by one the deposited Bi atoms in order to study the behavior of the isolated Bi atoms on the GaAs surface until the formation of islands on the surface.

This section is structured as follows. Subsection 4.8.1 describes the method used to build the GaAs(001)-$c(4 \times 4)$ surface reconstruction and the parameters used to obtain the total energy of the adsorption configurations, the diffusion energy of the atoms on the surface and the electronic density in the atomic system. In Subsection 4.8.2, we study the adsorption energy of the possible sites of Bi atoms on the GaAs surface. Once the stable configurations are obtained, the capacity of Bi atom to diffuse on the substrate surface is studied using the ARTn calculation. Next, we study the effect of the presence of Bi islands on the GaAs surface on the adsorption process of the other deposited atoms and finally we discuss the electronic density results obtained with a Bader analysis. This section finally ends with a conclusion in Subsection 4.8.3

4.8.1 Method

The supercell structure creation

We modelled our GaAs(001) slab using a supercell containing 140 atoms. The surface is formed by 4×4 cubic unit cells of GaAs containing eight atoms each, and an additional As layer to form the surface reconstruction. This last consists in a row of As dimers and a channel placed along the $[1\bar{1}0]$ direction above the As monolayer (see Figure 4.17a). The depth of the supercell consists of 8 alternating layers of 16 As and Ga atoms terminated by a Ga monolayer. In order to simulate the bulk properties with a reduced number of atoms, the two lowest layers are kept fixed in their bulk positions during all the relaxations and the Ga dangling bonds underneath the bottom of the supercell are passivated by 32 hydrogen atoms. In addition, a 20 Å thick-vacuum space has been added above the surface to avoid the periodic boundary conditions imposed by the quantum software, thus giving a simulation box volume of $15.638 \times 15.638 \times 31.057$ Å^3 (see Figure 4.17b).

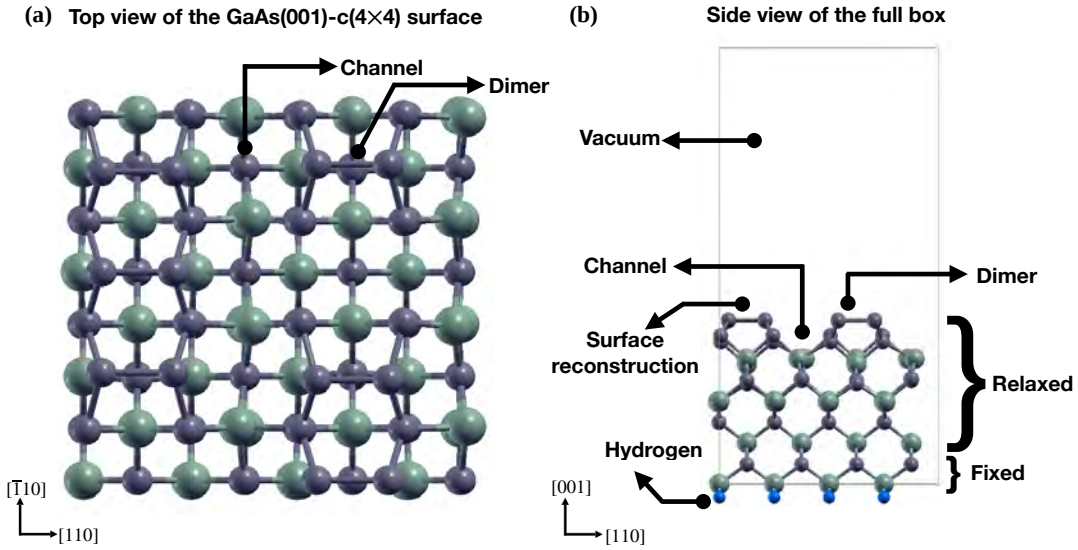

Figure 4.17: *(a) Top view of the GaAs(001)-c*(4×4) *surface reconstruction and (b) the side view of the full box. Ga and As are respectively represented by green and gray atoms.*

Ab initio parameters

Total energies of the supercell and its additional Bi atoms have been calculated within density functional theory (DFT) in the pseudopotentials and plane wave approach as implemented in Quantum Espresso [109]. The core electrons are represented by the projector-augmented wave (PAW) pseudopotentials [110]. The plane waves basis set has been limited by an energy cutoff of 70 eV and Brillouin zone sampled at Γ only as justified by the large size of the system. Generalised Gradient Approximation (GGA) is used to evaluate the exchange-correlation functional [111]. During the relaxation of the surface containing additional adsorbed Bi atoms, only the atomic positions are relaxed, while the lattice parameters of the supercell are kept fixed. To calculate the activation energies and identify reaction pathways, the nudged elastic band method (NEB) [112, 113] has been first used for a global overview, and the transition states have then been refined with the activation-relaxation technique (ARTn) [114, 115]. Finally, Bader calculations are performed to determine the electronic transfer in the atomic system and the chemical bond type at the interface between Bi atoms and GaAs substrate [116].

Formation energy

Adsorption energy E_n^{ad} for each studied position of the Bi atom on top of the GaAs(001)-$c(4 \times 4)$ surface is calculated as:

$$E_n^{ad} = E_{total} - (n\mu_{Bi} + E_{surface}) \tag{4.1}$$

where μ_{Bi} is the chemical potential of Bi atoms, calculated from the bulk Bi, $E_{surface}$ is the energy of the GaAs(001)-$c(4 \times 4)$ surface, "n" is the number of deposited Bi atoms and E_{total} is the energy of the relaxed system containing both the GaAs(001)-$c(4 \times 4)$ surface and the "n" Bi atoms.

The adsorption energy of n Bi atoms relatively to $n-1$ atoms is defined as:

$$E_{rel}^{ad} = E_n^{ad} - E_{n-1}^{ad} \tag{4.2}$$

where E_{n-1}^{ad} is the adsorption energies of the most stable position obtained during the deposition of the $(n-1)$th Bi adatom.

4.8.2 Results

Strategy for finding stable sites

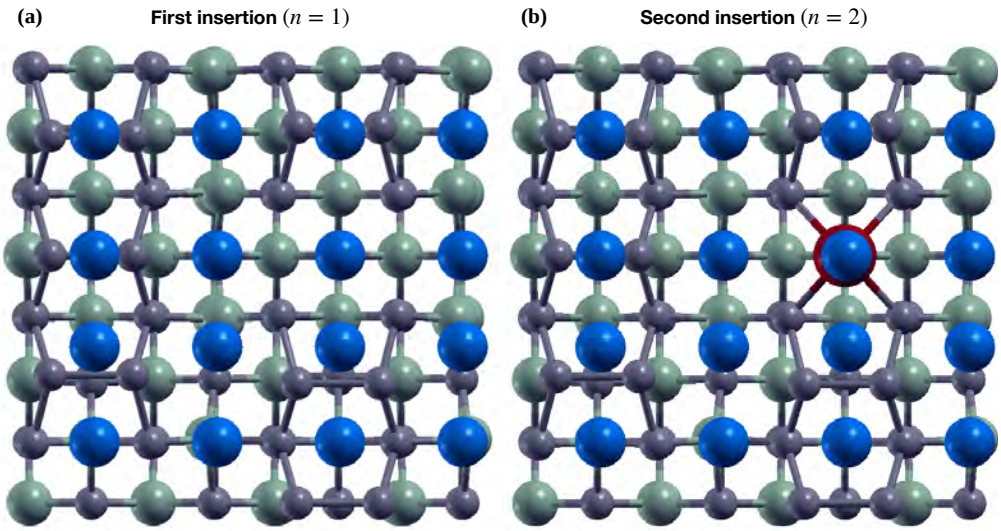

Figure 4.18: *Top view showing the sixteen tested initial sites. The blue, green and gray atoms represent the Bi sites tested, Ga and As atoms, respectively. The red atom in panel (b) represents the most stable Bi site obtained when depositing a single Bi atom.*

In order to find the most thermodynamically stable sites, sixteen initial positions of Bi above the surface were tested on the GaAs(001)-$c(4 \times 4)$ (see Figure 4.18a). These sites were chosen according to the topology of the reconstructed GaAs surface. The same strategy is used each time the number of Bi atoms (n) is increased, taking as reference the most stable configuration obtained during the "$n-1$" Bi atom deposition (see Figure 4.18b in the case of $n = 2$).

Addition of a single Bi atom: the stable positions

The top image of Figure 4.19 shows the five inequivalent stable configurations obtained after relaxation of the initial sixteen positions for Bi atoms, given the symmetry of the GaAs(001)-$c(4\times4)$ surface: the "mds", "mdc", "ch", "tdi" and "th" configurations. Here, the configuration where an adatom is absorbed

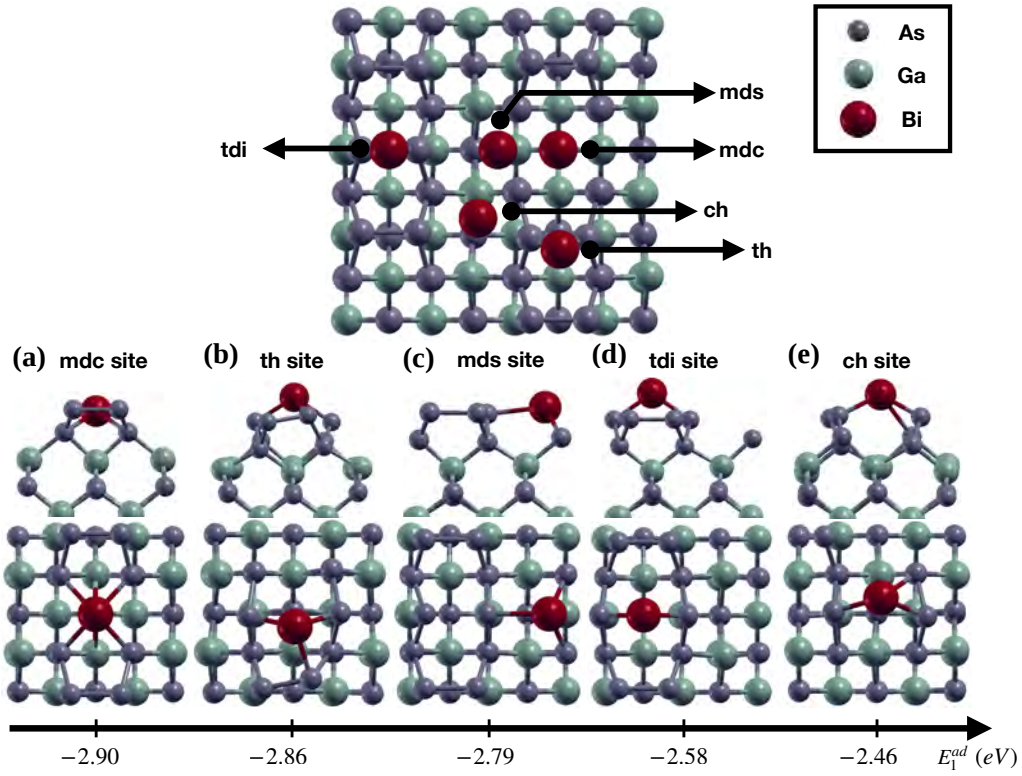

Figure 4.19: *Top view where the sites are after relaxation (top figure) and energy diagram of the sites found (bottom figure). (a), (b), (c) (d) and (e) show top and side views of the "mdc", "th", "mds", "tdi" and "ch" configurations, respectively. Bi, As and Ga are respectively represented by red, green and gray atoms.*

in the missing dimer site referred as “md” adsorption site, while that adsorbed in the channel is named by “ch” adsorption site. More precisely, the "md" site is called "mds" if the adatom is positioned on one of the missing dimer sites and called "mdc" if the adatom is at the center of the missing dimer. Two other configurations are also studied, where the adatom is adsorbed above an internal As dimer denoted "tdi" or on the top of the As hexagonal pattern and called “th”.

Thermodynamics

The bottom images of Figure 4.19 show separately each of these configurations and their adsorption energy. It can be seen that the "mdc" adsorption site is the most stable adsorbed site (see Figure 4.19a) , followed by the "th" and "mds" sites (see Figure 4.19b and c). The stability of the "mdc" site is due to the fact that the Bi atom tends to fill the empty dimer.

Kinetics

After getting clues on the adsorbed configuration stability, ARTn calculations are performed in order to study the diffusion of the single Bi atom on the GaAs(001)-$c(4 \times 4)$ surface. Here, the transition pathways and the energy barriers are obtained between the stable configurations obtained in Figure 4.19. Figure 4.20 shows the minimum energy paths taken by one Bi atom to diffuse on the substrate surface.

Diffusion barrier of about 0.57 eV (0.44+0.13) is needed for this 2D surface diffusion, highlighting the high mobility of the Bi atom on the surface. Using the equation 2.26, in Chapter 2, Section 2.3 and taking the optimised growth temperature used when growing BiSb films ($T_r = 144$°C, see Figure 4.1, Section 4.3), we extracted the Bi transition rate between two "mdc" positions $\Gamma_{mdc-mdc}$ of $\sim 6.41 \times 10^6\ s^{-1}$, revealing that Bi atoms can move freely on the substrate surface. From $\Gamma_{mdc-mdc}$, the Bi adsorption residence time τ_{mdc} is derived and it is about $1.56 \times 10^{-7}\ s$.

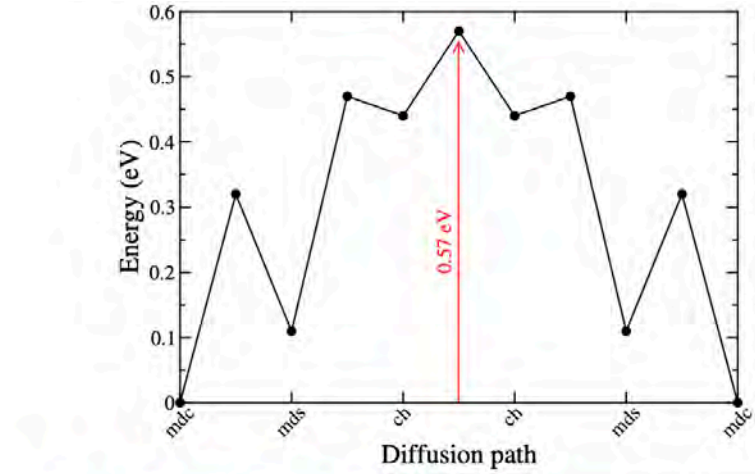

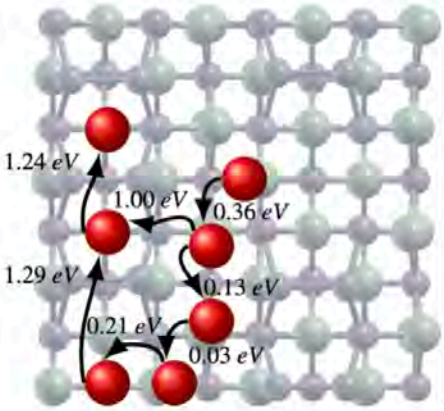

From / To	mdc	th	mds	ch
mdc		1.25 eV	0.21 eV	not linked
th	1.29 eV		1.18 eV	1.00 eV
mds	0.32 eV	1.25 eV		0.03 eV
ch	not linked	1.4 eV	0.36 eV	
E_1^{ad} (eV)	−2.90	−2.86	−2.79	−2.46
ΔE (eV)	0.00	0.04	0.11	0.44

Figure 4.20: *(Top) The minimum energy path calculated for Bi atom to diffuse on the GaAs(001)-c(4 × 4) from "mdc" to "mdc" sites. (Bottom left) A top view of this 2D surface diffusion from a "mdc" site to a "mdc" site allows to highlight all the intermediate sites on the surface involved during the diffusion. (Bottom right) Summary table of the associated energy barrier between the different stable configurations. ΔE presents the energy difference with the most stable "mdc" site.*

Addition of two Bi atoms: filling the dimers

Thermodynamics

In this section, we add a second Bi atom in addition to the first Bi atom placed in the most stable "mdc" site to study the clustering effect and to simulate an increasing coverage of Bi. As before, we tested the sixteen initial sites presented in Figure 4.18. The clustering effect of Bi atoms is thus

studied by depositing several Bi atoms in compact or non-interacting configurations and comparing both the resulting configuration energies and the activation barriers to form Bi islands. Here, we are interested in the two Bi atoms placed on the "mdc-mds", "mdc-ch", "mdc-th" and "mdc-tdi" sites once as close neighbourhood and another as second neighbourhood.

Figure 4.21 shows the final position taken by the two Bi atoms obtained in different configurations after the deposition of the second Bi atom: the "mds-mds", "mdc-th" and "mdc-ch" sites in compact configuration or/and non-interacting one. It can be seen that Bi placed in close vicinity as "mdc-

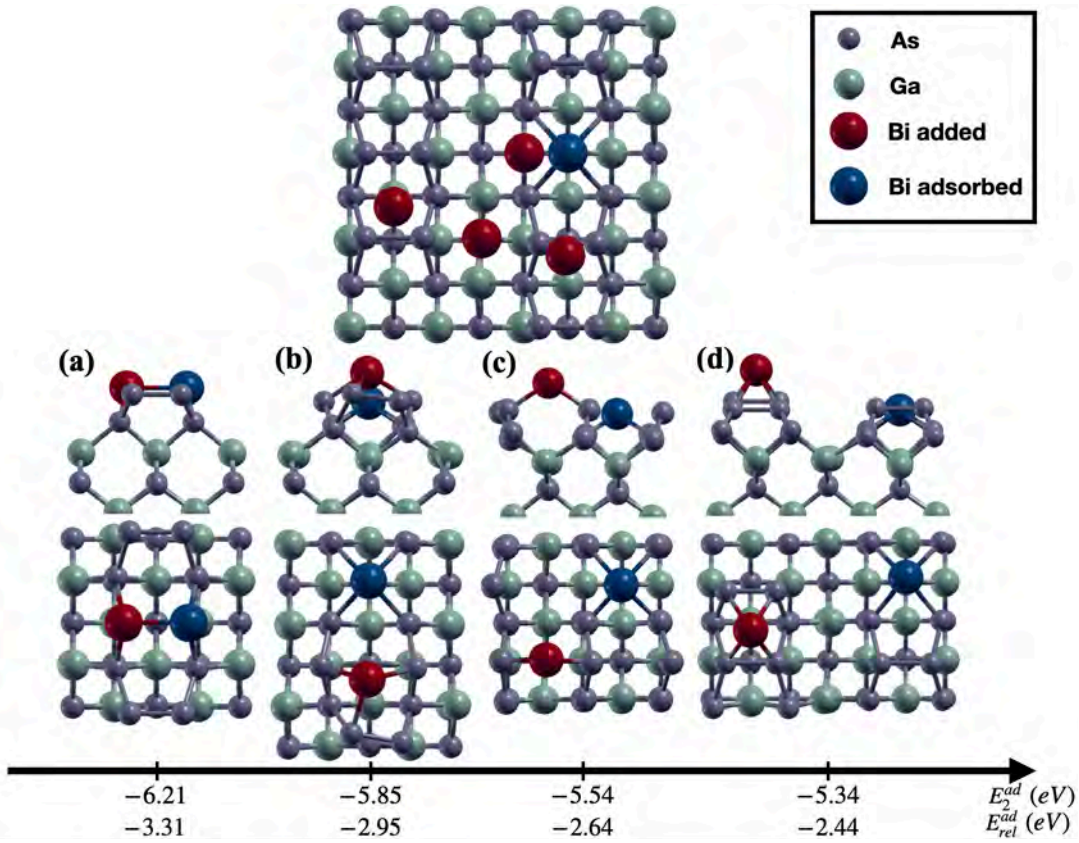

Figure 4.21: *Top view identifying the stable positions on the surface found after relaxation (top figure) and energy diagram of these sites with corresponding relaxed adsorbed configurations (bottom figure). (a), (b) and (c) show respectively top and side views of Bi atoms placed in close packed as "mds-mds", "mdc-th", "mdc-ch" configurations and (d) non-interacting configuration as "mdc-th". The added Bi atom is represented by a red atom while the first adsorbed one is coloured blue. As and Ga are represented by green and gray atoms, respectively.*

mds" positions (see Figure 4.21a) ultimately leads to the filling of the dimer initially missing in the reconstructed surface: the first Bi atom initially adsorbed in "mdc" is then moved to a "mds" position and the final configuration obtained is then a "mds-mds" type configuration. The Bi placed on "mdc-th" and "mdc-ch" relaxes on their initial sites (see Figures 4.21b and c). "mdc-tdi" initial position leads to the "mdc-th" final position (see Figure 4.21d). These results show that it is thermodynamically favourable for Bi atoms to complete the rows of dimers since the "mds-mds" configuration is the most stable adsorbed configuration (the adsorption energy is around -6.21 eV). All the close-packed configurations are more stable than the non-interacting configurations and the adsorption energy of the stable configuration (-6.21 eV) is lower than $2 \times E^{ad}_{1\ (mdc)} = -5.80$ eV (i.e. the adsorption energy of the isolated Bi atom in "mdc" position), indicating that Bi atoms tend to connect rather than separate. Interestingly, $E^{ad}_{rel(mds-mds)}$, $E^{ad}_{rel(mdc-th)}$ and $E^{ad}_{rel(mdc-ch)}$ of the "mds-mds", "mdc-th" and "mdc-ch" configurations are respectively lower than the adsorption energy of the "mds", "th" and "ch" configurations presented in Figure 4.19b ($E^{ad}_{rel(mds-mds)} = -3.31 < E^{ad}_{1\ (mds)} = -2.79$, $E^{ad}_{rel(mdc-th)} = -2.95 < E^{ad}_{1\ (th)} = -2.86$ and $E^{ad}_{rel(mdc-ch)} = -2.64 < E^{ad}_{1\ (ch)} = -2.46$), which gives an indication that the presence of another Bi atom minimises the adsorption energy of neighbouring deposited Bi atoms.

Kinetics

Figure 4.22 shows the minimum energy path in order to check whether the formed Bi dimer is able to dissociate (and conversely the tendency to form the Bi-Bi dimer). To initiate the diffusion path of the Bi atom, the initial configuration is therefore a Bi dimer positioned in the missing dimer of the surface, i.e. an adsorbed "mds-mds" configuration.

We calculate the activation energy needed to dissociate the Bi dimer in order to allow one of these Bi atoms to migrate either to the "ch" site or to the "th" site. It can be seen that it costs high energies of 1.31 eV to migrate towards the "ch" site and of 0.91 eV toward the "th" site. The activation energy required to move from the "mds-mds" to the "mdc-ch" configuration (1.31 eV) is much higher than that between "mds" and "ch" (0.36 eV) obtained in Figure 4.20. On the other hand, it is observed that the migration from the "mds-mds" to the "mdc-th" configuration (0.91 eV) costs less energy than moving from "mds" to "th" site (1.18 eV). The Table in Figure 4.22 showing the activation energies between the different configurations highlights that it is kinetically favourable to form a Bi dimer: the lowest activation energies are obtained when the Bi atom diffuses on the surface to form a Bi dimer

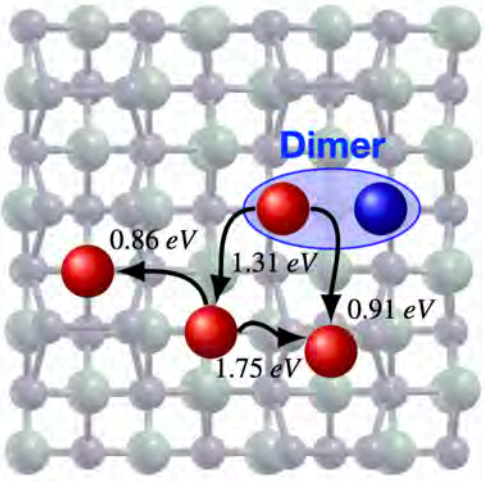

From / To	mds-mds	mdc-th(b)	mdc-ch	mdc-th(d)
mds-mds		0.55 *eV*	0.64 *eV*	not linked
mdc-th(b)	0.91 *eV*		1.75 *eV*	not linked
mdc-ch	1.31 *eV*	1.44 *eV*		0.66 *eV*
mdc-th(d)	not linked	not linked	0.86 *eV*	
E_{rel}^{ad} (*eV*)	−3.31	−2.95	−2.64	−2.44
ΔE (*eV*)	0.00	0.36	0.67	0.87

Figure 4.22: *Minimum energy path for the diffusion of Bi atom on the GaAs substrate surface from a mds-mds configuration (left figure) and a table (right figure) showing the calculated activation energies between stable sites, the relative energies with respect to the "mdc" configuration* ($E_{rel}^{ad} = E_2^{ad} - E_{1\ (mdc)}^{ad}$) *and the energy difference with the most stable configuration obtained* ($\Delta E = E_2^{ad} - E_{2\ (mds-mds)}^{ad}$). *Note that "mds-th(b)" and "mds-th(d)" refer to the configurations obtained in panels (b) and (d) of Figure 4.21, respectively.*

(about 0.55-0.64 eV), while a high diffusion barrier is obtained to break the dimer between the "mds-ch" and "mds-th(b)" configurations. It is important to note that the back reaction of this last diffusion has an activation barrier of 0.55 eV, and then tends to recreate the dimer. Moreover, the barrier to move "th" away from this configuration (to further separate the two Bi atoms) is of the order of 1.2 eV (i.e. single atom diffusion) and also indicates that it is not favorable to dissociate the dimer formed. Moreover, the complete pathway calculated from the Bi dimer initial position to the non-interacting "mdc-th" configuration shows the need of an activation energy of 1.53 eV. The activation energy between the "mdc-th(d)" and "mdc-ch" configurations (0.66 eV) is lower than that between the "th" and "ch" sites (1.4 eV) obtained in Figure 4.20, indicating that the Bi atoms diffuse more easily in the presence of another neighbouring Bi atom so that they can stick together and not separate.

Finally these results show that Bi atoms can diffuse easily only if they remain close to other neighbouring Bi atoms: we can argue that the decrease of activation energy opens however the possibility for the atoms to reorganize around the Bi core formed on the surface.

Addition of more Bi atoms: islands formation

After finding the stable configuration upon depositing two Bi atoms, a third Bi atom is deposited in addition to the Bi dimer on the substrate surface. The added Bi atom is placed each time on one of the sixteen sites represented in Figure 4.18a. Interestingly, placing the Bi atom as close neighbour of the Bi dimer only leads to two final configurations. The first is the "triangle" configuration where the three Bi atoms form a triangular island (see Figure 4.23a), while the second, the "th1-Bi dimer" configuration, is obtained when the third atom is on the "th" site in close proximity to the Bi dimer (see Figure 4.23b). While placing the new Bi atom in a non-interacting configuration as

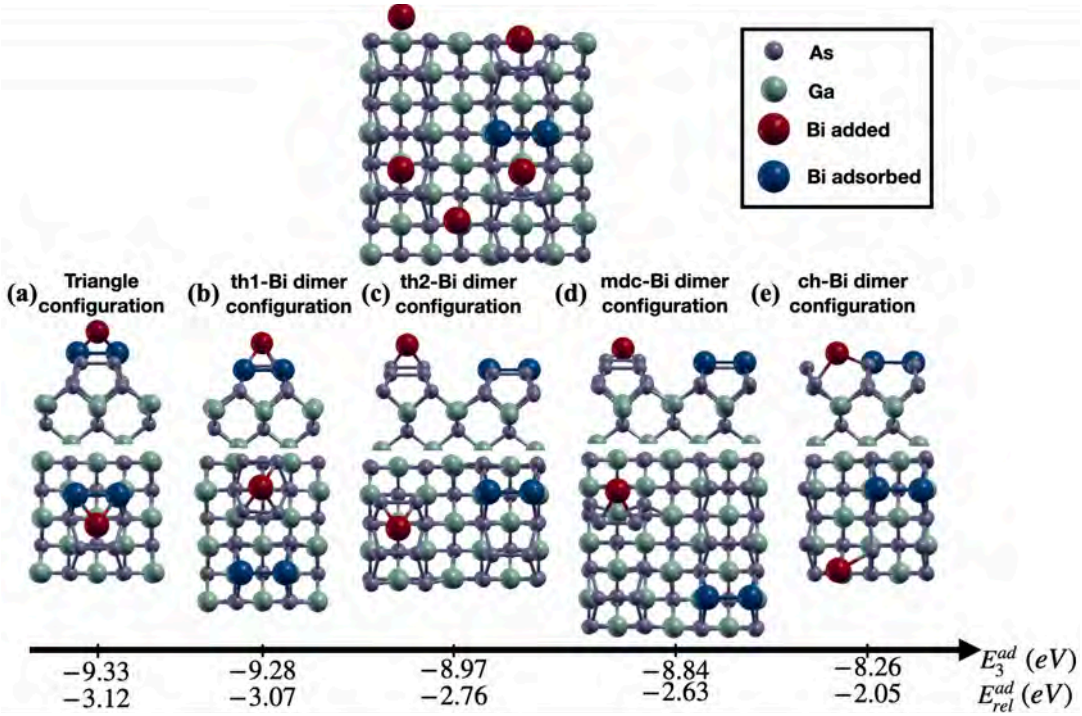

Figure 4.23: *Top view where the sites are after relaxation (top figure). Panels (a), (b), (c), (d) and (e) show the top and side views of the final configurations with their formation energy. The added Bi atom is represented by a red atom while those already adsorbed are coloured blue. As and Ga are represented by green and gray atoms, respectively.*

"th-Bi dimer" and "tdi-Bi dimer" leads to the "th2-Bi dimer" configuration (see Figure 4.23c). Placing the third Bi atom in the “mdc” and “ch” sites without interaction with the Bi dimer leads to the final positions “mdc-Bi dimer” and “ch-Bi dimer” respectively (see Figure 4.23d and 4.23e). These

results highlight the tendency of Bi atoms to **form islands** on the surface of GaAs and again confirm a favourable interaction energy between the Bi atoms since the compact configurations are more energetically favourable than the non-interacting ones.

In order to check if this tendency is still true with high coverage, the number of deposited Bi atoms is increased from 4 to 5 and finally to 6. Each time a Bi atom is added to the surface of the substrate, all sites shown in Figure 4.18a are examined to find the most stable one. Figure 4.24 shows the most stable configurations obtained each time a new Bi atom is adsorbed

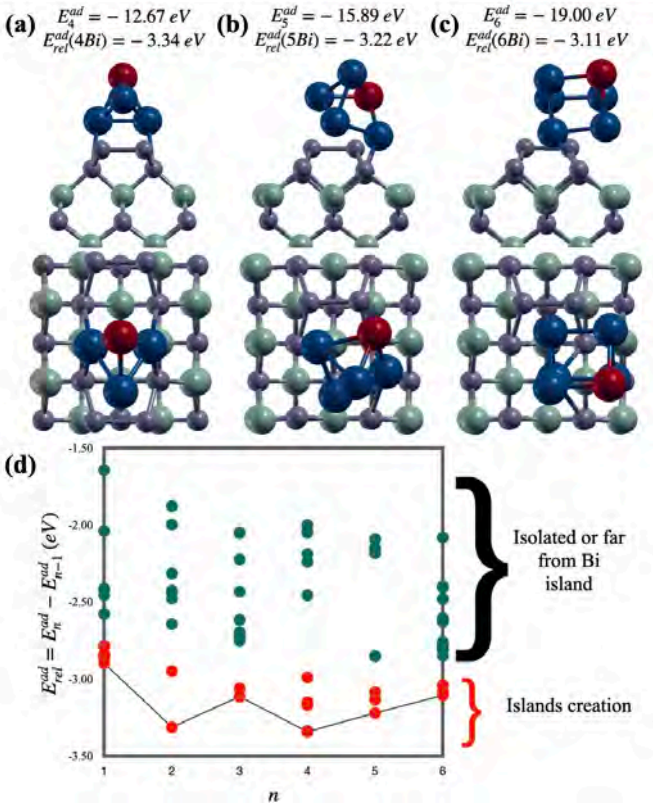

Figure 4.24: *Top and side view of the most stable configuration obtained after depositing (a) four, (b) five and (c) six Bi atoms on the GaAs(001)-c*(4×4) *surface. The added Bi atom is represented by a red atom while those already adsorbed are coloured blue. As and Ga are represented by green and gray atoms, respectively. (d) Evolution of* E_{rel} *as a function of the number of Bi atoms deposited on the GaAs surface. The red dots represent the* E_{rel} *of the most stable configurations, while the green dots represent the* E_{rel} *of the others. The red dashed line in panel (d) is a separator between creating island and non-interacting configurations.*

on the surface of GaAs. It can be seen that by increasing the coverage, the added Bi atom binds only to the adsorbed Bi atoms, leading to the formation of tall islands (see Figures 4.24a-c). Interestingly, Figure 4.24c shows the beginning of the formation of the same crystal pattern observed experimentally in Figure 4.15, Section 4.7 with a tilt angle of about 5° with respect to the GaAs substrate. These results are consistent with our experimental result obtained in Sections 4.4 and 4.7. Figure 4.24d shows $E_{rel}^{ad} = E_n^{ad} - E_{n-1}^{ad}$ as a function of the number of Bi atoms deposited. It can be seen that E_{rel}^{ad} is always lower than the adsorption energy of a single deposited Bi ($E_1^{ad}{}_{(mdc)} = -2.90$ eV, see Figure 4.19a), which highlights the strong interaction between the Bi atoms on the GaAs(001) substrate.

Influence of the Bi island: Clustering effect

The goal of this section is to know at which distance the isolated Bi atoms are under the influence of a formed Bi island. This information is one of the key parameters needed by simulation tools able to simulate the deposition and growth of materials such as Kinetic Monte Carlo or other TCAD tools and also to identify the growth mode during a deposition.

To study this, we deposited an island formed by four Bi atoms on top of a GaAs supercell (see Figure 4.25a). This latter is constructed by doubling the GaAs cell shown in Figure 4.17 only along the x direction. Once this supercell and the Bi island were relaxed, we added one Bi in each of the sites represented in Fig. 4.25a. The shaded area in this figure is periodically equivalent to that on the right of the island.

Among the tested sites, there are 2 "mdc" (red) , 3 "th" (orange) and 2 "ch" (yellow) at different distances $d_{Bi-island}$ from the island. In each group, the atoms are designated in ascending order by increasing $d_{Bi-island}$ (1-2-3). Figure 4.25b shows the variation of the formation energy of the atoms of the three groups as a function of $d_{Bi-island}$. The formation energies of isolated atoms ($d_{Bi-island} \to \infty$) in all groups are also shown in this Figure and were taken from the results obtained for the deposition of a single Bi atom. We can see that the formation energy decreases with decreasing $d_{Bi-island}$ in all groups, indicating that the closer the Bi atom is to the Bi island, the more stable it is. This result can be explained due to the fact that the surface is electrically stable and does not require addition of Bi atoms. Therefore, it is preferable that the electronic destabilisation is localised at one location instead of several.

In the three groups of atoms that have been studied, the difference of formation energy between the isolated Bi (∞) and the Bi close to the island becomes significant, *i.e* lower than 0.1eV, only if the Bi is in the very close

vicinity (number 1) of the island. This permits to conclude that the influence of the island is negligible above the distance separating two dimer rows.

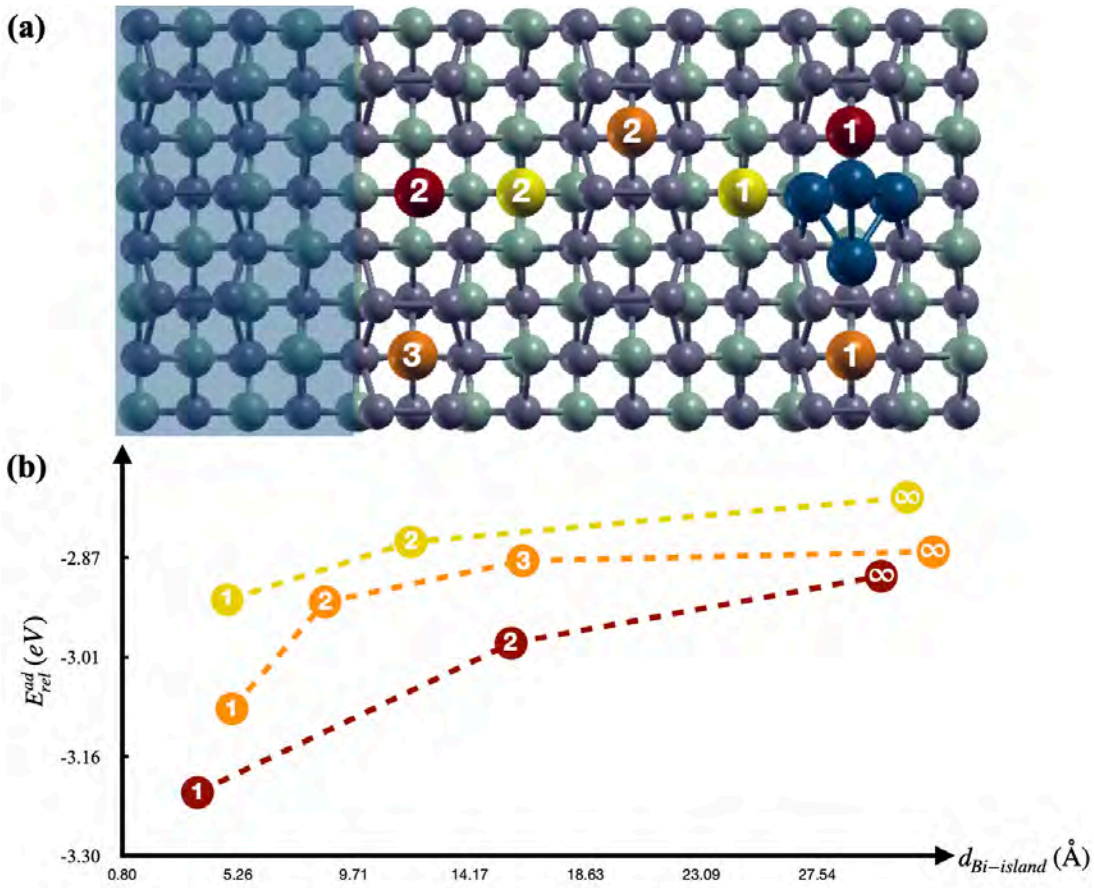

Figure 4.25: *(a) Top view of the sites tested around the adsorbed Bi island. Atoms that are in equivalent sites are coloured the same colour. The atoms are listed in ascending order according to the distance to the island. The shaded area is the periodically equivalent to the area close to the island (b) The plot of the adsorption energy of these atoms as a function of the distance separating between the tested site and the island. The notation (∞) in each of these groups defines the isolated atom (i.e. the single Bi atom deposited on the surface of GaAs).*

Analysis of the electronic transfer between the atoms

The purpose of this part is to understand whether the Bi atoms are strongly or weakly bound to the surface and to deduce the orientation of the crystal

growth.

To answer this question, the Bader charges have been calculated in all the structures presented in this chapter. Bader charges represent the number of electrons that surround each atom in the system, calculated as the 3D integral of the electronic density up to the extremum values. The Bader charge varies thus in a material compared to the value obtained in the case of an isolated atom due to the electronic exchange that are involved between the atoms that create the bonds. For this reason, in the following we do not plot the Bader charges, but we plot their difference with the one of the corresponding isolated atom, noted ΔB in the following.

GaAs unit cell and surface

GaAs is a covalent material where the bonds between the Ga and As atoms are asymmetric due to their different electronegativity (Ga: 1.81 and As: 2.18), as shown in Figure 4.26a. The Bader analysis shows that each Ga atom gives ΔB=0.6 electrons to an As atom since As is more electronegative. Once the As dimers are deposited and relaxed on the GaAs surface to form the c(4×4) surface reconstruction, the As dimers act as electron acceptors since they accept electrons from the outermost As layer (see Figure 4.26b). Interestingly, As dimers are asymmetric: one of the As atoms accepts more electrons than its partner (ΔB=-0.1 versus ΔB=-0.2).

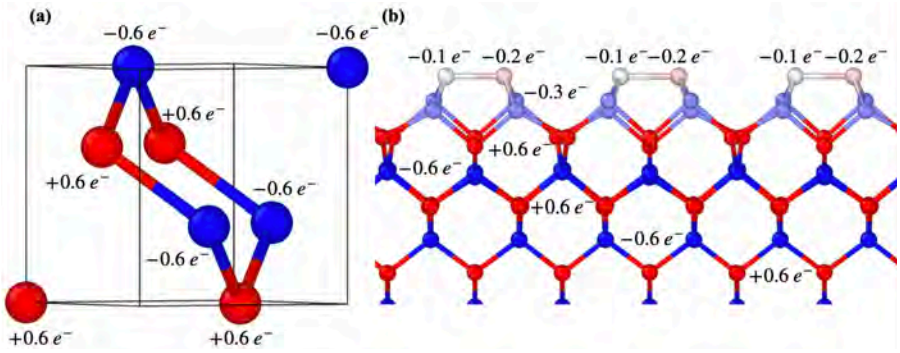

Figure 4.26: *The electronic density distribution (a) between atoms in the GaAs unit cell and (b) in the presence of As dimers on the GaAs surface. The atom colour corresponds to their charge density.*

Charges needed to form a Bi island

Figure 4.27a shows the values of ΔB when zero, one, two, three, four and five Bi atoms are deposited on the GaAs-c(4×4) surface. It can be seen that the deposition of one and two Bi atoms leads to an electronic transfer from

the Bi atoms toward the GaAs surface (the Bi atoms are blue:ΔB=-0.5), whereas the other subsequent depositions, on a second top layer does not imply an electronic transfer. (the Bi atoms are white: ΔB$\sim$ 0). From this analysis, we understand that the Bi island is bound to the surface only by the two Bi atoms that fill the missing dimers. In fact, since the reconstructed surface is already electronically stable, it does not need to share its electrons. Finally, since only two atomic bonds connect the whole Bi island to the surface through the dimers, we can say that the Bi island once formed is weakly bonded to the surface. Moreover, since the Bi atoms placed above the Bi dimer do not interact with GaAs anymore, the Bi crystal structure (bond lengths and angles) is directly identified from the second layer.

In order to see precisely whether the electrons given by the 2 first Bi atoms are taken by the whole bulk structure or only by the first neighbors atoms, the difference of ΔB between each step of addition of Bi atom has been plotted in Figure 4.27b. It can be seen that only the contact atoms have a change of their Bader charge, indicating that the shared electrons form covalent bonds: The electronic density is between the Bi and As atoms (not shown).

A side effect of the presence of the extra Bi is that the surrounding dimers change their asymmetric charge (atoms with ΔB=-0.1 have -0.2 and vice versa), but this does not change the conclusions of the study.

Consequence of this bonding

Although the addition of the fourth first atom seems to have a small number of low-energy symmetric positions (center, dimer, triangle, tetrahedron), the addition of the fifth Bi atom can be done anywhere around the already formed island, in an energetically favorable way as long as this fifth atom is connected to the island to contribute to the growth of the Bi crystal. It is noted that each of the possible sites of adsorption of the fifth Bi atom is likely to shift the growth of the Bi crystal into a different orientation by rotating the starting tetrahedron about the dimer axis. Once this Bi nucleus composed with five Bi atoms is formed, we do not observe any change in the growth mode nor in the orientation of the crystal in our computational approach: the Bi crystal clearly appears at the sixth deposited atom and the growth of a perfect crystal can then continue.

Thanks to this step by step theoretical study, we are able to validate the difference in crystal growth directions observed in the experimental samples: the Bi layers grow in such a way that the [0001] direction is not totally orthogonal to the surface, but makes an angle of large amplitude varying from 2 to 40°.

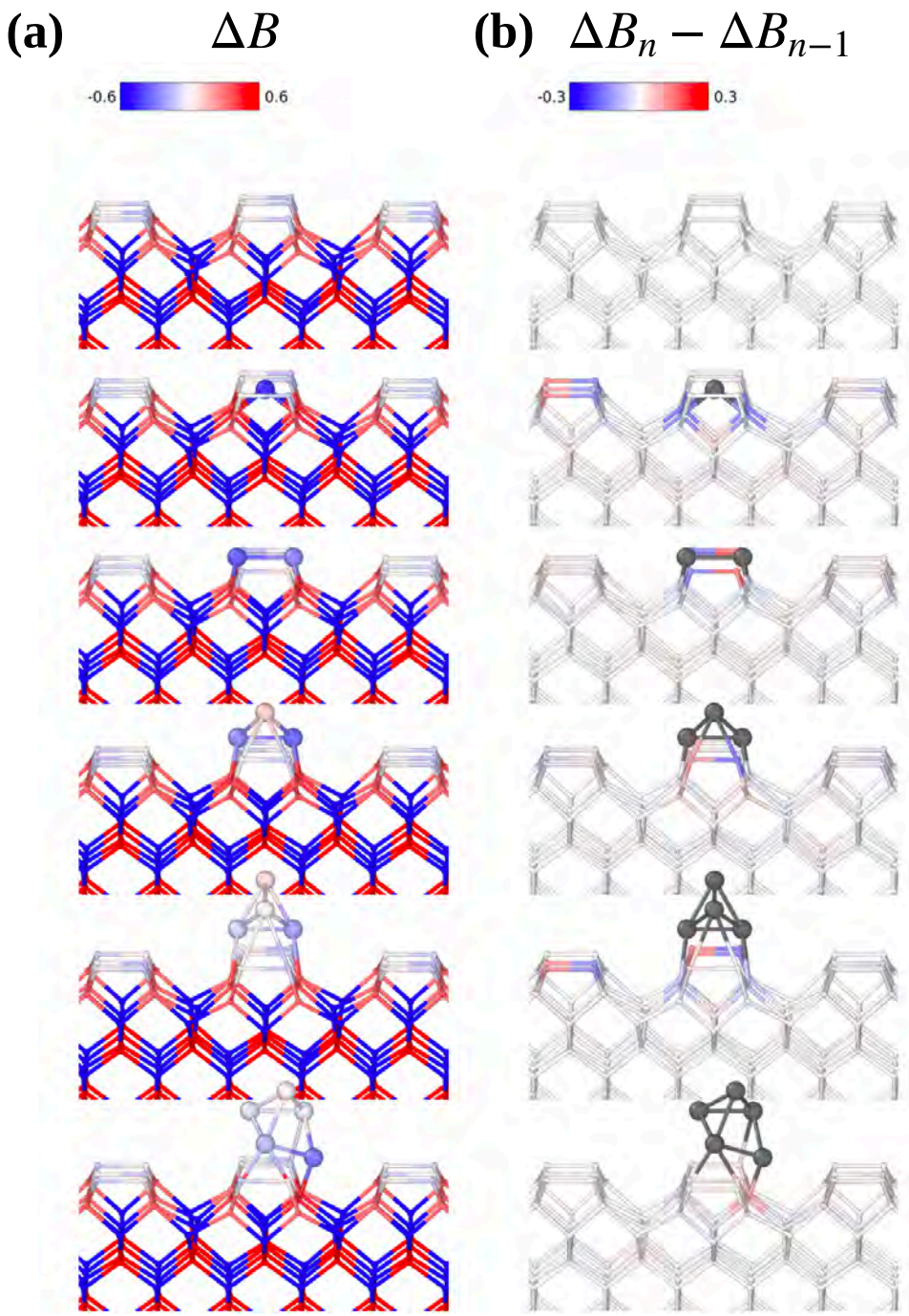

Figure 4.27: *Evolution of the electronic transfer during the addition of the Bi atoms using a Bader analysis.*

4.8.3 Conclusion

This section has considered the experimental results using DFT calculations. We have shown that Bi atoms form island during the deposition on the GaAs substrate surface, so confirming the Volmer-Weber growth mode, helped by a high mobility of Bi atom at the early stages of deposition. Then we showed the beginning of the formation of the same crystal pattern observed experimentally with a tilt angle of about 5° once the sixth Bi atom was deposited on the substrate surface. We also observe a weak interaction of the Bi crystal once formed with the GaAs substrate. Finally, we seek to perform Monte Carlo simulations in order to study the influence of the deposition rate on the Bi atoms behaviour on the GaAs(001)-$c(4 \times 4)$ surface.

4.9 Conclusion

In this chapter, we have investigated the growth of a V/V thin film on an As-rich GaAs(001) cubic substrate using a MBE system. We have shown that despite the large mismatch and the different crystalline structure between the epitaxial film and the substrate, it is possible to obtain a high quality BiSb thin film by optimising the growth conditions. The first crucial step in obtaining an epitaxial BiSb thin film is the substrate surface preparation. Here, the substrate surface was prepared in order to obtain GaAs-c(4×4) surface reconstruction; the substrate was deoxidised under As-rich condition, then a 1 μm-thick GaAs buffer with a V/III ratio of 2 was grown at 580°C and then the temperature was cooled below 300°C. Then, four samples series have been synthesised in order to evaluate and understand the influence of the growth parameters including the growth temperature, the Sb composition, the thickness and the growth rate. We have confirmed the existence of a relationship between the growth temperature and the Sb composition. We have found that the optimum growth temperature is 215°C for a Sb composition of 10% while is 195°C for 5% and 235°C for 15%. In addition, we have shown that increasing (decreasing) temperature more (less) than the optimum growth temperature leads to the surface morphology degradation. A low temperature shortens the diffusion length of the BiSb system and a high temperature decreases its adhesion rate and thus gives rise to disoriented grains and even to the adatoms re-evaporation. On the contrary by optimising the growth conditions, it is possible to obtain more than 80% of grains having a negligible tilt with the substrate and the epitaxial films are totally relaxed. Moreover, we have found that islands formations occur once the BiSb is deposited on the substrate surface and some islands are larger due

to their absorption of adatoms from other neighbouring islands. Then after reaching a critical thickness ($\approx$ 30 nm) the islands interconnect and thus form a continuous layer. These results allowed us to conclude that the BiSb growth mode is Volmer-Weber. Furthermore, we have demonstrated here that the BiSb growth rate must be low to let the thermodynamics process control the BiSb growth rather than the kinetics in order to have continuous layers and reduce the disoriented grains density.

5

Integration of the Rhombohedral BiSb(0001) Topological Insulator on a GaAs(111)A Hexagonal Substrate

5.1 Overview

In order to improve the quality of the synthesised $Bi_{1-x}Sb_x$ thin films, researchers looked for a suitable substrate. Generally, it is recommended that the substrate and the epitaxial film have the same in-plane lattice constant and the same atomic arrangement. As it is extremely rare that the lattice mismatch between the substrate and the deposited film is negligible, we focus here on the search for a substrate sharing a crystalline matrix close to that of BiSb. Since BiSb has a rhombohedral crystalline structure ($R\bar{3}m$), close to an hexagonal one, we choose the GaAs(111)A substrate.

In this chapter, we report the epitaxial growth of quasi-hexagonal BiSb materials on semi-insulating hexagonal GaAs(111)A substrates by Molecular Beam Epitaxy (MBE). All influencing parameters such as substrate surface preparation, temperature, Sb composition, BiSb film thickness and growth rate are studied one by one in order to optimise the growth conditions.

This chapter is organised as follows. Section 5.2 describes the substrate surface preparation for obtaining a smooth substrate surface compatible with the deposited material. In Section 5.3, we studied the temperature dependance on the BiSb films quality. This parameter is the most important one because of its crucial role in crystal growth, and its effect on the other parameters. After fixing the growth temperature, the influence of the Sb composition on the $Bi_{1-x}Sb_x$ surface morphology is investigated in Section 5.4. This Section highlights additionally the relationship between the Sb composition and the growth temperature. Section 5.5 discusses the growth

mode of BiSb on GaAs(111)A by presenting the evolution of crystal growth as a function of the BiSb films thickness. Next, Section 5.6 presents the effect of the deposition rate on the structural and morphological properties of BiSb films. In Section 5.7, advanced characterisations are performed to access the crystalline structure of the BiSb/GaAs(111)A interface. Finally, the chapter ends with conclusions in Section 5.8.

5.2 Methods

First, 2 inches undoped GaAs(111)A wafers (350 μm-thick) from AXT are loaded into our MBE Riber 412 system. They are degassed at 300°C for one hour into the preparation chamber. Then, they are transferred into the growth chamber, where they are heated up to the GaAs deoxidation temperature (635°C) under an As flux of 2×10^{-5} Torr. It must be noted that the As shutter opens as soon as the temperature is higher than 400°C. The substrate temperature is maintained at 635°C for 10 min to ensure that all oxide is removed. At this point, the RHEED pattern appears confirming the removal of the superficial oxide layer of the GaAs substrate. Next, the temperature is ramped down to the GaAs buffer layer growth temperature. Generally, the GaAs(111)A surface preparation is more complex than that of GaAs(001) due to the very low adhesion coefficient of As atoms on the Ga-terminated surface [73]. The surface preparation of GaAs(111)A requires a very high As flux since an As atom can only bond to one Ga atom of the outermost layer of a GaAs(111)A substrate instead of 2 as in the case of GaAs(001). Besides the As flux, the substrate temperature is also an important parameter to obtain smooth GaAs layers. Da Woolf et al. [117] have shown that setting the substrate temperature above 560°C or below 500°C leads to pyramid-shaped defects and rough surface, respectively. Based on this, a GaAs buffer layer is grown with a V/III ratio of 10 at 550°C until an atomically smooth surface is obtained (thickness of about 0.3 μm). During this process, a GaAs(111)A-(2×2) surface reconstruction is observed using RHEED. Finally, the samples are cooled down to the $Bi_{1-x}Sb_x$ growth temperature, keeping the As flux on for temperatures above 400°C. Bi and Sb are evaporated simultaneously, and the $Bi_{1-x}Sb_x$ layer is grown with growth parameters selected according to the objective of the study.

According to the RHEED records, GaAs(111)A exhibits only the (2×2) surface reconstruction even at low temperature, which is in agreement with [117]. Indeed, this surface reconstruction presents two different configurations depending on the growth conditions (see Chapter 2 in Subsection 2.4.1). The former is observed under As-rich conditions and consists in three As

atoms bonded in a triangular configuration [88, 89]. On the contrary, the second is obtained under Ga-rich conditions and has one Ga vacancy per unit cell [90]. In view of our growth conditions (rich in As), we only considered this configuration. Note that the Sb composition and the BiSb films thickness are derived from the Bi and Sb flux and the growth time. After growth, samples are taken out of the MBE and characterised by SEM, TEM and XRD.

5.3 The temperature series

In order to emphasise the influence of the temperature on crystal growth, three 300 nm-thick samples with x composition being in the TI range are grown at growth temperatures of 150, 215 and 245°C. Note that these temperatures are measured by thermocouple. Here the growth rate is 0.13 $\mu m/h$, lower than that of the case of GaAs(001) since it was deduced in Chapter 4, Section 4.6 that the lower the growth rate, the more the surface is organised. Moreover, the Sb composition is set at 20% in order to study if the optimal growth temperature for this composition will be moved to a lower temperature (in the case of GaAs(001), the optimal growth temperature is above 235°C for 20%) . Before BiSb growth begins, the Bi and Sb fluxes are calibrated to obtain fluxes of 2×10^{-7} and 5×10^{-8} Torr, respectively, giving a Sb composition of 20% matching that measured by XRD after growth. Care is taken to stabilise the BiSb growth temperature before simultaneously opening the Bi and Sb shutters. Note that regardless of the growth temperature, the RHEED recordings always show the GaAs(111)A-(2 × 2) surface reconstruction prior to BiSb deposition.

Figures 5.1a,b and c show SEM images of as-grown $Bi_{0.8}Sb_{0.2}$ samples with a growth temperature of 150, 215 and 245°C, respectively. Different surface morphologies can be observed in these Figures: at $T_G = 150$°C, the

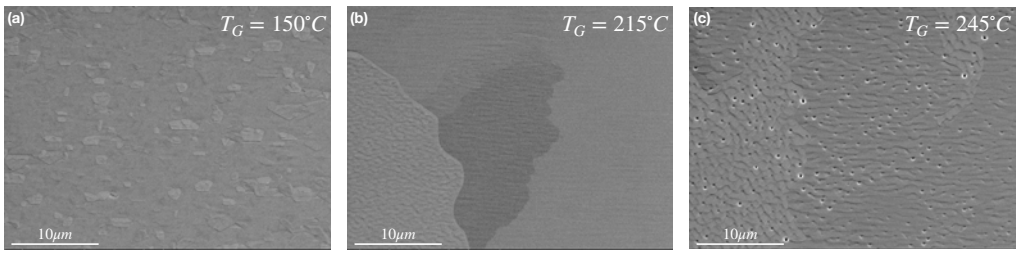

Figure 5.1: *Determination of the surface morphology of $Bi_{0.8}Sb_{0.2}$ films deposited on a GaAs(111)A substrate with a growth temperature of (a) 150° C, (b) 215° C and (d) 245° C.*

surface is rough due to the presence of a large number of holes (see Figure 5.1a). By increasing the temperature to 215°C, the surface becomes organised, flattens and is covered with large terraces (see Figure 5.1b). A further increase in temperature to 245°C, leads to a rougher and less organised surface, which presents holes (see Figure 5.1c). In order to study the crystalline orientation of the $Bi_{0.8}Sb_{0.2}$ layers, X-ray diffraction measurements are performed in a symmetric 2θ-ω configuration in a Bruker D8 Discover diffractometer.

Figure 5.2 shows the diffraction pattern of the samples reported in Figure 5.1. The GaAs(111) and GaAs(222) peaks represent the GaAs(111)A substrate and the 0.3 μm-thick buffer layer. The strong BiSb(0003), BiSb(0006) and BiSb(0009) peaks correspond to the $Bi_{0.8}Sb_{0.2}$ layers and show that the growth direction is (0001). These results therefore indicate that the (0001) planes of the $Bi_{0.8}Sb_{0.2}$ layers are parallel to the (111) direction of the GaAs(111)A substrate. Interestingly, no shift of the BiSb peaks is detected by comparing these three diffraction patterns, indicating that the

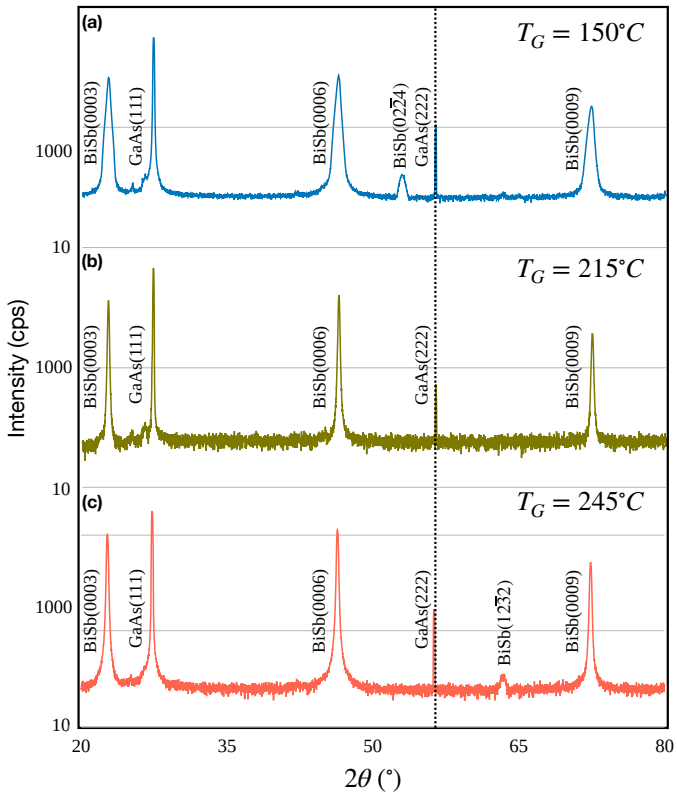

Figure 5.2: *X-ray diffraction of $Bi_{0.8}Sb_{0.2}$ layers deposited on a GaAs(111)A substrate with a growth temperature of (a) 150° C, (b) 215° C and (c) 245° C.*

re-evaporation rate is nearly zero regardless of temperature. Moreover, one can notice that the layer crystalline quality is degraded at $T_G = 150°C$, since a new peak corresponding to BiSb(02$\bar{2}$4) appears and that the BiSb peaks reported in Figure 5.2a widens. The increase in temperature to 215°C sharpens the BiSb peaks indicating a better crystallinity of the $Bi_{0.8}Sb_{0.2}$ films (see Figure 5.2b). In Figure 5.2c, a new peak appears corresponding to BiSb(12$\bar{3}$2) showing that the surface becomes less organised at 245°C.

In order to better understand the influence of the temperature on the BiSb films quality, its phase diagram, theoretically predicted by [24], is introduced in Figure 5.3. Note that this diagram is calculated at atmospheric pressure. In order to compare our growth conditions with this diagram, we need to use the "real" substrate temperature (T_r) measured by kSA BandiT (band edge thermometry). The correspondance graph is given in Figure 4.1, Section 4.3, Chapter 4.

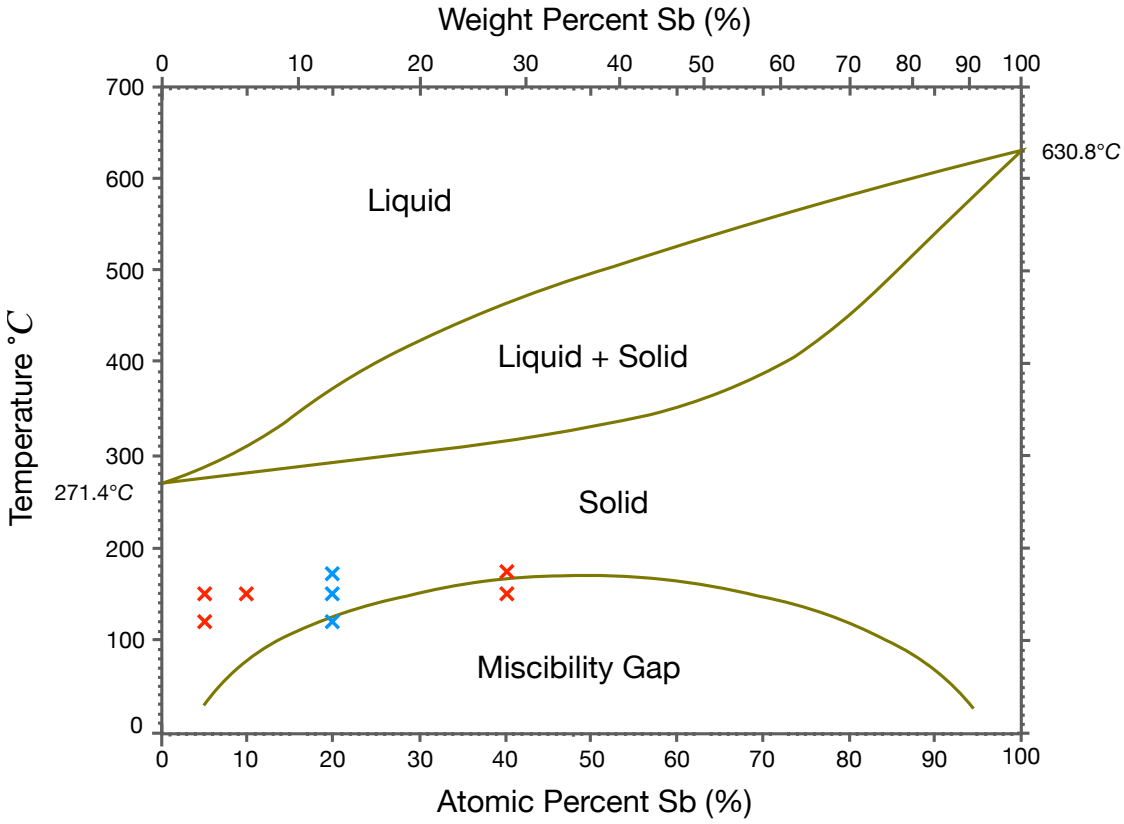

Figure 5.3: *The theoretical phase diagram of the $Bi_{1-x}Sb_x$ system calculated at atmospheric pressure [24]. The crosses mark indicate our growth conditions adopted in each $Bi_{1-x}Sb_x$ growth.*

In this section, we only focus on the comparison between the $Bi_{0.8}Sb_{0.2}$ samples grown at different temperatures (indicated by blue crosses) and the theoretical phase diagram. The other samples indicated by red crosses will be discussed in Section 5.4. This phase diagram shows that for a Sb composition of 20%, the BiSb alloy is in the solid phase at $T_G = 245°C$ ($T_r = 170°C$) and $T_G = 215°C$ ($T_r = 150°C$), while it is in the miscibility gap at $T_G = 150°C$ ($T_r = 120°C$). This means that an epitaxial growth is predicted at $T_G = 245°C$ ($T_r = 170°C$) and $T_G = 215°C$ ($T_r = 150°C$), while a polycrystalline with different compositions surface is expected at $T_G = 150°C$ ($T_r = 120°C$). Ours results at $T_G = 245°C$ ($T_r = 170°C$) and $T_G = 215°C$ ($T_r = 150°C$) are consistent with this diagram. Despite $T_G = 150°C$ ($T_r = 120°C$) falling within the miscibility gap for $x = 20\%$, no peaks degeneracy is observed in Figure 5.2a, which confirms the shift of the whole phase diagram to lower temperature in the UHV environment, as reported previously (see Chapter 4, Section 4.3). The optimal growth temperature is therefore around 215°C for $x = 20\%$, which is lower than that of the GaAs(001). This may be due to the change in growth rate. In the case of GaAs(001) (see Chapter 4), samples with Sb composition of 20% were grown with higher growth rate (0.26 $\mu m/h$) than those grown on GaAs(111)A (0.13 $\mu m/h$). This causes the increase of the adatoms density at the surface and thus a decrease of the adatom diffusion length. In this case, an increase of the temperature is required to flatten the surface by increasing diffusion lengths.

5.4 The composition series

After finding the optimal temperature window to grow $Bi_{1-x}Sb_x$ films, the effect of Sb composition on the BiSb surface morphology is investigated. Four samples were grown with x composition of 5, 10, 20 and 40%, by changing the Sb flux while keeping all other parameters constant. The Bi flux is maintained at 2×10^{-7} Torr and the Sb fluxes are calibrated to 1.05, 2.2, 5 and 13.3×10^{-8} Torr for compositions about 5, 10, 20 and 40%, respectively. The growth rate is of the order of 0.13 $\mu m/h$ for compositions of 5, 10 and 20%, while it is 0.16 $\mu m/h$ for a composition of 40%. The BiSb growths are triggered once the substrate temperature stabilises at 215°C ($T_r = 150°C$). Finally, the growths end when 300 nm-thick BiSb films are obtained. After growth, the Sb composition is measured by XRD and corresponds interestingly to the BEP ratio calibrated by the Bayard-Alpert gauge.

Figures 5.4a, b, d and e show SEM images of $Bi_{1-x}Sb_x$ films with x composition of 5, 10, 20 and 40%, respectively. It is observed that a low Sb composition (x=5%) leads to a rough and lowly organised surface due

to a polycrystalline growth mode and the presence of holes in between (see Figure 5.4a). Interestingly, different deformed hexagonal holes are observed. An increase of the Sb composition to 10-20% promotes the formation of large flat grains, covering the entire substrate surface, which result in an organised and smooth top layer (see Figures 5.4b and d). Increasing further

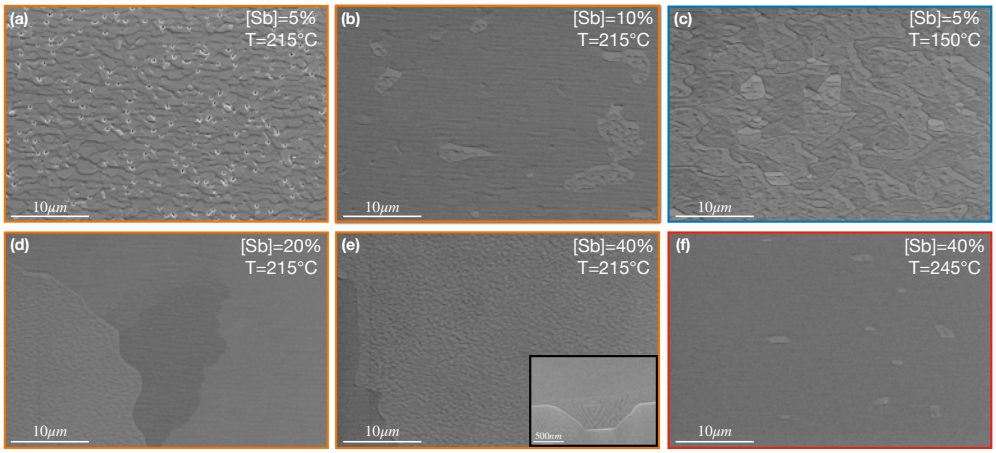

Figure 5.4: *Surface morphology of BiSb layers grown on a GaAs(111)A substrate with a x composition of (a) 5%, (b) 10%, (c) 5%, (d) 20%, (e) and (f) 40%. The blue, red and orange frame indicate a growth temperature of 150, 245 and 215°C, respectively.*

the Sb composition to 40% generates surface defects. The inset in Figure 5.4e shows a spiral structure on top of triangular grains which is characteristic of a screw dislocation. Figures 5.5b-e show the diffraction pattern of the samples presented in Figure 5.4a-d. The GaAs(111) and GaAs(222) peaks correspond to the GaAs(111)A substrate and to the 0.3 μm-thick buffer layer. The BiSb(0003), BiSb(0006), and BiSb(0009) peaks reveal that the growth direction of $Bi_{1-x}Sb_x$ films is [0001], which means that the [0001] direction of the $Bi_{1-x}Sb_x$ corresponds to the [111] direction of the GaAs. From these results, it is possible to conclude that the rhombohedral BiSb matrix grows on top of the hexagonal GaAs(111)A one. It can be noticed that the peaks shift to larger 2θ with increasing x, which indicates the evolution of $Bi_{1-x}Sb_x$ lattice parameters and underlies the homogenous incorporation of Bi and Sb in the BiSb films. The increase of x to 40% broadens the BiSb(0001) peaks and leads to the appearance of a new one corresponding to BiSb(02$\bar{2}$4) (see Figure 5.5e). The large full width at half maximum (FWHM) of the BiSb(0001) peaks compared to the substrate one may be due to the tilting of the BiSb grains or to the presence of a non-uniform strain in the $Bi_{0.6}Sb_{0.4}$ film [118].

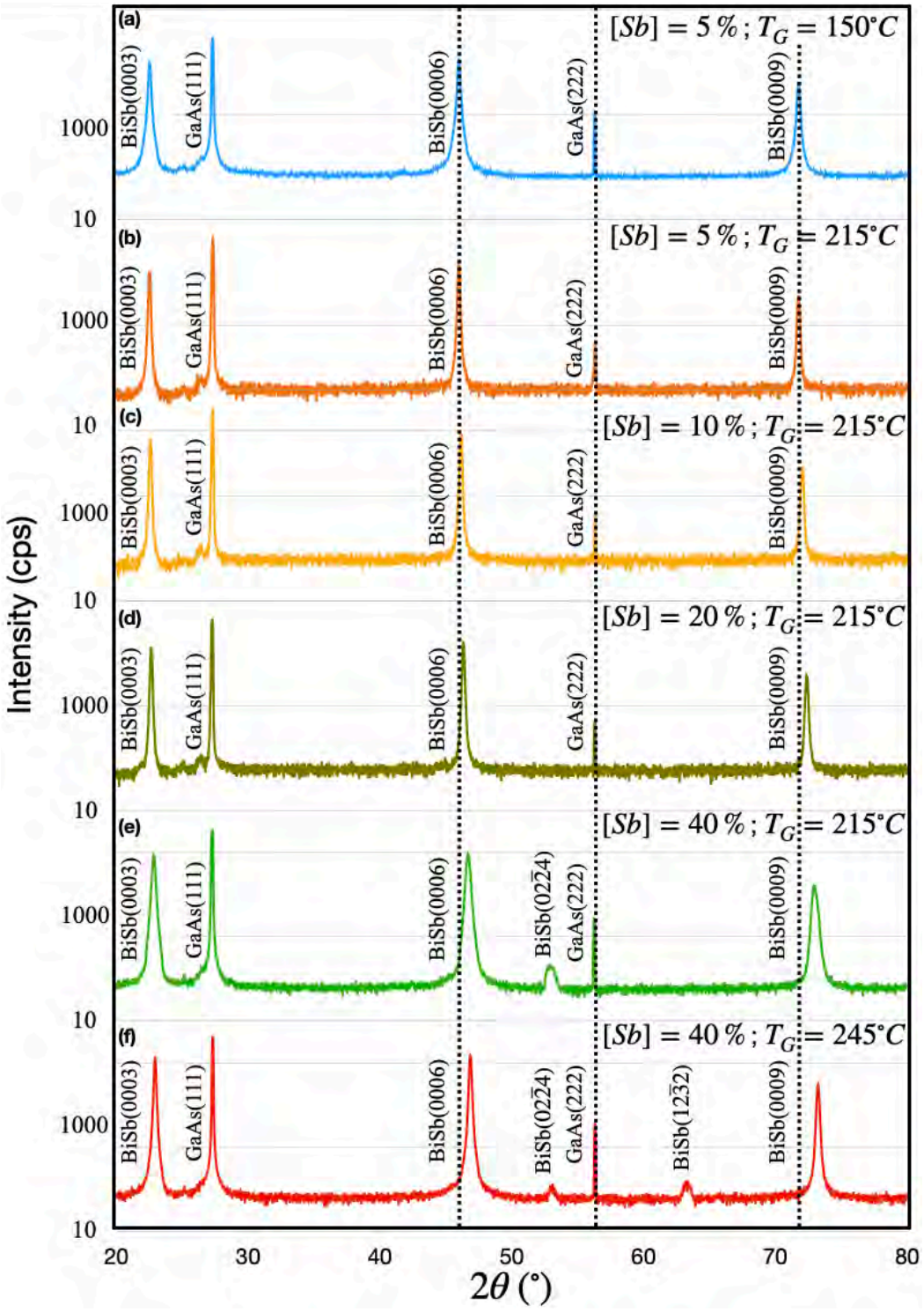

Figure 5.5: *Determination of the BiSb grains orientation. X-ray diffraction of (a) $Bi_{0.95}Sb_{0.05}$, (b) $Bi_{0.95}Sb_{0.05}$, (c) $Bi_{0.9}Sb_{0.1}$, (d) $Bi_{0.8}Sb_{0.2}$, (e) and (f) $Bi_{0.6}Sb_{0.4}$. Panels (b) to (e) show X-ray diffraction of $Bi_{1-x}Sb_x$ layers grown at $T_G = 215°C$ while panel (a) at $T_G = 150°C$ and panel (f) at $T_G = 245°C$.*

In order to probe the stress accumulating during the $Bi_{1-x}Sb_x$ growth, an in situ optical monitoring of the wafer curvature is performed on the samples with a Sb composition of 5, 10 and 40%, as reported in Figure 5.6a-c. This technique is based on magnification inferred curvature (MIC) [100].

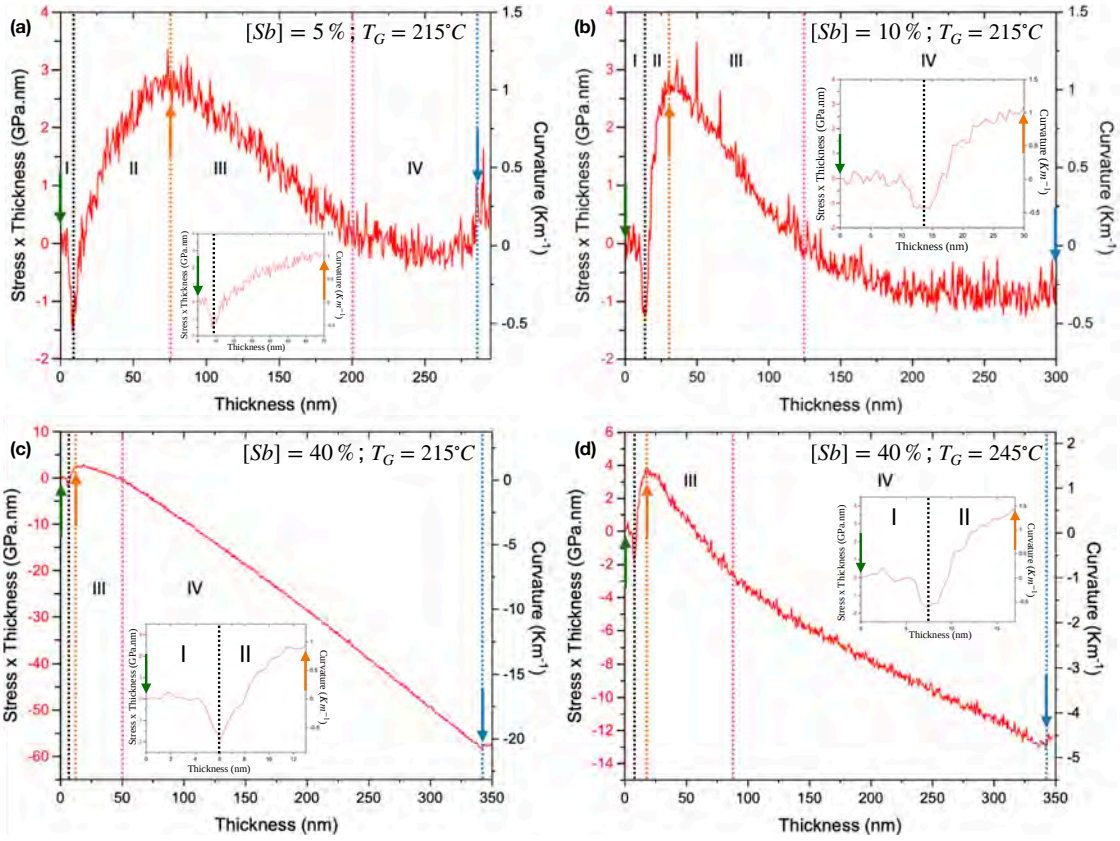

Figure 5.6: *Stress × thickness and related curvature as a function of the thickness of $Bi_{1-x}Sb_x$ films deposited on a GaAs(111)A substrate with a Sb composition of (a) 5%, (b) 10%, (c) and (d) 40%. The growth temperature is 215°C in panels (a) to (c) while it is 245°C in panel (d). The green and blue arrows in all panels indicate the start and end of BiSb growth, respectively. Note that Bi and Sb shutters are opened and closed simultaneously. The dashed lines in the panels shows the transition from one stage to the next. Each stage is labeled by I, II, III and IV respectively. The inset in each panel represents the stress × thickness evolution in stage I and II, and their beginning and end are indicated by green and orange arrows respectively in each panel.*

It can be seen that the stress evolution is roughly the same in the case of x of 5 and 10%, where four different stages during the BiSb growth are observed. In stage I, an adrupt drop of stress is observed once BiSb growth begins, indicating the accumulation of a compressive stress × thickness of about −1.6 GPa.nm due to grain nucleation [119]. Then in stage II, a strong tensile stress × thickness takes place until reaching ∼ 3 GPa.nm for $x = 5\%$ and ∼ 2.4 GPa.nm for $x = 10\%$. This corresponds to the grains coalescence, as reported in [120, 121]. At this point, the accumulated stress gradually decreases in stage III until it relaxes in both cases in stage IV (see Figures 5.6a and b). In the case of 40% (see Figure 5.6c), four different stages are detected. The first two follow the same trend as those observed in Figures 5.6a and b: at the beginning of the $Bi_{0.6}Sb_{0.4}$ growth, a compressive stress × thickness of ∼ −1.6 GPa.nm appears (see stage I) followed by a tensile one of ∼ 2.5 GPa.nm (see stage II). This indicates that the $Bi_{0.6}Sb_{0.4}$ grains nucleate after a 6 nm growth, and that they develop and coalesce once a thickness of 13 nm is reached. At this point, the developed $Bi_{0.6}Sb_{0.4}$ films relax a little due to the dislocation formation (see stage III in Figure 5.6c) [119]. The stress variation ΔS in stage III can be extracted from the slope of the linear curve fit and it is equal to -0.086 GPa. Once a critical thickness is reached (∼ 50 nm indicated by an pink dashed line in Figure 5.6c), the stress × thickness plot appears to be steeper (ΔS increases and is equal to -0.2 GPa), highlighting the presence of a high compressive stress along the remaining growth time. These results therefore confirm that the broadening of the BiSb(0001) peaks observed in Figure 5.5e is due to the stress accumulation in the $Bi_{0.6}Sb_{0.4}$ films.

In summary, more Bismuth promotes the growth of a rough surface while an excess of Antimony produces defects. The growth conditions are clearly optimised for a Sb composition between 10 and 20%. This can be explained by the fact that Bi atoms modify the surface chemical potential and lead thus to an increase of the Ehrlish-Schowbel (ES) barrier potential. As a result, the adatoms cannot overcome the ES barrier leading to island growth. On the contrary, increasing the Sb composition reduces the ES barrier potential since the growth mode is Volmer-Weber, which allows adatoms to overcome this barrier and incorporate into the lower layer to form large grains. The more these grains develop, the more stable they become and thus attract additional adatoms. As a result, grains coalesce and form a continuous layer covering the entire substrate surface. Therefore, increasing the composition (with $x < 40\%$) promotes the growth of a smooth layer instead of a disorganised one.

Two additional $Bi_{1-x}Sb_x$ samples are grown with x compositions of 5 and 40% at a growth temperature of 150°C and 245°C, respectively. Their

surfaces morphology is probed using SEM, as shown in Figures 5.4c and f. Interestingly, the surface morphology of the $Bi_{0.6}Sb_{0.4}$ sample grown at 245°C (T_r = 170°C) is better organised and smoother than that at 215°C (T_r = 150°C) and no holes are detected. In the case of x composition of 5%, the decrease in temperature from 215°C (T_r = 150°C) to 150°C (T_r = 120°C) degrades the sample crystallinity; the weak thermal agitation of the adatoms shortens their diffusion length leading to the appearance of a large number of defects on the substrate surface.

Figures 5.5a and f show the XRD pattern of $Bi_{0.95}Sb_{0.05}$ and $Bi_{0.6}Sb_{0.4}$ samples grown at 150°C (T_r = 120°C) and 245°C (T_r = 170°C), respectively. The XRD pattern of the $Bi_{0.95}Sb_{0.05}$ sample grown at 150°C (T_r = 120°C) (see Figure 5.5a) reveals its crystalline degradation compared to that grown at 215°C (T_r = 150°C) (see Figure 5.5b). Interestingly, the BiSb peaks remain at their position while changing temperature indicating that the Sb composition remains constant. In the case of 40%, it can be seen that the full width at half maximum (FWHM) of the BiSb peaks at 245°C (T_r = 170°C) is smaller than that at 215°C (T_r = 150°C), which indicate that the surface is more organised at 245°C (T_r = 170°C). Moreover, a new peak appears at 245°C (T_r = 170°C) corresponding to the BiSb(12$\bar{3}$2). These results are in good agreement with the BiSb phase diagram (see Figure 5.3): they show that the growth temperature must be modified according to the composition. Moreover, the XRD patterns of $Bi_{0.6}Sb_{0.4}$ show that the decrease in temperature from 245°C (T_r = 170°C) to 215°C (T_r = 150°C) leads to the BiSb peaks displacement towards smaller 2θ, contrary to the case of 5%. This can be due either to a change in composition or to the stress accumulation.

The stress of the $Bi_{0.6}Sb_{0.4}$ sample grown at 245°C (T_r = 170°C) is probed during growth, as shown in Figure 5.6d. Four different stages are observed, the first two of which is similar to those detected in the case of 215°C (T_r = 150°C) (see Figure 5.6c): a compressive strain × thickness of ~ -1.6 GPa.nm occurs once the BiSb growth starts (see stage I), followed by a tensile strain × thickness of $\sim$ 3.8 GPa.nm (see stage II). Then a strong compressive strain occurs at stage III with ΔS of -0.095 GPa. Contrary to the strained $Bi_{0.6}Sb_{0.4}$ layer grown at 215°C (T_r = 150°C), a partial stress relaxation occurs during the stage IV with ΔS of -0.04 GPa. This further confirms that the displacement of the BiSb peaks with decreasing temperature is due to the stress accumulated at 215°C (T_r = 150°C) ($\Delta S_{215} = -0.2$ GPa greater than $\Delta S_{245} = -0.04$ GPa), which can be considered as a low temperature for a Sb composition of 40%, as reported in Figure 5.3. The adatoms diffusion length is reduced due to the weak thermal agitation, which results in roughness and accumulation of stress in the BiSb layers. On the contrary, at a temperature of 245°C (T_r = 170°C), the thermal agitation increases the adatoms diffusion

length, which favours the thermodynamics and thus the strain relaxation in the layer.

5.5 The thickness series

In order to study the growth mode of BiSb films on the GaAs(111)A, six samples are prepared with thicknesses of 5, 10, 25, 50, 100 and 300 nm. The BiSb film thickness is estimated from the growth time. Here, the Sb composition and the growth temperature are fixed to 10% and 215°C, respectively. The Bi and Sb fluxes are calibrated to 4.5×10^{-7} and 5×10^{-8} Torr, respectively. Once the substrate temperature reaches 215°C, the BiSb growth starts with the simultaneous opening of the Bi and Sb shutters and ends when the BiSb film thickness is obtained.

Figure 5.7 shows SEM images of these six samples. The islands formation is observed at the start of growth (5 nm), indicating the Volmer-Weber growth mode (see Figure 5.7a). Figures 5.7b-d shows that the islands start coalescing to form large interconnected domains. By further increasing the thickness to 100 nm (see Figure 5.7e), these domains expand, merge with others and form large terraces covering the entire surface. In the end, an organised and smooth surface is obtained for a thickness of 300 nm.

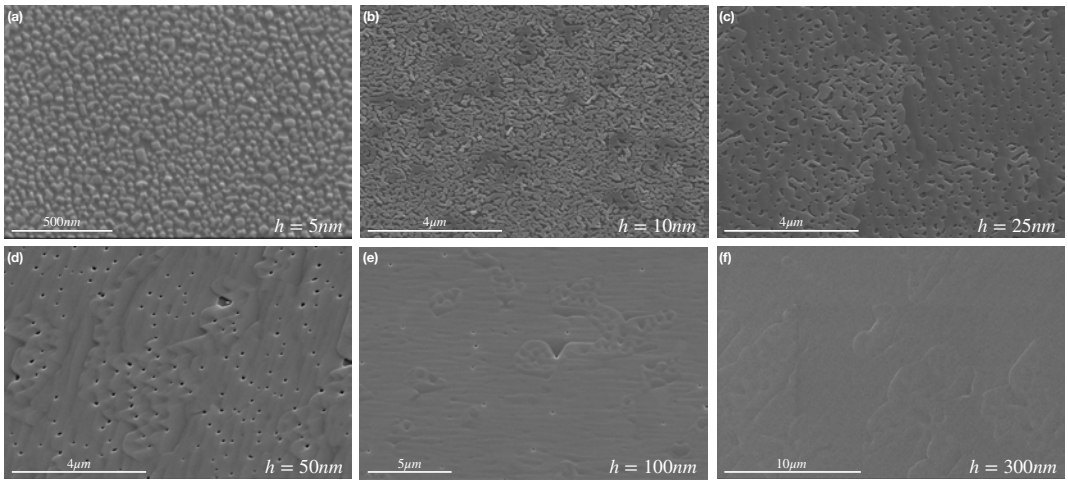

Figure 5.7: *SEM images of $Bi_{0.9}Sb_{0.1}$ layers having a thickness of (a) 5 nm, (b) 10 nm, (c) 25 nm, (d) 50 nm, (e) 100 nm and (f) 300 nm. All samples were grown at 215°C with a Sb composition of 10%.*

5.6 The kinetics series

The objective of this section is to study the influence of the growth rate on the substrate surface. Three samples with a x composition of 10% were synthesised with growth rates of 0.13, 0.26 and 0.4 $\mu m/h$. Referring to the BiSb phase diagram (see Figure 5.3 [24]), the BiSb system is in stable phase at 215°C, which means that the evaporation rate can be neglected. BiSb growth starts by simultaneously depositing Bi and Sb and ends once a 300 nm-thick sample is obtained. Note that whenever the growth rate is changed, the growth time must also be adapted in order to obtain the same thickness for all samples. For a growth rate of 0.13 $\mu m/h$, the growth time is 140 min, whereas it is 70 min for 0.26 $\mu m/h$ and 47 min for 0.4 $\mu m/h$. The XRD measurements performed after each growth confirmed a Sb composition of 10%.

Figures 5.8a,b and c show SEM images of samples grown with a growth rate of 0.4, 0.26 and 0.13 $\mu m/h$, respectively. It can be observed that increasing the growth rate results in a disorganised and rough surface with a large number of holes (see Figure 5.8a). On the contrary for low growth rates, the surface is organised, smooth and covered by large terraces, as shown in Figures 5.8b and c. Indeed, depositing a large number of adatoms at

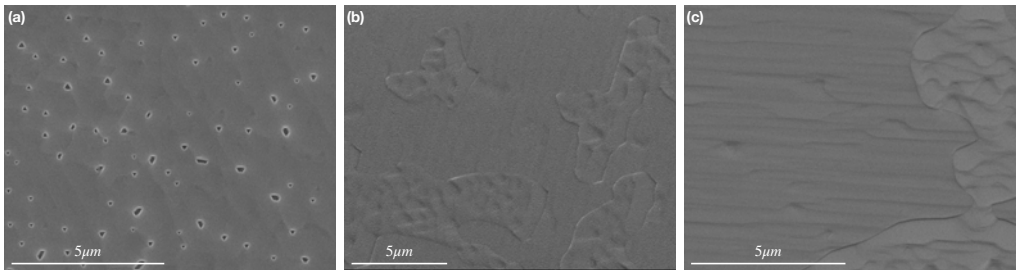

Figure 5.8: *Determination of the surface morphology of 300 nm-thick $Bi_{0.9}Sb_{0.1}$ films deposited on a GaAs(111)A substrate with a growth rate of (a) 0.4 µm/h, (b) 0.26 µm/h and (c) 0.13 µm/h.*

the same time, increases their possible collision. As a result, their mobility decreases which prevents them from reaching their energetically favourable sites. At this stage, the growth thermodynamics is reduced and kinetics processes control the growth. As a consequence, the adatoms form grains with their neighbouring adatoms in order to reduce the surface chemical potential, which leads to the formation of multi-grains. Over time, these grains coalesce and form large interconnected rough domains. On the contrary, a decrease in growth rate increases the probability for adatoms to reach their thermody-

namics equilibrium by adhering to existing islands. As a result, the existing islands develop, coalesce with others to form a smooth, organised surface.

5.7 Advanced characterisations

In order to investigate the BiSb/GaAs(111)A interface and the crystalline quality of the epitaxial films, TEM measurements are carried out on the 500 nm-thick $Bi_{0.9}Sb_{0.1}$ films. First, carbon and platinum depositions are performed on a selected region of the sample, chosen for the focused ion beam (FIB) cut. A thin lamella is then cut from the sample using FIB and then measured by TEM. A TEM image of the BiSb/GaAs(111)A interface is reported in Figure 5.9a. This figure shows that a monocrystalline BiSb layer having a flat surface has been grown on the GaAs(111)A substrate and that the interface between them is smooth. Moreover, this epitaxial layer does not present any structural defect thus confirming its high crystallinity. The distribution of Bi and Sb atoms as a function of the film thickness is reported in Figure 5.9b. This Figure confirms that the film thickness is roughly 500 nm and the Sb composition is 10% which is in good agreement with the XRD measurements. Interestingly, the Sb and Bi distribution is uniform in the whole cross-section of the BiSb film.

To better access the crystalline quality of the BiSb layer and the BiSb/GaAs interface, a high-resolution TEM image is performed (see Figure 5.9c) and an epitaxial relationship between the two materials can be observed with $[11\bar{2}]_{GaAs}//[1\bar{1}00]_{BiSb}$. The BiSb layer growth direction is [0001], which is in good agreement with the XRD measurements reported in Figure 5.5b. Moreover, the BiSb layer is relaxed and form covalent bonds with the GaAs(111)A substrate, which is also confirmed by the in-situ optical monitoring of the wafer curvature, shown in Figure 5.9d. This figure shows that stress in a 90 nm-thick sample evolves in three different stage. When BiSb growth begins, the BiSb layer is compressively strained for 100 s due to grain nucleation. Then, the grains start to coalesce at stage II leading to a tensile strain $\times$ thickness of 2 GPa.nm for 100 s before reaching a plateau at stage III. At this stage, the BiSb layer is partially relaxed. The presence of a stress $\times$ thickness of about $|\pm 2|$ GPa.nm negates the existence of Van der Waals forces and confirms the creation of covalent bonds between the epitaxial layer and the substrate.

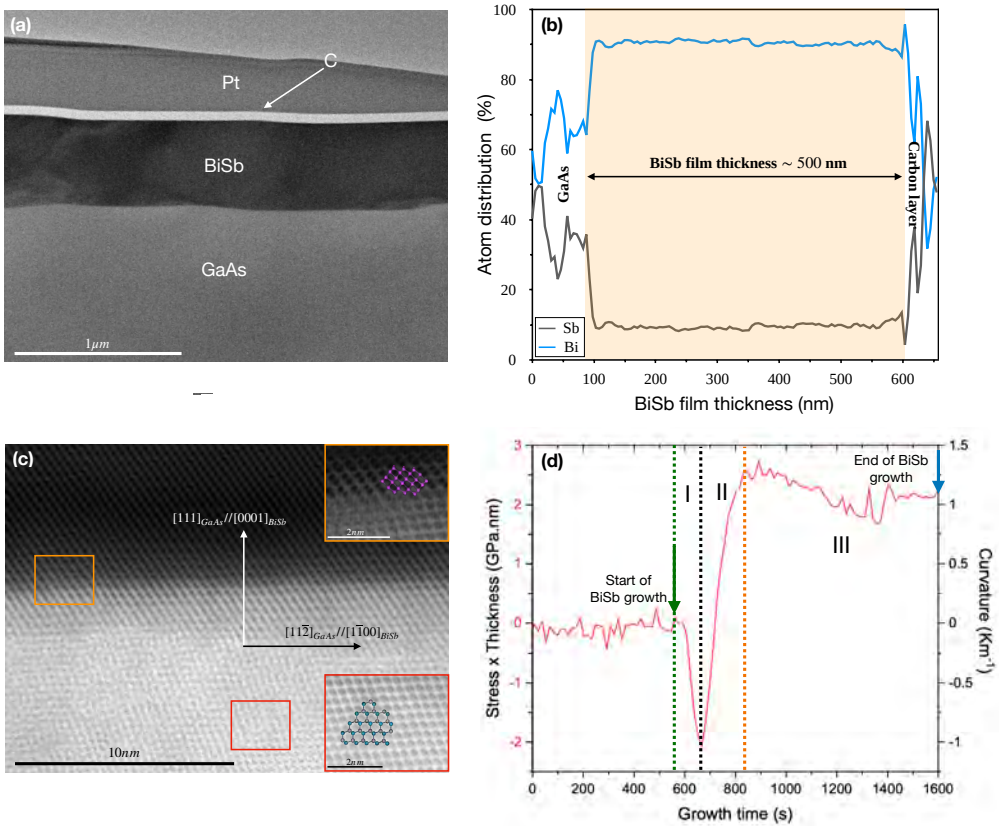

Figure 5.9: *Cross sectional characterisation of a 500 nm-thick* $Bi_{0.9}Sb_{0.1}$ *layers. (a) TEM image of the BiSb/GaAs interface. (b) Distribution of Bi and Sb atoms in the cross-section. (c) High-resolution TEM image taken along the* $[1\bar{1}0]$ *zone axis of the GaAs. The red and orange inset images are a zoomed image of the zone indicated by a red and orange square, respectively. Both insets show the side views of the crystal structure of GaAs and BiSb grain. Bi, As and Ga are represented by pink, blue and gray, respectively. (d) Stress* $\times$ *thickness and associated curvature as a function of growth time measured on a 90 nm-thick sample. The green and blue arrows indicate the start and end of BiSb growth, respectively.*

5.8 Conclusion

In this chapter, we have studied the growth of BiSb films on a GaAs(111)A substrate using MBE. We show that it is possible to integrate high quality BiSb films on this substrate by optimising the growth conditions. Any increase in Sb composition must be accompanied by an increase in tem-

perature, as predicted by the phase diagram of the BiSb system calculated in [122]. We observe that the optimal growth temperature is 215°C for a Sb composition around 10% while it is 245°C for a Sb composition of 40%. A decrease in temperature leads to a stress accumulation in the BiSb films and prevents its relaxation. Moreover, we have detected the islands formation from the beginning of the BiSb growth. Once a critical thickness is reached, these islands coalesce, which leads to the formation of a continuous layer. From these results, we deduce that the growth mode of the BiSb films on GaAs(111)A is Volmer-Weber. The growth rate must be reduced in order to favours the growth of a continuous layer. Finally, an epitaxial relationship between BiSb and GaAs with $[11\bar{2}]_{GaAs}//[1\bar{1}00]_{BiSb}$ is observed using TEM. The majority of samples grown on the GaAs(111)A substrate are not completely relaxed contrary to those grown on GaAs(001). This is related to the monocrystalline nature of those grown on GaAs(111)A, where residual stress is always present at the grain boundaries.

6
The transport properties of the BiSb(0001) layer

6.1 Overview

The technological interest of topological insulators lies in their unique electronic properties. Nevertheless, the big challenge is to disentangle the electronic contribution of the surface metallic states from that of the bulk, in particular at the nanoscale. The presence of impurities and structural defects in TI materials strongly affects their electronic properties and can even mimic their topological state signature, making it difficult to detect their true nature. This is considered a serious issue, significantly affecting the performance of the devices. However, by manufacturing them in a careful and controlled way, these new materials will pave the way to ground breaking applications in the field of spintronics and quantum computing.

This chapter highlights the crucial role of fabrication processes on the electrical properties of the BiSb material. The influence of the substrate and the BiSb film thickness on the transport measurements is exhibited. These measurements are performed using the four-terminal method with a Van der Pauw configuration. Sections 6.2 and 6.3 address respectively the GaAs(001) and GaAs(111)A substrates. In both Sections, the electronic measurements are carried out in the $20 - 300$ K temperature range in order to probe a transition from the bulk contribution to the metallic states one. First the sample sheet resistance (R_s) is extracted from standard four probes measurements and the resistivity (ρ) is then derived. The Hall coefficient (R_H) is then measured using an external magnetic field of 0.3 Tesla orthogonal to the sample surface. From these two parameters, the Hall bulk carrier concentration (C_H), the Hall sheet carrier concentration (N_H) and the Hall mobility (μ_H) are calculated.

6.2 $Bi_{1-x}Sb_x$ films grown on GaAs(001)

This section considers transport measurements performed on $Bi_{0.9}Sb_{0.1}$ samples with different thicknesses grown on semi-insulating GaAs(001) substrates. Eight $Bi_{0.9}Sb_{0.1}$ samples of 10 nm, 20 nm, 30 nm, 60 nm, 90 nm, 200 nm, 450 nm and 1 μm thicknesses are grown at 215°C using Bi and Sb fluxes of 4.5×10^{-7} and 5×10^{-8} Torr, respectively. Samples are then prepared for electrical characterisations using the fabrication processes described in Figure 6.1.

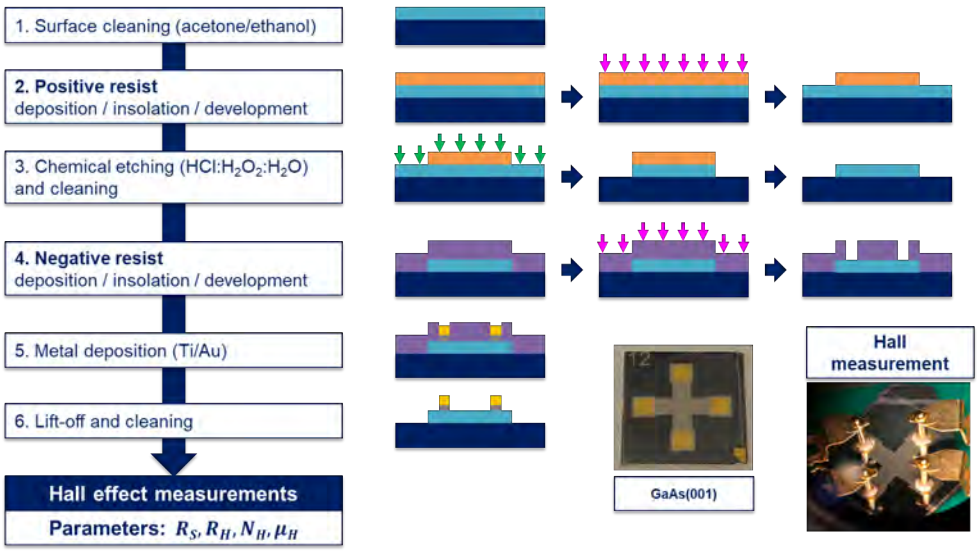

Figure 6.1: *Fabrication steps of the Hall effect samples.*

The electronic measurements are first performed at room temperature without any external magnetic field. Figure 6.2a shows the evolution of the sheet resistance per square (R_s) as a function of the sample thickness at room temperature. For a 20 nm-thick sample (or below) (blue squares in Figure 6.2a), the sheet resistance is high, close to the substrate one ($\sim 10^7 - 10^8$ Ω). As we mentioned earlier in Chapter 4, Subsection 4.5, these thicknesses correspond to BiSb materials forming small isolated grains rather than a continuous layer. In these conditions, the current is carried through the GaAs substrate rather than in the BiSb grains, which explain the measured sheet resistance of $R_s \sim 10^7$ $\Omega/\square$ close to the substrate one ($\sim 10^7 - 10^8$ Ω). At 30 nm, the sheet resistance drops quickly since the critical layer thickness is reached. The transition observed in the sheet resistance indicates the grains start coalescing to form large interconnected domains, which is consistent with SEM images in Figure 4.11, Subsection 4.5, Chapter 4, opening thus a

new channel of much higher conductance. Further increase of the thickness increases the size of these domains and leads to the formation of a continuous layer with much lower resistance, down to 2.3 $\Omega/\square$ for a 1 μm thick one.

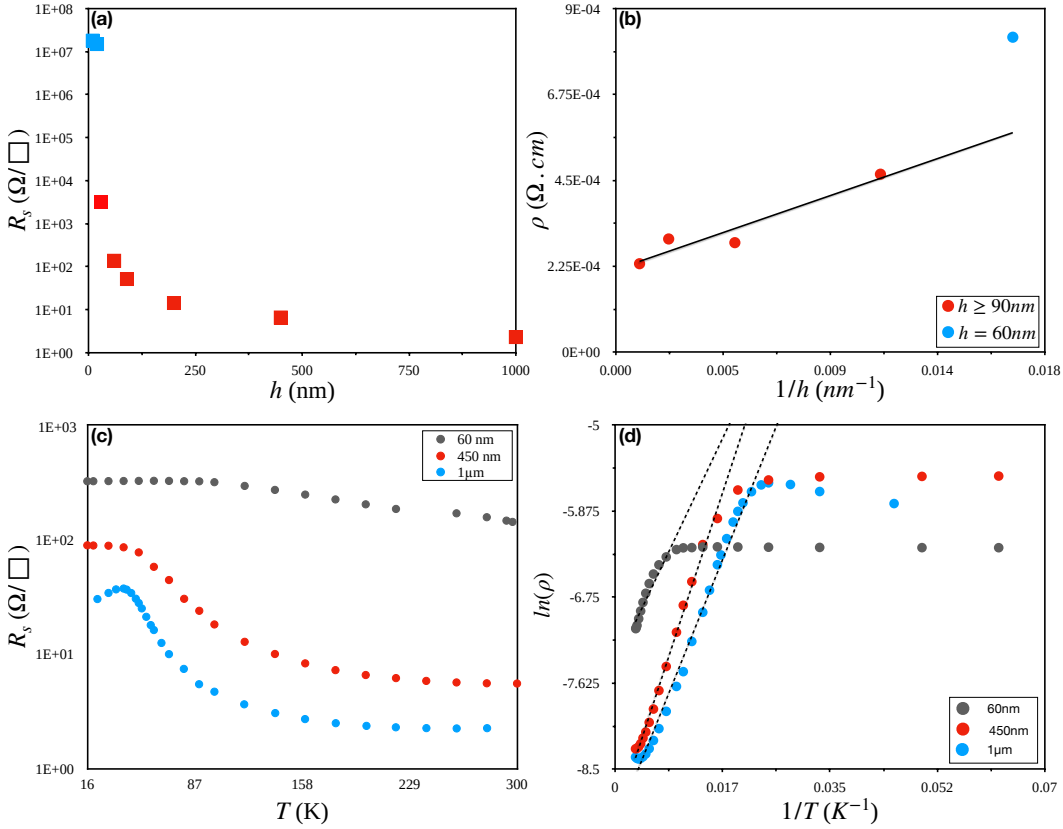

Figure 6.2: *Four point probe measurements on the BiSb layers. (a) Evolution of the sheet resistance (R_S) as function of the BiSb layer thickness (h). Blue and red dots refer to non-uniform and continuous growth regimes, respectively. (b) Evolution of the resistivity (ρ) with the inverse thickness. Values depicted in red dots fulfill the Tellier et al. [123] limitation conditions. The electron mean free path is extracted from the slope of the black straight line. (c) Sheet resistance variations with the temperature (T) for three different BiSb layer thicknesses, highlighting bulk conduction at high temperature and surface states currents at low temperature. (d) Calculated values of the resistivity (from R_S) plotted as function of the reverse temperature. The activation energies of the BiSb layers can be extracted from the linear dependences at high temperature, showed in dotted lines.*

Assuming the current flowing through the GaAs substrate is negligible

for thicknesses of 60 nm and above, we calculated the resistivities (ρ) from the corresponding sheet resistance values and the BiSb layers thicknesses. It appears that the resistivity is thickness dependent, as shown in Figure 6.2b. Generally, the thin films transport properties differ from those of bulk due to the additional scattering of the carriers at the sample surface. As a result, the thin film has a higher resistivity than that of the bulk. Indeed, Fuchs and Sondheimer (FS) attempted to explain the origin of this difference by describing the electrical properties of any type of thin film taking into account the surface scattering. Their model defines a probability "p" of charge carriers specularly scattered on the material surface [124]. Shortly after, Mayadas and Shatzkes (MS) proposed an alternative model to that of FS by considering the effect of grain boundaries in addition to surface scattering on electronic transport. The MS model predicts the electrical properties inside polycrystalline layers. Based on this extended version of the FS model [123, 125], we extracted an electron mean free path l_g about 265 nm which is better than the one mentioned in the literature ($\sim$ 150 nm) [126, 127].

In this model, the thin film resistivity is given by:

$$\rho_f = \rho_0[1 + \frac{3}{8h}(1-p)l_0] \tag{6.1}$$

Where ρ_0, l_0 and h are respectively the bulk crystal resistivity, the mean free path and the thickness.

In the case of a polycrystalline thin film, Tellier et al. [123] showed that equation 6.1 remains valid using ρ_g , the hypothetical polycrystalline bulk resistivity, instead of ρ_0 and substituting l_0 by an effective mean free path l_g defined by: $l_g \approx \frac{\rho_0}{\rho_g} l_0$. The validity of this model is restricted by grains and boundaries being identical for the different thicknesses and by the h/l_0 ratio being greater than 0.6 [123]. In our case, these conditions are verified for layer thicknesses greater than 90 nm (see red dots in Figure 6.2b). In our calculations, we assume that all charge carriers are diffusely scattered at the surface, which means that p is considered zero and that the calculated value for l_g is minimised.

Figure 6.2c shows the evolution of the sheet resistance R_s as a function of the temperature for three samples with thicknesses of 60 nm, 450 nm and 1 μm. For the three thicknesses, the sheet resistance R_s increases as the temperature decreases (starting at $T = 300$ K), indicating the semiconductor behaviour of the BiSb film. The 60 nm curve reaches a plateau for $T < 100$ K. The 450 nm and 1 μm ones exhibit both a transition around 55 K. Below this transition, R_s saturates for the 450 nm thick sample and starts decreasing for the 1 μm one. These trends are consistent with many studies published in the

literature [33]. Figure 6.2d shows that $ln(\rho)$ has a linear dependence with $1/T$ for temperatures above the aforementioned transition. This Arrhenius plot of the resistivity indicates a thermally activated behaviour. From the slope of the linear fit, we extracted an activation energy for the different thicknesses: 15.4 meV for a 1 μm thick sample, 17.7 meV for the 450 nm one and 18.0 meV for the 60 nm one. These activation energies are of comparable values than the half BiSb bandgap energy indicated in the literature [128], which confirms the intrinsic semiconductor behaviour of our BiSb bulk materials.

The understanding of the electrical properties of the BiSb layers can be pursued by analysing Hall parameters values. One must consider that only pure Hall values will be analysed since the Hall scattering coefficient r_H of BiSb is unknown. Figure 6.3 shows the temperature dependence of (a) the

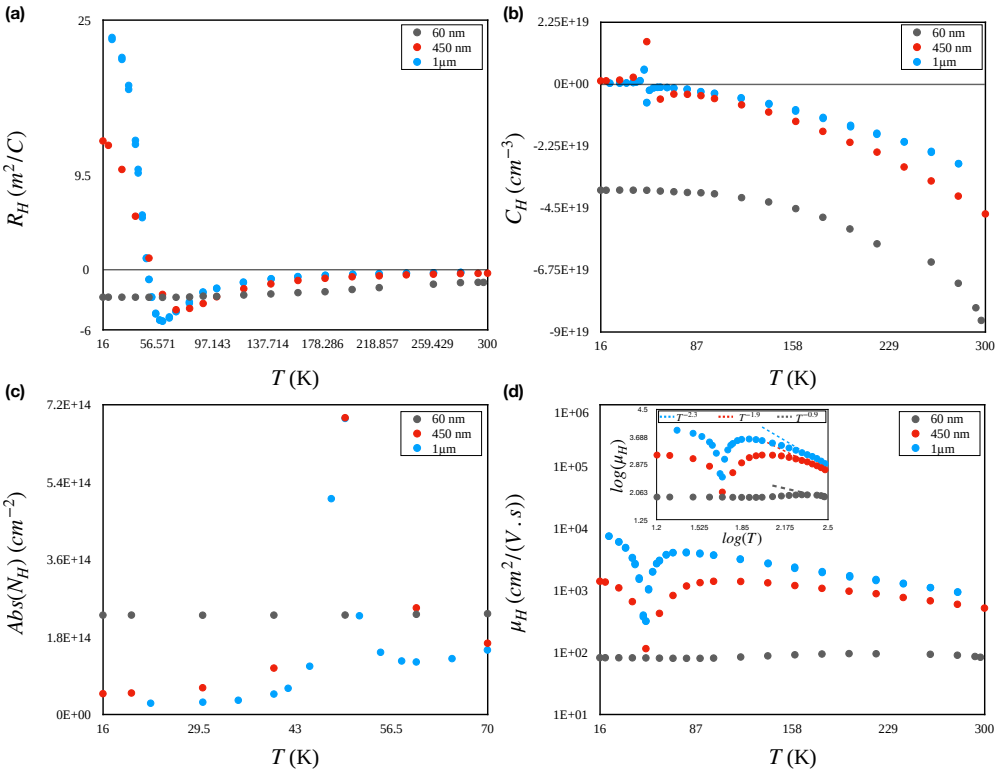

Figure 6.3: *Hall effect measurements on the BiSb layers. (a) Evolution of the Hall coefficient (R_H), (b) the Hall concentration (C_H), (c) the absolute values of the Hall sheet concentration (N_H) and (d) the Hall mobility (μ_H) as a function of the temperature. The inset in (d) shows the Hall mobility as function of the temperature, in logarithm scales, along with the T^α dependencies, in dotted lines.*

Hall coefficient (R_H), (b) the Hall carrier concentration (C_H), (c) the absolute value of the Hall sheet carrier concentration ($Abs(N_H)$) below the transition temperature and (d) the Hall charge carrier mobility (μ_H).

The first striking feature is that R_H changes sign from negative to positive at 55 K for the 450 nm and 1 μm thick samples (Figure 6.3a). At high temperature, R_H is negative (electrons are majority carriers), but an abrupt transition occurs when decreasing the temperature and holes become majority carriers. This transition occurs at the same temperature that the one observed in Figure 6.2c and is consistent with the transition from a bulk to a surface conduction regime. For the 60 nm thick sample, R_H remains negative over the whole temperature range, exhibiting a different behaviour than thicker layers. For all samples and in the high temperature range ($T > 150$ K), carriers are thermally activated, as expected for intrinsic semiconductors, and their concentration decreases while decreasing temperature (Figure 6.3b). At 300 K, the carrier concentrations per volume of the three samples are in the same order of magnitude ($3-9\times10^{19}$ cm^{-3}, Table 6.1), indicating a similar bulk behaviour. On the contrary, below 55 K a distinction between thick (450 nm and 1 μm) and thin (60 nm) samples is noticeable (see Figure 6.3c). Considering a possible conduction channel at the surface, due to gapless surface states, one cannot consider anymore per volume values at low temperature.

Thickness (μm)	C_H (300 K) (cm^{-3})	N_H (20 K) (cm^{-2})
0.06	8.82×10^{19} (electrons)	2.32×10^{14} (electrons)
0.45	4.72×10^{19} (electrons)	4.90×10^{13} (holes)
1.00	3.37×10^{19} (electrons)	2.70×10^{13} (holes)

Table 6.1: *Hall concentrations at 300 K and Hall sheet concentration at 20 K. The values are extracted from Hall effet measurements performed on $Bi_{0.9}Sb_{0.1}$ layers of different thicknesses.*

The absolute value of the Hall sheet carrier concentration is reported in Figure 6.3c. A clear divergence, about one order of magnitude, is visible between thick (450 nm, 1 μm) and thin (60 nm) samples. These results are compatible with a BiSb TI behaviour at low temperature and strongly

suggest a n-type bulk conduction for all samples at high temperatures ($>$ 100 K), a trivial n-type surface conduction for the 60 nm thick sample at low temperature ($<$ 55 K) and p-type topological surface states for the 450 nm and 1 μm thick samples at low temperatures ($<$ 55 K).

The evolution of the Hall mobilities as a function of the temperature is reported in Figure 6.3d for the three samples. Here again, the distinction between thin and thick samples is clearly visible. For the 450 nm and 1 μm samples, the Hall mobilities show a temperature dependence between 100 K and 300 K close to $T^{-1.9}$ and $T^{-2.3}$, respectively. These asymptotes seem to correspond to a phonon scattering behaviour of the electron inside the bulk (known to have $T^{-1.5}$ dependence in conventional semiconductor, like silicon [129]). For the thinnest layer, we found a $T^{-0.9}$ dependence between 220 K and 300 K. The slope lessening from -2.3 to -0.9 with the thickness reduction might be caused by surface scattering enhancement due to a degraded surface morphology.

At low temperature ($<$ 55 K), the electron Hall mobility of the 60 nm thick sample remains constant around 80 $cm^2/V.s$. On the contrary, a continuous increase of the hole Hall mobility is reported for the thick samples when decreasing the temperature from 55 K to 20 K. The hole Hall mobilities are respectively 1430 $cm^2/V.s$ at 16K for the 450 nm thick sample and 7670 $cm^2/V.s$ at 22 K for the 1 μm one. Temperature dependences in $T^{-0.4}$ and $T^{-0.6}$ are respectively reported, for temperatures below 55 K (see inset in Figure 6.3d) and are comparable to gapless surface states in others TI [130]. Adding to this observation the very high hole mobilities makes it reasonable to assume that these surface states are topologically protected, which confirms the high quality of our BiSb layers directly integrated in GaAs(0001). This is in good agreement with the BiSb topological insulator phase on (111) surfaces, for which holelike bands are predicted to have significant contribution to the surface conduction [5, 131].

6.3 $Bi_{1-x}Sb_x$ films grown on GaAs(111)A

This section addresses the electronic characterisations of $Bi_{1-x}Sb_x$ thin films grown on a GaAs(111)A substrate. Four samples are grown with different thicknesses of 50 nm, 100 nm, 500 nm and 2 μm at 215°C by keeping Bi and Sb fluxes to 4.5×10^{-7} and 5×10^{-8} Torr, respectively. These samples are then prepared using the fabrication processes reported in Figure 6.1. First, the transport measurements are carried out in a four-terminal Van der Pauw configuration at room temperature and at zero-magnetic field. Figure 6.4a shows the thickness dependance of the sheet resistance per square (R_s) at

300 K. It can be seen that the sheet resistance decreases from 80 to 1 Ω/□ with thickness and is completely different from that of GaAs ($\sim 10^7 - 10^8$ Ω/□) even at low thickness. As mentioned earlier in Section 5.5, for thickness greater than 25 nm, the surface is covered with large interconnected domains until they merge and form a continuous layer for thickness above 60 nm. In these cases, the charge carriers move through the BiSb grains rather than the GaAs substrate through a low resistance channel.

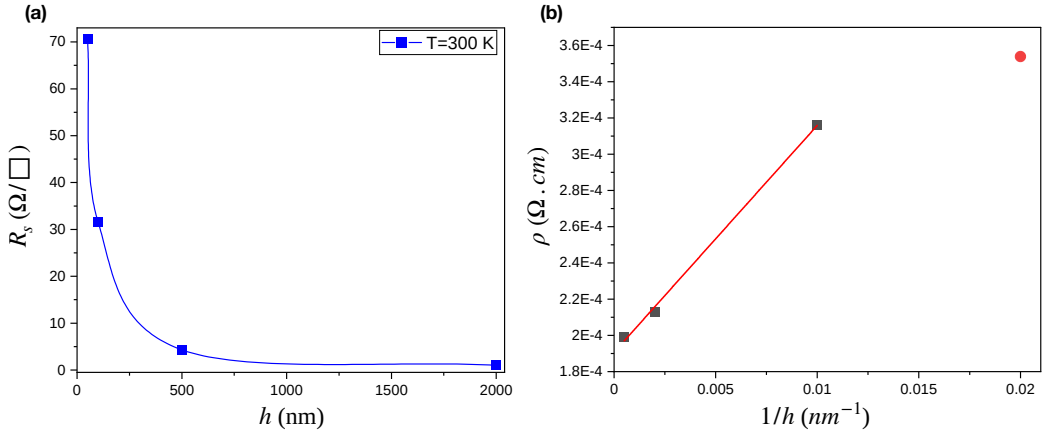

Figure 6.4: *The effect of the thickness film on the surface morphology on the electrical resistance of BiSb films. (a) Evolution of the sheet resistance as a function of the BiSb film thickness. (b) Electrical resistivity as a function the thickness inverse.*

In the following, we will assumed that the current passing through the GaAs substrate is close to zero for thicknesses greater or equal to 50 nm. Figure 6.4b shows the evolution of the resistivity (ρ) as a function of the thickness inverse. Note that resistivities are deduced from the sheet resistance shown in Figure 6.4a and the corresponding BiSb film thickness. It seems that ρ has a linear dependence with the thickness inverse for $h \geq 100$ nm, which is in good agreement with Tellier's model [123]. Similarly to Section 6.2, we only used this model on samples having a h/l_0 ratio greater than 0.6 and thus to sample thicknesses greater than 100 nm (gray squares in Figure 6.4b). From the plot of ρ as a function of the thickness inverse, ρ_g can be deduced from the intercept at the origin and the effective mean free path l_g can be extracted from the slope $((3/8)(1-p)\rho_g l_g)$. Contrary to the case of GaAs(001), we consider here $p = 0.5$ [132, 133] since the BiSb films grown on GaAs(111)A are monocrystalline. l_g is about 350 nm which is slightly better than that obtained in the case of BiSb layers grown on GaAs(001) ($\sim$ 265 nm see Section 6.2) and better than that mentioned in the literature

(162 nm) [126]. In fact, the grain boundaries induced in the polycrystalline BiSb films grown on GaAs(001) are considered as disordered regions that trap the charge carriers leading to the decrease of l_g [134]. However, as mentioned before (see section 6.2), a high conductivity is measured in the case of GaAs(001) comparable to that of GaAs(111)A, which can be due either to dislocation conduction, or to the fact that the electrons are protected from the environment in a TI material, thus preventing their backscattering in the grain boundaries. As mentioned previously (see Section 4.7, Chapter 4), 90° dislocations are present at the BiSb/GaAs(001) interface, which can induce a 1D gapless state leading to an excess of conductivity [135]. Therefore, dislocation conduction could compensate partially the decrease in conductivity resulting from the trapped carriers in grain boundaries.

The temperature dependance of the sheet resistance (R_s) for different thicknesses is shown in Figure 6.5a. For temperatures above 150 K, R_s increases with decreasing the temperature, which indicates a semiconductor behaviour. The thickest samples (2 μm and 500 nm) show a decreases in R_s for temperatures below $\sim$ 70 K, which is attributed to a metallic behaviour. By decreasing the thickness to 100 and 50 nm, this metallic behaviour appears at higher temperature (100 K).

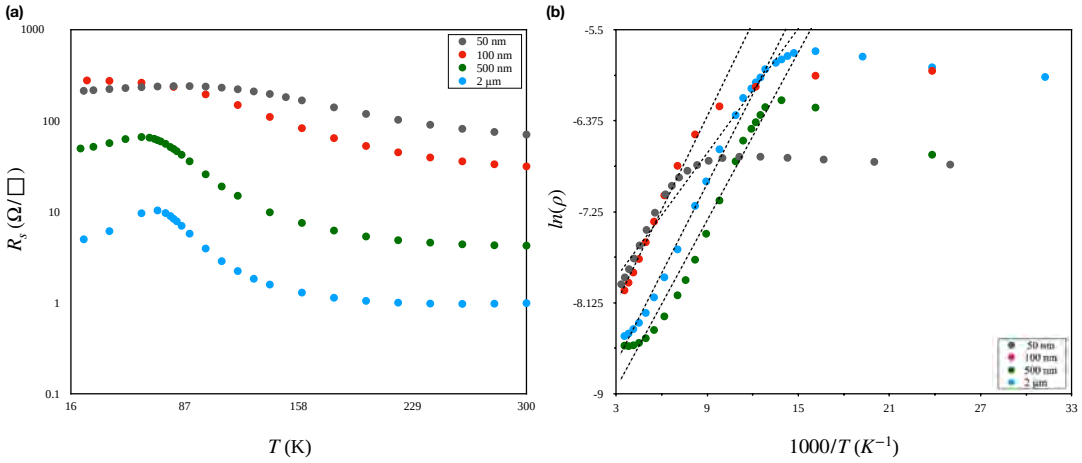

Figure 6.5: *(a) Sheet resistance evolution with the temperature for four BiSb layer thicknesses, highlighting bulk conduction at high temperature and surface states currents at low temperature. (b) Plot of $ln(\rho)$ as function of the temperature inverse. Activation energies can be extracted from the linear dependences at high temperature, showed by dotted lines.*

Figure 6.5b shows the plot of $ln(\rho)$ as a function of $1/T$, and its linear fit for temperatures above the previously mentioned transition. As in the case of GaAs(001), the thermally activated behaviour is detected by the Arrhenius plot of the resistivity. From the slopes of these fits, activation energies (E_a) of 25.3 meV, 24.3 meV, 22.5 meV and 21.7 meV are obtained for thicknesses of 50 nm, 100 nm, 500 nm and 2 μm, respectively. These activation energies are slightly greater than the half BiSb bandgap energy reported in the literature [128]. As mentioned in Chapter 5, Section 5.8, a compressive stress accumulation is always present in the BiSb layers grown on GaAs(111)A contrary to the fully relaxed ones grown on GaAs(001). In these cases, the compressive strain can increase the bandgap width, which has already been observed in other materials [136, 137].

In order to probe the electronic properties of the BiSb samples grown on GaAs(111)A, Hall effect measurements are performed using an external magnetic field of 0.3 Tesla orthogonal to the sample's surface. As the Hall

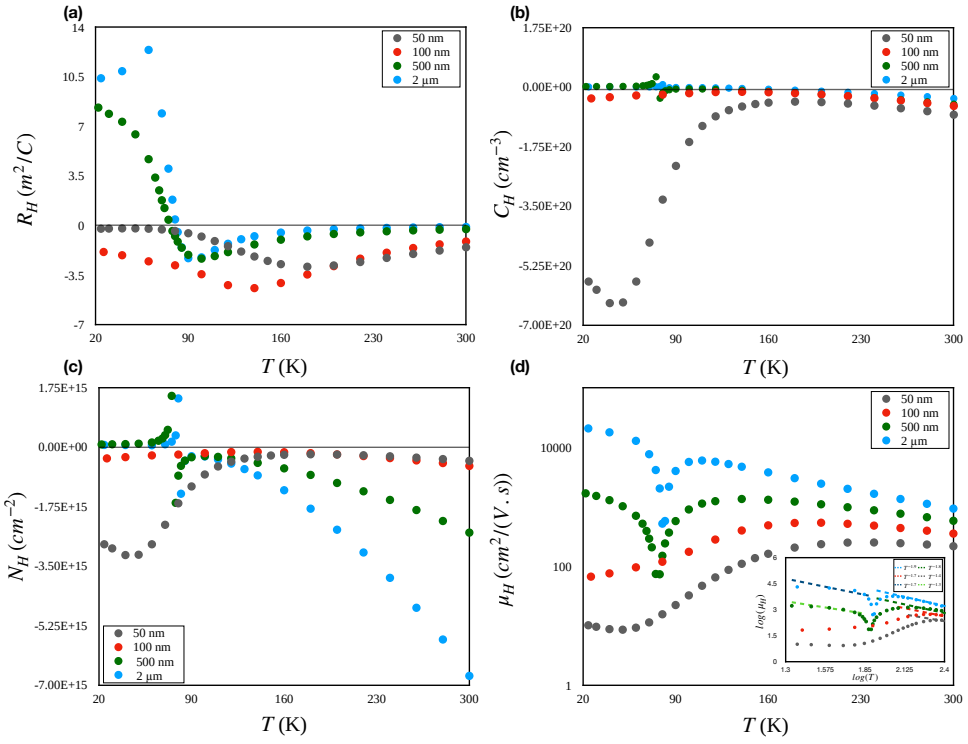

Figure 6.6: *Hall effect measurements on the BiSb layers. (a) Evolution of the Hall coefficient R_H, (b) the Hall concentration C_H, (c) the Hall sheet concentration N_H and (d) the Hall mobility μ_H as a function of the temperature. The inset in (d) shows the Hall mobility as function of the temperature, in logarithm scales, along with the T^α dependencies, in dotted lines.*

scattering coefficient (r_H) is not defined, we only consider pure Hall values. Figure 6.6 shows the temperature dependence of (a) the Hall coefficient (R_H), (b) the Hall carrier concentration (C_H), (c) the Hall sheet carrier concentration (N_H) and (d) the Hall charge mobility (μ_H).

Figure 6.6a shows a different behaviour between the thickest (2 μm and 500 nm) and the thinnest films (100 nm and 50 nm). The thinnest ones only exhibit a negative R_H over the entire temperature range indicating that the majority of the carriers are electrons. On the contrary, the 2 μm and 500 nm samples both show a transition from negative to positive R_H while decreasing in temperature indicating a change in carrier type from electrons to holes. Interestingly, the transition occurs at the same temperature mentioned earlier ($\sim$ 70 K).

In Figure 6.6b, and for temperatures above 150 K, all samples exhibit a decrease of C_H when reducing the temperature. This is characteristic of the thermal activation of carriers and the intrinsic n-type semiconductor behaviour of the BiSb thin films. Interestingly, all samples have equivalent C_H at high temperature (see Table 6.2), which is attributed to the BiSb bulk conduction. On the contrary, at low temperature, the thicker samples ($2\mu m$ and 500 nm) behave differently than the thinner ones (100 nm and 50 nm) and have equivalent C_H values. This is compatible with hole-like metallic states.

Thickness (μm)	C_H (300 K) (cm^{-3})	N_H (22 K) (cm^{-2})
0.05	8.14×10^{19} (electrons)	2.86×10^{15} (electrons)
0.10	5.58×10^{19} (electrons)	3.35×10^{14} (electrons)
0.50	5.04×10^{19} (electrons)	7.49×10^{13} (holes)
2.00	3.37×10^{19} (electrons)	6.03×10^{13} (holes)

Table 6.2: *Hall concentrations at 300 K and Hall sheet concentration at 22 K. The values are extracted from Hall effet measurements performed on $Bi_{0.9}Sb_{0.1}$ layers of different thicknesses.*

The evolution of the charge carrier concentration per surface is plotted in Figure 6.6c as a function of the temperature and Table 6.2 reports the N_H

values at 22 K of the $Bi_{1-x}Sb_x$ samples having different thicknesses. It is clear that the thicker samples (2 μm and 500 nm) share almost the same N_H, which differ by about an order of magnitude from those of the thinnest samples (100 nm and 50 nm). These results are consistent with a TI behaviour at low temperatures. They thus reveal the n-type bulk semiconductor behaviour of all samples at high temperature ($T \geq 70$ K) and the presence of p-type metallic surface states at low temperature ($T \leq 70$ K) only in the thickest ones.

Due to the thermal activation of charges in the high temperature range (see Figure 6.6b), the mobility of all samples is low and increases while decreasing temperature, as shown in Figure 6.6d. A temperature dependence close to $T^{-1.9}$ and $T^{-1.8}$ is detected for the 2 μm and 500 nm-thick samples respectively for temperature above 100 K (see the inset of Figure 6.6d). A temperature dependence in $T^{-1.7}$ is detected for the 100 nm-thick samples for temperature above 140 K. In literature, the temperature dependence of mobility is generally attributed to two scattering mechanisms: the first one is related to ionised impurities and the second is the lattice vibration scattering. In the first case, the temperature-dependent mobility has a positive power law whereas it is negative in the second. Our trends are thus attributed to the scattering of bulk electrons with the matrix phonons. These trend follows a $T^{-\alpha}$ behaviour with $\alpha \geq 1.5$, which is compatible with an intrinsic behaviour. In the case of 50 nm, a $T^{-1.4}$ dependence is detected indicating a decrease of α while decreasing thickness. As mentioned in Chapter 5, Section 5.5, decreasing the sample thickness leads to surface degradation due to large interconnected domains. As a result, the electrons surface scattering increases, causing α to decrease.

At low temperature, both the 50 nm and 100 nm-thick samples exhibit low mobilities of 10.2 $cm^2/V.s$ and 66.9 $cm^2/V.s$, respectively. Adding the metallic behaviour leads us to consider the presence of trivial metallic surface states in these samples. This can be explained by rough surfaces and the presence of structural holes in the BiSb layers. On the contrary, the 2 μm and 500 nm-thick samples show high hole mobilities of 20700 $cm^2/V.s$ and 1680 $cm^2/V.s$ at 22 K, respectively. These values are in agreement with those mentioned in other works on BiSb alloys [126, 138, 139]. In [126], a mobility of 28000 $cm^2/V.s$ is measured in a $Bi_{0.85}Sb_{0.15}$ at 5 K, which is also expected in our cases if we try to extend our curve to 5 K. The mobilities of both samples decrease with temperature and follow a trend with a negative power law. In the case of the 2 μm-thick sample, the mobility shows a temperature dependence close to $T^{-1.7}$ for a temperature below 75 K. For the 500 nm-thick sample, the mobility follows a $T^{-1.3}$ behaviour up to 75 K (see the inset of Figure 6.6d). By comparing these trends with those obtained at

high temperature for each of the samples, it can be noticed that the slope (α) has decreased. Therefore, the high mobility and the low charge carriers density obtained at low temperature in the intrinsically doped BiSb thick layers, allow us to conclude that the transport properties of these layers are similar to those of a gapless material. In fact, the latter is characterised by its high mobility caused by its zero bandgap and the linear dispersion [140, 141].

6.4 Conclusion

In this chapter, the intrinsically doped BiSb topological insulators are studied on GaAs(001) and GaAs(111)A. On both substrates, the n-type semiconductor behaviour of the BiSb bulk is demonstrated at temperatures above 140 K. The material bandgap calculated from our Hall measurements in the case of GaAs(001) corresponds roughly to that mentioned in the literature, while it is a little larger in the case of GaAs(111)A . This may be due to the residual stress present in the BiSb layers. A small difference of l_g (see Table 6.3) is detected between both substrates, despite the polycrystalline nature of BiSb grown on GaAs(001). On both substrates, a change of the carrier type is observed when decreasing the temperature for thick samples (450 nm and 1 μm in the case of GaAs(001) and 500 nm and 2 μm in the case of

<table>
<tr><th></th><th colspan="2">GaAs(001)</th><th colspan="2">GaAs(111)A</th></tr>
<tr><td>Effective mean free path (l_g)</td><td colspan="2">265 nm</td><td colspan="2">350 nm</td></tr>
<tr><td rowspan="4">Hall mobility (μ_H) ($cm^2/V.s$)</td><td rowspan="2">1 μm-thick sample</td><td>7670 (at 22 K)</td><td rowspan="2">2 μm-thick sample</td><td>20700 (at 22 K)</td></tr>
<tr><td>819 (at 300 K)</td><td>931 (at 300 K)</td></tr>
<tr><td rowspan="2">450 nm-thick sample</td><td>1430 (at 16 K)</td><td rowspan="2">500 nm-thick sample</td><td>1680 (at 22 K)</td></tr>
<tr><td>528 (at 300 K)</td><td>581 (at 300 K)</td></tr>
</table>

Table 6.3: *Summary of some results obtained on GaAs(001) and GaAs(111)A. The calculated effective mean free path and mobilities of some samples at 300 K and 16-22 K extracted from Tellier's model and Hall effect measurements, respectively.*

GaAs(111)A). Standard metallic surface states are reported in the case of thin layers (60 nm in the case of GaAs(001) and 50 nm and 100 nm in the case of GaAs(111)A). At low temperature, high hole mobilities are reported for thick samples grown either on GaAs(001) or GaAs(111)A: 1430 $cm^2/V.s$ and 7670 $cm^2/V.s$ are reported for respectively 450 nm and 1 μm thick samples grown on GaAs(001) and 1680 $cm^2/V.s$ and 20700 $cm^2/V.s$ are reported for respectively 500 nm and 2 μm thick samples grown on GaAs(111)A (see Table 6.3). Interestingly, the mobilities of BiSb films of similar thicknesses integrated on GaAs(001) and GaAs(111)A are in the same order of magnitude at 300 K and at 16-22 K, indicating that the two samples have almost the same transport properties. Considering the change in the carrier type, the ultra high mobility and the temperature-dependent mobility slope, we assume the presence of topological surface states in the case of thickest samples. These measurements are in good agreement with the literature and the presence of topologically protected surfaces states. To our knowledge, this is the first demonstration of the topological behaviour of BiSb integrated on an industrial GaAs(001) substrate with almost the same transport properties as the BiSb layers developed on GaAs(111)A substrates. Therefore, these results are promising for future industrial applications, especially for quantum and spintronics devices.

Conclusion and Perspectives

General Conclusions

This thesis considered the 2D integration of the BiSb topological insulator by molecular beam epitaxy on GaAs(001) and GaAs(111)A substrates and proved its high crystalline quality and exceptional electrical properties. In Chapter 1, we discussed the relevance of such systems by presenting their structural and electrical characteristics with some motivating examples and comparing them with other TIs. Chapters 2 and 3 discuss the general epitaxial process and the tools used to develop and characterise $Bi_{1-x}Sb_x$ thin layers. The first three chapters, therefore, provide a brief introduction and an overview of topics treated in this thesis. The main results of this manuscript are then organised in three final chapters, whose technical contributions are listed below:

- **In Chapter 4**, we report the growth of high-quality BiSb thin films on industrial standard GaAs(001) despite large mismatches and different crystalline matrices. We demonstrate the integration of the rhombohedral BiSb material on a standard GaAs(001) cubic substrate. We find that optimised growth conditions yield to more than 80% of the grains having a negligible tilt with the substrate. A clear epitaxial relationship is found between the GaAs and the BiSb with the in-plane [110] direction of the GaAs corresponding to that of the BiSb[11$\bar{2}$0]. The surface roughness and disorder are reduced, and the BiSb thin film is fully relaxed. These results are confirmed by SEM, AFM, EBSD, HR-TEM and STM characterisations. By coupling our experimental results and the DFT calculations, the Volmer-Weber growth mode and the creation of covalent bond between the BiSb layer and the GaAs(001) substrate are confirmed.

- **In Chapter 5**, with a better understanding of the BiSb epitaxy from Chapter 4, we improve the quality of BiSb thin films. We demonstrate that the use of a substrate having an atomic arrangement close

to that of BiSb contributes to the epitaxy of a BiSb layer having a smooth and organised surface. We show that the optimised growth temperature changes as a function of the Sb composition. We find that the phase diagram of the $Bi_{1-x}Sb_x$ system should be shifted to lower temperatures in an UHV environment. Similarly to GaAs(001), a Volmer-Weber growth mode is detected during the early stages of growth. A 2D layer is obtained once the critical thickness is reached. For optimised growth conditions, a partially relaxed BiSb layer is obtained with a [0001] growth direction.

- **In Chapter 6**, we study the electronic transport of selected BiSb films grown on GaAs(001) and GaAs(111)A substrates as a function of film thickness. Those grown on GaAs(001) all behave as n-type semiconductors at high temperature due to the dominance of the bulk contribution. Only in the case of thick samples, we observe a change of the carrier type from bulk electrons to surface holes accompanied by a strong increase in the hole mobilities while decreasing the temperature. The material bandgap extracted from the Hall measurements is about 30 meV, corresponding to that mentioned in the literature. Samples grown on GaAs(111)A behave similarly to those developed on GaAs(001), but have a larger bandgap due to residual compressive stress in the layers. All these observations are considered as a demonstration of the topological insulator behaviour of BiSb films.

Perspectives

Building up on the work summarised in previous section, let us conclude this dissertation by indicating certain possible paths for future researches which may emerge from the work presented here.

Characterisations

Several immediate questions of interest emerge from our work. The first is to measure the electronic band structure of the BiSb film using Angle-Resolved photoemission spectroscopy (ARPES) in order to observe the gapless surface states within the bulk bandgap. These measurements allow to map and count the number of Dirac cones at the surface and thus to identify the topological insulator behaviour. A recent study [31] predicted that that the number of Dirac cones may vary depending on many factors such as Sb composition and BiSb film thickness, but no experiments confirm this. It

is therefore interesting to prove or invalidate this proposition using ARPES experiments. One can also explore the effect of the Sb composition on the electronic transport of BiSb thin films by adopting the same strategy as that used in Chapter 6. This would allow to map the entire BiSb TI range. It would also be interesting to probe the topological protection of the surface states against disorder by performing STM measurements. The production of LDOS maps (local density of state) by tunnel effect spectroscopy makes it possible to analyse the scattering between surface states and surface defects. These defects can be vacancies, atomic steps naturally present on the surface, or intentionally created defects (for example atoms deposited on the surface), which will create surface scattering. Trivial electronic surface states will interact and leave a signature on the LDOS maps. Regarding the topological states, these states are protected, and they should not interact and thus leave no trace. Indeed, these states exhibit helical spin-momentum locking i.e the spin orientation is locked perpendicular to the carrier propagation ($\vec{k}$) direction. This means that the defects (i.e magnetic defects) causing the scattering (change in $\vec{k}$ direction) must also change the spin orientation (to maintain a spin-momentum locking of 90°).

Heterostructure of topological insulator with a superconductor material

Majorana bound states are of great interest since they are identical to their own antiparticles. Realising a localised pair of these states separated from each other can unlock new applications in the quantum computing field [142]. A BiSb TI in contact with a superconductor shows promises for hosting and protecting these states and thus building extremely robust quantum bits (Qubits) [143]. After optimising the surface morphology of BiSb films in Chapter 4 and 5, it is time to check the feasibility of quantum Qubits by coupling a BiSb layer($\sim$ 300 nm) with an Aluminium (Al) one ($\sim$ 10 nm). Since our MBE system contains an Al cell, it would be interesting to grow the Al layer directly on top of the BiSb one. After growth, these layers will be patterned by lithography to design our TI/superconductor device, as shown in Figure 6.7. Note that the Al bar must be implemented on the central part of the BiSb in order to separate the MZM pair [144]. In order to study the presence of Majorana zero modes (MZM) states at the TI/superconductor interface, transport measurements should be performed. The MZM signatures could be observed by applying an external magnetic field which will lead to "zero-bias conductances anomalies" [142]. We expect to measure then a half-integer longitudinal conductance plateau at low temperature, which is

considered as the signature of single Majorana edge modes [144].

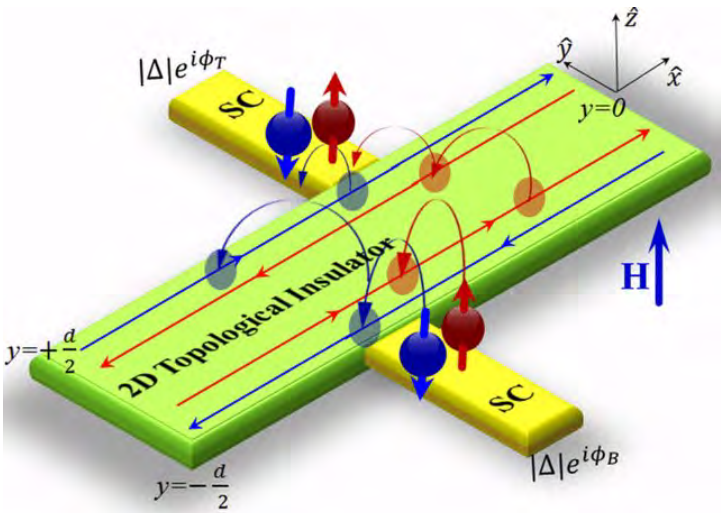

Figure 6.7: *Schematic structure of a 2D topological insulator material coupled to a superconductor [145].*

Heterostructure of topological insulator with a ferromagnetic material

Another potential application of our work relies on the possibility of creating spin-orbit torques (SOT) at the TI surface, which is particularly interesting for the realisation of magneto-resistive random access memories (MRAMs). Contrary to spin-transfer torque (STT) switching, SOT switching does not cost much energy and can thus lead to an ultralow power MRAM. For this, it is necessary to have a pure spin current with a large spin Hall angle ($\theta > 1$ and a high electrical conductivity ($\sigma > 10^5\ \Omega^{-1}m^{-1}$) [14].

Figure 6.8 show the schematic structure of the SOT-MRAM and STT-MRAM devices. Both cases are based on the use of a magnetic tunnel junction (MTJ) consisting of two ferromagnetic layer separated by a thin insulating layer. One of the ferromagnetic layers is called the reference layer or fixed layer due to its fixed magnetisation. The second one, called the recording layer or free layer, stores the binary bits in its magnetisation direction. A "0" code is displayed when the resistance of the MTJ is high due the antiparallel magnetisation of these two layers. Otherwise, a "1" code is displayed when the resistance is low due to the parallel magnetisation of the ferromagnetic layers. This effect is known as "tunnel magnetoresistance" and is used for read operation. The writing operation is based on switching the recording

layer magnetisation, which can be caused by STT or SOT. The difference between these two is that STT has only one path for reading and writing, while SOT has two different paths allowing separate optimisation for read and write operations [146]. Moreover, the STT injects a spin-polarised current through the reference layer in order to induce a spin current and thereby switch the recording layer magnetisation. This phenomena costs energy and the amount of spin current generated is limited to the charge current injected [14]. However, in the case of SOT, the use of a topological insulator layer coupled to the recording layer reduces the power cost and thus leads to an ultralow power MRAM. The spin current is simply generated in the topological insulator layer when a current passes through it, which produces a spin torque in the recording layer.

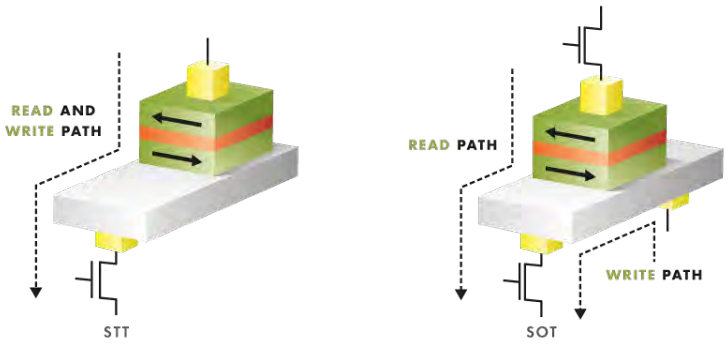

Figure 6.8: *Schematic structure of the STT-MRAM (the left figure) and the SOT-MRAM (the right figure), respectively [147].*

$Bi_{1-x}Sb_x$ TI material has great potential in realising SOT-MRAM devices due to high electrical conductivity and the colossal spin Hall angle ($\theta_{SH} \approx 52°$) [14]. Combining a BiSb TI thin film to a ferromagnetic material having a magnetic moment perpendicular to the interface is considered to be the key to producing faster and scalable MRAMs. A first step to verify the possibility of realising a SOT-MRAM consists in studying the influence of a current flowing in BiSb on the ferromagnetic layer in contact [14]. For this reason, we seek to fabricate a bilayer of BiSb($\sim$ 30 nm)/Co($\sim$ 10 nm) on GaAs(001) or GaAs(111)A substrates, and then pattern it into a Hall bar. An in-plane current flow will be applied inside the BiSb layer. At this point, we will study the effect of a perpendicular external magnetic field (B) on the magnetoresistance of the system. For reference, the temperature dependence of the resistance R_0 will be measured at zero magnetic field ($B = 0$). Then the evolution of the resistance ($\Delta R = R - R_0$) with respect to R_0 will be plotted as a function of the external magnetic field at different temperatures. We expect to obtain a large variation of $\Delta R/R_0$ at low temperature due

to metallic surface states while a negligible variation is expected once the semiconductor bulk behaviour is dominant.

Homojunction topological insulator

One more direction of research that could emerge from our results is to create a homojunction device based on the BiSb material by applying a strain in one of these junctions. Recent studies [148] have shown that the strain can cause a topological phase transition in addition to the change of the bulk bandgap width. It can adjust the band topology by inducing a gap at the Dirac point or by causing a gapless surface state. As a result, the number of Dirac cones can be controlled and a transition from a non-trivial topological insulator to a trivial topological insulator can occur and vice versa. We therefore expect that the introduction of a stress in one layer of the junction may lead to a change in the engineering of the bulk and surface electronic band structure of the other junction.

Bibliography

[1] M. Bellis, "The History of the Transistor." https://www.thoughtco.com/the-history-of-the-transistor-1992547.

[2] C. L. Kane and E. J. Mele, "Z 2 topological order and the quantum spin hall effect," *Physical review letters*, vol. 95, no. 14, p. 146802, 2005.

[3] J. E. Moore, "The birth of topological insulators," *Nature*, vol. 464, no. 7286, pp. 194–198, 2010.

[4] S. Tang and M. S. Dresselhaus, "Electronic properties of nanostructured bismuth-antimony materials," *Journal of Materials Chemistry C*, vol. 2, no. 24, pp. 4710–4726, 2014.

[5] D. Hsieh, Y. Xia, L. Wray, D. Qian, A. Pal, J. Dil, J. Osterwalder, F. Meier, G. Bihlmayer, C. Kane, *et al.*, "Observation of unconventional quantum spin textures in topological insulators," *Science*, vol. 323, no. 5916, pp. 919–922, 2009.

[6] S. M. Young, S. Chowdhury, E. J. Walter, E. J. Mele, C. L. Kane, and A. M. Rappe, "Theoretical investigation of the evolution of the topological phase of bi 2 se 3 under mechanical strain," *Physical Review B*, vol. 84, no. 8, p. 085106, 2011.

[7] M. Z. Hasan and C. L. Kane, "Colloquium: topological insulators," *Reviews of modern physics*, vol. 82, no. 4, p. 3045, 2010.

[8] H.-Y. Hui, J. D. Sau, and S. D. Sarma, "Bulk disorder in the superconductor affects proximity-induced topological superconductivity," *Physical Review B*, vol. 92, no. 17, p. 174512, 2015.

[9] H.-Y. Hui, J. D. Sau, and S. D. Sarma, "Disorder-induced subgap states and majorana zero-energy edge modes in two-dimensional topological insulator-superconductor hybrid structures," *Physical Review B*, vol. 90, no. 17, p. 174206, 2014.

[10] W. Yu, C.-Y. Niu, Z. Zhu, X. Cai, L. Zhang, S. Bai, R. Zhao, and Y. Jia, "Strain induced quantum spin hall insulator in monolayer β-bisb from first-principles study," *RSC advances*, vol. 7, no. 44, pp. 27816–27822, 2017.

[11] S. Singh and A. H. Romero, "Giant tunable rashba spin splitting in a two-dimensional bisb monolayer and in bisb/aln heterostructures," *Physical Review B*, vol. 95, no. 16, p. 165444, 2017.

[12] O. Breunig and Y. Ando, "Opportunities in topological insulator devices," *Nature Reviews Physics*, pp. 1–10, 2021.

[13] A. Mellnik, J. Lee, A. Richardella, J. Grab, P. Mintun, M. H. Fischer, A. Vaezi, A. Manchon, E.-A. Kim, N. Samarth, *et al.*, "Spin-transfer torque generated by a topological insulator," *Nature*, vol. 511, no. 7510, pp. 449–451, 2014.

[14] N. H. D. Khang, Y. Ueda, and P. N. Hai, "A conductive topological insulator with large spin hall effect for ultralow power spin–orbit torque switching," *Nature materials*, vol. 17, no. 9, pp. 808–813, 2018.

[15] B. Volkov and O. Pankratov, "Two-dimensional massless electrons in an inverted contact," *Soviet Journal of Experimental and Theoretical Physics Letters*, vol. 42, p. 178, 1985.

[16] O. Pankratov, S. Pakhomov, and B. Volkov, "Supersymmetry in heterojunctions: Band-inverting contact on the basis of pb1xsnxte and hg1 xcdxte," *Solid state communications*, vol. 61, no. 2, pp. 93–96, 1987.

[17] B. A. Bernevig, T. L. Hughes, and S.-C. Zhang, "Quantum spin hall effect and topological phase transition in hgte quantum wells," *science*, vol. 314, no. 5806, pp. 1757–1761, 2006.

[18] M. König, S. Wiedmann, C. Brüne, A. Roth, H. Buhmann, L. W. Molenkamp, X.-L. Qi, and S.-C. Zhang, "Quantum spin hall insulator state in hgte quantum wells," *Science*, vol. 318, no. 5851, pp. 766–770, 2007.

[19] L. Fu and C. L. Kane, "Topological insulators with inversion symmetry," *Physical Review B*, vol. 76, no. 4, p. 045302, 2007.

[20] L. Fu, C. L. Kane, and E. J. Mele, "Topological insulators in three dimensions," *Physical review letters*, vol. 98, no. 10, p. 106803, 2007.

[21] P. Roushan, J. Seo, C. V. Parker, Y. S. Hor, D. Hsieh, D. Qian, A. Richardella, M. Z. Hasan, R. J. Cava, and A. Yazdani, "Topological surface states protected from backscattering by chiral spin texture," *Nature*, vol. 460, no. 7259, pp. 1106–1109, 2009.

[22] J. A. Hagmann, "Chalcogenide topological insulators," in *Chalcogenide*, pp. 305–337, Elsevier, 2020.

[23] D. Hsieh, D. Qian, L. Wray, Y. Xia, Y. S. Hor, R. J. Cava, and M. Z. Hasan, "A topological dirac insulator in a quantum spin hall phase," *Nature*, vol. 452, no. 7190, pp. 970–974, 2008.

[24] Y. Feutelais, G. Morgant, J. Didry, and J. Schnitter, "Thermodynamic evaluation of the system bismuth-antimony," *Calphad*, vol. 16, no. 2, pp. 111–119, 1992.

[25] J. Dismukes, R. Paff, R. Smith, and R. Ulmer, "Lattice parameter and density in bismuth-antimony alloys," *Journal of Chemical & Engineering Data*, vol. 13, no. 3, pp. 317–320, 1968.

[26] Y. Liu and R. E. Allen, "Electronic structure of the semimetals bi and sb," *Physical Review B*, vol. 52, no. 3, p. 1566, 1995.

[27] Y.-H. Su, W. Shi, C. Felser, and Y. Sun, "Topological weyl semimetals in bi 1- x sb x alloys," *Physical Review B*, vol. 97, no. 15, p. 155431, 2018.

[28] H.-J. Zhang, C.-X. Liu, X.-L. Qi, X.-Y. Deng, X. Dai, S.-C. Zhang, and Z. Fang, "Electronic structures and surface states of the topological insulator bi 1- x sb x," *Physical Review B*, vol. 80, no. 8, p. 085307, 2009.

[29] B. Lenoir, A. Demouge, D. Perrin, H. Scherrer, S. Scherrer, M. Cassart, and J.-P. Michenaud, "Growth of bi1- xsbx alloys by the traveling heater method," *Journal of Physics and Chemistry of Solids*, vol. 56, no. 1, pp. 99–105, 1995.

[30] X.-G. Zhu, M. Stensgaard, L. Barreto, W. S. e Silva, S. Ulstrup, M. Michiardi, M. Bianchi, M. Dendzik, and P. Hofmann, "Three dirac points on the (110) surface of the topological insulator bi1- xsbx," *New Journal of Physics*, vol. 15, no. 10, p. 103011, 2013.

[31] S. Tang and M. S. Dresselhaus, "Constructing a large variety of dirac-cone materials in the bi 1- x sb x thin film system," *Nanoscale*, vol. 4, no. 24, pp. 7786–7790, 2012.

[32] S. Tang and M. S. Dresselhaus, "Constructing anisotropic single-dirac-cones in bi1–x sb x thin films," *Nano letters*, vol. 12, no. 4, pp. 2021–2026, 2012.

[33] Y. Xu, I. Miotkowski, C. Liu, J. Tian, H. Nam, N. Alidoust, J. Hu, C.-K. Shih, M. Z. Hasan, and Y. P. Chen, "Observation of topological surface state quantum hall effect in an intrinsic three-dimensional topological insulator," *Nature Physics*, vol. 10, no. 12, pp. 956–963, 2014.

[34] D. Shin, Y. Lee, M. Sasaki, Y. H. Jeong, F. Weickert, J. B. Betts, H.-J. Kim, K.-S. Kim, and J. Kim, "Violation of ohm's law in a weyl metal," *Nature materials*, vol. 16, no. 11, pp. 1096–1099, 2017.

[35] H. Zhang, C.-X. Liu, X.-L. Qi, X. Dai, Z. Fang, and S.-C. Zhang, "Topological insulators in bi 2 se 3, bi 2 te 3 and sb 2 te 3 with a single dirac cone on the surface," *Nature physics*, vol. 5, no. 6, pp. 438–442, 2009.

[36] A. Isaeva, B. Rasche, and M. Ruck, "Bismuth-based candidates for topological insulators: Chemistry beyond bi2te3," *physica status solidi (RRL)–Rapid Research Letters*, vol. 7, no. 1-2, pp. 39–49, 2013.

[37] D.-X. Qu, Y. S. Hor, J. Xiong, R. J. Cava, and N. P. Ong, "Quantum oscillations and hall anomaly of surface states in the topological insulator bi2te3," *Science*, vol. 329, no. 5993, pp. 821–824, 2010.

[38] Y. Chen, J. G. Analytis, J.-H. Chu, Z. Liu, S.-K. Mo, X.-L. Qi, H. Zhang, D. Lu, X. Dai, Z. Fang, *et al.*, "Experimental realization of a three-dimensional topological insulator, bi2te3," *science*, vol. 325, no. 5937, pp. 178–181, 2009.

[39] M. Neupane, S.-Y. Xu, L. A. Wray, A. Petersen, R. Shankar, N. Alidoust, C. Liu, A. Fedorov, H. Ji, J. M. Allred, *et al.*, "Topological surface states and dirac point tuning in ternary topological insulators," *Physical Review B*, vol. 85, no. 23, p. 235406, 2012.

[40] Z. Alpichshev, J. Analytis, J.-H. Chu, I. R. Fisher, Y. Chen, Z.-X. Shen, A. Fang, and A. Kapitulnik, "Stm imaging of electronic waves on the surface of bi 2 te 3: topologically protected surface states and hexagonal warping effects," *Physical review letters*, vol. 104, no. 1, p. 016401, 2010.

[41] O. Caha, A. Dubroka, J. Humlicek, V. Holy, H. Steiner, M. Ul-Hassan, J. Sanchez-Barriga, O. Rader, T. Stanislavchuk, A. A. Sirenko, *et al.*,

"Growth, structure, and electronic properties of epitaxial bismuth telluride topological insulator films on baf2 (111) substrates," *Crystal growth & design*, vol. 13, no. 8, pp. 3365–3373, 2013.

[42] G. R. Hyde, H. Beale, I. Spain, and J. A. Woollam, "Electronic properties of bi2se3 crystals," *Journal of Physics and Chemistry of Solids*, vol. 35, no. 12, pp. 1719–1728, 1974.

[43] Y. Xia, D. Qian, D. Hsieh, L. Wray, A. Pal, H. Lin, A. Bansil, D. Grauer, Y. S. Hor, R. J. Cava, *et al.*, "Observation of a large-gap topological-insulator class with a single dirac cone on the surface," *Nature physics*, vol. 5, no. 6, pp. 398–402, 2009.

[44] V. Greanya, W. Tonjes, R. Liu, C. Olson, D.-Y. Chung, and M. Kanatzidis, "Determination of the valence band dispersions for bi 2 se 3 using angle resolved photoemission," *Journal of applied physics*, vol. 92, no. 11, pp. 6658–6661, 2002.

[45] P. Larson, V. Greanya, W. Tonjes, R. Liu, S. Mahanti, and C. Olson, "Electronic structure of bi 2 x 3 (x= s, se, t) compounds: Comparison of theoretical calculations with photoemission studies," *Physical review B*, vol. 65, no. 8, p. 085108, 2002.

[46] S. Mishra, S. Satpathy, and O. Jepsen, "Electronic structure and thermoelectric properties of bismuth telluride and bismuth selenide," *Journal of Physics: Condensed Matter*, vol. 9, no. 2, p. 461, 1997.

[47] E. Mooser and W. Pearson, "New semiconducting compounds," *Physical Review*, vol. 101, no. 1, p. 492, 1956.

[48] J. Black, E. Conwell, L. Seigle, and C. Spencer, "Electrical and optical properties of some m2v- bn3vi- b semiconductors," *Journal of Physics and Chemistry of Solids*, vol. 2, no. 3, pp. 240–251, 1957.

[49] D. Kim, S. Cho, N. P. Butch, P. Syers, K. Kirshenbaum, S. Adam, J. Paglione, and M. S. Fuhrer, "Surface conduction of topological dirac electrons in bulk insulating bi 2 se 3," *Nature Physics*, vol. 8, no. 6, pp. 459–463, 2012.

[50] X. He, T. Guan, X. Wang, B. Feng, P. Cheng, L. Chen, Y. Li, and K. Wu, "Highly tunable electron transport in epitaxial topological insulator (bi1-x sb x) 2te3 thin films," *Applied Physics Letters*, vol. 101, no. 12, p. 123111, 2012.

[51] D. Kong, Y. Chen, J. J. Cha, Q. Zhang, J. G. Analytis, K. Lai, Z. Liu, S. S. Hong, K. J. Koski, S.-K. Mo, *et al.*, "Ambipolar field effect in the ternary topological insulator (bi x sb 1–x) 2 te 3 by composition tuning," *Nature nanotechnology*, vol. 6, no. 11, pp. 705–709, 2011.

[52] J. Zhang, C.-Z. Chang, Z. Zhang, J. Wen, X. Feng, K. Li, M. Liu, K. He, L. Wang, X. Chen, *et al.*, "Band structure engineering in (bi 1-x sb x) 2 te 3 ternary topological insulators," *Nature communications*, vol. 2, no. 1, pp. 1–6, 2011.

[53] Z. Ren, A. Taskin, S. Sasaki, K. Segawa, and Y. Ando, "Large bulk resistivity and surface quantum oscillations in the topological insulator bi 2 te 2 se," *Physical Review B*, vol. 82, no. 24, p. 241306, 2010.

[54] J. Xiong, A. C. Petersen, D. Qu, Y. S. Hor, R. J. Cava, and N. P. Ong, "Quantum oscillations in a topological insulator bi2te2se with large bulk resistivity (6ωcm)," *Physica E: Low-dimensional Systems and Nanostructures*, vol. 44, no. 5, pp. 917–920, 2012.

[55] S.-Y. Xu, L. Wray, Y. Xia, R. Shankar, A. Petersen, A. Fedorov, H. Lin, A. Bansil, Y. Hor, D. Grauer, *et al.*, "Discovery of several large families of topological insulator classes with backscattering-suppressed spin-polarized single-dirac-cone on the surface," *arXiv preprint arXiv:1007.5111*, 2010.

[56] Z. Ren, A. Taskin, S. Sasaki, K. Segawa, and Y. Ando, "Optimizing bi 2- x sb x te 3- y se y solid solutions to approach the intrinsic topological insulator regime," *Physical Review B*, vol. 84, no. 16, p. 165311, 2011.

[57] H. Lohani, P. Mishra, A. Banerjee, K. Majhi, R. Ganesan, U. Manju, D. Topwal, P. A. Kumar, and B. Sekhar, "Band structure of topological insulator bisbte 1.25 se 1.75," *Scientific reports*, vol. 7, no. 1, pp. 1–10, 2017.

[58] G. Kozhemyakin and S. Zayakin, "Magnetoresistance in doped bi0. 85sb0. 15 single crystals," *Journal of Applied Physics*, vol. 122, no. 20, p. 205102, 2017.

[59] M. J. Rost, L. Jacobse, and M. Koper, "The dualism between adatom- and vacancy-based single crystal growth models," *Nature communications*, vol. 10, no. 1, pp. 1–7, 2019.

[60] G. Stringfellow, "Thermodynamic and kinetic aspects of iii/v epitaxy," tech. rep., UTAH UNIV SALT LAKE CITY DEPT OF MATERIALS SCIENCE AND ENGINEERING, 1992.

[61] K. A. Lozovoy, A. G. Korotaev, A. P. Kokhanenko, V. V. Dirko, and A. V. Voitsekhovskii, "Kinetics of epitaxial formation of nanostructures by frank–van der merwe, volmer–weber and stranski–krastanow growth modes," *Surface and Coatings Technology*, vol. 384, p. 125289, 2020.

[62] S. Jain, A. Harker, and R. Cowley, "Misfit strain and misfit dislocations in lattice mismatched epitaxial layers and other systems," *Philosophical Magazine A*, vol. 75, no. 6, pp. 1461–1515, 1997.

[63] D. Pashley, "Epitaxy growth mechanisms," *Materials science and technology*, vol. 15, no. 1, pp. 2–8, 1999.

[64] C. V. Thompson, "Stress evolution during volmer-weber growth of thin films," *p. Dept. of Materials Science and Engineering, Massac*, 2005.

[65] A. S. Tanushree Nagori, "Doubtnut ." https://www.doubtnut.com/question-answer-chemistry.

[66] G. Rosenfeld, B. Poelsema, and G. Comsa, "Growth and properties of ultrathin epitaxial layers," *The Chemical Physics of Solids Surfaces*, vol. 8, p. 66, 1999.

[67] M. David and D. Connétable, "Diffusion of interstitials in metallic systems, illustration of a complex study case: aluminum," *Journal of Physics: Condensed Matter*, vol. 29, no. 45, p. 455703, 2017.

[68] M. Trochet, L. K. Béland, J.-F. Joly, P. Brommer, and N. Mousseau, "Diffusion of point defects in crystalline silicon using the kinetic activation-relaxation technique method," *Physical Review B*, vol. 91, no. 22, p. 224106, 2015.

[69] L. K. Béland, P. Brommer, F. El-Mellouhi, J.-F. Joly, and N. Mousseau, "Kinetic activation-relaxation technique," *Physical Review E*, vol. 84, no. 4, p. 046704, 2011.

[70] L. J. Schowalter, "Heteroepitaxy and strain: applications to electronic and optoelectronic materials," *MRS Bulletin*, vol. 21, no. 4, pp. 18–20, 1996.

[71] K. Oura, M. Katayama, A. Zotov, V. Lifshits, and A. Saranin, "Structural defects at surfaces," in *Surface Science*, pp. 229–260, Springer, 2003.

[72] DBpedia, "About: Terrace ledge kink model." https://dbpedia.org/page/Terrace_ledge_kink_model.

[73] S. Blanc, *Matériaux III-V épitaxies sur substrats GaAs (111) pour structures laser émettant au-delà du micromètre*. PhD thesis, Toulouse 3, 2002.

[74] A. Cullis, "Strain-induced modulations in the surface morphology of heteroepitaxial layers," *Mrs Bulletin*, vol. 21, no. 4, pp. 21–26, 1996.

[75] J. Asare, B. Agyei-Tuffour, E. A. Amonoo, D. Dodoo-Arhin, E. Nyankson, B. Mensah, O. O. Oyewole, A. Yaya, and B. Onwona-Agyeman, "Effects of substrates on the performance of optoelectronic devices: A review," *Cogent Engineering*, vol. 7, no. 1, p. 1829274, 2020.

[76] I. universitywafer, "Indium Phosphide Substrates for research and production." https://www.universitywafer.com/indium-phosphide-inp.html.

[77] A. Kley, P. Ruggerone, and M. Scheffler, "Novel diffusion mechanism on the gaas (001) surface: the role of adatom-dimer interaction," *Physical review letters*, vol. 79, no. 26, p. 5278, 1997.

[78] A. Ohtake, "Surface reconstructions on gaas(001)," *Surface Science Reports*, vol. 63, no. 7, pp. 295–327, 2008.

[79] Q. Xue, T. Hashizume, J. Zhou, T. Sakata, T. Ohno, and T. Sakurai, "Structures of the ga-rich 4× 2 and 4× 6 reconstructions of the gaas (001) surface," *Physical review letters*, vol. 74, no. 16, p. 3177, 1995.

[80] A. Ohtake, M. Ozeki, T. Yasuda, and T. Hanada, "Atomic structure of the gaas (001)-(2× 4) surface under as flux," *Physical Review B*, vol. 65, no. 16, p. 165315, 2002.

[81] H. Farrell and C. Palmstro/m, "Reflection high energy electron diffraction characteristic absences in gaas (100)(2× 4)–as: A tool for determining the surface stoichiometry," *Journal of Vacuum Science & Technology B: Microelectronics Processing and Phenomena*, vol. 8, no. 4, pp. 903–907, 1990.

[82] V. P. LaBella, M. R. Krause, Z. Ding, and P. M. Thibado, "Arsenic-rich gaas (0 0 1) surface structure," *Surface science reports*, vol. 60, no. 1-4, pp. 1–53, 2005.

[83] E. Penev, P. Kratzer, and M. Scheffler, "Atomic structure of the g a a s (001)- c (4× 4) surface: First-principles evidence for diversity of heterodimer motifs," *Physical review letters*, vol. 93, no. 14, p. 146102, 2004.

[84] A. Ohtake, P. Kocán, J. Nakamura, A. Natori, and N. Koguchi, "Kinetics in surface reconstructions on gaas (001)," *Physical review letters*, vol. 92, no. 23, p. 236105, 2004.

[85] D. Chadi, C. Tanner, and J. Ihm, "Theoretical study of the atomic and electronic structure of the c-4x4 reconstructed gaas (100) surface," *Surface Science Letters*, vol. 120, no. 1, pp. L425–L430, 1982.

[86] K. Haberern and M. Pashley, "Gaas (111) a-(2× 2) reconstruction studied by scanning tunneling microscopy," *Physical Review B*, vol. 41, no. 5, p. 3226, 1990.

[87] D. Woolf, D. Westwood, and R. Williams, "Surface reconstructions of gaas (111) a and (111) b: A static surface phase study by reflection high-energy electron diffraction," *Applied physics letters*, vol. 62, no. 12, pp. 1370–1372, 1993.

[88] J. Thornton, P. Unsworth, M. Jackson, P. Weightman, and D. Woolf, "Existence of ga-vacancy and as-trimer induced (2× 2) phases on the gaas (111) a surface," *Surface science*, vol. 316, no. 3, pp. 231–237, 1994.

[89] E. Kaxiras, K. Pandey, Y. Bar-Yam, and J. D. Joannopoulos, "Role of chemical potentials in surface reconstruction: A new model and phase transition of gaas (111) 2x2," *Physical review letters*, vol. 56, no. 26, p. 2819, 1986.

[90] D. Chadi, "Vacancy-induced 2× 2 reconstruction of the ga (111) surface of gaas," *Physical review letters*, vol. 52, no. 21, p. 1911, 1984.

[91] C. Freysoldt, B. Grabowski, T. Hickel, J. Neugebauer, G. Kresse, A. Janotti, and C. G. Van de Walle, "First-principles calculations for point defects in solids," *Reviews of modern physics*, vol. 86, no. 1, p. 253, 2014.

[92] J. Dai, D. West, X. Wang, Y. Wang, D. Kwok, S.-W. Cheong, S. Zhang, and W. Wu, "Toward the intrinsic limit of the topological insulator bi 2 se 3," *Physical review letters*, vol. 117, no. 10, p. 106401, 2016.

[93] Y. Ando, "Topological insulator materials," *Journal of the Physical Society of Japan*, vol. 82, no. 10, p. 102001, 2013.

[94] M. Brahlek, J. Lapano, and J. S. Lee, "Topological materials by molecular beam epitaxy," *Journal of Applied Physics*, vol. 128, no. 21, p. 210902, 2020.

[95] J. Arthur Jr, "Interaction of ga and as2 molecular beams with gaas surfaces," *Journal of Applied Physics*, vol. 39, no. 8, pp. 4032–4034, 1968.

[96] J. G. Speight, *Lange's handbook of chemistry*. McGraw-Hill Education, 2017.

[97] W. Braun, H. Möller, and Y.-H. Zhang, "Reflection high-energy electron diffraction during substrate rotation: A new dimension for in situ characterization," *Journal of Vacuum Science & Technology B: Microelectronics and Nanometer Structures Processing, Measurement, and Phenomena*, vol. 16, no. 3, pp. 1507–1510, 1998.

[98] J. Floro, E. Chason, S. Lee, R. Twesten, R. Hwang, and L. Freund, "Real-time stress evolution during si 1-x ge x heteroepitaxy: Dislocations, islanding, and segregation," *Journal of Electronic Materials*, vol. 26, no. 9, pp. 969–979, 1997.

[99] E. Chason and P. R. Guduru, "Tutorial: Understanding residual stress in polycrystalline thin films through real-time measurements and physical models," *Journal of Applied Physics*, vol. 119, no. 19, p. 191101, 2016.

[100] A. Arnoult and J. Colin, "Magnification inferred curvature for real-time curvature monitoring," *Scientific Reports*, vol. 11, no. 1, pp. 1–11, 2021.

[101] SciMed, "A Brief Introduction to SEM (Scanning Electron Microscopy)." https://www.scimed.co.uk/education/sem-scanning-electron-microscopy/.

[102] F. B. J. Bradbury, Savile and D. C. Joy, "Transmission electron microscope." Encyclopedia Britannica, October 10, 2022. https://www.britannica.com/technology/transmission-electron-microscope.

[103] T. Güner, *Entropic tunneling time and its applications*. PhD thesis, Izmir Institute of Technology (Turkey), 2014.

[104] NuNano, "Common Imaging Problems (and how to fix them)." November 25, 2020. https://www.nunano.com/blog/2020/11/23/4-common-imaging-problems-and-how-to-fix-them.

[105] G. F. Harrington and J. Santiso, "Back-to-basics tutorial: X-ray diffraction of thin films," *Journal of Electroceramics*, pp. 1–23, 2021.

[106] M. Dede, *Development of nano hall sensors for high resolution scanning hall probe microscopy*. PhD thesis, Bilkent Universitesi (Turkey), 2008.

[107] K. Yao, N. H. D. Khang, and P. N. Hai, "Influence of crystal orientation and surface termination on the growth of bisb thin films on gaas substrates," *Journal of Crystal Growth*, vol. 511, pp. 99–105, 2019.

[108] C. Detavernier, A. Özcan, J. Jordan-Sweet, E. Stach, J. Tersoff, F. Ross, and C. Lavoie, "An off-normal fibre-like texture in thin films on single-crystal substrates," *Nature*, vol. 426, no. 6967, pp. 641–645, 2003.

[109] P. Giannozzi, S. Baroni, N. Bonini, M. Calandra, R. Car, C. Cavazzoni, D. Ceresoli, G. L. Chiarotti, M. Cococcioni, I. Dabo, A. D. Corso, S. de Gironcoli, S. Fabris, G. Fratesi, R. Gebauer, U. Gerstmann, C. Gougoussis, A. Kokalj, M. Lazzeri, L. Martin-Samos, N. Marzari, F. Mauri, R. Mazzarello, S. Paolini, A. Pasquarello, L. Paulatto, C. Sbraccia, S. Scandolo, G. Sclauzero, A. P. Seitsonen, A. Smogunov, P. Umari, and R. M. Wentzcovitch, "QUANTUM ESPRESSO: a modular and open-source software project for quantum simulations of materials," *Journal of Physics: Condensed Matter*, vol. 21, p. 395502, sep 2009.

[110] P. E. Blöchl, "Projector augmented-wave method," *Phys. Rev. B*, vol. 50, pp. 17953–17979, Dec 1994.

[111] J. P. Perdew, K. Burke, and M. Ernzerhof, "Generalized gradient approximation made simple," *Physical review letters*, vol. 77, no. 18, p. 3865, 1996.

[112] G. Henkelman, G. Jóhannesson, and H. Jónsson, "Methods for finding saddle points and minimum energy paths," in *Theoretical methods in condensed phase chemistry*, pp. 269–302, Springer, 2002.

[113] G. Henkelman, B. P. Uberuaga, and H. Jónsson, "A climbing image nudged elastic band method for finding saddle points and minimum energy paths," *The Journal of chemical physics*, vol. 113, no. 22, pp. 9901–9904, 2000.

[114] A. Jay, C. Huet, N. Salles, M. Gunde, L. Martin-Samos, N. Richard, G. Landa, V. Goiffon, S. De Gironcoli, A. Hémeryck, *et al.*, "Finding reaction pathways and transition states: r-artn and d-artn as an efficient and versatile alternative to string approaches," *Journal of Chemical Theory and Computation*, vol. 16, no. 10, pp. 6726–6734, 2020.

[115] A. Jay, M. Gunde, N. Salles, M. Poberžnik, L. Martin-Samos, N. Richard, S. de Gironcoli, N. Mousseau, and A. Hémeryck, "Activation–relaxation technique: An efficient way to find minima and saddle points of potential energy surfaces," *Computational Materials Science*, vol. 209, p. 111363, 2022.

[116] G. Henkelman, A. Arnaldsson, and H. Jónsson, "A fast and robust algorithm for bader decomposition of charge density," *Computational Materials Science*, vol. 36, no. 3, pp. 354–360, 2006.

[117] D. Woolf, D. Westwood, and R. Williams, "The homoepitaxial growth of gaas (111) a and (111) b by molecular beam epitaxy: an investigation of the temperature-dependent surface reconstructions and bulk electrical conductivity transitions," *Semiconductor science and technology*, vol. 8, no. 6, p. 1075, 1993.

[118] C. Yu, H. Li, Y. Luo, L. Zhu, Z. Qian, and T. Zhou, "Thickness-dependent magnetic order and phase-transition dynamics in epitaxial fe-rich ferh thin films," *Physics Letters A*, vol. 383, no. 20, pp. 2424–2428, 2019.

[119] J. Colin, *Potentialités des techniques de caractérisation in-situ et en temps réel pour sonder, comprendre et contrôler les processus de nucléation-croissance durant le dépôt de films minces métalliques*. PhD thesis, 2015. Thèse de doctorat dirigée par Abadias, GrégoryMichel, Anny et Mastail, Cédric Milieux denses et matériaux Poitiers 2015.

[120] B. W. Sheldon, A. Rajamani, A. Bhandari, E. Chason, S. Hong, and R. Beresford, "Competition between tensile and compressive stress

mechanisms during volmer-weber growth of aluminum nitride films," *Journal of Applied Physics*, vol. 98, no. 4, p. 043509, 2005.

[121] A. Bhandari, B. W. Sheldon, and S. J. Hearne, "Competition between tensile and compressive stress creation during constrained thin film island coalescence," *Journal of Applied Physics*, vol. 101, no. 3, p. 033528, 2007.

[122] H. Okamoto, "Bi-sb (bismuth-antimony)," *Journal of Phase Equilibria and Diffusion*, vol. 33, no. 6, pp. 493–494, 2012.

[123] C. Tellier, A. Tosser, and C. Boutrit, "The mayadas-shatzkes conduction model treated as a fuchs-sondheimer model," *Thin Solid Films*, vol. 44, no. 2, pp. 201–208, 1977.

[124] K. Fuchs, "The conductivity of thin metallic films according to the electron theory of metals," *Mathematical Proceedings of the Cambridge Philosophical Society*, vol. 34, no. 1, p. 100–108, 1938.

[125] K. Fuchs, "Cambridge philos," *Soc*, vol. 34, p. 100, 1938.

[126] E. Osmic, J. Barzola-Quiquia, W. Böhlmann, P. Bercoff, L. Venosta, and P. Häussler, "Thermopower and magnetotransport properties of bi100- xsbx topological insulator thin films prepared by flash evaporation," *Journal of Physics and Chemistry of Solids*, p. 110734, 2022.

[127] A. Taskin and Y. Ando, "Quantum oscillations in a topological insulator bi 1- x sb x," *Physical Review B*, vol. 80, no. 8, p. 085303, 2009.

[128] B. Lenoir, A. Dauscher, M. Cassart, Y. I. Ravich, and H. Scherrer, "Effect of antimony content on the thermoelectric figure of merit of bi1- xsbx alloys," *Journal of Physics and Chemistry of Solids*, vol. 59, no. 1, pp. 129–134, 1998.

[129] H. M. Inoue, H. I. H. Iwamura, S. E. S. Endo, H. U. H. Uozaki, and N. T. N. Toyota, "Transport properties in inp/inalas type ii single heterostructure," *Japanese journal of applied physics*, vol. 36, no. 8B, p. L1085, 1997.

[130] C. Shekhar, S. Ouardi, A. K. Nayak, G. H. Fecher, W. Schnelle, and C. Felser, "Ultrahigh mobility and nonsaturating magnetoresistance in heusler topological insulators," *Physical Review B*, vol. 86, no. 15, p. 155314, 2012.

[131] D.-X. Qu, S. K. Roberts, and G. F. Chapline, "Observation of huge surface hole mobility in the topological insulator bi 0.91 sb 0.09 (111)," *Physical review letters*, vol. 111, no. 17, p. 176801, 2013.

[132] A. Mayadas, M. Shatzkes, and J. Janak, "Electrical resistivity model for polycrystalline films: the case of specular reflection at external surfaces," *Applied Physics Letters*, vol. 14, no. 11, pp. 345–347, 1969.

[133] G. Ding, C. Clavero, D. Schweigert, and M. Le, "Thickness and microstructure effects in the optical and electrical properties of silver thin films," *AIP advances*, vol. 5, no. 11, p. 117234, 2015.

[134] J. Dutta, R. Pal, S. Bhattacharyya, S. Chaudhuri, and A. Pal, "Studies on the grain boundary effect in polycrystalline cdte films using optical reflectance measurements," *Materials chemistry and physics*, vol. 36, no. 1-2, pp. 177–182, 1993.

[135] Y. Tokumoto, K. Sugimoto, Y. Hattori, and K. Edagawa, "Electronic transport properties of pb (bi1- x sb x) 2 (te1- y se y) 4 topological insulator," *Journal of Applied Physics*, vol. 131, no. 18, p. 185105, 2022.

[136] J. Novak, S. Hasenöhrl, M. Alonso, and M. Garriga, "Influence of tensile and compressive strain on the band gap energy of ordered ingap," *Applied Physics Letters*, vol. 79, no. 17, pp. 2758–2760, 2001.

[137] G. Olsen, C. Nuese, and R. Smith, "The effect of elastic strain on energy band gap and lattice parameter in iii-v compounds," *Journal of Applied Physics*, vol. 49, no. 11, pp. 5523–5529, 1978.

[138] C. Will, M. Elm, P. Klar, B. Landschreiber, E. Güneş, and S. Schlecht, "Effect of nanostructuring on the band structure and the galvanomagnetic properties in bi1- x sb x alloys," *Journal of Applied Physics*, vol. 114, no. 19, p. 193707, 2013.

[139] H. Kitagawa, H. Noguchi, T. Kiyabu, M. Itoh, and Y. Noda, "Thermoelectric properties of bi–sb semiconducting alloys prepared by quenching and annealing," *Journal of Physics and Chemistry of Solids*, vol. 65, no. 7, pp. 1223–1227, 2004.

[140] J.-H. Chen, C. Jang, S. Xiao, M. Ishigami, and M. S. Fuhrer, "Intrinsic and extrinsic performance limits of graphene devices on sio2," *Nature nanotechnology*, vol. 3, no. 4, pp. 206–209, 2008.

[141] S. Ouardi, G. H. Fecher, C. Felser, J. Hamrle, K. Postava, and J. Pištora, "Transport and optical properties of the gapless heusler compound ptysb," *Applied Physics Letters*, vol. 99, no. 21, p. 211904, 2011.

[142] V. Mourik, K. Zuo, S. M. Frolov, S. Plissard, E. P. Bakkers, and L. P. Kouwenhoven, "Signatures of majorana fermions in hybrid superconductor-semiconductor nanowire devices," *Science*, vol. 336, no. 6084, pp. 1003–1007, 2012.

[143] J. J. Cha, K. J. Koski, and Y. Cui, "Topological insulator nanostructures," *physica status solidi (RRL)–Rapid Research Letters*, vol. 7, no. 1-2, pp. 15–25, 2013.

[144] Q. L. He, L. Pan, A. L. Stern, E. C. Burks, X. Che, G. Yin, J. Wang, B. Lian, Q. Zhou, E. S. Choi, *et al.*, "Chiral majorana fermion modes in a quantum anomalous hall insulator–superconductor structure," *Science*, vol. 357, no. 6348, pp. 294–299, 2017.

[145] A. Zyuzin, M. Alidoust, J. Klinovaja, and D. Loss, "Supercurrent reversal in two-dimensional topological insulators," *Physical Review B*, vol. 92, no. 17, p. 174515, 2015.

[146] M. Imani, A. Rahimi, Y. Kim, and T. Rosing, "A low-power hybrid magnetic cache architecture exploiting narrow-width values," in *2016 5th Non-Volatile Memory Systems and Applications Symposium (NVMSA)*, pp. 1–6, IEEE, 2016.

[147] Antaios, "The SOT-MRAM Pioneer." https://antaios.fr/-SOT-MRAM-.

[148] H. Aramberri and M. Muñoz, "Strain-driven tunable topological states in bi2se3," *Journal of Physics: Materials*, vol. 1, no. 1, p. 015009, 2018.

Abstract

This thesis focuses on the growth and the structural and electrical characterisations of the BiSb topological insulator epitaxially integrated on GaAs(001) and GaAs(111)A. Topological insulators (TIs) are promising materials for new nanoelectronics and spintronics applications thanks to their unique physical properties. Bismuth-antimony alloy ($Bi_{1-x}Sb_x$) is the first reported 3D topological insulator (TI), and remains the most interesting one because its electronic band structure can be controlled by changing the stoichiometry, the thickness or the temperature. Contrary to hybrid semiconductor-superconductor devices, a $Bi_{1-x}Sb_x$ TI coupled to a superconductor material shows promise for harbouring and protecting Majorana bounds states against environment and thus building extremely robust quantum bits (Qubits). Moreover, the high electrical conductivity and the colossal spin Hall angle of this alloy are interesting for spintronics applications. The coupling of $Bi_{1-x}Sb_x$ TI to a ferromagnetic material induces an efficient transfert of spin-orbit torques (SOT) and thus allows the realisation of magnetoresistive random access memories (MRAM).

Integrating this material on an industrial substrate remains a challenge. Here, I investigate the growth, the structural and the electrical properties of BiSb materials epitaxially deposited on industrial GaAs(001) substrates. We report the influence of key growth parameters such as temperature, antimony composition, thickness and growth rate on the crystal quality. We manage to optimise the growth conditions while keeping the $Bi_{1-x}Sb_x$ composition within the TI range (between 7 and 22%). Despite large lattice mismatches and different crystalline matrices between the deposited material and the substrate, we successfully grow high-quality rhombohedral BiSb(0001) films on a cubic GaAs(001) substrate. We demonstrate a clear epitaxial relationship at the interface, a fully relaxed TI layer, and the growth of a rhombohedral matrix on top of the cubic substrate.

Continuing our study to improve the quality of $Bi_{1-x}Sb_x$ films, we integrate it on GaAs(111)A substrates, sharing a crystalline matrix close to that of $Bi_{1-x}Sb_x$. All influencing parameters such as substrate surface, growth

temperature, antimony composition, film thickness and growth rate are studied in order to optimise the layer quality. We report the influence of temperature and Sb composition on crystal growth and stress relaxation in the epitaxial film. For optimised growth conditions, the high-quality rhombohedral BiSb(0001) layer grows epitaxially on the hexagonal GaAs(111)A substrate with the in-plane epitaxial relationship of $[11\overline{2}]_{GaAs}$ parallel to $[1\overline{1}00]_{BiSb}$. A Volmer-Weber growth mode is detected during nucleation, which leads to the formation of a relaxed layer once a critical thickness is reached.

In both cases, electrical measurements highlight two channels transport, with a n-type semiconductor behaviour of the bulk at room temperature and metallic surface states at low temperature. For optimised growth conditions, the samples generates topologically protected surface states, while decreasing temperature below 55 K, which are manifested by a change of carrier type and by high holes mobilities.

Keywords: Topological Insulator; $Bi_{1-x}Sb_x$ alloys; epitaxy; industrial substrate; GaAs(001); GaAs(111)A.

Résumé

Cette thèse porte sur la croissance ainsi que les caractéristiques structurales et électriques de l'isolant topologique $Bi_{1-x}Sb_x$ épitaxialement intégré sur GaAs(001) et GaAs(111)A. Les isolants topologiques (IT) sont des matériaux d'avenir pour les filières nanoélectronique et spintronique du fait de leurs propriétés physiques uniques. Parmi eux, l'antimoniure de bismuth ($Bi_{1-x}Sb_x$) est le premier isolant topologique 3D à avoir été étudié, et reste le plus intéressant car sa structure de bande électronique peut être contrôlée en changeant sa stœchiométrie, son épaisseur ou la température.

Contrairement aux interfaces hybrides semiconducteurs/supraconducteurs qui souffrent de problèmes d'interface (toute impureté réduira le temps de cohérence des dispositifs dans ce telles structures); un IT couplé à un supraconducteur permet de protéger topologiquement les états quantiques de l'interface. Il est ainsi théoriquement possible d'y recréer des états d'excitation quantique ayant les mêmes propriétés que les fermions de Majorana et ainsi fabriquer des bits quantiques extrêmement robustes (Qubits). Par ailleurs, la conductivité électrique élevée et l'angle de spin Hall de l'alliage $Bi_{1-x}Sb_x$ le rendent également intéressant pour des applications en spintronique. Le couplage d'un IT avec un matériau ferromagnétique permet en effet de contrôler la "free layer" dans une mémoire vive magnétorésistive (MRAM) grâce aux spin-orbite torques (SOT).

L'intégration de ce matériau sur un substrat industriel reste un défi. Dans cette thèse, nous étudions la croissance, les propriétés structurales et électriques de alliages de BiSb épitaxiés sur des substrats industriels de GaAs(001). Nous mettons en évidence l'influence de paramètres de croissance tels que la température, la composition en antimoine, l'épaisseur et la vitesse de croissance sur la qualité du cristal. Nous parvenons à optimiser les conditions de croissance tout en maintenant la composition du $Bi_{1-x}Sb_x$ dans la gamme IT (entre 7 et 22%). Malgré une grande différence de paramètre de maille ainsi que différentes structures cristallines, nous avons intégré des couches minces de BiSb(0001) rhomboédriques sur substrat GaAs(001) cubique. Nous démontrons une relation épitaxiale à l'interface, une couche

de BiSb relaxée ainsi que la croissance d'une matrice quasi hexagonale sur substrat carré.

Poursuivant notre étude pour améliorer la qualité des films de $Bi_{1-x}Sb_x$, nous l'intégrons sur substrat GaAs(111)A, qui partage une matrice cristalline proche de celle de $Bi_{1-x}Sb_x$. La préparation de la surface du substrat, la température de croissance, la composition en antimoine, l'épaisseur du film et la vitesse de croissance sont étudiés afin d'optimiser la qualité de la couche IT. Pour des conditions de croissance optimisées, une couche BiSb(0001) rhomboédrique de haute qualité est épitaxiée sur le substrat GaAs(111)A. La relation épitaxiale à l'interface fait correspondre le plan $[11\overline{2}]_{GaAs}$ avec le plan $[1\overline{1}00]_{BiSb}$. Un mode de croissance Volmer-Weber est détecté lors de la nucléation, ce qui conduit à la formation d'une couche relaxée dès qu'une épaisseur critique est atteinte.

Dans les deux cas, les mesures électriques mettent en évidence deux canaux de conduction en parallèle. On observe un comportement semi-conducteur de type n dans le bulk à température ambiante ainsi que des états de surface métalliques à basse température (< 55 K). Pour des conditions de croissance optimisées, les échantillons génèrent des états de surface topologiquement protégés qui se manifestent par un changement de type de porteur et par des mobilités de trous élevées.

Mots Clés: Isolant Topologique; alliage $Bi_{1-x}Sb_x$; épitaxie; substrat industriel; GaAs(001); GaAs(111)A.